



A University of Sussex PhD thesis

Available online via Sussex Research Online:

<http://sro.sussex.ac.uk/>

This thesis is protected by copyright which belongs to the author.

This thesis cannot be reproduced or quoted extensively from without first obtaining permission in writing from the Author

The content must not be changed in any way or sold commercially in any format or medium without the formal permission of the Author

When referring to this work, full bibliographic details including the author, title, awarding institution and date of the thesis must be given

Please visit Sussex Research Online for more information and further details



Developing a probabilistic recession model through
characterisation and quantification of the erosion of chalk
sea cliffs in Brighton.

Jamie Mark Gilham

Thesis submitted for the degree of Doctor of Philosophy

Department of Geography

University of Sussex

Submitted
December 2017

Revised
May 2018

Declaration

I hereby declare that this thesis has not been and will not be, submitted in whole or in part to another University for the award of any other degree. I also declare that this thesis is my own work and where ideas of others have been referred to they are acknowledged accordingly.

Signature: *J. M. Gilham*

Executive Summary

This research has developed a methodology for high precision monitoring of coastal chalk sea cliffs using both terrestrial and unmanned aerial vehicle (UAV) digital photogrammetry. Two contrasting study sites of similar geology at Brighton Marina and Telscombe enabled a comparative assessment of cliff behaviour, for an engineered cliff with toe protection and cliff face stabilisation versus a natural cliff subject to active toe erosion respectively. The site at Brighton Marina was monitored between November 2014 and March 2017, during this period no rockfall was detected above the surface change threshold of 0.07 m. For the Telscombe site, monitored between August 2016 and July 2017, volumetric estimations of rockfalls populated a rockfall inventory. Frequency-magnitude analysis of the monthly inventories demonstrated negative power law scaling over seven orders of magnitude with 10,085 mass wasting events and a total volumetric flux of 3,889.35 m³. Statistically significant correlations were found, for the first time, between significant wave height (H_s) and the power law scaling coefficients, β and s with R^2 values of 0.4971 and 0.5793 respectively. The model was an accurate predictor of erosion evidenced by the R^2 of 0.9981 between the model predictions and observations over the data collection period. A Monte Carlo simulation of potential erosion scenarios between 2020 and 2089 was established using these relationships based on H_s probabilities and sea level forecasts derived from the UKCP09 medium emission climate model (A1B) to assess the impact of future climate change on cliff recession. For the most likely cliff recession scenario the model predicts an approximate 6% increase in recession between the current and future (UKCP09 medium emission scenario) conditions from 20.45 m to 21.76 m. The model also estimates the probability of recession breaching the A259 coastal road by 2089, this revealed an increase from 0.0778 to 0.1056 due to the influence of future climate. The photogrammetric models were also used to characterise the Newhaven Chalk cliffs and through kinematic analysis found wedge failure to be the most likely mechanism of failure, with 39.97% of mapped intersections favourable to this mode. A limit equilibrium analysis of the observed conjugate joint sets within

the defended section of cliffs between Brighton Marina and Telscombe was undertaken to assess the risk of any future failure to infrastructure. This revealed that the coastal road would not be at immediate threat (breach) due to any of the modelled wedge failures occurring, however measures would need to be put in place to maintain the road in its current location were any of these failures to occur. A probabilistic recession model using current industry best practice, in the absence of a rockfall inventory, was used to predict future recession for the defended section of cliffs. Within identified 'pinch-points' where the distance between the road and cliff edge was less than 10 m the probability of recession reaching the road over the next 100 years did not exceed 0.0014. A comparison between approaches identified the benefits of the scientific method presented in this research. The outputs of this research offer a new approach for the collection and processing of coastal monitoring data which ultimately drives the prediction of future coastal cliff recession and facilitates effective planning and mitigation.

As part of this research the following papers have been published:

Barlow, J., Gilham, J., & Cofrã, I. I. (2017). Kinematic analysis of sea cliff stability using UAV photogrammetry. *International Journal of Remote Sensing*, 38(8-10), pp. 2464-2479. [Online] DOI: 10.1080/01431161.2016.1275061

Gilham, J., Barlow, J., & Moore, R. (2018). Marine control over negative power law scaling of mass wasting events in chalk sea cliffs with implications for future recession under the UKCP09 medium emission scenario. *Earth Surface Processes and Landforms*. [Online] DOI: 10.1002/esp.4379

Acknowledgements

I would like to acknowledge, the Engineering and Physical Sciences Research Council (EPSRC) and Halcrow Group Ltd. (A CH2M Company) for my funding through an industrial Co-operative Award in Science and Engineering (iCASE) studentship which made this research possible.

There are many people who I owe a great deal of thanks to for their assistance, support and advice throughout my PhD research. Firstly to my supervisors, Dr John Barlow and Professor Roger Moore, whose guidance, expertise and vision have provided me with the opportunity to develop my ideas and ultimately produce this research. John, thank you for always providing me with your time, sharing of knowledge and advice. I am in no doubt that under your supervision I have become a better researcher. Your support and clear focus has assisted me in developing my skillset and I am truly grateful for that. Roger, thank you for always being on hand to assist me whether on site or remotely. Your knowledge, experience in industry and contacts have provided me with perspective to my research whilst enabling me to efficiently network with key contacts and build relationships to develop my thesis. Thank you for your role in providing software available through CH2M and for the regular meetings with geotechnical specialists within the company in developing the modelling aspect of my research.

I would also like to thank Martin Eade at Brighton and Hove City Council. Whose contribution to my research in the sharing of data, publications and expertise alongside the procurement of the thermal imaging camera I am very thankful for. I hope this research has gone some way in providing an answer or two to some of your 'big' questions.

A special mention to the teams at the Channel Coastal Observatory and the British Oceanographic Data Centre whose support and sharing of data in a timely fashion has been very much appreciated and has significantly added to my research.

Thank you to my examiners, Professor Cherith Moses (Univeristy of Sussex) and Dr James Lawrence (Imperial College London) for reviewing my thesis, your pertinent questions and our discussion during my viva, you have both added to the quality of this thesis.

To my fellow researchers and colleagues, thank you for your support, for listening and for the laughs, I will miss you all. A special mention for my 'Saffa sister' Melissa...thank you for your support, your positivity and always being there for me. You are a true friend and I will miss seeing you as often.

To my family, especially my parents, thank you for everything. Your support not only over the past four years but throughout my life has enabled me to achieve what I have thus far. I appreciate everything you have done for me. Also to my 'in-laws' Claire and Alan, thank you for your support over the years it truly means a lot to me.

Finally, to my fiancée Sheryl. I do not have words to convey how much you mean to me or what your unwavering support has helped me to achieve over the years. You have always provided me with context, listened to my struggles and always put a smile on my face. Even through the most difficult of times recently you have stood strong, pushed through and I am full of admiration for you. It is to you that I dedicate this work.

Contents

Declaration.....	i
Executive summary.....	ii
Acknowledgements.....	iv
Contents.....	vi
List of Figures.....	x
List of Tables.....	xiv
Abbreviations.....	xvi
Chapter 1 - Introduction.....	1
1.1. Justification and context for the research.....	1
1.2. Research aims and objectives.....	3
1.3. Structure of the thesis.....	4
Chapter 2 – Literature review.....	6
2.1. Introduction.....	6
2.2. Coastal rock cliffs – an understanding.....	7
2.2.1. Cliff classification.....	8
2.2.2. Chalk cliff failure mechanisms.....	13
2.2.3. Cliff development.....	15
2.3. Processes operating on cliffs.....	18
2.3.1. Cliff processes – marine drivers.....	18
2.3.2. Cliff processes – subaerial drivers.....	21
2.3.3. Subaerial drivers – salt weathering.....	22
2.3.4. Subaerial drivers – thermal weathering – freeze thaw.....	24
2.3.5. Subaerial drivers – meteorological conditions and hydrogeology.....	25
2.3.6. Cliff processes – the influence of future climate.....	26
2.4. Methodologies for recording cliff change.....	27
2.4.1. Historical recession rates.....	27
2.4.2. Terrestrial Laser Scanning (TLS).....	28
2.4.3. Digital photogrammetry.....	30
2.5. Numerical modelling of coastal cliffs.....	32
2.5.1. Deterministic analysis.....	34
2.5.1.1. Limit equilibrium models.....	34
2.5.2. Stochastic methods in parameterising deterministic models.....	38

2.5.3. Processed based numerical modelling of coastal cliffs	38
2.6. Chalk parameters	39
2.7. Management of cliffs and risk	40
2.7.1. Management of cliffs – Cliff Behaviour Units (CBUs)	41
2.7.2. Management of cliffs – cliff recession prediction methods	42
2.7.3. The concept of risk.....	44
2.7.4. Risk management.....	45
2.7.5. Risk assessment	45
2.7.6. Managing future risks	47
2.8. Summary – Current understanding	47
Chapter 3 – Methods	49
3.1. Orthorectification of aerial imagery and recession rate calculation (1957-2013)	49
3.1.1. Datasets	50
3.1.2. Processing of aerial imagery	50
3.1.3. Digitising cliff lines and calculating historical recession rates	52
3.2. Digital photogrammetry for detecting, characterising and quantifying chalk rockfalls ...	55
3.2.1. Photogrammetry workflow.....	55
3.2.2. Ground control networks.....	57
3.2.3. Camera and lens configuration.....	59
3.2.4. Camera settings and methods of capture	60
3.2.5. Interior orientations.....	64
3.2.5.1. Processing	68
3.2.5.2. Results.....	70
3.2.6. Exterior orientations	71
3.2.6.1. Processing	72
3.2.6.2. Results.....	74
3.2.7. Digital terrain model (DTM) generation	76
3.2.8. Processing of data for 2.5D change detection.....	79
3.2.9. Change detection.....	81
3.3. Environmental investigations – thermal imaging	84
3.3.1. Installation and set-up	85
3.3.2. Thermal image optimisation.....	86
3.3.3. Data collection issues.....	89
3.4. Numerical modelling of cliffs – kinematics and limit equilibrium	91

3.4.1. Discontinuity mapping and kinematics.....	91
3.4.2. Limit equilibrium modelling.....	94
3.4.2.1. Input data.....	94
3.4.2.2. Output data.....	96
3.5. Summary.....	96
Chapter 4 – Study area.....	97
4.1. Geomorphology of the coastal chalk cliffs.....	97
4.2. Historical recession rates 1957-2013.....	99
4.2.1. CBUs.....	100
4.2.2. Spatial and temporal trends in retreat rates.....	100
4.3. Coastal cliff protection.....	105
4.3.1. Undercliff Walk – sea wall.....	105
4.3.2. Cliff face stabilisation.....	107
4.3.2.1. Trimming of the cliff face.....	107
4.3.2.2. Rockfall netting.....	108
4.3.2.3. Soil nails (Black Rock).....	108
4.3.2.4. Rock bolting (Chalk).....	109
4.3.3. Impact of cliff protection on recession rates.....	109
4.4. Development and assets at risk from continued cliff recession.....	110
4.5. Environmental conditions.....	114
4.6. Kinematic analysis – Newhaven Chalk geological controls.....	123
4.7. Marine conditions.....	125
4.8. Study sites – Brighton Marina and Telscombe.....	126
Chapter 5 – Results and discussion.....	128
5.1. Change detection.....	128
5.1.1. Terrestrial photogrammetry – Brighton Marina.....	129
5.1.2. UAV photogrammetry – Telscombe.....	133
5.1.2.1. Successive block failures (August – December 2016).....	134
5.1.2.2. Toe erosion and subsequent failure (August 2016 – March 2017).....	140
5.2. Using negative power law scaling of rockfalls to develop a probabilistic recession model.....	142
5.2.1. Negative power law parameter estimation.....	144
5.2.2. Modelling cliff erosion with H_s and sea level rise (SLR).....	147
5.2.3. Model validation.....	152

5.2.4. Erosion modelling results.....	153
5.2.5. Scaling parameters.....	154
5.2.6. Erosion scenarios – probabilistic recession model	155
5.3. Deterministic modelling of wedge failures (limit equilibrium analysis)	160
5.3.1. Factor of Safety (FoS) outputs	160
5.3.2. Impact of potential failures	164
5.3.3. Sensitivity analysis	167
5.4. Probabilistic recession model for the protected section of cliff line between Brighton Marina and Saltdean.....	174
5.4.1. Observed recession rates and associated spatial probability.....	175
5.4.2. Impact of potential wedge failures.....	176
5.4.3. Impact of future climate	177
5.4.4. Projecting historical recession data using a probabilistic model.....	179
5.4.5. Probabilistic recession model – sensitivity analysis.....	181
5.4.6. Impact on the A259 – recession model at identified ‘pinch-points’	183
5.4.7. Comparison of methodological approaches.....	186
5.5. Summary of results	187
Chapter 6 – Conclusions.....	189
6.1. Benefits for the industrial sector	194
6.2. Recommendations for further research	195
References.....	197
Annex and Appendices	220
Annex A – Orthorectification of aerial imagery procedure details.....	220
Appendix A – ADAM 3DM object-distance spreadsheet	222
Appendix B(i) – Sony DSC-H300 interior orientation	223
Appendix B(ii) – Nikon D810 35mm varied lens interior orientation	225
Appendix B(iii) – Nikon D810 35mm fixed/prime lens interior orientation	227
Appendix C – Brighton Marina exterior orientation	229
Appendix D – Telscombe exterior orientation with GCN & flint digitised accuracy check....	232
Appendix E – Probabilistic recession model spreadsheet	235

List of Figures

Chapter 2 – Literature review

Figure 1: A selection of coastal landslide classifications.....	10
Figure 2: A matrix of active sea cliff profiles to be expected on differing bedrock homogeneity versus relative effectiveness of Marine versus Subaerial erosion	11
Figure 3: Types of shore platform.....	13
Figure 4: Basic classification of types of rock failure broadly divided into fall and slides	15
Figure 5: Models for cliff recession due to wave notch development	16
Figure 6: Cliff instability and erosion following the removal of wave action or construction of coastal defences	17
Figure 7: Coastal cliff recession system	19
Figure 8: Factors affecting cliff base erosion for undefended cliff coastlines	20
Figure 9: Comparison of LiDAR and TLS data capture.....	29
Figure 10: Levels of landslide analysis and mechanisms of failure.....	33
Figure 11: The geometric conditions for wedge failure.....	35
Figure 12: Resolution of forces to calculate factor of safety of wedge	36
Figure 13: The Cliff Behaviour Unit framework	42
Figure 14: The constraints to be taken into account in erosion risk management	46

Chapter 3 – Methods

Figure 15: Orthorectification workflow using ENVI 4.8	51
Figure 16: Orthorectification exterior orientation example, Saltdean 1957	52
Figure 17: Digital photogrammetry workflow for terrestrial and UAV applications	56
Figure 18: Ground control networks for photogrammetry study sites Brighton Marina and Telscombe	58
Figure 19: Terrestrial photogrammetry image capture procedures strip and converging image set.....	62
Figure 20: DJI S1000 octocopter and Nikon D810 FX DSLR pre-flight and tabulated UAV information	64
Figure 21: Interior orientation/calibration set up.....	66
Figure 22: Exterior orientation rotation parameters for terrestrial photogrammetry.....	72
Figure 23: Exterior orientation processing from ADAM 3DM CalibCam Manager view.....	72
Figure 24: Example of digitised flint in ADAM 3DM CalibCam	73

Figure 25: DTM generation workflow from raw imagery to DTM surface with imagery using ADAM 3DM CalibCam and 3DM Analyst.....	76
Figure 26: Boxes installed on rear splash wall to determine threshold of detection for terrestrial photogrammetry, Brighton Marina	81
Figure 27: Threshold of change detection for terrestrial photogrammetry, image captured with Nikon D810 35mm prime lens	83
Figure 28: Location of thermal camera and meteorological station at cliffs in Brighton Marina.....	85
Figure 29: Installation of thermal camera in Brighton Marina and calculating thermal image reflectance for the study site in Brighton	88
Figure 30: Thermal image flattening undertaken on 18/12/2014.....	89
Figure 31: Thermal imagery data capture issues.....	90
Figure 32: Discontinuity mapping illustrating joints and faults digitised on the 3D model generated for Telscombe 07/09/2016 using ADAM 3DM analyst.....	92
Chapter 4 – Study area	
Figure 33: Study area geology and elevation.....	98
Figure 34: Retreat rates from 1957-2013 for the entire study area of Brighton Marina to Belle Tout	103-104
Figure 35: Location and dates for installation of sea defences and cliff stabilisation measures.....	106
Figure 36: Cliff trimming of the chalk cliffs in Brighton Marina.....	107
Figure 37: Distance between 2013 cliff top edge and A259	112-113
Figure 38: Cliff failures in Brighton Marina during the winter of 2000/2001	114
Figure 39: Minimum daily air temperature between 2014 and 2016 recorded by met station in Brighton Marina	116
Figure 40: Hourly thermal imagery captured in Brighton Marina between 28-29/12/2014	118-119
Figure 41: Air temperature, average cliff face temperature and minimum cliff face temperature between 31/01/2015 and 07/02/2015	120
Figure 42: Air temperature and minimum cliff surface temperature by section between 31/01/2015 – 07/02/2015	121
Figure 43: Hourly thermal imagery captured in Brighton Marina showing top-down cooling of the cliff face	122
Figure 44: Wolf equal angle stereographic projection of discontinuity data from Telscombe cliffs.....	124

Figure 45: Stereographic representation of discontinuity data for points of intersection between joints and faults for wedge failure.....	125
Figure 46: Location of photogrammetry study sites.....	126
Chapter 5 – Results and discussion	
Figure 47: Surface change between November 2014 and January 2016 at Brighton Marina using terrestrial photogrammetry captured from the Sony DSC-H300 and Nikon D810 35 mm varied lens respectively, raster cell size=0.03 m	130
Figure 48: Surface change between January 2016 and March 2017 at Brighton Marina using terrestrial photogrammetry captured from the Nikon D810 35 mm varied lens and prime lens respectively, raster cell size=0.02 m	131
Figure 49: Surface change between July 2016 and March 2017 at Brighton Marina using terrestrial photogrammetry captured from the Nikon D810 35 mm prime lens, raster cell size=0.02 m	132
Figure 50: Surface change between August 2016 and March 2017 at Telscombe using UAV photogrammetry captured from the Nikon D810 24 mm prime lens, raster cell size=0.10 m	135
Figure 51: Surface change monitoring successive failures in the Newhaven Chalk at Telscombe between 05/08/16 and 06/12/16, cell size=0.10m	136
Figure 52: Wedge failure at Telscombe cliffs leaving overhanging cliff material which failed between the 11th November and the 6th December 2016	137
Figure 53: 3D models in Cloud Compare of successive block failures in the Newhaven Chalk at Telscombe between August and December 2016.....	138
Figure 54: Peacehaven type failure in the Newhaven Chalk	139
Figure 55: Surface change monitoring toe erosion and subsequent failure in the Newhaven Chalk at Telscombe between 05/08/16 and 07/03/17.....	141
Figure 56: Limit equilibrium model of wedge failure between February and March 2017 using Swedge.....	143
Figure 57: Limit equilibrium analysis of wedge failure in Newhaven Chalk, Telscombe effect of toe erosion in steepening of cliff face	144
Figure 58: Power law estimation parameters for August to September 2016.....	146
Figure 59: Normalised power law estimation parameters β and s vs. H_s	149
Figure 60: Example of H_s vs. cumulative distribution probability.....	150
Figure 61: Cumulative probability plot for max failure.....	151
Figure 62: Modelled V_T vs observed V_T for the undefended (no beach) section of Telscombe cliffs.....	152
Figure 63: Example of a simulated erosion model for Telscombe run for 840 months (70 years)	155

Figure 64: Monte Carlo simulation histogram of Log10 transformation of total recession between 2020 and 2089	156
Figure 65: Model predictions of Telscombe cliffline position by 2089	158
Figure 66: Decadal probability of recession breaching the A259 along the unprotected section of cliff line at Telscombe	159
Figure 67: Location of observed conjugate joint sets in the defended section of cliff line from Brighton Marina to Saltdean.....	161
Figure 68: Example of conjugate joint set in protected Newhaven Chalk cliffs between Brighton Marina and Saltdean	162
Figure 69: Frequency of different volumes for potential wedge failures generated from observed conjugate joint sets between Brighton Marina and Saltdean	162
Figure 70: Wedge failure modelling in defended cliffs near Roedean School	165
Figure 71: Wedge failure modelling in defended cliffs 500m west of Saltdean	166
Figure 72: Wedge failure modelling in defended cliffs 700m west of Saltdean	168
Figure 73: Wedge failure modelling near Roedean School representing the second closest distance from cliff edge to A259.....	169
Figure 74: Wedge failure modelling near Roedean School representing the third closest distance from cliff edge to A259.....	170
Figure 75: Sensitivity analysis of modelled wedge failures along defended cliff lines in Brighton using the 25th, 50th and 75th percentile of wedges with reference to FoS value	172
Figure 76: Sensitivity analysis of modelled wedge failures along the defended cliff line in Brighton showing the impact of the range of dip direction for JS1 and JS2.....	173
Figure 77: Brighton Marina to Saltdean road units, classified by distance from cliff edge to A259	175
Figure 78: Probabilistic recession model with present climatic conditions projected for 50 years for the defended cliff line between Brighton Marina and Saltdean	180
Figure 79: Probabilistic recession model with present climatic conditions projected for 100, 200 and 400 years for the defended cliff line between Brighton Marina and Saltdean	181
Figure 80: Probabilistic recession model sensitivity analysis accounting for change in future climatic conditions projected for 50, 100, 200 and 400 years for the defended cliff line between Brighton Marina and Saltdean	182
Figure 81: Probabilistic recession model sensitivity analysis accounting for change in future climatic conditions projected for 50, 100, and 200 years for unit 19.....	184
Figure 82: Probabilistic recession model sensitivity analysis accounting for change in future climatic conditions projected for 50, 100, and 200 years for unit 6.....	186

List of Tables

Chapter 2 – Literature review

Table 1: Average peak strengths of triaxial compression tests	23
Table 2: Pore water salinity test of the Newhaven Chalk formation at Birling Gap East Sussex	23
Table 3: Performance of chalk slopes/cliffs in south east England.....	40

Chapter 3 – Methods

Table 4: Uncertainty for the historical aerial imagery required as input data for DSAS.....	53
Table 5: Camera and lens specifications	59
Table 6: Optimum camera shooting parameters for the Nikon D810	61
Table 7: Exterior orientation component and overall accuracy for monthly UAV photogrammetry models from August 2016 to July 2017	75
Table 8: Camera and model parameters in development of terrestrial photogrammetry methodology	78
Table 9: UAV photogrammetry monthly images captured and individual DTM statistics	80

Chapter 4 – Study area

Table 10: Cliff retreat rates between 1957 and 2013 grouped by aspect	101
Table 11: Comparison of calculated recession rates with Dornbusch et al. (2008).....	102
Table 12: Impact of defences on cliff recession rates.....	110
Table 13: Meteorological data from identified periods of freezing air temperatures between November 2014 and December 2016.....	115
Table 14: Minimum and average cliff surface temperature recordings with time and date of capture.....	117
Table 15: Identified sets from discontinuity analysis using Dips 7.0	123

Chapter 5 – Results and discussion

Table 16: Volume of monthly toe erosion and the subsequent failure between August 2016 and March 2017	140
Table 17: Monthly observed V_T for the unprotected and naturally protected cliff line at Telscombe	153
Table 18: Results of Monte Carlo simulation	157
Table 19: Summary of representative wedge analysis sample for sensitivity analysis.....	171
Table 20: Sensitivity analysis of dip direction for JS1 and JS2 versus FoS.....	174
Table 21: Classified volume of failures observed in BHCC rockfall inventory assigned an annual recession rate.....	177

Table 22: UKCP09 winter and summer changes in precipitation and temperature for south-east England under different emission scenarios and varying probabilities	178
Table 23: Probability and scaling/adjustment factors for winter rainfall and temperature used in the probabilistic recession model for Brighton cliffs between Brighton Marina and Saltdean.....	178

Abbreviations

3DSE	Three Dimensional Standard Error
ALS	Airborne Laser Scanning
BHCC	Brighton and Hove City Council
BODC	British Oceanographic Data Centre
CAA	Civil Aviation Authority
CBU	Cliff Behaviour Unit
CCO	Channel Coastal Observatory
DEFRA	Department for Environment, Food and Rural Affairs
DEM	Digital Elevation Model
dGPS	differential Global Positioning System
DSAS	Digital Shoreline Analysis System
DTM	Digital Terrain Model
EA	Environment Agency
FEA	Finite Element Analysis
FEM	Finite Element Model
FoS	Factor of Safety
GCN	Ground Control Network
GCP	Ground Control Point
H _s	Significant wave height
IPCC	Intergovernmental Panel on Climate Change
LiDAR	Light Detection and Ranging
LRR	Linear Regression Rate
PDOP	Position Dilution of Precision
QRA	Quantitative Risk Assessment

RACE	Risk Assessment of Coastal Erosion
RMSE	Root Mean Squared Error
ROP	Relative Only Point
RPC	Rational Polynomial Coefficient
RSL	Relative Sea Level
SCAPE	Soft Cliff and Platform Erosion
SfM	Structure from Motion
SLR	Sea Level Rise
SMP	Shoreline Management Plan
TLS	Terrestrial Laser Scanning
UAV	Unmanned Aerial Vehicle
UCS	Uniaxial Compressive Strength
UKCP	United Kingdom Climate Projections
USGS	United States Geological Society
WLR	Weighted Linear Regression

Chapter 1 – Introduction

1.1. Justification and context for the research

Rock coasts have been considered a neglected coastal landform (Trenhaile, 1980; 2002; Stephenson, 2000; Kennedy et al., 2014). However, since the turn of the century there has been a notable increase of academic research within this subdiscipline (e.g. Lee et al., 2001; Trenhaile, 2002; Dong & Guzzetti, 2005; Treixeira, 2006; Marques, 2008; Lim et al., 2010; Kennedy et al., 2014; Hurst et al., 2016). This is primarily due to the emergence of new technologies and methods which allow remote sensing data to be captured more efficiently over larger spatial scales in previously difficult to access sites and regions. The ability to acquire these high-resolution datasets, of sub-decimetre accuracy, has enhanced our knowledge of the system and enables the operating processes to be better understood and quantified in terms of their impact on coastal cliff development (Lim, 2014).

An estimated 53% of the coastline in England and Wales are cliffs which are subject to instability and erosion (Moore & Davis, 2015). Approximately 26% of these cliffs have some form of existing engineering protection (Moore & Davis, 2015) to prevent or reduce the rate of recession. The reality of a changing climate (Trenhaile, 2014) compounds the risk to coastal communities as detailed by the United Kingdom Climate Projections 2009 (UKCP09), through sea level rise (Lowe et al., 2009) and increased winter rainfall (Murphy et al., 2009) potentially leading to more severe instability and erosion in the cliff environment. The demand for national guidance in the UK (DEFRA, 2006; 2009a; 2010) on coastal risk management has risen significantly as legacy and growing coastal populations alongside continued development are at ever increasing risk from natural hazards.

Sea cliff environments are dynamic in nature and their evolution can be explained through endogenic and exogenic properties. The mechanical properties of rock slopes (e.g. Selby, 1993; Wyllie & Mah, 2004; Stead & Coggan, 2012) and the significance of geological controls are well

established in the research literature (Trenhaile, 1987; 1997; Mortimore et al., 2004a; 2004b) as they strongly determine the mode of failure. This is exemplified in chalk cliffs by Mortimore et al. (2004a) who determined the mechanical properties of the chalk formations along the East Sussex coast through an assessment of strength properties and by discussing the impact of joint sets which act as shear surfaces.

Sea cliffs are subject to exogenic forcing from both sub-aerial and marine processes. It is widely accepted that the driving force promoting the recession of coastal cliffs is through wave action (Lee & Clark, 2002). Yet the impact of this force is only one component of what is a relatively complex multistage process (Moore & Davis, 2015). When the cliff is decoupled from wave action, as is the case for large sections of the coast in Brighton, the recession of the cliff line does not cease. Weathering and instability higher up the cliff (Moore & Davis, 2015) result in continued landward retreat until a stable angle is reached. The sub-aerial weathering processes of; rainfall leading to saturation (Mortimore et al., 2004b), salt weathering inducing crystallisation in pore spaces (Robinson & Jerwood, 1987; Jerwood et al., 1990; Busby et al., 2004; Lawrence et al., 2013) freeze thaw weathering which leads to fracturing within the rock (Walder & Hallet, 1985; Robinson & Jerwood, 1987; Griggs & Trenhaile 1994; Greenwood & Orford, 2007; Mortimore & Lawrence, 2008) and heat expansion, desiccation and surface slaking, all form a complex multi-process weathering of the rock mass post protection.

Mortimore et al. (2004a) infer from the style and scale of failures observed at Brighton during the winter of 2000-2001 that it takes in the region of 15-20 years after trimming of the cliff face for weathering processes to sufficiently weaken the rock mass to induce failures. The timescale from installation of toe protection measures to the ultimate stable angle of any cliff will vary on a case by case basis due to the individual characteristics, climatic setting and operating processes but may range from decades to millennia (Hutchinson, 1975; Lee & Clark, 2002; Moore et al.,

2010a). Through an appreciation of the suite of processes operating over a variety of spatial and temporal scales the behaviour of the coastal chalk cliff environment can be better understood.

This research explores the instability processes, mechanisms and recession rates of the chalk cliffs at Brighton which pose a significant hazard and risk to people and infrastructure located within close proximity. Brighton and Hove City Council have implemented a variety of coastal defences and cliff stabilisation measures to manage and reduce this risk. A process based systems approach utilising emergent technologies and methodologies forms the basis of the development of recession models presented within this research. This provides coastal managers with a probabilistic tool to evaluate potential risk to infrastructure through time whilst enhancing the strategic regional coastal monitoring of the chalk cliffs.

1.2. Research aims and objectives

This research has developed a probabilistic recession model to assess the risk to infrastructure in Brighton through characterisation and quantification of the erosion and instability of chalk sea cliffs. This was achieved through assimilating a number of geospatial datasets to determine the operating processes in both defended and undefended sites and their impact in the continued development of the system. The following aims and objectives directed the research:

(A1) The primary aim was to characterise and quantify the recession of defended and undefended chalk cliffs between Brighton Marina and Telscombe.

This was achieved through the following objectives:

(O1) Determine the historical rates of recession for defended and undefended chalk cliffs of similar characteristics and exposure in the area.

(O2) Develop a reliable methodology using photogrammetry for high precision monitoring of sea cliffs.

- (O3) Quantify the erosional mass flux from defended cliffs in Brighton Marina and undefended cliffs in Telscombe using terrestrial and UAV photogrammetry respectively.
- (O4) Develop a probabilistic model of chalk cliff recession using negative power law scaling of rockfalls.
- (A2) The secondary aim of the research was to establish the effectiveness of current mitigation approaches.

This was achieved through the following objectives:

- (O5) Determine the dominant mechanism of failure for the chalk cliffs in Brighton and the impact of these failures within defended cliff sections.
- (O6) Estimate the time for cliff recession to impact infrastructure, namely the A259 road for defended and undefended cliffs in Brighton.

1.3. Structure of the thesis

The structure of the thesis reflects the aims and objectives as outlined above. The geo-spatial analysis of historical data provided context for the study site and focused the research into a comparative assessment of defended versus undefended cliffs in Brighton. Application of digital photogrammetry provided an innovative methodological approach to high-precision monitoring of the coastal cliff environment. This enabled the opportunity to better quantify the processes operating over temporal and spatial scales within the cliff system in order to develop a numerical model to predict future recession. The content of the chapters are:

- Chapter 2 Reviews the current knowledge of the coastal rock cliff subdiscipline and assesses the current methodologies for understanding the development of these systems. The concept of risk and the management context is also explored before a summary which outlines the opportunities available for this research.
- Chapter 3 Presents the methodological approaches used in the research. This includes; orthorectification of aerial imagery, development of advanced terrestrial and

UAV photogrammetry surveys, environmental investigations using meteorological data and thermal imaging, kinematic analysis of the Newhaven Chalk and the numerical modelling approaches used to predict future recession.

Chapter 4 Introduces the study sites from a geomorphological perspective, identifies the infrastructure at risk from continued recession and provides context for both the natural, climatic and marine influences, and the anthropogenic influences which have affected the development of the chalk cliffs. This chapter also provides the context for the research through the use of historical recession rates and environmental conditions for the cliffs in Brighton.

Chapter 5 Presents the key results of the research which includes the change detection from the terrestrial and UAV photogrammetry, the statistical numerical modelling enabling future recession to be predicted, deterministic modelling of potential failures within the defended cliff section and an alternative method to recession modelling. Discussion of these results and methodologies is presented within this chapter to outline the key contributions of this research.

Chapter 6 Is the concluding chapter for the research assessing the development of methodologies the impact of the results and the contributions to scientific research. Opportunities for further research are also presented.

Chapter 2 – Literature review

2.1. Introduction

The formation and evolution of coastal rock cliffs are inevitably influenced by spatial and temporal change (e.g. Trenhaile, 1987; Sunamura, 1992; Lee & Clark, 2002; Moore et al. 2010a; Kennedy et al., 2014; Lim, 2014; Moore & Davis, 2015). However data collected to appropriately express these and other aspects are limited, due to the hostile environment which can lead to damage or malfunction of equipment. This, in combination with restricted access and safety issues form key limitations for study and instrumentation. Meanwhile large populations and infrastructure are located at the coast which creates conflict and associated risk. This drives the need for management and demand for knowledge and quantitative data for understanding and prediction which will ultimately lead to more affordable and well informed mitigation.

The current state of coastal cliff research is explored in this chapter through a systems approach, which requires an understanding of the form, materials and processes or drivers which operate and continue to characterise these complex settings. Research to find causal links between recession and exogenic processes through time will enable quantification of these drivers and subsequent development of process driven numerical models would increase the reliability of future recession predictions. Current monitoring methodologies in remote sensing will then be explored to illustrate the procedures and advances in data collection before highlighting the areas for further development and the opportunities this provides. Quantification and monitoring of the coastal cliff environment over greater temporal scales still provides a significant challenge to determining the behaviour of the system. The management context in conjunction with the emergent concept of risk will then be presented as a framework for successful application of the reviewed knowledge and data. The final section of this chapter will contextualise the understanding of the coastal cliff environment and summarise the findings to provide the direction for this research.

2.2. Coastal rock cliffs – an understanding

Rock coasts result from the landward retreat of bedrock at the shoreline (Kennedy et al., 2014) and occupy 80% of the world's coastline (Emery and Kuhn, 1982). These erosional environments form one of the most dynamic in nature yet have received little attention within the research literature (Trenhaile, 1980, 2002; Stephenson, 2000, Kennedy, 2014) with very little reference to the morphology and dynamics of these environments (Guilcher, 1958; Zenkovic, 1967; Bird, 1969; Davies, 1972; King, 1972; Pethick, 1984; Trenhaile, 1987). This recognised trend has notably altered within the last decade due to the ever increasing anthropogenic interaction with these systems (Hopson, 2005) but in the main, due to the emergence of new technologies enabling the opportunity to address problems which were previously inaccessible and on much wider scales (Kennedy et al., 2014). The subdiscipline of rock coasts is in relative infancy in comparison to many other landform systems (Kennedy et al., 2014) with current research being mainly site specific with the hope of inferring a wider system understanding. There is little doubt however that with the notable advances in technology and the ever increasing knowledge base exemplified over the past decade, this provides the catalyst for a change in ethos from speculation (Trenhaile, 1987; Sunamura, 1992; Trenhaile, 1997) to the ability to confidently understand the rock coast system.

There are many definitions of a cliff (Emery & Kuhn, 1982; Sunamura, 1992; Lim, 2014) which are used interchangeably and vary upon application and purpose. Most define the coastal cliff as a steep to near vertical slope as a junction between the terrestrial and marine environments. For the purpose of this research the cliff will be defined from a geomorphological perspective as a system which is a composition of materials, forms and processes comprising of a cliff top, steep slope and cliff toe which forms the boundary between the marine and terrestrial environments (Rendel Geotechnics, 1995; Hooke, 1999; Lim, 2014).

Rock formations dating from the Pre-Cambrian to the Holocene outcrop on the world's coastlines but many have been shaped during the Pleistocene and Holocene covering the last 6,000 years when sea levels were similar to the present level (Bird, 2007). This is detailed by Griggs and Trenhaile (1994) who note that coastal cliffs vary widely as a result of their tectonic setting, structural and lithologic framework and recent geologic history and are a legacy of marine and sub aerial processes that have been operating for thousands of years (Trenhaile, 1987). Griggs and Trenhaile (1994, p.427) raise the pertinent issue, that "even if we completely understood the nature of contemporary erosive processes, it would be difficult to explain morphology of coasts that often retain the vestiges of environmental conditions that were quite different from today."

Understanding the formation and evolution of the coastal environment under investigation is critical in pursuing research within this field (Trenhaile, 1987; Griggs & Trenhaile, 1994; Trenhaile, 1997; Bird, 2000; Lee & Clark, 2002; Mortimore & Duperret, 2004; Bird, 2007; Davidson-Arnott, 2010; Fookes et al., 2012), so that reliable predictions can be made in the future development of the coastal cliff system.

2.2.1. Cliff classification

Classification of cliff environments vary greatly depending on the extent and scale of the environment being studied (Lee & Clark, 2002), and as a result they have been formulated based on criteria which is deemed most important to the author's study, context and application. The simplicity in classifying cliffs by form, geology, temporal or spatial variations and in some cases retreat rates are limited as each neglect some aspect of the complex cliff system (Lim, 2006). Whilst Robinson (1974) and Kimber (1998) express the dynamism of the cliff environment, to attempt to encompass all eventualities in one model would not only become unmanageable but increase significantly in complexity.

Consequently many previous classifications have incorporated the variations between geology and process and as a result been formed on the basis of retreat rates differentiated by hard versus soft rock cliffs (Emery & Kuhn, 1980; Allison, 1989; Lee & Clark, 2002). Figure 1 illustrates a selection of these coastal landslides classified by the Lee and Clark (2002) which demonstrates the variety of modes of failures in different geological formations.

Other classifications have attempted to produce a temporal framework such as Brunsden and Lee (2004) who proposed stages of; initiation, consolidation, readjustment and abandonment although importantly each stage does not necessarily lead to the next. Whilst Emery and Kuhn (1982, p. 646) provided a temporal classification which refers to three main stages of sea cliffs:

1. Active cliffs - exposed to continuous retreat under the influence of both marine and subaerial erosion,
2. Inactive cliffs – which are commonly mantled by a cover of talus supporting land vegetation,
3. Former cliffs – that have been removed from the influences of marine erosion so that subaerial erosion can round the crest.

These stages provide the most simplistic of classifications, Emery and Kuhn (1982) express that the active cliffs are the most complex in nature however overlook the complexities of understanding and quantifying the effects of processes and managing former sea cliffs which will be illustrated throughout this research.

Active sea cliffs are controlled by two major agents; marine erosion and subaerial erosion, and three major characteristics; homogeneity, structure and local pre-cliff topography (Emery & Kuhn, 1982). The interaction between these agents and characteristics provide the basis for the type of cliff profile that will be experienced (Figure 2). The matrix of profiles (Figure 2) illustrate the types of cliff profiles expected under varying marine versus subaerial erosion patterns.

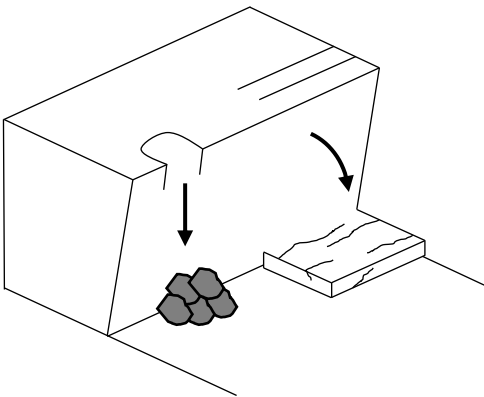
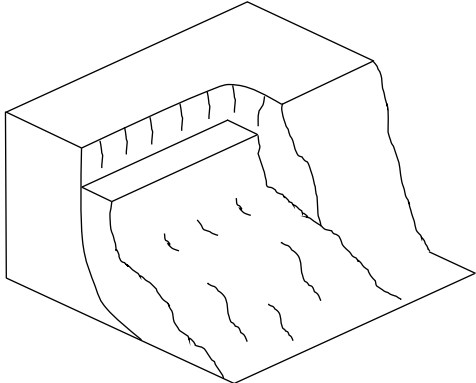
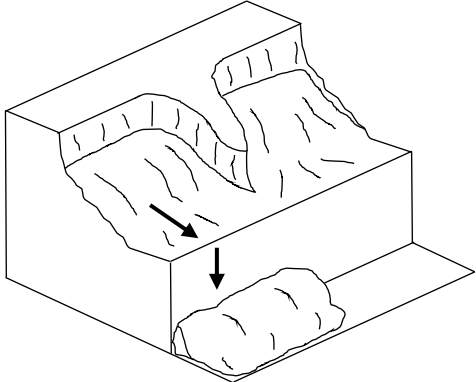
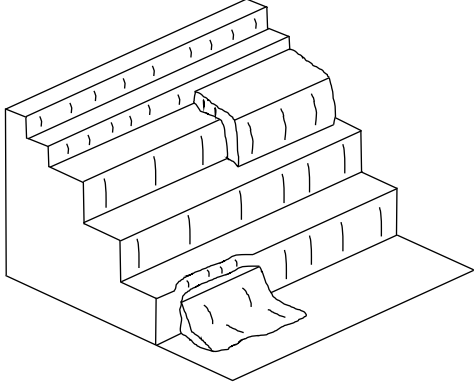
	Schematic	Example
Simple cliff		 Birling Gap, East Sussex
Simple landslide		 Scarborough, North Yorkshire
Composite cliff		 Purbeck, Dorset
Complex cliff		 Black Ven, Dorset

Figure 1: A selection of coastal landslide classifications. (Images as presented in Moore & Davis, 2015).

In environments where marine erosion dominates, more frequent larger magnitude events are more likely to occur, under these conditions the cliff will exhibit a steep to near vertical profile. Whereas, when subaerial erosion dominates cliff profiles tend to be shallower in gradient due to regular spalling of material until a stable angle is reached. The effect of varying resistance of geology is explored which can lead to an overhang of material where the cliff top is more resistant and the toe is undercut or conversely a more shallow profile above the more resistant rock at the toe of the cliff. It is critical to mention that Emery and Kuhn's (1982) classification does not include the interaction of shore platforms or variations in geology throughout the cliff profile which are both equally important criteria in the classification of cliffs.

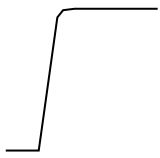
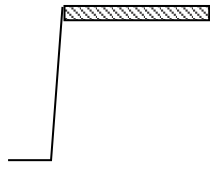
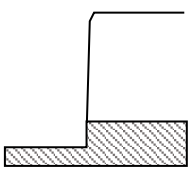
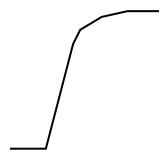
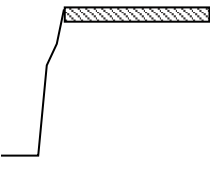
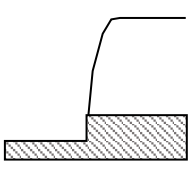
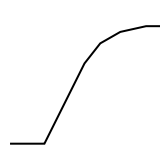
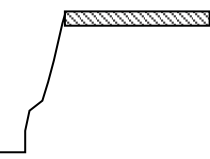
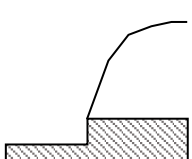
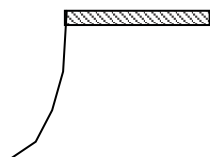
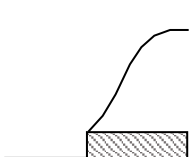
	Homogenous	Resistant at top	Resistant at toe
$M \gg SA$			
$M > SA$			
$M = SA$			
$M < SA$			

Figure 2: A matrix of active sea cliff profiles to be expected on differing bedrock homogeneity versus relative effectiveness of Marine (M) versus Subaerial (SA) erosion (Adapted from Emery & Kuhn, 1982, p. 645).

Many cliff studies and therefore classifications, focus on quantities, mechanisms and causes of failures and as a result overlook the wider connection with the development of shore platforms

(Moses & Robinson, 2011). Shore platforms are present on over half of the coastline of the British Isles (Bird, 2007; Moses, 2014) and provide yet another aspect to classifying the coastal cliff environment. Similarly, our understanding of shore platforms is limited (Moses, 2014) with the change in term from wave cut platform implying genesis to shore platform a clear example of this. There are various types of shore platform (Figure 3) which are characterised by geology and process which can be exposed by the tidal regime (Phillips, 1969; Steers, 1973; Trenhaile 1974; Sissons, 1976; Davies & Stephens, 1978; Moses, 2014). Seaward sloping shore platforms (Figure 3) are commonly planation surfaces, formed primarily through abrasion, that extend from the high tide limit at the base of the cliff and slope gently but not always uniformly offshore beyond the low tide line. The result is a steeply inclined cliff face, as opposed to a vertical profile if no platform existed (Bird, 2007). High tide shore platforms are horizontal or near horizontal (slope of less than 1°) and are exposed to subaerial erosion for much of the tidal cycle with wave action only occurring during high spring tides or storm events. They are well developed in microtidal climates with low energy waves particularly on sandstone and mudstone. It is also possible that shore platforms above the mean high tide level were originally formed when sea level was higher than today. It is common for this type of platform to end abruptly in a steep drop or small cliff (Bird, 2007). Similar platforms are found at the low tide level which are submerged for long periods of the tidal cycle and are common on limestone coasts, they are generally subhorizontal in nature with subaerial erosion only possible at low tide. Plunging cliffs (Figure 3) can be formed under a number of conditions, these include; cliffs of resistant geology where the period of time that sea level has been at its current level has not been long enough for waves to erode the cliff, soft rock cliffs where high energy waves cut a platform below the low tide level (Bird, 2007) and faulting where a rock has been uplifted and a shore platform has not developed due to insufficient time for wave action to erode the rock mass.

Sunamura (1992) proposed that the type of shore platform exhibited is largely due to the balance between wave action and rock resistance, with sloping platforms formed in relatively

weak rock and subject to energetic waves whilst sub-horizontal platforms are more likely to develop in more resistant rock with a less energetic wave climate. Whilst Trenhaile (1999) found strong positive relationships between platform gradient and tidal range which can, at least partially, explain the observed sloping platforms along the macrotidal UK coastline versus the sub-horizontal microtidal coastline of Australia. Formulating an understanding of these systems is crucial in defining and classifying differing coastal cliff settings as the shore platform environments can act as a natural barrier to marine processes or drivers depending upon type (Figure 3).

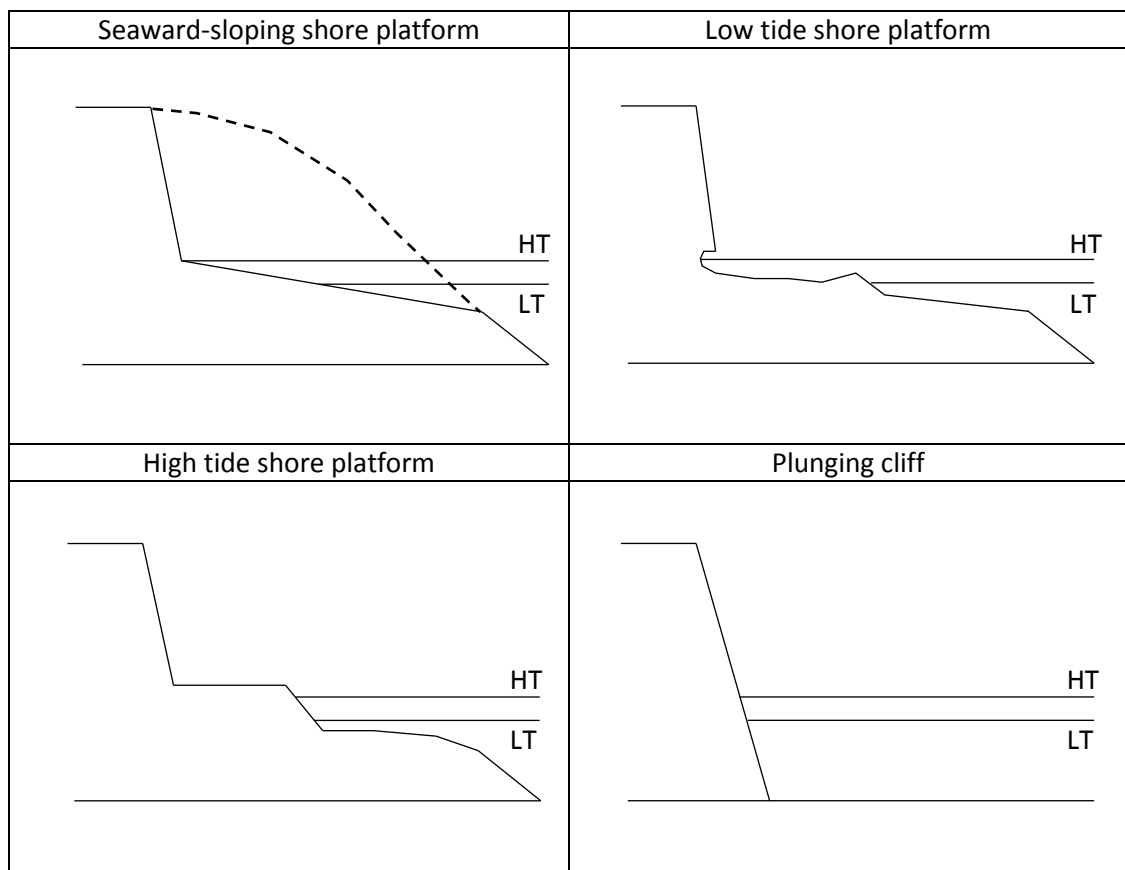


Figure 3: Types of shore platform, (HT) high tide and (LT) low tide (Adapted from Bird, 2007, p. 76).

2.2.2. Chalk cliff failure mechanisms

The interaction of the foreshore environment in combination with the geologic setting and the variety of drivers operating over differing spatial and temporal scales ultimately governs the development of the coastal landform. Importantly, the resisting force of the cliff is derived from its material properties and formation, with failures occurring along planes of weakness which

include joints, faults or bedding surfaces. These areas of weakness in cliffs of varying or seemingly homogenous geology can be exploited by the environmental factors operating locally through; weathering, hydrological conditions, tidal and wave regimes and even anthropogenic interaction.

The varying susceptibility of the coastal cliff environment to the drivers or processes influencing the system development often results in a state equilibrium (Cambers, 1976; Bray & Hooke, 1997; Lee & Clark, 2002) which is validated with the known episodic nature of location and magnitude of failures in coastal cliffs. Due to the inherent complexities within this field, likewise with classifications, cliff development has been broadly divided into the types of failure; sliding, falling and toppling (DeFreitas, 1972; DeFreitas & Watters, 1973; Pritchard & Savigny, 1990; Cruden & Varnes, 1996; Dikau et al., 1996; Hantz et al., 2003; Hungr et al., 2014). The most common types of chalk cliff failure are presented in Figure 4. The criteria for each of these failure types will be briefly explained. Rockfalls are characterised by a mass that is detached from a cliff face or slope along a surface whereby no shear displacement occurs. Generally this type of failure is initiated by a climatic event, such as heavy rainfall freeze thaw or weathering of the rock over a greater period of time all of which can impact the forces acting within the rock mass. Failure through toppling occurs when individual columns of rock are formed by discontinuities that dip steeply into the face. This type of failure can be subdivided into block and flexural toppling. Block toppling is when the steeply inclined discontinuities coincide with a set of orthogonal joints which determine the column height thus forming failure blocks which push forward. Whereas flexural toppling is characterised by the steeply inclined continuous columns of rock (Wylie & Mah, 2004) which break in flexure as they bend forward. Sliding occurs when either a single or combination of discontinuities in the rock mass form blocks or wedges. Planar sliding takes place on a relatively uniform single failure plane surface (Goodman, 1989) that fails by sliding down the slope parallel to the dip of the plane of weakness. Whereas wedge failure occurs when a combination of discontinuities intersect and dip out of the cliff face, the geometry

of the wedge and slope face determines the failure surface(s) and the direction of sliding along the line of intersection (Wylie & Mah, 2004). Although in chalk cliffs which have been decoupled from wave erosion spalling of material due to subaerial weathering can occur over time and recession continues albeit at a much slower rate.

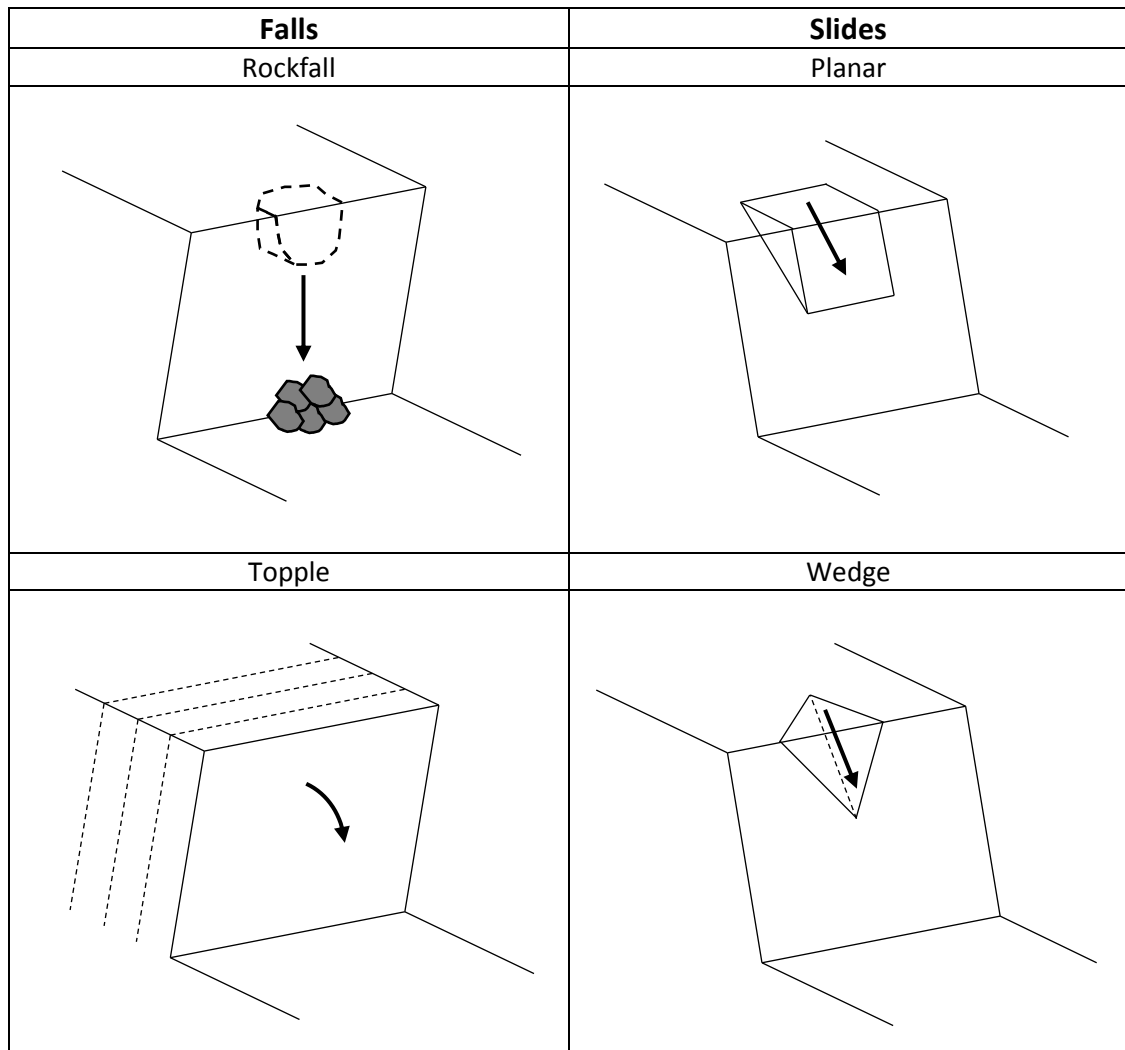


Figure 4: Basic classification of types of rock failure broadly divided into fall and slides (Adapted from Wylie & Mah, 2004).

2.2.3. Cliff development

May and Heeps (1985) reported, for the chalk cliffs of South-East England, the formation and evolution of the cliffs was as a result of wave action which led to toe erosion and subsequent failure (Figure 5). Stage 1 (Figure 5) represents a vertical cliff profile, when the cliff is subject to wave action erosion occurs and develops a wave cut notch (Stage 2 – Figure 5). This

creates weakness in the rock mass and increases strain which propagates from the notch through the cliff. This can extend from the notch (B' Stage 2, Figure 5) through to the cliff top (A' – Stage 2, Figure 5) or to a tension crack if one is present. The material then fails and is removed by wave action before the cycle can restart from (B'' to A' – Stage 4, Figure 5).

	Model 1 - Failure Plane extends to cliff top	Model 2 - Tension Crack Failure
Stage 1		
Stage 2		
Stage 3		
Stage 4		

Figure 5: Models for cliff recession due to wave notch development [A- initial position of cliff top, A'- cliff top location after failure, B- initial cliff toe position, B'- cliff toe location with debris, B''- cliff toe position after debris removed, C- debris extent (Adapted from Sunamura, 1992, p.112).

Although this classification is rather basic in nature as it assumes homogeneity throughout the cliff, without planes of weakness which are characteristic of the chalk cliffs of South-East England, it illustrates the well-established mode of sea cliff failure. Whilst other classifications cover a wealth of differing geologic conditions or the ability to include multiple failures of varying mechanisms (Geomorphological Services Ltd, 1986; Lee & Clark, 2002), Figure 4 and Figure 5 represent the differing modes of failure exhibited in coastal chalk cliffs.

When sea cliffs are decoupled from wave erosion the development of the system alters. The episodic failures initiated by toe erosion are removed and the equilibrium in the system changes (Moore & Davis, 2015). Figure 6 presents the effects of removing the dominant driving force which develops sea cliffs. The construction of sea defences still impacts the cliff-shore platform system with increased downwearing of the platform (Dornbusch et al., 2007). Landward of the

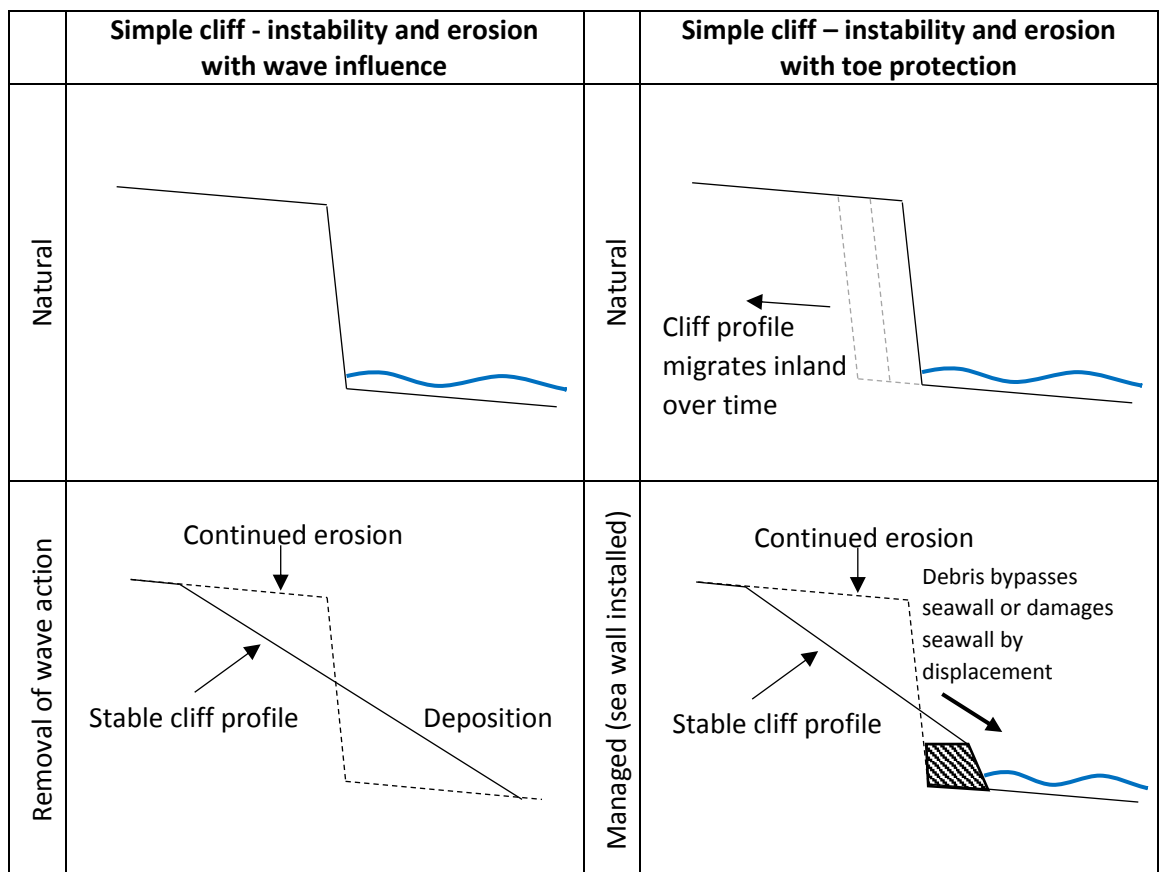


Figure 6: Cliff instability and erosion following the removal of wave action or construction of coastal defences (Adapted from Moore & Davis, 2015).

defences subaerial weathering dominates continued recession as the cliff moves towards a new equilibrium and ultimately a stable cliff angle. Temporally, this process can range from tens to hundreds, or even thousands of years (Hutchinson, 1975; Lee & Clark, 2002; Moore et al. 2010a; Moore & Davis, 2015).

2.3. Processes operating on cliffs

As discussed formulating a quantifiable understanding of the coastal cliff environment is challenging. This is because many exogenic processes operate over differing scales and the ability to isolate and measure the impact of any individual factor in the natural environment remains difficult. For context, Lim (2014) discusses the varying scales of environmental controls on cliff behaviour; such as the regional processes of relative sea level and climatic fluctuations, alongside the local factors of rainfall, hydrogeology and the impact of wave climate. To ascertain the current state of the system the drivers of change need to be understood, these are readily classified into the marine and subaerial. The relative importance of marine and subaerial processes is still contested (Stephenson & Kirk 2000a, 2000b; Trenhaile, 2001; Lawrence et al., 2013; Lim, 2014; Dornbusch, 2015; Lawrence & Mortimore, 2015). This section shall provide a review of the current literature to provide clarification of these processes within the coastal cliff system before highlighting the effect future climate change may have on coastal cliffs.

2.3.1. Cliff processes – marine drivers

It is widely accepted that the two main factors leading to cliff collapse are marine driven (May, 1971; May & Heeps, 1985; Sunamura, 1992; Hutchinson, 2002; Lee & Clark 2002; Dornbusch et al., 2006a, 2006b; Bird, 2007; Lim et al., 2010; Lim, 2014; Dornbusch, 2015) through wave attack and water weakening due to the saturation of the cliff material. Sunamura (1992) summarises (Figure 7) the major controls on coastal cliff recession.

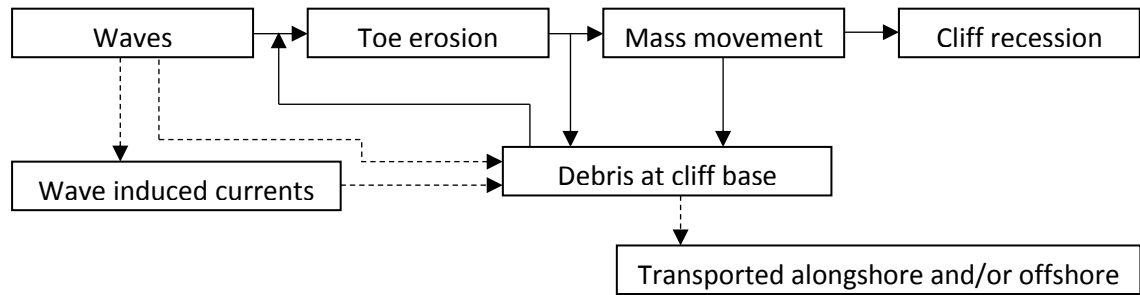


Figure 7: Coastal cliff recession system (Sunamura, 1992, p. 76).

Instability within the cliff can be due to the increase in slope angle or in slope stress caused by basal erosion (Sunamura, 1992) resulting in mass movements through the various types presented in Figure 4. The occurrence of these failures is determined by the geology, structure and properties of the material (Sunamura, 1992) with the interaction of these criteria displayed in Figure 8. The failures caused as a result of basal erosion commonly result in high magnitude low frequency events and are more common along unprotected cliff coastlines. The ability to confidently interpret the respective effects of multiple marine variables is restricted (Lim et al., 2011; Lim, 2014). This is due to the quantity and complex interactions between various site specific attributes; the foreshore and offshore topography, coastline orientation and sediment availability as well as regional controls which include; offshore wave climates, tidal regimes and prevailing wind directions.

The forces involved in toe erosion through marine interaction are primarily the assailing force of waves and the resisting force of rocks (Sunamura, 2015). The impact of waves plays a key role in the development of the cliff environment (Lee & Clark, 2002) namely the direct undercutting and over steepening of the cliff face (Sunamura, 1992). The assailing force of waves exerts both a hydraulic and mechanical action on the cliff face. Hydraulic action can be subdivided into compression, tension and shearing as detailed by Sunamura (2015) and can occur simultaneously when the wave interacts with the cliff face. Compression is defined as the force which acts perpendicular to the cliff, whereas tension represents the force when the wave

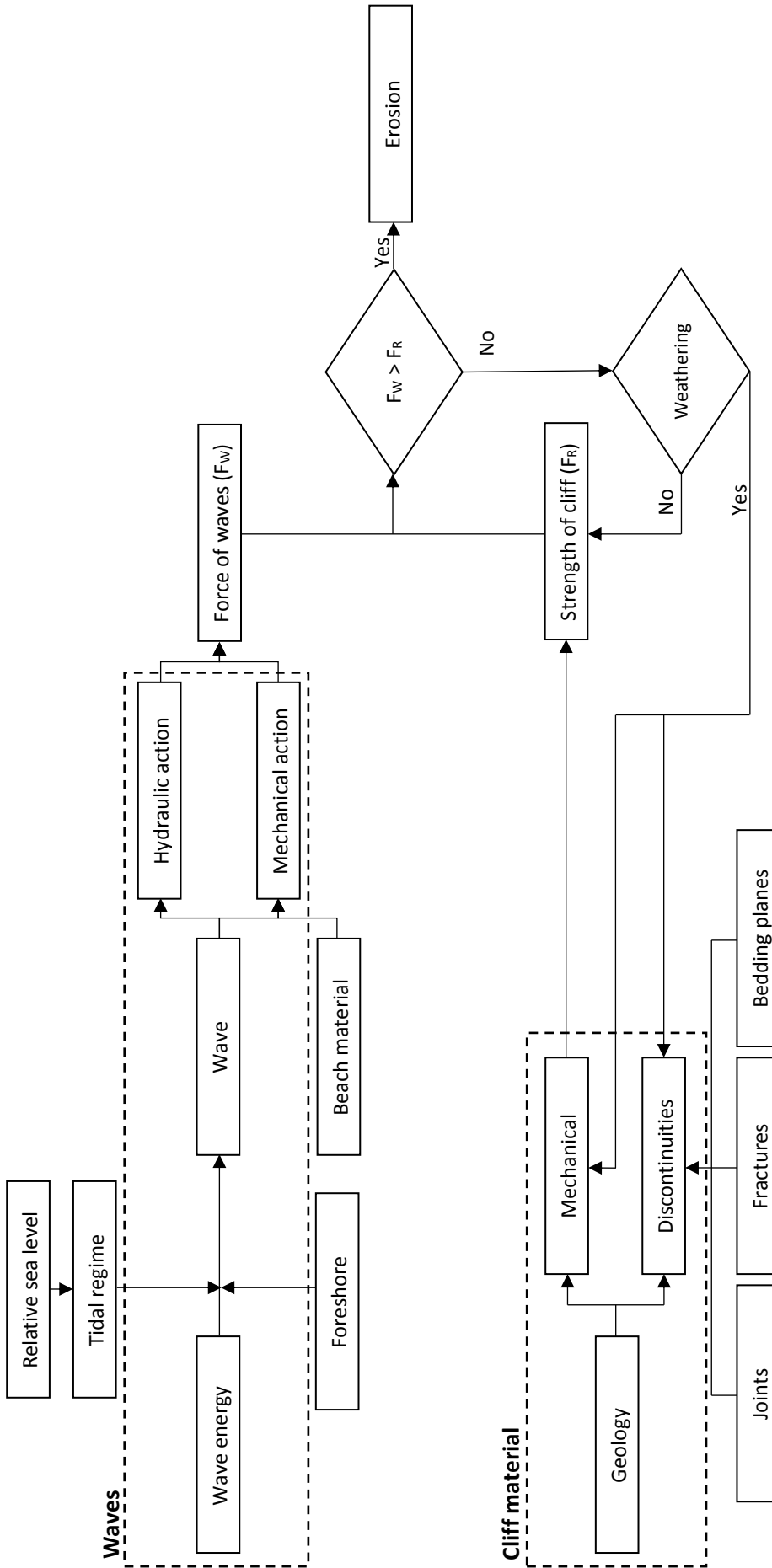


Figure 8: Factors affecting cliff base erosion for undefended cliff coastlines (Adapted from Sunamura, 1992, p. 77, after Sunamura, 1983).

recedes which can induce plucking or quarrying. Shearing represents a tangential force which occurs when the wave strikes the cliff face and water is driven upwards. The interaction between wave action and the endogenic properties of the rock mass can lead to explosive forces produced upon the delivery of waves along discontinuities (Sunamura, 2015). Prolonged compressive action increases the stress environment in the rock mass leading to a reduction in overall strength. In attempts to quantify the impact of waves on cliffs significant wave height (Trenhaile, 2009; Kline et al., 2014) and significant breaking wave height (Walkden & Hall, 2005; 2011) have been used to derive models to estimate toe erosion (Sunamura, 2015). Other key roles of waves within the system include the removal of debris and shore platform lowering, the latter can prove vital as the foreshore will widen dissipating wave energy if little or no lowering occurs.

2.3.2. Cliff processes – subaerial drivers

The accepted dominant driver to cliff development, the marine processes, have been overwhelmingly studied (Sunamura, 1992; Lim, 2014) disproportionately considering the opposition to this assumption being raised over 50 years ago (Steers, 1962). The debate still exists within current literature (Lawrence et al., 2013; Dornbusch, 2015; Lawrence & Mortimore, 2015) with the dispute over the relative importance of salt-weathering on chalk cliffs, reaffirming the difficulty in quantifying the effect of a single process and the subsequent application in applying relative importance to the various processes marine or subaerial that operate in this dynamic environment. There is agreement, in recent research (Lawrence et al., 2013; Dornbusch, 2015; Lawrence & Mortimore, 2015) that surface weathering takes place through a range of subaerial processes (Dornbusch, 2015) which can have a profound effect on the behaviour of the cliff system (Mortimore et al., 2004a; 2004b). The subaerial processes which will be reviewed are salt weathering and freeze-thaw whilst other weather induced

processes such as wetting and drying and the role of hydrogeology will be introduced and their importance noted.

2.3.3. Subaerial drivers – salt weathering

Salt weakening affects both hard and soft rock cliffs (Lawrence et al., 2013) yet has only been sporadically investigated (Williams & Robinson, 1981; Robinson & Jerwood, 1987; Jerwood et al., 1990; Busby et al., 2004; Williams & Robinson, 2006; Lawrence et al., 2013). Trenhaile (2008) identified that weathering processes, including salt weakening, play an indirect role in quarrying jointed rocks. Although the primary focus of Trenhaile (2008) was on the processes operating on the shore platform, Lawrence et al. (2013) infer this would be similar to the processes which operate with the salt which remains on the cliff face as a result of wave action.

Lawrence et al. (2013) highlight two types of salt weakening which affects the strength of the cliff; physical attack known as haloclasty, the formation of salt crystals previously identified by Jerwood et al. (1990) and Busby et al. (2004) and chemical salt weathering through dissolution (Fookes & Hawkins, 1988). Lawrence et al. (2013) conducted several triaxial compression tests (Table 1) on the Seaford and Lewes Chalk formations, with sample locations at various cliff height locations, exposed to differing amounts of spray and wave interaction against the Shoreham cement quarry (SCQ) acting as a control. The cell pressures were chosen to represent the following cliff settings (Lawrence et al., 2013); 5 m below ground level (bgl) representative of the stresses near the cliff top in the weathered zone of bedrock, 30 m bgl which is the minimum height of the majority of cliff sections in the chalk and all the research sites were at least this height and 60 m bgl characteristic of a high chalk cliff.

The triaxial testing undertaken by Lawrence et al. (2013) identified a salt weakening process in the chalk which resulted in up to a 55% decrease in peak strength from the inland control saturated cores. Duperret et al. (2005) found a higher, 70% reduction in Uniaxial Compressive Strength (UCS) of chalk in North-West France due to the same process. Furthermore, Lawrence

Locality	Chalk formation	CP (kPa)	Ave. peak strength saturated (MPa)			Ave. peak strength dry (MPa)			Percentage strength retained from dry to saturated strength (% to 1dp)		
			80	470	970	80	470	970	80	470	970
Birling Gap	Seaford Chalk		2.97	3.16	4.04	7.24	9.74	9.8	41.0%	32.4%	41.2%
SCQ	Seaford Chalk		3.50		6.77	11.37		18.47	30.8%		36.7%
SCQ salt saturated	Seaford Chalk		2.84		4.02						
Hope Gap	Lewes Chalk		2.26	3.82	4.85	4.96		5.63	45.6%		86.1%
France	Lewes Chalk		2.34	4.31	3.22	7.73		10.26	30.3%		31.4%
SCQ	Lewes Chalk		4.31			7.95			54.2%		
SCQ salt saturated	Lewes Chalk		1.98			8.31			23.8%		

Table 1: Average peak strengths of triaxial compression tests (adapted from Lawrence et al., 2013, p.18) [CP - Cell pressures refer to depths within the cliff at 5 m back from the face, 80 - 5 m bgl, 470 - 30 m bgl, 970 - 60 m bgl].

et al. (2013) tested the pore water salinity of the Newhaven Chalk located at Birling Gap, East Sussex, UK (Table 2). The salinity of sea water is approximately 35 parts per thousand (ppt), the results achieved 16 m back from the cliff edge at this location were 12 ppt greater than sea water with the base of the cliff and high tide mark exhibiting values six times greater in concentration.

Sample site description	Salinity (ppt) [seawater salinity is approximately 35 ppt.]
Base of cliff (direct contact with cliffs)	232
2m above high tide mark	234
Top of cliff	No pore water extracted
Top of cliff 16m back from the edge	45

Table 2: Pore water salinity test of the Newhaven Chalk formation at Birling Gap East Sussex (Lawrence et al., 2013, p. 18).

The combination of the haloclasty and salt chemical weathering alongside the wettability of the chalk tested by Lawrence et al. (2013) consistently reduces the strength of the rock material by 75 to 80% irrespective of formation, triaxial cell pressure or material properties (Lawrence et al., 2013). The results achieved by Lawrence et al. (2013) provide a quantification of previous work (Robinson & Jerwood, 1987; Jerwood et al., 1990; Busby et al., 2004) on the effects of salt weakening of rock, the growth of crystals identified through Scanning Electron Microscope (SEM) imaging within the chalk matrix alters and mechanically weakens the structure of the rock and consequently plays a key role in subaerial weathering of the cliff face.

2.3.4. Subaerial drivers – thermal weathering - freeze thaw

Hales and Roering (2007) determine that the depth and intensity of frost cracking, in rock, is primarily dependent on mean annual temperatures. The effects of thermal weathering processes on coastal cliffs are also relatively unexplored (Walder & Hallet, 1985; Robinson & Jerwood, 1987; Griggs & Trenhaile 1994; Greenwood & Orford, 2007) especially within temperate climates (Mortimore & Lawrence, 2008). There is little reference to thermal data collection and studies of thermal behaviour of cliff faces in the literature. The results from the European funded INTERREG IIIa INFORM (Information for cliff recession management) project (Mortimore & Lawrence, 2008) provide the only thermal images of the coastal chalk cliff face albeit sporadic in both location and duration of collection and with the research goal to determine whether fractured cliff faces showed different thermal characteristics to intact rock due to the effect of reduced moisture content within the main body of rock.

The few available studies of thermal behaviour within the coastal environment have tended to focus on the shore platform (Robinson & Jerwood, 1987) with others focussing on laboratory experiments (Goudie, 1974; Williams & Robinson, 1981; McGreevy, 1982). The processes which operate to cause the weakening of the rock structure can occur due to hydrostatic pressure as water is drawn to freezing points (Walder & Hallet, 1985; Robinson & Jerwood, 1987) or through volumetric changes as the water forms ice in discontinuities within the rock structure (Goudie, 1974; Robinson & Jerwood, 1978; Williams and Robinson, 1981; McGreevey, 1982; Hallet, 1983; Fahey, 1985; Walder and Hallet, 1986; Williams and Robinson, 1991). Robinson & Jerwood (1987) conclude that the degree of damage that freeze thaw cycles cause is directly related to the duration of exposure to freezing temperatures, this accompanied with the presence of salt weakening can lead to a compounding process although this is disputed (McGreevy, 1982). The impact and behaviour of thermal variation in coastal cliff faces is clearly underrepresented in the literature, this may be due to the difficulty in accessing and collecting datasets at the same

temporal scale as readily available meteorological data however there is opportunity to explore this field and provide explanation to this significant subaerial process.

2.3.5. Subaerial drivers – meteorological conditions and hydrogeology

Meteorological conditions play an important and often overlooked role in determining the mechanisms of coastal cliffs recession (Hutchinson 1972; Lee & Clark, 2002; Lim, 2014). Of the meteorological processes rainfall is the most influential in detaching cliff material (Lee & Clark, 2002) through compacting the soil, reducing infiltration capacity, increasing pore water pressure and by removing particles directly. The combination of heavy rainfall and wind which drives into the cliff face can compound the effect and lead to increase impact force and saturation. Importantly, Lee and Clark (2002) detail two types of rainfall event and their effects; short lived high intensity storms where the infiltration capacity is exceeded and prolonged low intensity rainfall which saturates the rock or soil. However, Mortimore et al. (2004b) conclude that the prevailing control on rain-induced cliff failure is the geology of the cliff, with the location and mode of failure controlled by the jointing, faults or planes of weakness.

The effect of water within the cliff face and wider rock mass can play a pivotal role in cliff recession (Attewell & Farmer, 1976; Lee & Clark, 2002; Brunsten & Lee, 2004; Lim, 2014) and in some cases dramatically alter the behaviour of the material. An important measure of the impact of water within a rock mass is the pore water pressure. This is the pressure exerted by water within fractures or pore spaces within the material. The water table for coastal cliffs is commonly at sea level but rises hinterland. The effect of pore water pressures varies between rock mass dependent on how well drained the material is and its homogeneity. For example chalk cliffs with marly beds may lead to perched water tables and an increase in pore water pressure along these planes. Thus, the impact of heavy or prolonged rainfall can lead to a change in the stress environment as the pore water pressure increases, the shear strength decreases which leads to instability with the rock mass. Duperret et al. (2005) investigated the

effect of groundwater and sea weathering cycles on the North-Western chalk cliffs of France and reported that saturation of the varying chalk types; Newhaven, Lewes and Seaford produce a distinct decrease of UCS of 47%, 33% and 20% respectively. Furthermore it has been widely suggested that this water weakening effect is a triggering mechanism for chalk cliff collapses following prolonged periods of heavy rainfall. Importantly this pattern is not uniformly recorded across the cliff cross section, the greatest decrease of chalk UCS was noted at the base of the cliff which was not inundated by sea water but experienced regular salt spray and crystallisation (Duperret et al., 2005). With lower recordings of reduction in UCS on the shore platform and the lowest near the cliff base with freshwater springs. Duperret et al. (2005) conclude that when the chalk is submitted to a 10 day wetting and drying cycle the strength and Young's modulus of the material reaches the lowest value recorded due to disaggregation and salt crystallisation. Lageat et al. (2006) reaffirm the importance of subaerial weathering by stating that the subaerial processes are the main drivers of failure in the chalk cliffs of France and that the marine influences only act as a transportation mechanism to remove rock fall.

2.3.6. Cliff processes – the influence of future climate

Future climatic change is likely to have a noticeable influence on the marine environment through increased frequency of storms and greater wave energy consequently leading to more rapid development of coastal cliffs (Moore & Davis, 2015). This issue is scarcely quantified in the literature (Lim, 2014) with only a few studies (Clarke & Smethurst, 2010; Dijkstra & Dixon, 2010; Moore et al., 2010a; 2010b) attempting to quantify climatic variations impact on slope processes. Whilst various models exist which propose future climatic scenarios (Lowe et al., 2009; Murphy et al., 2009) the ability to use this data in formulating future behaviour and therefore recession of coastal cliffs is more challenging. Therefore, an appreciation of the cliff as a system is imperative to understand the processes which form recessive change both

presently but also with reference to future predictions. This provides a key focus to this research and is explored within the following chapters.

2.4. Methodologies for recording cliff change

This section will review the methodologies utilised in recording cliff change through historical cliff recession rates as well as the high resolution data capturing techniques in Terrestrial Laser Scanning (TLS) and digital photogrammetry, which provide the opportunity for much larger spatial datasets to be captured in relatively short timescales. The increasing availability and reliability of data collected for geomorphological investigations have provided a more robust and holistic understanding of coastal cliff environments which were previously unreachable or methodologically unachievable (Adams & Chandler, 2003; Lim, 2014). Whilst issues still remain in appropriately differentiating between continuous and episodic change (Lim et al., 2005) through acquisition of remotely sensed datasets in the coastal cliff environment evidently progress has been made.

2.4.1. Historical recession rates

Many studies which have recorded cliff change have been undertaken to quantify recession as a measure of cliff top or cliff toe landward recession, this is exemplified by the amount of research undertaken for the south-east coastline of the UK (May, 1971; Thorburn, 1977; May & Heeps, 1985; Cleeve & Williams, 1987; Dornbusch et al., 2006a; Dornbusch et al., 2008) and likewise in northern France (Prêcheur, 1960; Bialek, 1969, LCHF, 1972; Costa et al., 2004; Pierre & Lahousse, 2006).

The process of calculating historical recession rates has relied upon historical maps and aerial photography to plot or digitise cliff lines and measure change from user defined transects over the study period of interest. However, the former of these datasets introduce significant errors (Anders & Byrnes, 1991; Thieler & Danforth, 1994; Dornbusch et al., 2006b) due to plotting accuracies, pencil width and contraction and expansion of the paper which are further

exacerbated by rescaling various maps to overlay sequential datasets. The use of aerial photography has reduced these errors (Dornbusch et al., 2006a; 2006b) however noticeable error is still introduced through georeferencing images whereby error can be equal to the annual recession rate calculated, as opposed to orthorectifying which changes the images from a perspective to orthogonal dataset, correct in all three planes (Moore et al., 2003; Paine & Kiser, 2003; Dornbusch et al., 2008; Kloehn et al., 2008; Morgan et al., 2010). The importance of previous results which are published should not be underestimated as they provide valuable insights into cliff behaviour over many decades. Critically, the known associated errors need to be reported and the resultant effects understood and applied to determine a statistical confidence for the recession rates.

2.4.2. Terrestrial Laser Scanning (TLS)

Terrestrial Laser Scanning (TLS) is a relatively recent advancement in spatial data acquisition (Buckley et al., 2008) which allows high resolution digital data to be collected. Analysis of sequential models can be used to quantify change and determine the geomorphic processes in operation through a systems understanding. Operationally, TLS records the reflected laser light from the equipment's location to the ground logging the time taken. A distance is then computed and a model constructed, this method could be undertaken at various resolutions dependent on the requirement of the final output and can be deployed terrestrially or aurally.

The above method is very useful in attaining a ground model of areas without abrupt changes in elevation such as a cliff. LiDAR data is collected as a series of points but is limited in the number which can be captured from a near vertical slope (Figure 9A) as aircraft sensors are typically downward looking. As a result cliff faces are not well represented in the point cloud. To overcome this limitation, terrestrial sensors have been used to map the cliff face directly from the foreshore (Figure 9B).

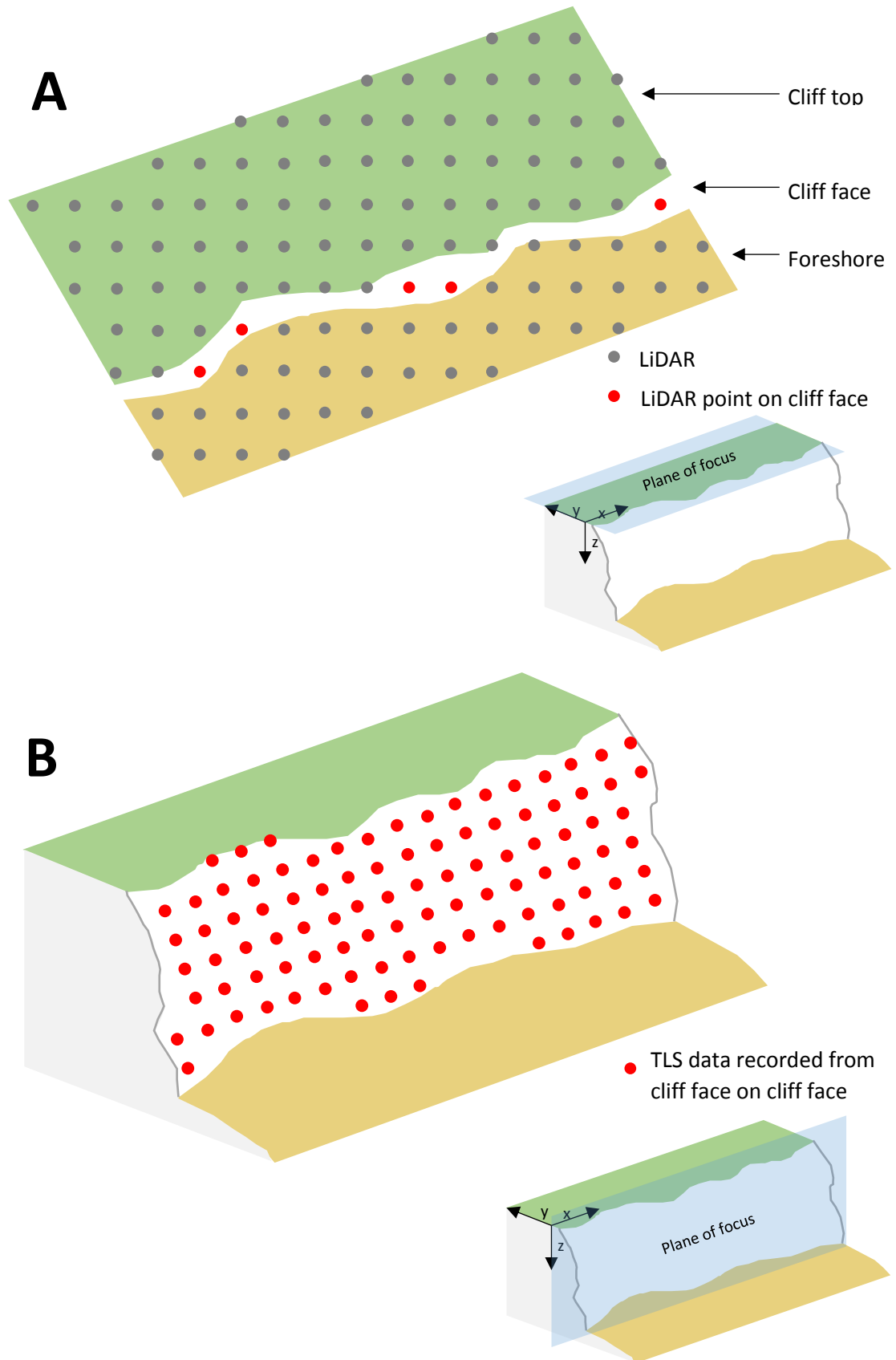


Figure 9: Comparison of (A) LiDAR and (B) TLS data capture.

There have been various studies which have used this methodology as a source of data capture (Lim et al., 2005; Rosser et al., 2007; Buckley et al., 2008; Abellán et al., 2009; Bovington, 2013a) with various reported accuracies, from centimetre accuracy (Abellán et al., 2009) to detection of rockfalls only greater than 0.25 m (Bovington, 2013a) although the latter is largely due to the post-processing of the data rather than the equipment or methodology itself. TLS provides the opportunity to obtain repeatable surveys with consistently high accuracy (Rosser et al., 2005) using a more advantageous view point in the 'x' and 'z' plane as illustrated in Figure 9. The advancement and application of this technology including the ability to use Airborne Laser Scanning (ALS) has provided accessibility to the cliff environment and the ability to capture large datasets in a relatively short timescale. The promise of repeat surveys with either TLS or ALS provide a new and valuable insight into quantifying cliff behaviour both temporally and spatially (Lim, 2014) although importantly, as with all remote sensing data, the errors associated with these datasets need to be carefully understood to provide meaningful results (Buckley et al., 2008; Lim, 2014).

2.4.3. Digital photogrammetry

The emergence of digital photogrammetry, which followed the technological advances in small and medium format digital cameras, over a decade ago (Graham & Koh, 2002; Westoby et al., 2012) has seen terrestrial and automated aerial photogrammetry become an influential tool in the advancement of remote sensing for three dimensional topographic modelling (Huang, 2000; Lim, 2006; Remondino & El-Hakim, 2006; Matthews, 2008; Eisenbeiß, 2009; Fraser & Cronk, 2009; Lim, 2014). The method has advanced significantly in recent years with the development of soft copy triangulation and image based terrain extraction algorithms (Westoby et al., 2012) which has enhanced the data and model outputs formulated from stereo-pairs.

Digital photogrammetry has been used on various projects from close-range applications including gully erosion (Betts & DeRose, 1999; Marzloff & Poesen, 2009) and river bed

topography (Lane, 2000; Chandler et al., 2002) to larger site wide investigations in the field of glacial surface change (Keutterling & Thomas, 2006) and geological discontinuity characterisation (Krosley et al., 2006; Sturznegger & Stead, 2009; Barlow et al., 2017).

Lim et al. (2005) combined time of flight laser scanning and photogrammetry to locate and quantify sequential datasets on the hard rock cliffs in North Yorkshire, where the datasets could be aligned with 0.04 m accuracy. A crucial comparison reported by Lim et al. (2005) highlights the over estimations of volumetric loss from aerial derived cliff recession rates. Based on the two sites surveyed (A & B) which were predicted to retreat at 0.075 m per year the volumetric loss was predicted to be 15.75 m³ and 13.31 m³ respectively however the average change detected were 57% (6.80 m³) and 25% (9.99 m³) lower using the data collected through the laser scanner and photogrammetry. Although these results could not be attributed directly to the low accuracy of the retreat rates calculated or the natural episodic nature of cliff recession through frequency and magnitude of events, the results provided by Lim et al. (2005) raise pertinent questions with regards to the accuracy of retreat rate data. It is apparent that a combination of these techniques is required to formulate a quantifiable understanding of cliff development.

Westoby et al. (2012) used digital photogrammetry to build three dimensional models of several topographic locations based in Aberystwyth, Wales. The data outputs included point clouds which formed the basis for Digital Elevation Models (DEMs). Results varied extensively from neighbouring locations with point densities in excess of 8,700 points/m² compared to a site-wide median of 7.35 points/m² leading to large areas of interpolation of the final model created. As with many other cases deploying UAV photogrammetry, the structure from motion (SfM) method used to generate the models utilises a relative image space requiring post processing to transform the model to a real-world coordinate system. The SfM method can yield results of sub-decimetres in accuracy (Rehak et al., 2013) but requires convergent imagery from a variety

of ranges to obtain optimum accuracy (James & Robson, 2014). Barlow et al. (2017) present the traditional photogrammetry method by using a calibrated camera and strip data capture to maximise the spatial extent of data capture in modelling sea cliffs. Whilst there are clear successes in deploying digital photogrammetry to geomorphological investigations the continued advances in both hardware and software means there is opportunity for methodological and data precision improvements to be attained.

2.5. Numerical modelling of coastal cliffs

Failures in rock masses are complex four dimensional events (Lim, 2014) which vary considerably based on the internal; geological and geotechnical properties and external; marine and subaerial erosion controls. There have been various applications of numerical models in the cliff environment (Hencher et al., 1996; Davies et al., 1998; Kimber et al., 1998; Stead et al., 2004; Quinn et al., 2010) as reported by Lim (2014), with the sophistication of these methods increasing in line with technological advances (Stead & Coggan, 2012). Coupled with an increased understanding of the system and the mathematical simulations achievable, the application of modelling increases the knowledge base for successful implementation of any management decision.

Numerical modelling of slopes is useful in a variety of situations whether there be a wide range of geotechnical data available or data is limited and the mechanism of failure not well constrained (Stead & Coggan, 2012). The first stage in developing a numerical model of a rock slope is through kinematic or stereographic analysis (Stead et al., 2006; Stead & Coggan, 2012). By mapping the orientations of penetrative discontinuities, determining the angular associations between such planes and given the shear strength along these surfaces (Barlow et al., 2017) within the rock slope an assessment of the mechanisms of failure can be undertaken (Kliche, 1999; Wylie & Mah, 2004). A kinematic analysis is not able to locate the discontinuities in space, quantify the size of a failure block nor account for hydrogeological conditions or any other

exogenic forcing on the rock mass. The plotting of poles on a stereonet does however provide discontinuity variables such as dip and dip direction and is useful in determining clusters or sets of discontinuities in the rock mass for which averaged dip and dip direction can be calculated. This data can prove very useful in subsequent modelling of the rock mass to determine the potential of any future failures under the mechanisms identified. Current platforms for such analysis include DIPS (Rocscience, 2011) which allows significant detail on discontinuity variables to be included in the analysis (orientation, persistence, waviness, roughness). Barlow et al. (2017) conducted a kinematic analysis of the Newhaven Chalk cliffs in Telscombe which forms the initial investigation of slope stability within the defended cliff sections developed in this research. Stead and Coggan (2012) present a toolbox of slope analytical methods (Figure 10) which are dependent on the complexity of the rock slope failure mechanism under investigation. From limit equilibrium methods along a persistent discontinuity on basal or lateral surfaces to complex translation or rotation failures which require hybrid finite or discrete element models. For this

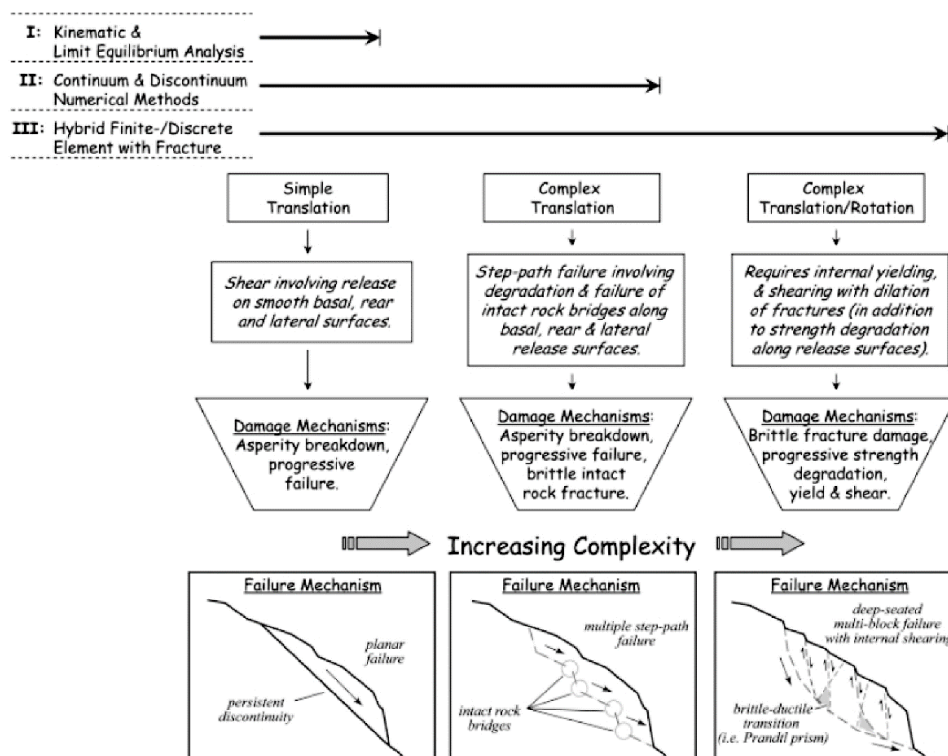


Figure 10: Levels of landslide analysis and mechanisms of failure (Stead & Coggan, 2012, p. 145 after Stead et al., 2006).

research the distinct element modelling approach was used. Deterministic and stochastic methodological approaches are reviewed within this section.

2.5.1. Deterministic analysis

Deterministic analyses are based on constitutive properties of slope materials and shear surfaces using values which have been measured or obtained from geological parameters at the site (Park & West, 2001). Various methodological approaches using the deterministic approach exist, two of the most common are limit equilibrium models and finite element models (FEMs).

2.5.1.1. Limit equilibrium models

The traditional method to determine risk of slope failure utilises the limit equilibrium analysis (Park & West, 2001). The method was introduced by Jaeger (1971) and Kutter (1974) for the purpose of rock slope stability and has been developed into commonly applied methods by Hoek and Bray (1981) and Goodman (1976). Stead and Coggan (2012) note that the limit equilibrium method remains the most common form of slope stability analysis both for rock and soil slopes when failure is planar, multiplanar or wedge in nature. The analysis is usually undertaken using data averages, for example the mean dip direction of respective joint sets from a given dataset. Traditionally this method is utilised to determine the risk of failure through the factor of safety (FoS) (Park & West, 2001). This has enabled many applications of rock slope stability in engineering of slopes with distributed joint systems (Carter & Lajtai, 1991).

The method and physics of failure in limit equilibrium modelling is presented through wedge failure. This method has developed considerably (Stead & Coggan, 2012) in terms of the software to model these failures which now enables the user to include the persistence of the joint sets and complete probabilistic and combination analyses. The following variables are used to assist in the explanation of this failure mechanism: (α_i) trend of intersection, (ψ_i) plunge of intersection, (ψ_{fi}) inclination of the slope face and (α_i & α'_i) the possible range of sliding. The

geometry for wedge failure is illustrated in Figure 11 which describes the basic mechanics for sliding to occur, the general conditions of wedge failure are (Wyllie & Mah, 2004):

- Two planes that always intersect in a line (Figure 11A). This 'line' is represented by the point of intersection of the planes on the stereonet (Figure 11B) with the orientation defined by the trend (α_i) and plunge (ψ_i).
- The plunge of the line of intersection must be flatter than the dip of the face and steeper than the average friction angle of the two planes (where sliding would occur). This is expressed by $\psi_{fi} > \psi_i > \phi$ and illustrated in Figures 11B and 11C. The inclination of the slope face ψ_{fi} is measured at right angles to the line of intersection.

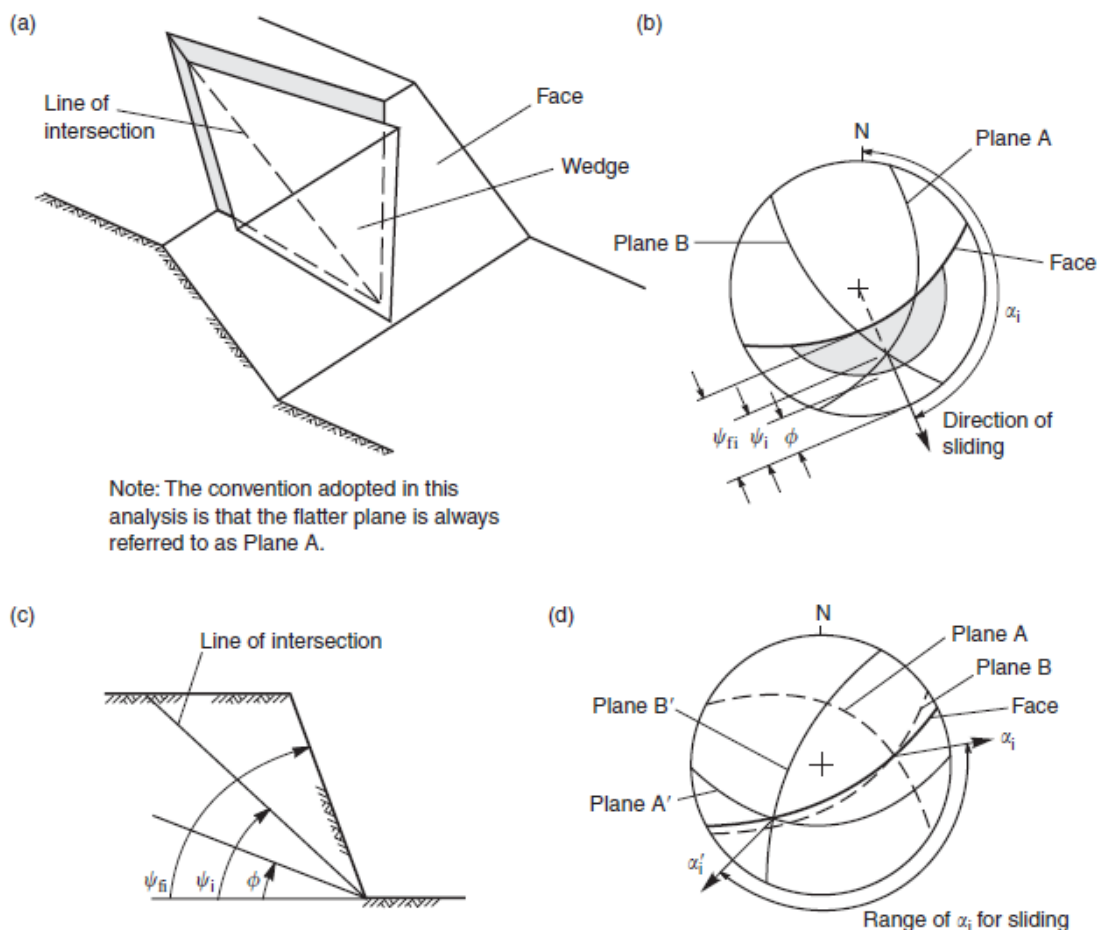


Figure 11: The geometric conditions for wedge failure: (A) pictorial view of wedge failure, (B) stereonet showing the orientation of the line of intersection, and the range of the plunge of the line of intersection ψ_i where failure is feasible, (C) view of slope at right angles to the line of intersection, (D) stereonet showing the range in the trend of the line of intersection α_i where wedge failure is feasible (Source: Wylie & Mah, 2004, p. 155).

- The line of intersection must dip out of the slope face for sliding to be feasible, illustrated in Figure 11D as the range between α_i and α'_i .

The FoS however cannot be determined from the stereonet output as it requires inputs pertinent to the site and rock mass which include geometry and the shear strength of each plane (Wyllie & Mah, 2004). Using the wedge presented in Figure 11 the FoS, assuming that friction provides the only resistance to sliding and the friction angle is equal for both planes, can be expressed by:

$$\text{FoS} = \frac{(R_A + R_B) \tan \phi}{W \sin \psi_i}$$

where R_A and R_B are the normal reactions provided by planes A and B, which are the discontinuities observed in the rock mass (Figure 12). The component of weight is expressed as $W \sin \psi_i$ and following Wyllie and Mah (2004) the forces of R_A and R_B can be found by resolving them into components normal and parallel to the direction along the line of intersection:

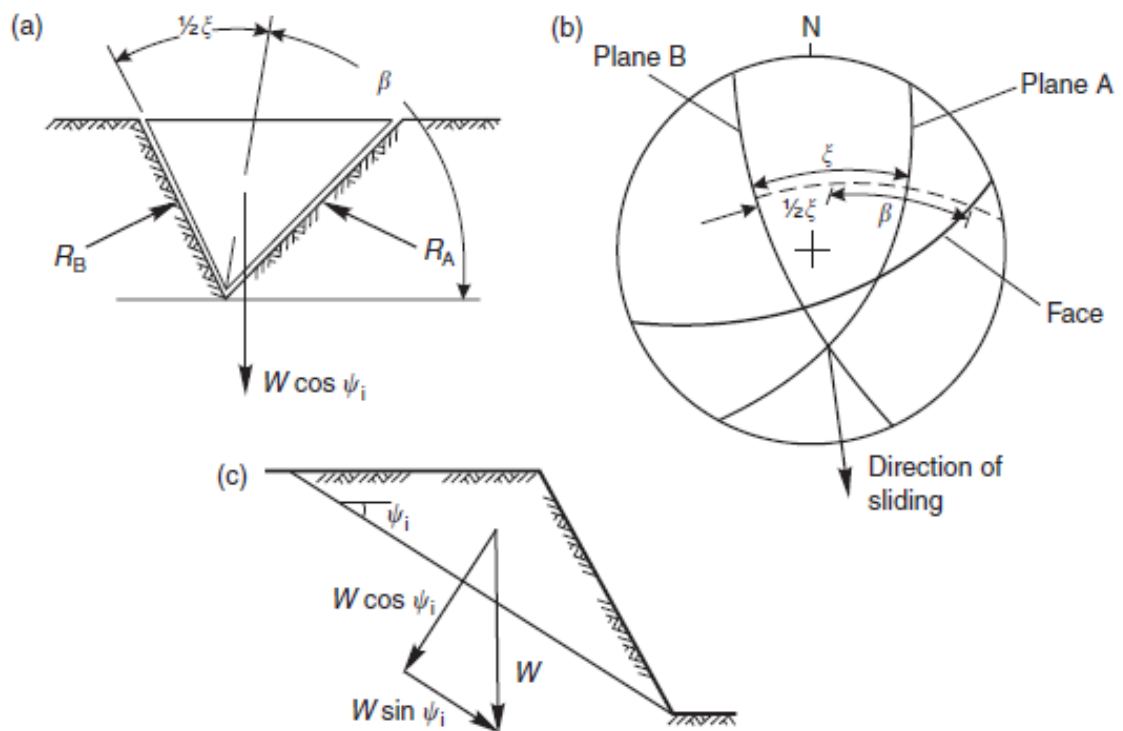


Figure 12: Resolution of forces to calculate factor of safety of wedge: (A) view of wedge looking at the slope face which shows the definition of angles β and ξ , and reactions on sliding planes R_A and R_B , (B) stereonet showing measurement of angles β and ξ , (C) cross-section of wedge showing resolution of wedge weight W (Source: Wyllie & Mah, 2004, p. 156).

$$R_A \sin\left(\beta - \frac{1}{2}\xi\right) = R_B \sin\left(\beta + \frac{1}{2}\xi\right)$$

$$R_A \cos\left(\beta - \frac{1}{2}\xi\right) + R_B \cos\left(\beta + \frac{1}{2}\xi\right)$$

$$= W \sin\psi_i$$

where the angles β and ξ are found in Figure 12B and represent the angles measured on the great circle which from the pole to the line of intersection. For the equilibrium state to be met the normal components have to be equal and the sum of the parallel components has to equal the component of the weight which acts down the line of intersection. The method presented here is the physics of failure in a simplistic form, however different friction angles and cohesion can be incorporated into the model alongside different shear strengths and the role of ground water pressure (Hoek et al., 1973). As the values of β and ξ cannot be measured in the field (Wyllie & Mah, 2004) dip and dip directions obtainable from measurements on 3D models or from field surveying are required to build the more complex model. The equations presented form the basis of the wedge stability analysis in software platforms such as Swedge (Rocscience, 2011) which is used within this research. An explanation of the comprehensive analysis used to determine limit equilibrium of wedge failures is presented in Wyllie and Mah (2004, Appendix III), which enables tension cracks and different values for each plane to be inputted into the analysis.

More complex methods exist for modelling rock slope systems with an increasing failure complexity (Figure 10) such as finite element models (Selby et al., 1988; Selby, 1993). Applications of such models have been limited with regards to chalk cliffs, due to the characteristic brittle nature of failure, with findings largely qualitative modelled from idealised chalk cliffs (Wolters & Müller, 2008) that only indicate trends found rather than accurate stress information.

2.5.2. Stochastic methods in parameterising deterministic models

Stochastic or probabilistic analysis accounts for the natural variability or uncertainty in parameters used in the deterministic approach. In rock slope engineering the geomorphological conditions have an inherent variability that is difficult to quantify particularly for the sub-surface (Park & West, 2001). Statistical parameters can be extracted from the geotechnical data and a region of uncertainty for input values mathematically distributed by the user (Tabba, 1984), for example normal or lognormal. These models produce outputs which classify the potential probability of failures commonly through the Monte Carlo simulation (Park & West, 2001). Applications of this method allowing for uncertainty in measurements and variation within the rock mass can therefore provide a more reliable output (Park & West, 2001).

The decision of which method to apply to any engineering geology study is dependent on the site characteristics and the desired output from the investigation. The option in most commercially available software for modelling these issues now include a combination of the approaches readily referred to as hybrid or combination processing.

2.5.3. Process based numerical modelling of coastal cliffs

Traditionally recession predictions of eroding cliff lines have been determined by extrapolating historical observations (Walkden & Dickson, 2008) over a given temporal period. This approach is problematic as measured recession rates are often similar to the precision of the data and extrapolation of these rates forward in time assumes erosion will not be influenced by projected changes in exogenic boundary conditions (Rosser et al., 2005; Walkden & Dickson, 2008; Lim et al., 2010). The impact of other cliff system parameters are also overlooked as the impact of shore platforms, beaches and anthropogenic structures which interact with the cliff are not accounted for. Walkden and Hall (2005) generated a process driven model, Soft Cliff And Platform Erosion (SCAPE), to simulate change of the cliff/platform coasts over decadal and centennial time scales. The SCAPE model through its development enabled inputs such as;

negative feedback to be included in the system under investigation and removal of coastal protection measures. The model has also been applied in practice to assess coastal management problems and strategies on the Naze peninsula in Essex (Walkden & Hall, 2005) and the North Norfolk coast (Walkden & Hall, 2011). Further development of the model was undertaken to account for future sea-level rise through 2D models (Walkden & Dickson, 2008; Ashton et al., 2011). The SCAPE model represented a shift in approach from the traditional extrapolation of observations over given temporal periods to account for the behaviour of the coastal cliff system and the potential future recession. However the model has several limitations, firstly although the generation of 2D models can account for cross shore sediment movement individual cross sections of the cliff are produced offering no 2.5D or 3D model output. The process driven models operate in abstract and behavioural terms, whereby a set of user inputted controlling parameters such as; rock strength, wave climate and foreshore environment are linked by a series of system interactions. However there is little appreciation of the geomorphic structure of the rock mass, how failures occur spatially along discontinuities in three dimension or temporally through erosional cycles. Although the behaviour of the system is accounted for the direct impact and relative importance of environmental parameters is limited. User processing time can also be increased by the inclusion of probabilistic data (Walkden, 2010), for example projections of sea level rise, as a single state has to be entered for each model run as an automated stochastic processing method is currently unavailable.

2.6. Chalk parameters

For the majority of chalk, which has not been substantially weathered to become disaggregated, mass strength is controlled by the network of discontinuities. This is due to the relatively low strength along these planes in proportion to the intact rock mass strength (Lord et al., 2002). Many joints occur as sets of fractures within the rock that are prevalent through much of the rock mass (Hencher, 2012), which exist due to processes of cooling, burial or orogenic events (Hancock, 1985; Mandl, 2005; Hencher, 2012). There is a wealth of literature which have

undertaken laboratory tests to define strength parameters of sampled chalk (Hutchinson, 1972; Lake, 1975; Clayton, 1978; Fletcher & Mizon, 1984; Twine & Wright, 1991; Mortimore, 2004a; 2004b) however these tests on core samples are not representative of the larger body of rock. In situ testing of the rock mass is rarely practical or economically feasible (Sjöberg, 1992) as a result many cores are compacted in an attempt to replicate natural conditions.

Lord et al. (2002) report moderately conservative strength parameters of the Upper Chalk (now White Chalk subgroup) with cohesion (c') of 20 kN/m² and a friction angle (ϕ') of 39° with the worst credible parameters of $c'=0$ kN/m² and $\phi'=34^\circ$. These values are in agreement with the back analysis of failures reported by Hoek and Bray (1981) who report a range of c' of 20-50 kN/m² and ϕ' of 39°. In the chalk at Joss Bay, Isle of Thanet, Hutchinson (1972) found a peak c' of 131 kN/m² and $\phi'=42^\circ$ with a residual c' of 0 kN/m² and $\phi'=30^\circ$. For ground modelling of the chalk cliffs in Brighton undertaken during the development of the stabilisation schemes a c' value of 15 kN/m² and $\phi'=37^\circ$ was used for undisturbed (shear along discontinuity) chalk (High-Point Rendel, 2002). The performance of chalk slopes in south-east England are summarised in Table 3. These results determine the type of cliff development that can be expected with cliffs of a given angle (Lord et al., 2002). This can be useful in implementing stabilisation schemes and provide insight into the future chalk slope/cliff environment.

Angle of slope or cliff face	Slope behaviour
75°	Short term stable angle or long term stable angle in massive chalk with spalling
63°	Actively eroding chalk cliffs
53°	Stable cut angle with some spalling
45°	Stable cut angle for long-term maintenance of vegetation
33°	Geological stable angle of a chalk escarpment and a stable cut angle in weathered chalk

Table 3: Performance of chalk slopes/cliffs in south east England (data derived from Lord et al., 2002).

2.7. Management of cliffs and risk

Chalk cliffs in England occupy more than 400 km or 10% of the coastline (Hopson, 2005) and in the broader scope of the UK over one million people live within 1 km of chalk cliffs resulting in

a significant percentage of the population and infrastructure exposed to the hazard of cliff collapse (Lawrence et al., 2013). As a result, the probability of adverse consequences to the environment, human and socio-economic infrastructure are increasing (Stavrou et al., 2011).

Management of the coastal zone has received increasing attention from both policy makers and practitioners at national and international levels over the last 20 years (McInnes & Moore, 2011). The move in the UK by the Department of Environment, Food and Rural Affairs (DEFRA) towards a new approach to coastal risk management in England led to the Environment Agency (EA) being given the overall responsibility for coastal risk management (DEFRA, 2007). The development of Shoreline Management Plans (SMPs) followed and is the framework for which risk is assessed, mitigation is considered and decisions are taken for units of the UK coastline.

There is now recognition that strategies are required at the various administrative levels in order to research, understand and adapt to the challenges of climate change in relation to cliff instability and coastal erosion (DEFRA, 2009b; McInnes, 2009; McInnes & Moore, 2011). These strategies are being introduced and implemented from the Government, Environment Agency (EA) and local authorities respectively.

2.7.1. Management of cliffs - Cliff Behaviour Units (CBUs)

To appropriately manage the cliff system an understanding for all aspects of the environment must be attained including the cliff top, cliff face and foreshore together with the operating processes. The concept of Cliff Behaviour Units (CBUs) provides an important framework for the management of these dynamic environments (Lee, 1997; Moore et al., 1998; Lee & Clark, 2002) spanning from the foreshore to cliff top within the wider framework of the coastal section and littoral cell (Figure 13). The functional application of defining these units is to provide a basis for explaining the interrelationships between process and form of cliff sections exhibiting similar characteristics and development in the recognised episodic and uncertain nature of the recession process (Lee & Clark, 2002).

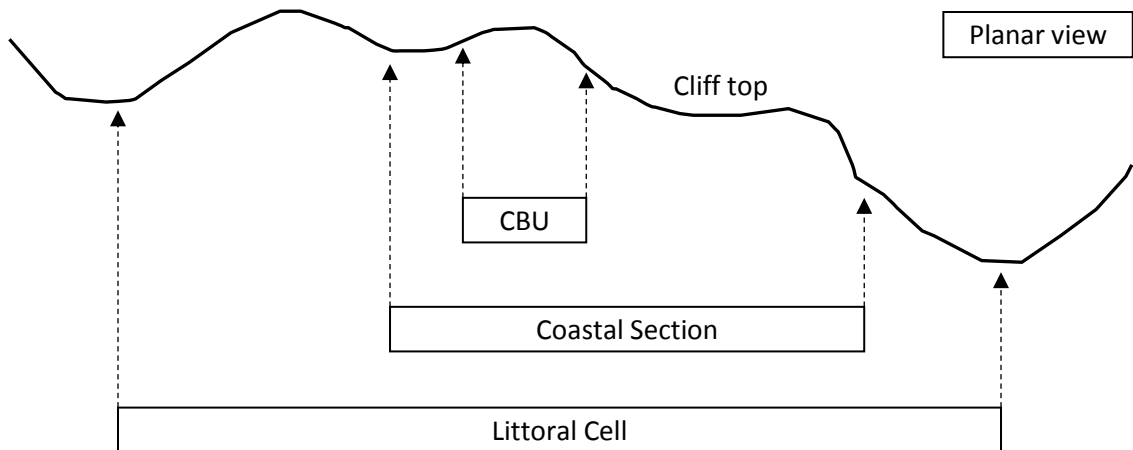


Figure 13: The Cliff Behaviour Unit framework (Adapted from Lee & Clark, 2002, p. 11).

Brunsdon & Lee (2000) highlight that CBUs often show clear evidence of self-regulation as a result of inherent adjustments in process and form. This results in a stable form or equilibrium often exhibiting distinguishable features described as the cliff characteristics (Lee & Clark, 2002). As long as thresholds within the system are not exceeded (Lee & Clark, 2002) the overriding stability of the CBU will be preserved.

2.7.2. Management of cliffs – cliff recession prediction methods

Recession of coastal cliffs present significant risk to infrastructure (Lee et al., 2001). This threat is likely to be exacerbated in the future with the influence of a changing climate as detailed by the UKCP09 (Murphy et al., 2009). In response there has been a proliferation of national guidance in the UK within the last decade (DEFRA, 2006; 2007; 2009a; 2009b; 2010) to develop coastal risk management and support the decision making process. Evidently predicting future coastal recession scenarios is challenging due to the limited temporal period for which historical recession data is available and the inherent uncertainty of whether future recession will resemble the past rates as conditions change (Lee et al., 2001). There is currently no direct process-response model for sea-cliff recession in the UKCP09 (Lowe et al., 2009; Murphy et al., 2009) or elsewhere in national guidance or the scientific literature and therefore there is limited empirical data to determine future erosion scenarios. Probabilistic recession modelling has largely relied on expert judgement (Lee, 2005; Moore et al., 2010b) grounded in the limited

empirical data from climate projections and historical recession to produce an informed range of future erosion scenarios.

A variety of approaches to predict cliff recession have been presented, as summarised by Lee et al. (2001). These include simple extrapolation of historical recession rates, models which account for incident wave energy and cliff strength parameters and the effect of sea level rise on recession rates (Bray & Hooke, 1997). These methodological approaches are deterministic and do not account for the natural variability within the system, the uncertainty in measurements or future climatic scenarios which will affect the cliff system's behaviour. Applications of probabilistic methods of cliff recession are presented by Lee et al. (2001) and implemented in national projects as reported by Moore et al. (2010b) such as the Risk Assessment of Coastal Erosion (RACE) (Halcrow, 2006). Hall et al. (2002) report that probabilistic methods provide a method of demonstrating the variability in predictions of coastal cliff recession forming the basis for planning, management and engineering decision-making (Lee et al., 2001).

More recent research has led to statistical numerical models generated from high resolution monitoring of cliffs. A notable application of this methodology is exhibited by Barlow et al. (2012) for the sea cliffs of North Staithes, North Yorkshire, which displays the beneficial progression from an extensive high resolution rockfall inventory to characterisation of rockfall erosion over decadal timescales through negative power law scaling. This method, as reviewed by Barlow et al. (2012), is well established for modelling landslide magnitude-frequency distributions using a single power law (Stark & Hovius, 2001; Dussauge et al., 2003; Brardinoni & Church, 2004; Guthrie & Evans, 2004; Malamud et al., 2004; Dong & Guzzetti, 2005; Van Den Eeckhaut et al., 2007; White et al., 2008; Marques, 2008; Brunetti et al., 2009; Rossi et al., 2010). The research by Barlow et al. (2012) provided probabilistic investigations for the power law scaling parameters which drive the subsequent recession model but were unable to constrain these by

marine or environmental parameters, although they do conclude this is a natural progression within the field of research. Such numerical models developed with the ability to account for future conditions which control the development of sea cliffs will improve the capability to assess the risk to nearby infrastructure.

2.7.3. The concept of risk

Risk is a human concept (Lee & Jones, 2014) derived by the human mind, moreover it is a human-centred concept (Lee & Jones 2014). Fundamentally, the concept is built upon the balance between risk versus reward. There are many definitions of risk which are readily formed to suite a particular purpose. Lee and Jones (2004, p.2) define risk from a scientific viewpoint as

A combination of the probability, or frequency, of occurrence of a defined hazard and the magnitude of the consequences of occurrence.

This definition is useful as it includes the agent or mechanism which leads to the potential risk. Furthermore Lee & Jones (2014, p. 8) contextualise risk within the landslide setting as

The potential for adverse consequences, loss, harm or detriment as a result of landsliding, as viewed from a human perspective, within a stated period and area.

Which provides a holistic viewpoint of not only risk but the application to the controlling hazard over a temporal and spatial scale which is required in management and assessing risk in the coastal cliff environment.

McInnes and Moore (2011, p. 13-14) note the variety of responses that are available to local authorities in terms of managing coastal instability and erosion, these include;

- Removal of the risks by avoiding or relocating inappropriate development away from the coast, e.g. through the land use planning system;
- Reducing the likelihood of damaging events through pro-active coastal risk management;

- Reducing the consequences of risk (e.g. by providing early warning systems);
- Protecting against potentially damaging events through civil engineering measures such as coastal protection, cliff or slope stabilisation or by means of building modifications and also through land instability management schemes.

2.7.4. Risk management

Management of instability and erosion in the coastal environment involves mitigating and monitoring of these risks (McInnes & Moore, 2011). The primary aim of government coastal defence policy is to reduce risks through the provision of technically sound, economically justifiable and environmentally sustainable coastal defence schemes (McInnes & Moore, 2011). Fell et al. (2005) report that risk assessment is not a substitute for good geotechnical engineering knowledge and judgement, it enhances it by adding insight. The outcomes of risk management through assessment will be either:

- The risks are tolerable (acceptable) and no mitigation is required
- or
- The risk are intolerable (unacceptable) and mitigation options need to be considered and implemented.

McInnes and Moore (2011) report that the risk management process is iterative, which requires consideration of the risk management options, the results following installation of the mitigation measures and from the continued monitoring. The constraints associated with risk management are illustrated in Figure 14.

2.7.5. Risk Assessment

An approach which has been widely used to improve the evaluation of risk is Quantitative Risk Assessment (QRA), which involves the use of measurable data to determine asset value,

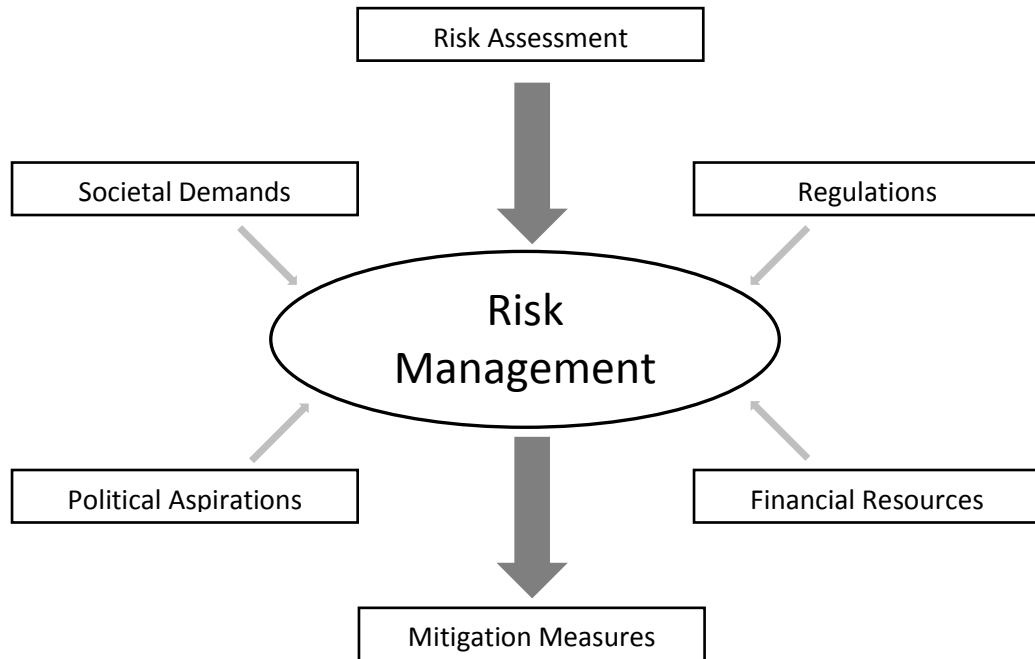


Figure 14: The constraints to be taken into account in erosion risk management. Effective coastal risk management requires reconciliation of stakeholders and politicians with coastal science, a wide range of regulations and legislation and the availability of resources. (McInnes & Moore, 2011, p. 26 – Adapted from Leroi et al., 2005).

probability of loss and the associated risks. Benefits of this method to landslide and erosion risk assessment include (McInnes & Moore 2011, p. 26):

- The encouragement of a rational, systematic approach to assessing the safety of natural and engineered slopes;
- The application to land use planning, with specific loss of life or economic loss acceptance criteria used to determine zoning;
- Some local and regional government planners are familiar with risk management principles, and welcome an understanding of the risk management presentation;
- The focus of attention on what happens if the coastal cliff or slope fails;
- The provision of a framework to put uncertainties and engineering judgement into a system;
- The provision of an open and transparent process on the nature and key contributions of landslide and erosion risk and corresponding uncertainty for discussion with the regulators, owners, stakeholders;

- That it allows systematic consideration of risk mitigation options and cost benefit ratios.

For example, a QRA was undertaken following a series of cliff collapses behind Brighton Marina in the winter of 2000/2001. The undercliff walk, a promenade at the base of cliff, was closed to the public and the risk to the users was assessed. The QRA estimated the rockfall and rock slide potential to provide the local authority with a baseline which then could be used to implement risk reductions measures (High-Point Rendel, 2005; Lee & Jones, 2014). A vulnerability model was developed to assess the risk of a fatality for a variety of landslides along this section of coastline, an overview of this model is presented within Lee and Jones (2014, p. 310-312).

2.7.6. Managing future risks

Through effectively monitoring ground movements and rates of coastal and cliff recession, predictions of future recession can be informed with particular reference to their timing and extent (McInnes & Moore, 2011). Monitoring of coastal and cliff retreat can also be used to form the basis of decision in relation to coastal protection policies especially in the cases where long-term analysis of data trends allow a sound understanding of spatial change.

The continued research within this field is a vital component of effective management of coastal instability (McInnes & Moore, 2011). It is anticipated that risk to coastal assets will increase into the future, the challenge facing central and local government will be to develop and implement policies which address the increasing risks whilst also meeting the inevitable financial constraints (Moore et al., 2010a).

2.8. Summary - Current understanding

This chapter has reviewed the current understanding of coastal cliffs, through forms and processes alongside the attempts at classifying these dynamic coastal environments. Contemporary methodologies have been explored which have provided access to capture large volume, high resolution datasets instantaneously. Thus providing the opportunity and ability to

compare these sequential datasets to monitor, quantify, locate spatially and identify temporally the development and recession of the cliff coastline. The relatively recent and increasingly influential concept of risk has been reviewed and contextualised for this and further research within the field of coastal management. Although there is an apparent wealth of knowledge with reference to coastal cliffs which has been exemplified throughout this chapter the subdiscipline remains in relative infancy to other geomorphological systems. As a result, there is an opportunity to further develop and refine the methodological approaches for obtaining data to improve our understating of these systems. By quantifying change within the system and establishing numerical relationships with environmental controls, this will enable the opportunity for more reliable, data driven probabilistic recession models of the cliffs in Brighton to be developed so that the risk to infrastructure can be better understood. The following chapter will present the methodologies used and developed throughout this research.

Chapter 3 – Methods

This chapter will present the methodological approaches used throughout this research. This includes; applying well known methodologies to the study area, such as orthorectification, to provide a more reliable historical recession rate dataset and developing innovative methodologies for the coastal cliff environment through terrestrial and UAV photogrammetry to quantify rockfalls. A method of obtaining high frequency environmental data for the cliff environment is developed through the use of thermography and the numerical modelling of the Newhaven Chalk is presented through kinematics and limit equilibrium analysis. The combination of these approaches enables two methods to be presented for producing probabilistic recession models of the undefended and defended cliffs in Brighton.

3.1. Orthorectification of aerial imagery and recession rate calculation (1957 – 2013)

The data derived from investigations using historical aerial photographs (Moore, 2000; Moore et al., 2003; Dornbusch et al., 2006a; 2006b; 2008) provide the basis for policy decisions through extrapolation of these recession rates over the short (25 years), medium (50 years) and long (100 years) management timescales (Environment Agency, 2009). The two readily applied methodologies used for processing aerial imagery are georeferencing and orthorectification. Georeferencing only assigns coordinates in the 'x' and 'y' plane and does not include elevation data. Information of how the image was captured through either camera or flight data (Morgan et al., 2010) is ignored, as a result georeferenced images are more susceptible to spatial error (Kloehn et al., 2008) due to potential 'warping' of the image (Moore et al., 2003). The orthorectification method utilises data capture information and is rectified in all three planes by extracting elevation from a DEM alongside the 'x' and 'y' data to transform the image to replicate the distortion of the image in the 'z' plane. The method of orthorectification, provides high resolution data whilst minimising spatial error and is therefore more reliable versus other image processing techniques (Moore et al., 2003; Paine & Kiser, 2003; Dornbusch et al., 2008; Kloehn

et al., 2008; Morgan et al., 2010). This is the first time a fully orthorectified dataset has been used for this area, the subsequent design of the analysis enables the behaviour of different CBUs to be identified within the defended and undefended cliff lines.

3.1.1. Datasets

The database used to calculate historical cliff recession comprised of images from; 1957 (RAF photography), 1973 (Environment Agency), 1991 (Geonex, University of Sussex Holdings) and 2013 (Channel Coastal Observatory - CCO) covering approximately 20km of cliff line from Brighton Marina to Belle Tout. Due to the image capture process some sections of the cliff line within the study area were missing from the dataset, these were; 1957 from Brighton Marina to west of Saltdean and 1991 a 1.5 km stretch west of Saltdean. The 2013 imagery which was pre-orthorectified with an accuracy of 0.15 m with a DEM of the area from 2007 made available by the CCO acted as the reference datasets.

3.1.2. Processing of aerial imagery

The orthorectification process was undertaken using the geospatial imagery software package ENVI 4.8. The workflow is presented in Figure 15. Relevant stages in the workflow (Figure 15) that represent readily accepted theory are available in Annex A. Figure 16 illustrates an example of the exterior orientation completed with an aerial image from 1957 of Saltdean. Following the completion of the orthorectification procedure a root mean squared error (RMSE) was generated for each image. This is a measure of how accurately the ground control points (GCPs) that were digitised in the historical image reflect the spacing in the coordinate system they were extracted from. All reported RMSE values were examined and only accepted if they were less than half the pixel value of the historical image. If the RMSE value was greater than this threshold GCP refinement was undertaken, which required removing 'bad points' or optimising the digitised points. This procedure improves the co-registration between the image and the DEM thus ensuring a more accurate geometric rectification (Chmiel et al., 2004).

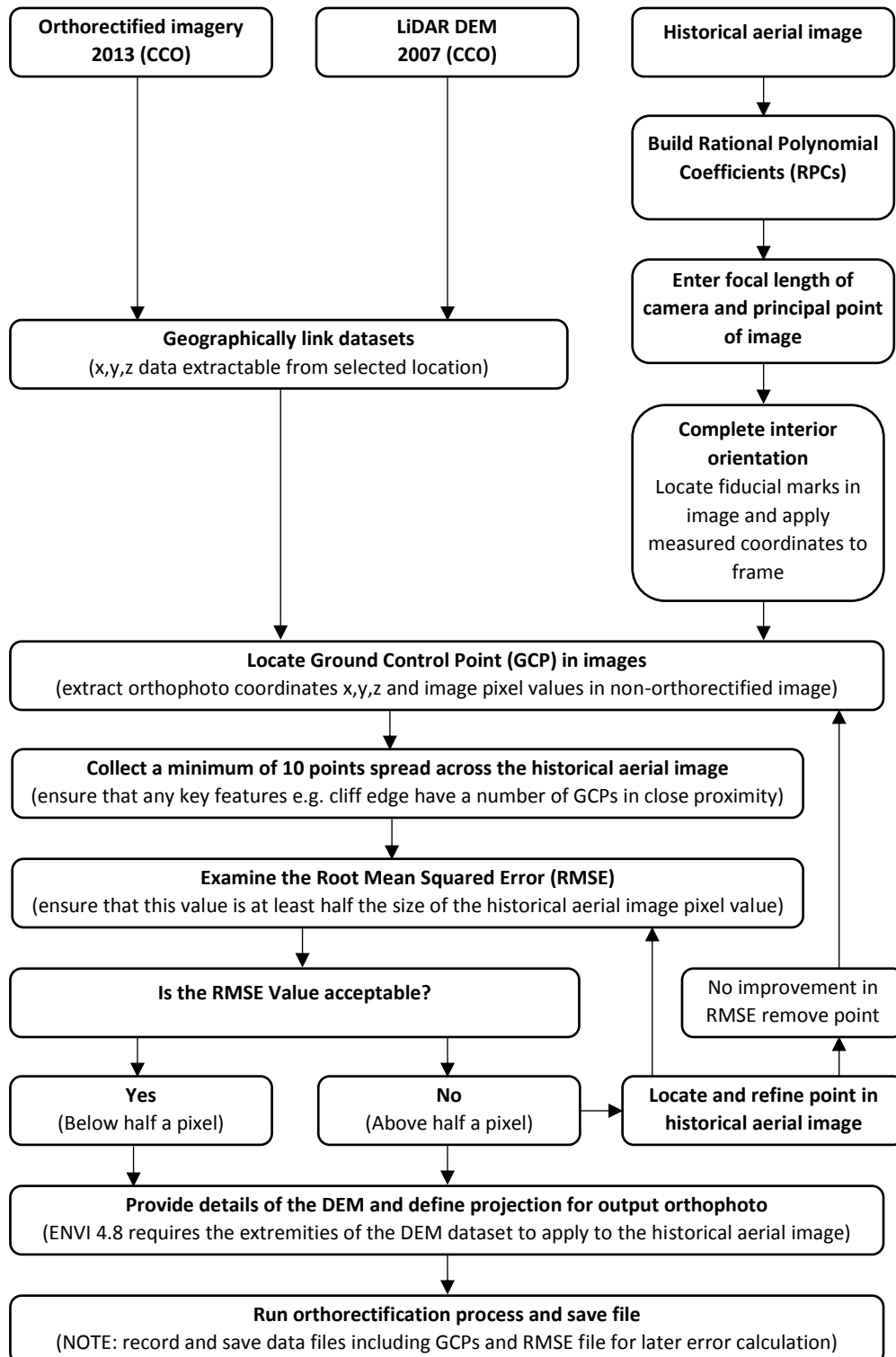


Figure 15: Orthorectification workflow using ENVI 4.8.



Figure 16: Orthorectification exterior orientation example, Saltdean 1957.

3.1.3. Digitising cliff lines and calculating historical recession rates

The cliff lines from the orthorectified image database were digitised in ArcGIS at a scale of 1:400. For large sections of the defended coastline the cliff top is mainly covered by grass or vegetation up until the cliff edge. This acts as an aid in depicting the cliff edge (Dornbusch et al., 2008). At more actively eroding sites this visual aid does not exist, however in these images the sharp

break in slope is readily depicted by a change in shade or colour in the image and the edge can be identified reliably using this method.

The historical recession rates were calculated using the ArcGIS extension Digital Shoreline Analysis System (DSAS) developed and made available by the United States Geological Survey (USGS) (Thieler et al., 2009). DSAS computes rate of change statistics for a given time series of shoreline vector data (Himmelstoss, 2009) and has been extensively used (Oyedotun, 2014) for investigations of cliff modelling (Hackney et al., 2013; Thébaudeau et al., 2013) and cliff retreat (Rio & Gracia, 2009; Brooks et al., 2012; Katz & Mushkin, 2013; Young et al., 2014). All data input used in calculating retreat rates in DSAS must be stored in a single geodatabase, the shoreline data required to be located in one feature class with the following attributes; object ID, shape, shape length, date and uncertainty. The uncertainty parameter for each of the images within the image database are displayed in Table 4. The RMSE calculated from the orthorectification procedure increases for the earlier images as the pixel size for these images were larger but all errors were below the half a pixel threshold. Existing error was introduced from datasets which had been pre-processed and the plotting error introduced by the width of the line, once scaled, which was used to digitise the cliff edge and as a result remains constant throughout.

Year	Site	RMSE	Existing error	Plotting error	Total error (m)
2013	All (CCO)	-	0.15	0.10	0.25
1991	Marina & Saltdean	0.14	-	0.10	0.24
1991	Peacehaven	0.10	-	0.10	0.20
1991	Seaford & Cuckmere	0.19	-	0.10	0.29
1991	Seven Sisters	0.19	-	0.10	0.29
1973	All (EA)	0.05	0.15	0.10	0.30
1957	Saltdean	0.35	-	0.10	0.45
1957	Peacehaven	0.24	-	0.10	0.34
1957	Seaford	0.35	-	0.10	0.45
1957	Cuckmere	0.38	-	0.10	0.48
1957	Seven Sisters	0.34	-	0.10	0.44

Table 4: Uncertainty for the historical aerial imagery required as input data for DSAS.

The final data input required in DSAS is a baseline feature. This can be defined as either the most recent shoreline or generated as a new vector field. The latter was selected and formed an arbitrary datum set landward of the cliff to enable the 2013 dataset to be included in the

calculations. This also removed the issue caused by the natural intricacies of the cliff edge in 2013 which would have affected the direction of the transect casting. Transects were cast offshore with a transect spacing of 10 metres and length of 100 metres. The positioning of the baseline ensured that transects orientation were cast normal to the cliff to avoid error. The 10 metre spacing is more frequent than previous studies in the area (Dornbusch et al., 2006a; 2006b; 2008) and was chosen to obtain a more representative dataset both spatially and temporally with relation to magnitude of failures.

There are a variety of statistical outputs available within the DSAS extension for recession rate calculation (Himmelstoss, 2009). This research utilised the linear regression rate (LRR) and the weighted linear regression (WLR), both of which provide confidence intervals determined by the user. The LRR is determined by fitting a least squares regression line to the data points, the regression line is positioned so that the sum of the squared residuals is minimised (Himmelstoss, 2009). The standard error of the rate of change is reported based on the confidence interval of 95.5% (2σ). This method can be used on sequential time periods or on the entire dataset. The WLR method requires a minimum of three shorelines and greater emphasis is placed on those positions with the smaller uncertainty values (Genz et al., 2007). The weighting of each point is calculated as

$$w = 1/(e^2)$$

where e represents the uncertainty value. This calculated recession rate can be a more robust estimator (Himmelstoss, 2009) as it accounts for the varying uncertainty of the processed datasets. Likewise, the confidence interval was set as 95.5% (2σ) to report the accuracy of the annual cliff line recession. The output databases can be observed spatially by joining the data to the transects which are presented later.

3.2. Digital photogrammetry for detecting, characterising and quantifying chalk rockfalls

Digital surface models have been predominantly acquired through airborne and terrestrial LiDAR (Haala & Rothermel, 2012; Gonçalves & Henriques, 2015; Barlow et al., 2012). Over the last 20 years the field of geomorphology and in particular cliff studies have benefitted from innovations in capturing and processing geospatial data (Bishop et al., 2011; Lim, 2014). Whether this be through terrestrial laser scanning (TLS), airborne laser scanning (ALS), digital photogrammetry or a combination of these techniques (Lim, 2014). High resolution data capture through the use of photogrammetry requires a face-on perspective better achieved through terrestrial rather than traditional aerial surveys (Lim, 2014). However with the development of unmanned aerial vehicles (UAVs) in recent years alongside the proliferation of inexpensive digital cameras and software platforms (Hugenholtz et al., 2013; Barlow et al., 2017) both terrestrial and aerial photogrammetry can provide comparable accuracy to TLS surveys whilst significantly reducing the cost, survey time (Slatton, et al., 2007; Remondino et al., 2011; Hugenholtz et al., 2013; Barlow et al., 2017) and risk during data collection. The progress in photogrammetry has allowed both qualitative and quantitative analyses of spatial and temporal development of the coastal cliff system. This section will present both terrestrial and aerial photogrammetry from a defended section of cliff at Brighton Marina and an undefended section of cliff at Telscombe respectively.

3.2.1. Photogrammetry workflow

Terrestrial photogrammetry had to be deployed within the defended section at Brighton Marina due to Civil Aviation Authority (CAA) guidelines regarding the use of drones in urbanised areas. Whereas the natural coastline at Telscombe enabled UAV surveys to be undertaken. Both the terrestrial and UAV photogrammetry methodology were developed using the ADAM 3DM Mine Mapping Suite 2.5.0 Build 1488, Figure 17 details the workflow which was refined throughout the research. Other software platforms were used following the generation of the 3D models

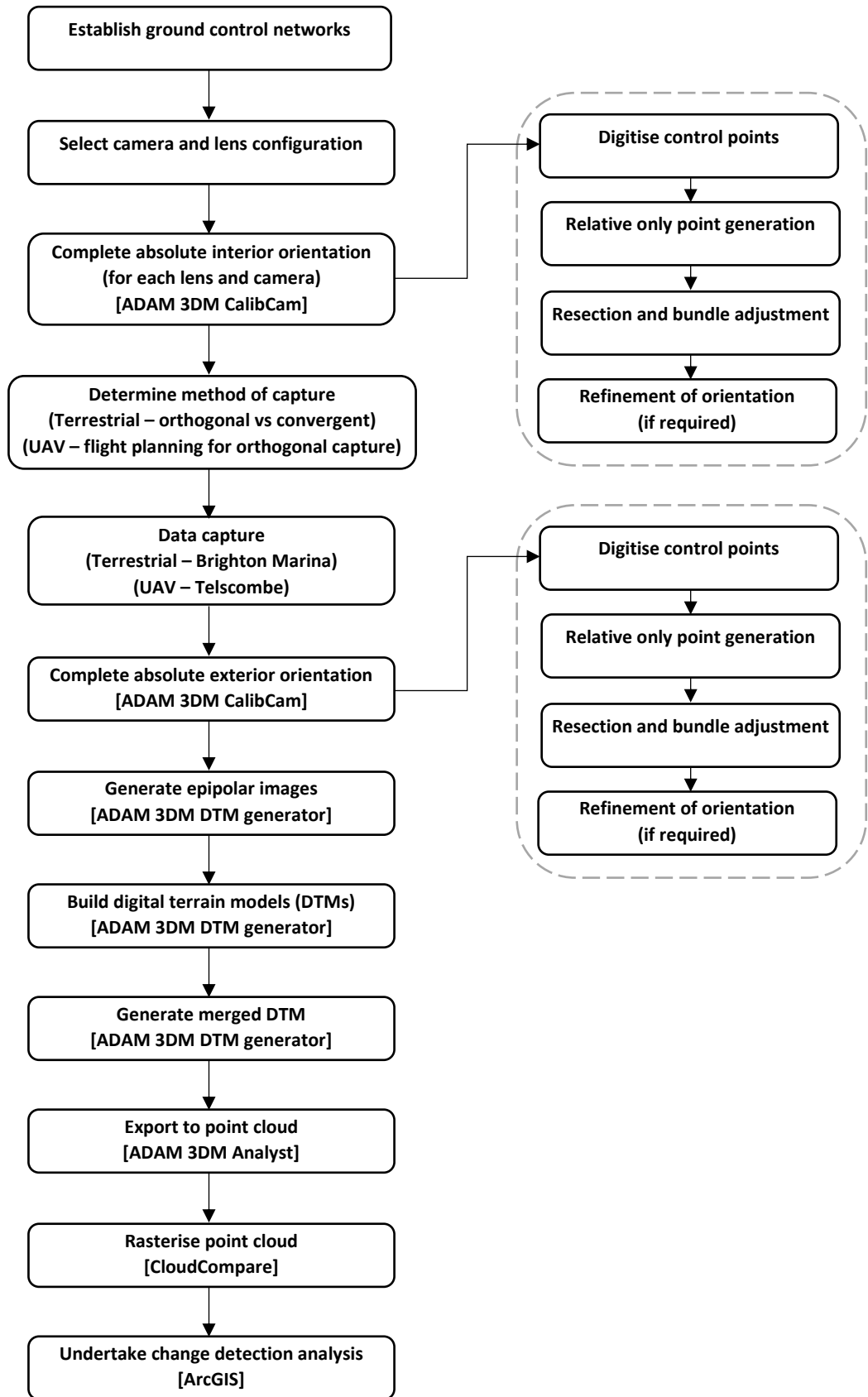


Figure 17: Digital photogrammetry workflow for terrestrial and UAV applications [software platform used].

to enable change detection to be completed, these included Cloud Compare (Cloud Compare v2.6.3, 2016) and ArcGIS. The following sections provide additional information for each stage of the methodology which highlights where the methods differ between the terrestrial and UAV photogrammetry approach. Data were collected weekly between November 2014 and March 2017 for the terrestrial photogrammetry, to provide a dataset of comparable frequency to readily available meteorological data to assess sub aerial impact on erosion, and monthly between August 2016 and July 2017 for the UAV photogrammetry. The terrestrial photogrammetry was deployed first and evolved to develop a robust methodology which optimised camera and software performance. The start of the UAV data capture was delayed due to technical failure of the UAV which led to damage beyond repair in April 2015. Due to unavoidable circumstances a delay of approximately one year was incurred to the commencement of data collection.

3.2.2. Ground control networks

The network of ground control points (GCPs) at the sites (Brighton Marina – terrestrial, Telscombe - UAV) were obtained through a combination of surveying techniques. Differential global positioning system (dGPS) was used to locate the cliff top points (Figures 18A & 18B) and base locations where a total station could be installed. This was to overcome the issue with obtaining ground control at the toe of the cliff where dGPS accuracy is reduced due to the effect of 'shadowing', a common problem in complex terrain morphologies (Young, 2012; Barlow et al., 2017). The defended site at Brighton Marina had nine fixed markers (Figure 18A) divided equally between the sea wall, the splash back wall and the cliff top fencing. The lower six were all acquired through total station surveying. A total of 23 GCPs were installed at the undefended Telscombe site, 18 were evenly spaced at the cliff toe captured from the total station from four base stations to account for the complex morphology, and five at accessible locations at the cliff top (Figure 18B). Following post-processing (Awange, 2012; Awange & Kiema, 2013) all dGPS

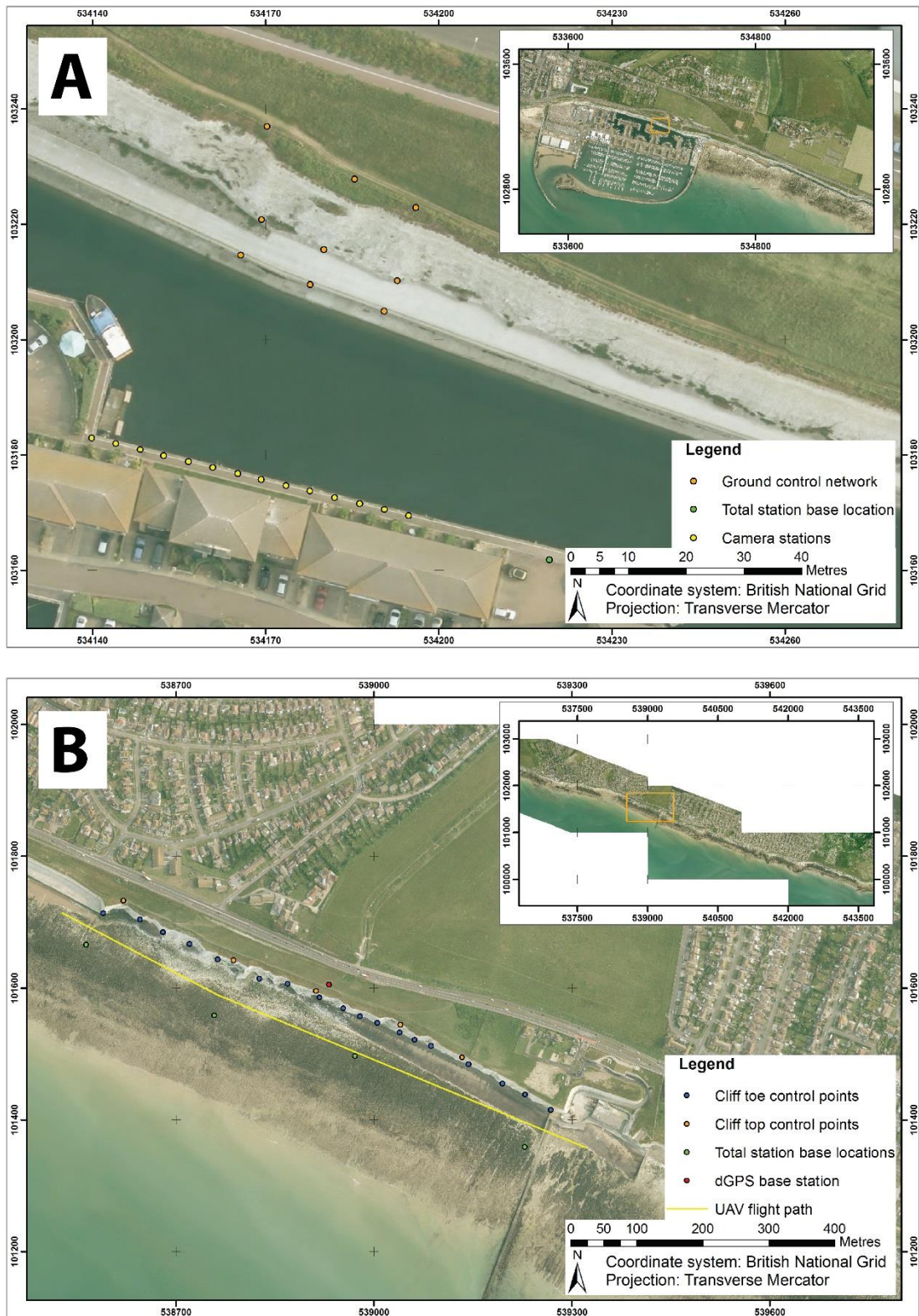


Figure 18: Ground control networks for photogrammetry study sites (A) Brighton Marina and (B) Telscombe (2013 imagery downloaded from the CCO).

points were accurate to 0.02 m in all planes with PDOPs ranging from 1.2 to 1.5. The maximum error introduced from the total station, obtained through known dGPS back sight coordinates was 0.006m. The maximum error ellipse for all GCPs was therefore set at 0.03 m.

3.2.3. Camera and lens configuration

The cameras used in developing the methodology are summarised in Table 5. By assessing a variety of lens types and frame sensor sizes the outputs could be compared to establish the optimum camera configuration. The decision to opt for a higher megapixel camera for extra resolution needs to be taken in conjunction with the sensor (or frame) size. The sensor size is a crucial parameter as it determines the amount of light which is used to create an image (Crisp, 2013).

	Camera (lens)		
	Sony DSC-H300 (35X optical zoom lens)	Nikon D810 (AF-S Nikkor 24-120mm 1:4 G ED)	Nikon D810 (AF Nikkor 24mm f/2.8D) (AF Nikkor 35mm f/2D)
			
Megapixels	20.1 MP	36.3 MP	36.3 MP
Frame size	1/2.3" Super HAD CCD	Full frame (35.9 x 24 mm) CMOS sensor	Full frame (35.9 x 24 mm) CMOS sensor
Focal length	4.5-157.5 mm (zoom)	24-120 mm (zoom)	24 mm (prime)* 35 mm (prime)**
Image Storage	JPEG	TIFF	TIFF
Capture mode	Auto	Manual	Manual

Table 5: Camera and lens specifications (*terrestrial, UAV**).

Comparing the Sony DSC-H300 used in the research (Nov 2014-Jan 2016) to the Nikon D810 (Jan 2016-Mar 2017) the camera frame is significantly smaller as is the case with many modern day compact cameras to DSLRs. As a result the Sony DSC-H300 requires a wide angle lens to capture the entire scene, the advantages therefore of a full frame sensor are that; it allows the

manufacturer to increase megapixel size without sacrificing other image quality attributes, better dynamic range, less noise and improved lighting capabilities (Crisp, 2013). This is exemplified by the ADAM 3DM (photogrammetry software) camera parameters spreadsheet (Appendix A) which indicates a desired circle of confusion of 9 pixels and 2.21 pixels for the Sony DSC-H300 and Nikon D810 respectively. This value sets the minimum acceptable limit of blur between pixels that the camera set up will be able to achieve, these values indicate that the images captured from the Sony camera will introduce more blur and reduce the pixel matching capabilities of the software especially at the extremities of the image where the greatest light refraction will take place. Further investigations were undertaken to assess the quality in lens types on the Nikon D810 camera. The adjustable lens (AF-S Nikkor 24-120 mm 1:4 G ED) introduced reliability issues regarding focal length. The Brighton Marina images were captured using a 35 mm focal length to ensure the best use of pixels in the image by removing sky and the foreground. However as this was not the minimum focal length on the variable lens it was difficult to achieve the same camera settings on subsequent field visits, as the camera would record focal lengths between 33 mm and 36 mm. As a result the prime, or fixed lens (AF Nikkor 35 mm f/2D), was used to ensure the critical parameter of focal length was comparable between datasets.

3.2.4. Camera settings and methods of capture

The cameras differed significantly in the ability to control the shooting parameters, the Sony DSC-H300 auto adjusted the camera parameters for the scene this included lighting conditions of aperture, ISO and shutter speed. This method produced the best quality images for sequential data capture. The Nikon D810 was set to manual shooting mode with the optimum camera parameters as outlined in Table 6.

The three camera settings which have the greatest effect on camera calibration and therefore accuracy of the models are focal length, focus and aperture (ADAM Technology, 2010a; Luhman

Parameter	Camera setting
Lens	Fixed (preferably)
Mode dial	Aperture priority
Aperture	F/8
Image recording quality/resolution	Fine mode (highest resolution) TIFF
ISO	100
White Balance (WB)	AWB (auto)
Lens (focusing mode)	MF (manual focus during shooting)
Metering mode	Evaluate
Auto image rotation	Off

Table 6: Optimum camera shooting parameters for the Nikon D810.

et al., 2011). Reaffirming the importance to maintain the focal length, the Nikon D810 used the manual focus to ascertain sharp images at the required shooting distance and retain the preferred aperture of f/8. The optimum camera parameters in Table 6 reduce the blur in the images which can be introduced by a high ISO setting or fixed aperture settings. By selecting aperture priority the camera is able to select the shutter speed to optimise the image clarity based on the natural lighting conditions. Both cameras used a self-timer where the image was captured 10 seconds after the trigger was pressed. This was to remove any movement of the camera introduced from the user during the shooting of the images, a remote trigger could be used to the same effect.

Two types of image capturing procedure were implemented for the terrestrial photogrammetry, strip (Figure 19A) and a convergent (Figure 19B). Both methods utilised all 14 stations with the camera mounted on a tripod. The strip photography consists of a series of parallel images with at least 60% horizontal overlap (ADAM Technology, 2004). As it was not possible to include any vertical overlap of images the distance between image stations was reduced to increase the horizontal overlap. The threshold to introduce redundancy is 80% (ADAM Technology, 2010a), the overlap between neighbouring stations was 90% (Figure 19A) and 83% between alternate images. The major benefit of using this method is that the substantial overlap between each image allows the orientation information to be accurately passed between models which reduces the amount of control points required whilst not impacting on accuracy (ADAM Technology, 2004). The notable disadvantage of this method is the poor camera geometry and

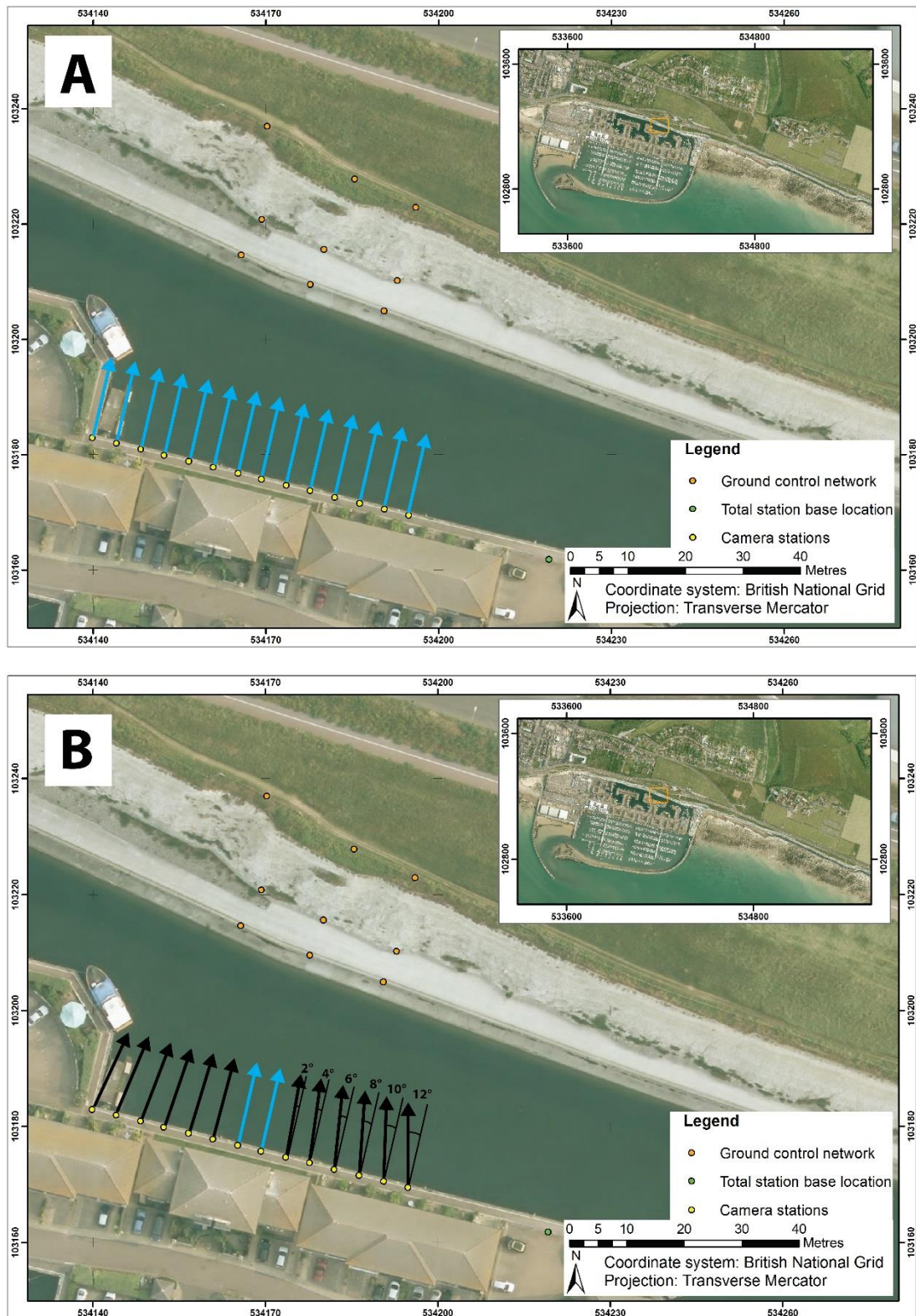


Figure 19: Terrestrial photogrammetry image capture procedures (A) strip and (B) converging image set (2013 imagery downloaded from the CCO).

relatively high distance-base ratios. This ratio is calculated as the distance from camera station to object of interest and distance between neighbouring stations with a suitable ratio defined as between 2:1 and 6:1 but should not lie outside the range 1:1 and 10:1 as the pixel matching becomes difficult (ADAM Technology, 2010a). For neighbouring stations this ratio is 10:1 and for alternate stations is 5:1. To account for this issue an alternative procedure of a convergent image set was used. As illustrated in Figure 19B the outer camera stations had a camera shooting angle of 12° from perpendicular towards the centre of the region of interest. This reduced by 2° on each camera station towards the centre of the camera station set up. This retains the same distance to base ratio but increases the overlap (Figure 19B) between neighbouring images and those at the extremities of the dataset. By increasing the number of points found in the images which are captured from stations further apart the final models depth accuracy will be improved as (ADAM Technology, 2010b):

$$\text{Depth accuracy} = \text{Planimetric accuracy} \times \frac{\text{Distance}}{\text{Base}}$$

where planimetric accuracy is the accuracy of the imagery in the horizontal and vertical planes. By using this method the overlap between neighbouring images increases to 95% enabling a greater proportion of pixels to be matched within each stereo image pair.

For the UAV photogrammetry the strip data collection method was applied however notable changes had to be made to the camera set-up. The Nikon D810 camera for the UAV surveys was fitted with an AF Nikkor 24mm f/2.8D prime lens to account for the greater elevation of the cliff in Telscombe whilst flying at a reasonable distance from the cliff face. The camera settings had to be adjusted from those recommended by ADAM Technology (2010a) as the aperture priority mode which provide unusable images due to image blurring as the camera was mounted on the UAV. The following settings were fixed for the capture of each dataset: aperture f/8, shutter speed 0.002 (1/5000) seconds. This meant that the critical parameters (ADAM Technology, 2010a) the focal length, focus distance and aperture were maintained for subsequent data

collections and the internal calibration. The ISO setting was adjusted between flights to account for variation in lighting conditions from a minimum of 400 in March to a maximum of 1600 in August. The ISO setting was manually adjusted to replicate the images taken under the optimum camera settings (ADAM Technology, 2010a) and provide the best quality images for processing. The UAV used for the flights was a DJI S1000 octocopter (Figure 20), using waypoints an automated flight path was determined that maintained a distance between the aircraft and cliff face of 50 m. Images were captured automatically on a timer with a 5 second interval and orthogonal to the cliff face through live streaming video (Barlow et al., 2017). The UAV had a flying height of approximately 21 m (mid-cliff height) and was set at a constant speed of 3 ms^{-1} generating a base distance of 15 m. This resulted in a horizontal overlap between images of 80%, the redundancy threshold identified by ADAM Technology (2010a) as there is no vertical overlap. This methodology for capturing large sections of cliff line is the best available with a relatively short object distance and focal length (Birch, 2006; Barlow et al., 2017). The total flight time for each survey was 8 minutes which is a significant reduction in data capture time in comparison to laser scanning methods.



UAV model	DJI S1000 octocopter
Max. take-off load	10.89 kg
Max. wind	10 m/s
Max. altitude	1000 m
Max. flight time	15 mins (with load)
Motors and type	8 motors (model 4114-11)
Batteries	Lithium polymer
Flight modes	Manual or GPS aided navigation

Figure 20: DJI S1000 octocopter and Nikon D810 FX DSLR pre-flight and tabulated UAV information (Barlow et al., 2017, p. 2468, Figure 3.)

3.2.5. Interior orientations

The interior orientation determines the internal geometric model of a camera (Luhman et al., 2011), each completed calibration is unique to the camera and lens configuration and capture settings used so must be recalibrated if these parameters are altered. This process is achieved

by measuring the deviation of light rays once they pass through the perspective centre of the lens and are projected onto the camera sensor (ADAM Technology, 2010a). The perspective centre is a known location in a relative reference system fixed within the camera known as the image coordinate system and the measured deviations from the ideal central projection are termed image distortion parameters (Luhman et al., 2011). The interior orientation process determines the following 11 parameters (ADAM Technology, 2010a):

C	Focal length or principal distance from the lens to the sensor
K1, K2, K3, K4	Radial lens distortion, constitutes the major imaging error in most cameras and is a function of: lens design, focus distance and object distance (Luhman et al., 2011).
Xp, Yp	Principal point offset in X and Y direction formed by the axial ray passing through the centre of the lens system
P1, P2	Decentring distortion, also termed radial-asymmetric or tangential. Mainly caused by decentring or misalignment of individual lens elements (Luhman et al., 2011) and exhibit much smaller adjustments than radial distortion in high quality lenses.
B1, B2	Scaling factors

By completing an interior orientation within ADAM 3DM CalibCam the true location of control points within the image are accurate to $1/10^{\text{th}}$ of a pixel despite 'apparent' locations caused by lens distortion leading to internal shifts, pre-orientation, of dozens of pixels on the image sensor (ADAM Technology, 2010a).

For the terrestrial photogrammetry the interior orientation set-up (Figure 21A) consisted of an equilateral triangle of six camera stations with each camera directed towards the centre of the area of interest (Figure 21B), this introduced a depth perspective to the calibration. The distance between station 1 and the scene should be greater than the hyperfocal distance unique to the

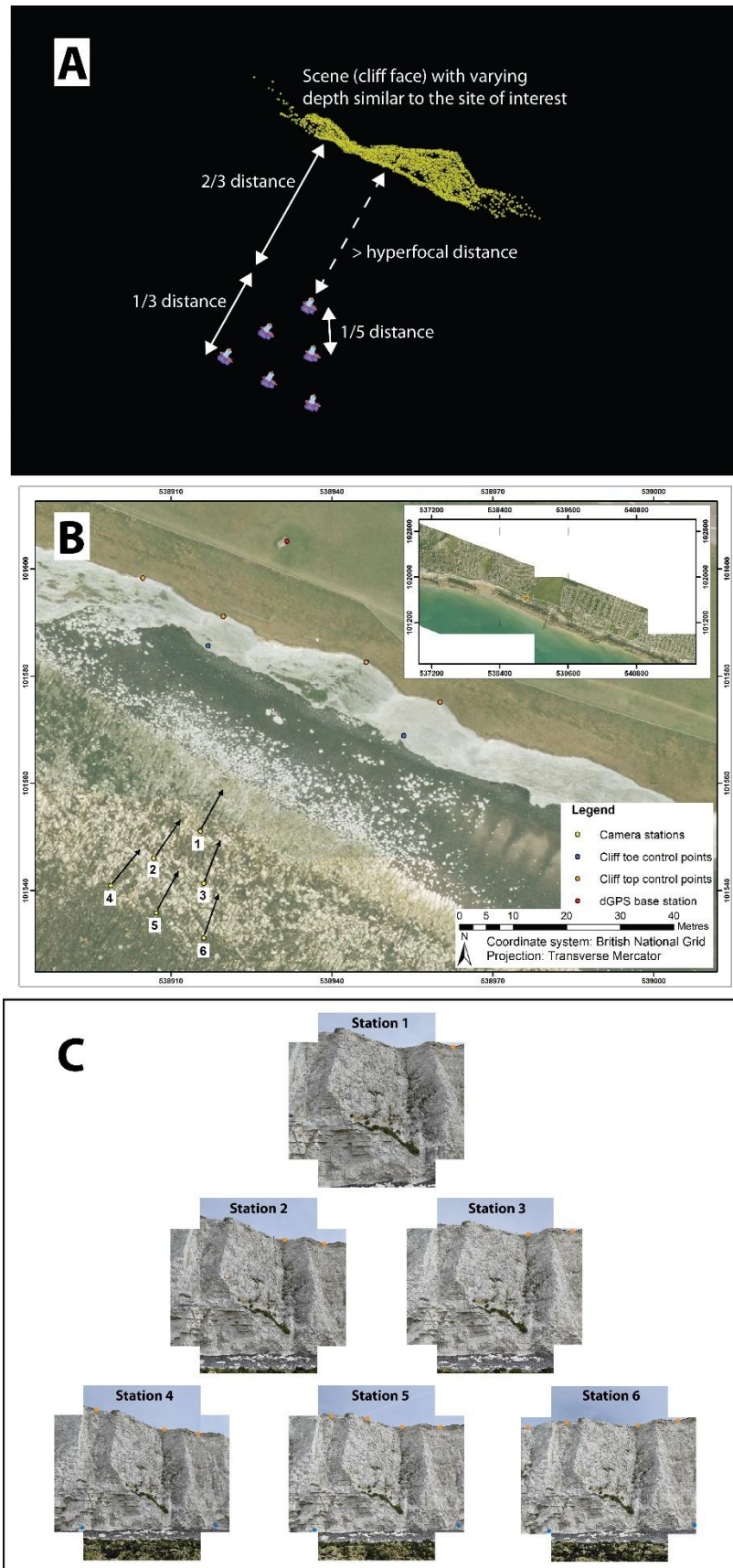


Figure 21: Interior orientation/ calibration set up (A) ADAM 3DM CalibCam 3D view of stations and relatively only points (yellow point cloud) with approximate spacing labelled, (B) Ground control network and camera direction and (C) landscape and portrait images from each station captured from Nikon D810 35mm fixed lens with cliff top targets marked in orange and cliff toe points in blue. (2013 imagery in (B) downloaded from the CCO).

camera and lens configuration, and be approximately $\frac{2}{3}$ of the distance from station 5 to the scene. The spacing between stations should be $\frac{1}{5}$ of the overall distance. ADAM Technology (2010a) stipulate that the distance between the camera stations 4, 5 & 6 should be approximately the same distance at which the images shall be captured for the intended photogrammetry application. For the configuration in Figure 21A and 21B the distance between station 5 and the cliff face was 50 m and the station spacing 10 m. Both a portrait and landscape image at each station are required (Figure 21C) and images were captured on a self-timer to reduce movement. The camera was rotated 90° , pivoting around the centre of the lens using an 'L-bracket', the height of the central column was lowered by 14 mm between taking the landscape and portrait images to compensate for the greater distance between the side of the camera to the centre of the lens. The scene which is photographed in the interior orientation should be similar to the scene of the application. To fill these requirements for the terrestrial photogrammetry both the fixed and varied lenses with focal length of 35 mm on the Nikon D810 were calibrated at Telscombe where the cliffs (maximum elevation 49 m) filled the majority of the frame (Figure 21C). Vegetated areas, moving objects, water and sky should be limited in the frame as pixel matching is much less reliable or unachievable. An absolute orientation was undertaken in Figure 21 with six GCPs and the camera station locations surveyed using dGPS and total station techniques for the cliff toe control points as previously discussed. The elevation of the centre of the lens was recorded for each station and this was added in the post processing of the coordinates.

The methodology for the interior orientation of the Nikon D810 with the 24 mm prime lens used for the UAV surveys differed from that presented for the terrestrial photogrammetry. This was due to the ground coverage of the 24 mm lens being much greater than the 35 mm lens, 74.8 m x 50 m and 51.3 m x 34.3 m respectively. The traditional method could not be applied at an object distance of 50 m. Trials were undertaken at the much taller cliffs at Beachy Head but these calibrations proved unsuccessful as they still included substantial foreground and sections

of sky within the images due to the tilt of the camera at the various stations to maintain a fixed central position to each image. When the previously presented method cannot be undertaken for a camera calibration ADAM Technology (2010a) note that if necessary or where good images cannot be captured, calibrations can be completed using photos which were taken by alternative methods. In this case the images produce a stable calibration if there is significant overlap both horizontally and vertically. To comply with the alternative requirements for an interior orientation images were collected following a strip plan with two passes. One pass was at approximately 17 m elevation and the other at 25 m. Both image sets were captured orthogonal and focussed on the centre of the cliff face, resulting in a convergent image set database. The flight path, speed and image capture settings remained as described in the previous section, the resultant overlap of the images in the horizontal plane was therefore maintained at 80% and the vertical overlap of the cliff face was 100%.

3.2.5.1. Processing

The following section details the process of completing an absolute orientation in ADAM 3DM CalibCam, whilst the theoretical basis is the same for any photogrammetry software application specific processes may be unique to this platform. The fixed camera parameters of image size (pixels), sensor size (mm), lens camera and C (focal length) are required as pre-orientation data, all other interior orientation entries should be left empty as these will be populated automatically at a later stage. To complete an absolute orientation six stations are added and set to 'no offset', meaning the pair of images taken at each station are in the exact location, or within the error ellipse, specified by the coordinate (ADAM Technology, 2010a). The ground control points are identified in the images by targets of a white circle on a black background, the optimum target type for the ADAM 3DM software, and are digitised through the centroiding algorithm which can identify the centre of the target to within $1/10^{\text{th}}$ of a pixel. All targets are identified in the 12 captured images before pixel matching is undertaken.

The generation of relative only points (ROPs), the ADAM 3DM terminology for pixel matching within images, forms the key automation process which has revolutionised digital photogrammetry through short processing-cycles (Konecny, 2003; Luhman et al., 2011). Image matching determines identical object features, of points or patterns of pixels in two or more stereo images (Awange & Kiema, 2013) through area-based or feature-based matching (Vosselman et al., 2004; Luhman et al., 2011; 2016; Konecny, 2014). The generated ROPs were then manually checked to remove any identified matching pixels which were found in either the limited areas of sky or within the foreground at the extremities of the image where the depth changes substantially within the image where there is no ground control.

Following the manual filtering of ROPs an image resection was required to derive the interior orientation utilising the relative image points and the absolute GCPs (Linder, 2003). The image resection process is implemented to determine an initial approximation of the ROPs in three dimensional space (Birch, 2009). The approximated points are processed, as a bundle adjustment (Clifford et al., 2004), which refines the construction of the model through creation of jointly optimal 3D models (Luhman et al., 2011; 2013). This process assesses the light rays from the view of each captured image which converge in the perspective centre of each camera position. The bundle of rays are then evaluated to determine the optimal solution (Triggs et al., 1999) using a least-squares methodology (ADAM Technology, 2010a). The completion of the orientation provides a computed image accuracy which forms the basis of an iterative process of adjusting the user defined image accuracy until the optimum solution between both variables provides a posteriori variance factor of around 1 or below (ADAM Technology, 2010a).

A similar process was followed for the UAV photogrammetry as the 23 GCPs were digitised using the centroiding tool in all images they were visible. ROPs were then generated following the aforementioned procedure and points were removed at the extremities of the image if there was a sudden change in depth, e.g. shore platform to cliff face, along with any matched pixels in

the sky which would have introduced error into the calibration. However no stations were defined as a stable absolute solution could be found without these coordinates. Rotation of the global coordinate system was completed for all processing so that orthophoto generation could be completed.

3.2.5.2. Results

Once the interior orientation absolute network has been completed adjustment results are produced (Appendix B(i)- Sony DSC H300, Appendix B(ii) Nikon D810 35 mm varied lens (AF-S Nikkor 24-120 mm 1:4 G ED), Appendix B(iii) Nikon D810 35 mm prime lens (AF Nikkor 35 mm f/2D)). This populates the camera details with the 11 parameters outlined in Section 3.2.5 and provides component (X, Y, Z) residuals and an overall 3DSE for the completed orientation based on the known GCPs and GCN. The component residuals between the GCN and the computed coordinates were no greater than 0.03 m with an overall 3DSE of 0.02 m for the terrestrial photogrammetry solution, both of which are within the error ellipse of the GCPs. An absolute stable calibration was also successfully achieved for the Nikon D810 with AF Nikkor 24 mm f/2.8D for the UAV photogrammetry with a 3DSE of 0.03 m. Focal length, as the critical parameter in interior calibration results (ADAM Technology, 2010a) were recorded as 4.51 mm (4.5 mm set), 34.95 mm (35 mm set), 35.94 mm (35 mm set) for the Sony DSC-H300, Nikon D810 35 mm varied lens and Nikon D810 35 mm prime lens respectively. The camera set up for the UAV surveys yielded a result of 24.25 mm (24 mm set). The interior radial distortion evident across all calibrations constitutes the major imaging error in most cameras (Luhman et al., 2011). It is well known that correlations exist between the image distortion parameters (Honkavaara et al., 2006) the most significant of these are the correlation between radial distortion parameters (K1, K2, K3, K4) and the correlation of principal point coordinates (Xp, Yp) with the decentring distortion (P1, P2) parameters (Honkavaara et al., 2006). The latter of these is evident in the interior orientation of the Nikon D810 35 mm prime lens with a correlation of -

0.94 and -0.91 between X_p and P_1 and Y_p and P_2 (Appendix B(iii)) respectively. A similar outcome was reported for the 24 mm prime lens (set-up for UAV surveys). These parameters have been highlighted by other photogrammetry software developers who state correlated parameters should only be of concern when they exceed a threshold of 95% correlation (Eos Systems, 2017) which these results do not. Furthermore the ADAM 3DM CalibCam software allows investigation of these parameters to determine whether they affect the stability of the calibration by selecting optimised parameters. This was undertaken and the calibration was deemed stable. An alternative method is to manually disable one of the correlated parameters to assess the results of the calibration however undertaking this for the parameters X_p , Y_p , P_1 and P_2 reduced the accuracy and overall quality of the interior calibration. The calibrations were therefore used with the aforementioned results for all photography captured from the relevant camera and lens configurations for the terrestrial photogrammetry at Brighton Marina and UAV photogrammetry at Telscombe.

3.2.6. Exterior orientations

The exterior orientation determines the spatial position and orientation of the camera in a global coordinate system (Clifford et al., 2004). Once the perspective centre of each captured image is located, the image is then rotated around the x, y and z axis by applying a rotation matrix using trigonometric functions of angles ω , φ and κ respectively. For terrestrial photogrammetry where the axis of the camera is aligned with the horizontal, to avoid singularities in the trigonometric functions, rotation can be altered to; ω tilt about the horizontal, κ the roll around the optical axis and φ rotation around the azimuth (Luhman et al., 2011) as illustrated in Figure 22. Alternatively the image coordinate system can be changed from the typical x and y axes to x and z.

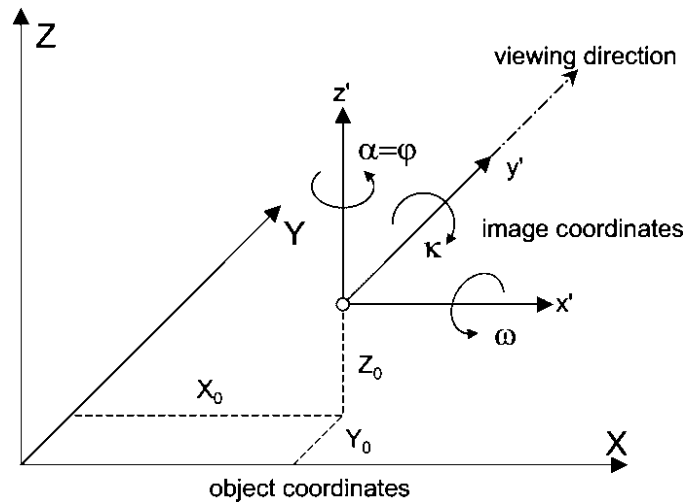


Figure 22: Exterior orientation rotation parameters for terrestrial photogrammetry (Source: Luhman et al., 2011, p. 204 Figure 4.3).

3.2.6.1. Processing

To obtain the matrix of points in the final model on the plane of interest, the cliff face, the axis of the global coordinate system were rotated from x to y , y to z and z to x as the ADAM 3DM software by default generates DTMs as if the imagery was captured under traditional aerial photography procedures. Digitisation of control targets and generation of ROPs follows the method detailed previously and is illustrated in Figure 23. All control targets were digitised in the images they were visible in. The process of exterior orientation works indirectly with the



Figure 23: Exterior orientation processing from ADAM 3DM CalibCam Manager view - digitised GCPs (Green) and ROPs (Red) of terrestrial photogrammetry in Brighton Marina on 20.01.2017, inset shows fixed target at cliff top residual scale at x100 for viewing purposes.

parameters generated after the known global coordinates are located within the image (green points in Figure 23). Every ROP within the database of images corresponds to a spatial measurement from the perspective centre to object point (Luhman et al., 2011). The length of each vector is, at first, unknown however by measuring along convergent rays from different image stations the intersection point can be determined in object space. This is repeated for all the points within the image database which generates a dense network of bundles of rays. Utilising the bundle adjustment method any number of images, known as multi-image processing, can be used simultaneously in an exterior orientation (Schenk, 2005; Luhman et al., 2011) to develop a 3D model utilising the ROPs the GCPs and their associated image coordinates and the object coordinate system (Luhman et al., 2013). The resection and bundle adjustment processing utilises the same iterative methodology between computed image accuracy and user defined image accuracy until the posteriori variance factor is recorded at around 1 or below (ADAM Technology, 2010a).

The same methodology of using control targets was initially implemented at Telscombe for the UAV surveys. However, to avoid monthly replacement of the GCN including resurveying of these points, flints were identified in the 3D models generated from the initial GCN of 23 GCPs with a 3DSE of 0.03 m. By extracting the coordinates of these flints from the 3D model and digitising the flints (Figure 24) in a reprocessing of the model these coordinates were added to the original



Figure 24: Example of digitised flint in ADAM 3DM CalibCam – point number 26, image captured from UAV flight on 10.10.16 (Red points and numbers are ROPs, green line in insert is residual for point 26 with a visual scaling factor of x100).

network. A total of 53 control points were processed 23 GCPs and 30 digitised flints, which acted as check points effectively assessing the accuracy of the extracted flint coordinates. The adjustment results reported component errors in X, Y and Z for the flint coordinates and provided adjusted coordinates based on the 3DSE of 0.03 m of the original GCN. The residuals reported from the software for the digitised flints were as a result of issues with point coordinate extraction. Therefore, the adjusted coordinates for the flints were extracted from the adjustment results and reprocessed in the model with a check point 3DSE of 0.00 m with reference to the known 0.03 m 3DSE of the original GCN (Appendix D). The flint coordinates were subsequently used to provide a global coordinate system to the 3D models.

3.2.6.2. Results

As with the interior orientation, following the completion of the exterior absolute network adjustment results were produced (Appendix C) detailing the residuals of the GCN with component standard errors and with a 3DSE. The absolute accuracy procedure produced a 3DSE of 0.02 m for the Nikon D810 35 mm prime lens within the error ellipse of the GCPs an improvement from 0.04 m for the Sony DSC-H300 which highlights the improvement through the developed methodology. The observations (digitised, adjusted and original) of the GCN targets and exterior orientation parameters, of image location and rotation, are also included in the adjustment results (Appendix C) which provides an opportunity for the user to assess any issues with individual points or images within the exterior orientation processing.

For the UAV exterior orientation results the monthly datasets varied with respect to the component and 3D standard errors (Table 7). There are several explanations for this variation which are explained in photogrammetric theory (Luhman et al., 2011) and by the software guidance (ADAM Technology, 2010a). Firstly the strip capture method endeavours to capture images orthogonal to the cliff face but this is entirely dependent on the accuracy of the user and the reliability of the live stream under varied environmental conditions, deviation from truly

orthogonal captured images directly effects the image overlap and pixel matching. The varied ISO setting introduces variation in the image pixel matching capability as blur introduced by an increased ISO (ADAM Technology, 2004; ADAM Technology, 2010a) can reduce the image accuracy. This is unavoidable as natural lighting conditions vary and flights are dependent on access to the shore platform at low tide so flight times are restricted. Environmental conditions also have an impact on the models, for example the dataset collected in January had four less images than most other months due to gusts of wind which increased the speed of the UAV near the western end of the flight, this evidently reduces the pixel matching through a decrease in horizontal overlap and therefore the model accuracy (Table 7). The models would likely have benefited from another pass as was undertaken for the interior orientation to increase accuracy, whilst this was achievable to determine an interior orientation the available processing capabilities would not allow generation of a merged DTM from the dual pass survey. The range of component errors was relatively small between sequential datasets at 0.03 m across X, Y and Z with the same range apparent in the overall 3DSE with a maximum of 0.06 m in January. The maximum component error from any GCP in any month was 0.10 m (December).

Axis	Residuals (m)				
	X	Y	Z	Standard Error (SE)	
Axis (rotated)	Y	Z	X	Overall	Max. Component
August 2016	0.02	0.02	0.01	0.03	0.05
September 2016	0.02	0.02	0.01	0.03	0.05
October 2016	0.01	0.02	0.01	0.03	0.04
November 2016	0.03	0.03	0.01	0.05	0.06
December 2016	0.01	0.05	0.01	0.05	0.10
January 2017	0.04	0.02	0.04	0.06	0.08
February 2017	0.02	0.02	0.03	0.04	0.06
March 2017	0.01	0.03	0.02	0.03	0.06
April 2017	0.02	0.05	0.01	0.05	0.08
May 2017	0.03	0.03	0.02	0.05	0.06
June 2017	0.02	0.03	0.03	0.05	0.07
July 2017	0.03	0.03	0.02	0.05	0.07

Table 7: Exterior orientation component and overall accuracy for monthly UAV photogrammetry models from August 2016 to July 2017.

3.2.7. Digital terrain model (DTM) generation

The generation of DTMs was undertaken by inputting viewer files which are images paired by ROPs to generate epipolar images. This procedure rectifies and rotates the initial images into an epipolar or stereo-vision pair (ADAM Technology, 2010a; Luhman et al., 2011) as illustrated in Figure 25. Points are then sampled from the image pair to generate the point cloud in Figure

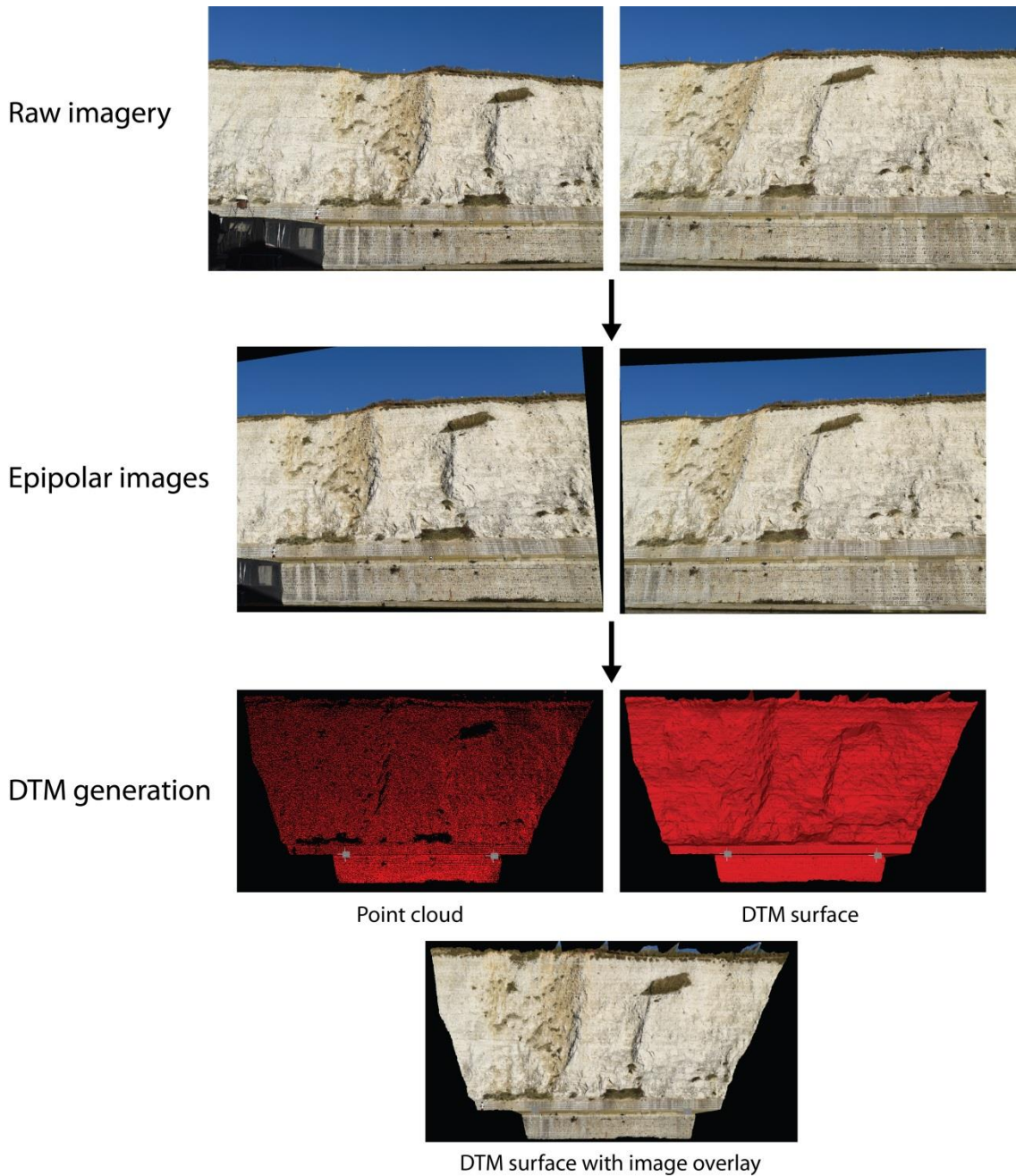


Figure 25: DTM generation workflow from raw imagery to DTM surface with imagery using ADAM 3DM CalibCam and 3DM Analyst (Images taken from Nikon D810 35mm prime lens on 20.01.17 from stations 1 & 6).

25 and are visualised as a surface through triangulation of the point cloud. The imagery is then draped over the surface to provide the final model for the stereo image pair (Figure 25). This procedure is repeated for all image pairs within the image database to generate a database of point clouds or DTMs for each week of data capture: 63 DTMs for Sony DSC-H300 and 76 for Nikon D810.

The individual DTMs provide subsections of the study area, for usability these files were merged into one DTM. This process uses version 6.13a of the screened poisson surface reconstruction (Kazhdan & Hoppe, 2013a) which generates a surface from all known orientated points and is highly resilient to data noise (Kazhdan et al., 2006). This surface is then sampled and the algorithm improvements (Kazhdan & Hoppe, 2013b) have improved the processing and accuracy of the final surface models. Full mathematical formulation and examples of the surface reconstruction are presented by Kazhdan et al. (2006) and Kazhdan and Hoppe (2013b).

The surface sampling is semi-automated with the user having control over the following parameters in the software:

Samples per node	number of input points to average in creating an output point
Minimum spacing	sampling distance of the merged surface, the distance between points of the new DTM/cloud
Max. spacing factor	multiple of the minimum spacing used to determine points which should remain connected, also acts as a clip to the edge of the merged surface
Point weighting	determines the smoothing effect of the generated surface. Importantly the accuracy of each point is determined by the image co-ordinate accuracy and model geometry, so points from image

pairs with relatively small base distances will be weighted less than other points

Table 8 provides an overview of the developed methodology of the terrestrial photogrammetry through the research, presenting the merged DTM outputs. The surface area is greatest on the Sony camera due to the wide angle zoom lens which captures more of the cliff face at the extremities of the dataset. The reduction in surface area from the fixed to varied focal length Nikon is due to the strip versus convergent image capture. The convergent strip model produces the most accurate model as distance to base ratio of matching points is increased due to the convergent nature of capture. The increased 3DSE of 0.044 m in the varied focal length Nikon can be primarily explained due to the difficulty in obtaining the exact same focal length between surveys, as the critical parameter in interior orientation any variation in this parameter will directly affect the model output (ADAM Technology, 2010a). The camera which provides the most accurate models (3DSE 0.021 m) with the highest resolution (3,832 pts/m²) was the Nikon D810 using the convergent strip method of capture.

Camera	Lens	Image Capture	3DSE (m)	Merged DTM Points	Surface area (m) [*]	Merged DTM point density (m ²) [*]	Point spacing (m) ^{**}
Sony DSC-H300	35X optical zoom	Strip	0.035	3,752,606	2836	1,323	0.028
Nikon D810	AF-S Nikkor 24-120 mm 1:4 G ED	Strip	0.044	7,908,082	2670	2,962	0.018
Nikon D810	AF Nikkor 35 mm f/2D	Convergent	0.021	8,341,269	2177	3,832	0.016

Table 8: Camera and model parameters in development of terrestrial photogrammetry methodology (*- rounded to the nearest significant figure, **- correct to 3 decimal places).

For the terrestrial photogrammetry merged DTMs the following settings were used; samples per node = 1 (selected as default for DTM generation, larger values up to 5 used for noisier datasets), minimum spacing = 0.02 m and 0.03 m for Nikon D810 and Sony DSC-H300 (Table 8) respectively

(calculated as the total number of points from the individual DTMs divided by the surface area generated from the extent of the DTMs), Maximum spacing factor = 8 (default this translates to 0.16 m for the Nikon D810 models and 0.24 m for the Sony DSC-H300, a boarder at the aforementioned values should be ignored as this is artificial data) and point weighting = 1 (default - range 0-4, chosen as the value which maintained detail within the final model but did not introduce noise into the merged DTM). The merged DTM files were then exported in point cloud format in preparation for further processing to detect and quantify surface change in other software platforms.

The individual DTMs for the UAV surveys were generated following the same process as the terrestrial photogrammetry. Table 9 displays the total images from each monthly dataset and the DTMs generated. The reduction in images and DTMs was due to environmental conditions as previously discussed. The point density per square metre varied from 604 to 808 (between the surveys from August 2016 to July 2017), which relates to a point every 0.035 m to 0.040 m. However due to limitations in processing capability the merged DTMs that were generated for the monthly datasets (Kazhdan et al., 2006; ADAM Technology, 2010a; Kazhdan & Hoppe, 2013a; 2013b) had a minimum point spacing of 0.05 m. An improvement in processing capability may enable a similar point density through multiple strip passes similar to that obtained in the terrestrial photogrammetry (>1,000 pts/m²). The monthly merged DTMs consisted of approximately 17,000,000 points each. Although this is a significant reduction from the raw point files/individual DTMs (Table 9) the average point density of 351 pts/m² is much greater than the current resolution of 25 pts/m² currently available from the post processed laser scan surveys (Bovington, 2010; 2012; 2013a; 2013b) for the same site. The merged models were then exported in point cloud format for further processing.

3.2.8. Processing of data for 2.5D change detection

The point clouds (generated from DTM files) were imported to Cloud Compare (Cloud Compare

Month	Number of images captured	Individual DTMs generated	Total points generated	Points/m ² *
August 2016	54	136	30,740,108	657
September 2016	54	128	37,335,837	798
October 2016	54	139	36,786,222	787
November 2016	54	116	30,562,846	653
December 2016	54	136	37,767,982	808
January 2017	50	99	30,692,864	656
February 2017	52	116	33,493,942	716
March 2017	53	117	34,086,217	729
April 2017	54	131	27,546,966	624
May 2017	53	122	29,610,906	604
June 2017	54	131	29,933,017	626
July 2017	54	133	31,419,732	607

Table 9: UAV photogrammetry monthly images captured and individual DTM statistics (*rounded to nearest significant figure).

v2.6.3, 2016) where a 'global shift' was applied to the data for ease of processing, there was no adjustment made to the coordinates position or scaling of the point cloud. All point clouds were then translated so that the average dip direction or cliff azimuth was parallel to the Z plane (true Y plane) so measurements between models would represent true depth change and 2.5D change detection results (Rosser et al., 2005) would be reliable estimates of the rockfall volumes. The conversion from point cloud to raster for the terrestrial photogrammetry models was undertaken in Cloud Compare (Cloud Compare v2.6.3, 2016) with a cell size replicating the minimum point spacing. As this varied dependent upon camera set up raster models were generated with a cell size of 0.03 m for the Sony DSC-H300 models and at 0.02 m and 0.03 m for the Nikon D810 prime and varied 35 mm lens. This enabled comparisons between different cameras and lens configurations spanning the entire period of data collection and between higher resolution datasets which were developed through methodological advances later in the research. For the UAV photogrammetry with a point spacing of 0.05 m an increased cell size of 0.10 m was selected. This was due to the complex morphology at the site which introduced edge effects, a common issue experienced in TLS datasets at the same location (Bovington, 2010; 2012; 2013a; 2013b). By increasing the cell size, a greater number of points were sampled in determining an average value for each cell which removed identified 'false surface change' and noise from the dataset. The projection of the raster was set so the cliff was orthogonal to the

cliff azimuth and any empty cells were set to 'interpolate' as this enabled any holes in the dataset, primarily associated with vegetation to be closed.

3.2.9. Change detection

The raster datasets were processed in ArcGIS to calculate surface and volumetric change. Surface change was simply undertaken by subtracting sequential weekly or monthly datasets for terrestrial and UAV photogrammetry respectively.

To determine the minimum detectable surface change boxes of volumes: 3 cm³, 5 cm³, 7 cm³, 10 cm³ and 15 cm³ were made. A set of images were taken with the boxes temporarily fixed to the rear splash wall in the study area (Figure 26) and another immediately after with the boxes



Figure 26: Boxes installed on rear splash wall to determine threshold of detection for terrestrial photogrammetry, Brighton Marina.

removed. The method of capturing two sets of data immediately after one another was previously applied by Lim et al. (2005) at the cliffs in Staithes, North Yorkshire to determine the accuracy of TLS captured data in complex geomorphological environments. The results of the study in Brighton Marina found that by using the terrestrial photogrammetry method 'false' change is detected in areas of vegetation (Figure 27A) where pixel matching is known to be poor (ADAM Technology, 2010a). Figure 27B provides an inset of the surface change between the

two datasets identifying the location of the boxes $5 \text{ cm}^3 - 15 \text{ cm}^3$ as the 3 cm^3 would be undetectable as it was at the limit of the error ellipse of the GCN. The volume of the detected remaining boxes were compared to the known volume, accounting for the maximum error introduced from the GCN (up to 3 cm^3) the smallest box to accurately record its correct volume was the 7 cm^3 with 98.49% detected. As a result the threshold of change detection for the terrestrial photogrammetry was set to 0.07 m for comparison of surface change between the generated models.

For the models generated at Telscombe (UAV photogrammetry) the surface subtraction revealed a few remaining edge effects, surface change within vegetated areas and substantial change due to variations in beach volume. To develop a method which enabled automatic detection of rockfalls these, either false or unrequired, data were removed. This was achieved by firstly setting the threshold of detectable change from the UAV photogrammetry to 0.10 m. This threshold was 0.03 m greater than the terrestrial photogrammetry approach and was selected to reflect the greatest component error between any monthly dataset from August 2016 to July 2017 (Table 7). To determine real change each monthly dataset was subtracted from the initial state, August 2016. For any change to be real the surface change would have to exist in two of these datasets. All of the monthly subtraction rasters (from the initial state), with the exception of July 2017, were reclassified to a binary dataset of surface change greater than 0.10 m equal to 1 and all other data set to 0. August - July 2017 followed the same threshold of classification as the other datasets but change was reclassified to 10 and all other data as 0. The justification for this alteration is that 'real change' is present in at least two months of data but as there is no comparative dataset for July, change must be classified differently or would be removed. The binary rasters were totalled and any value less than 12 (change recorded in two datasets plus July) was reclassified to 0 and all values greater than 12 were reclassified to 1, generating a mask which could be used to remove false change from all the monthly datasets

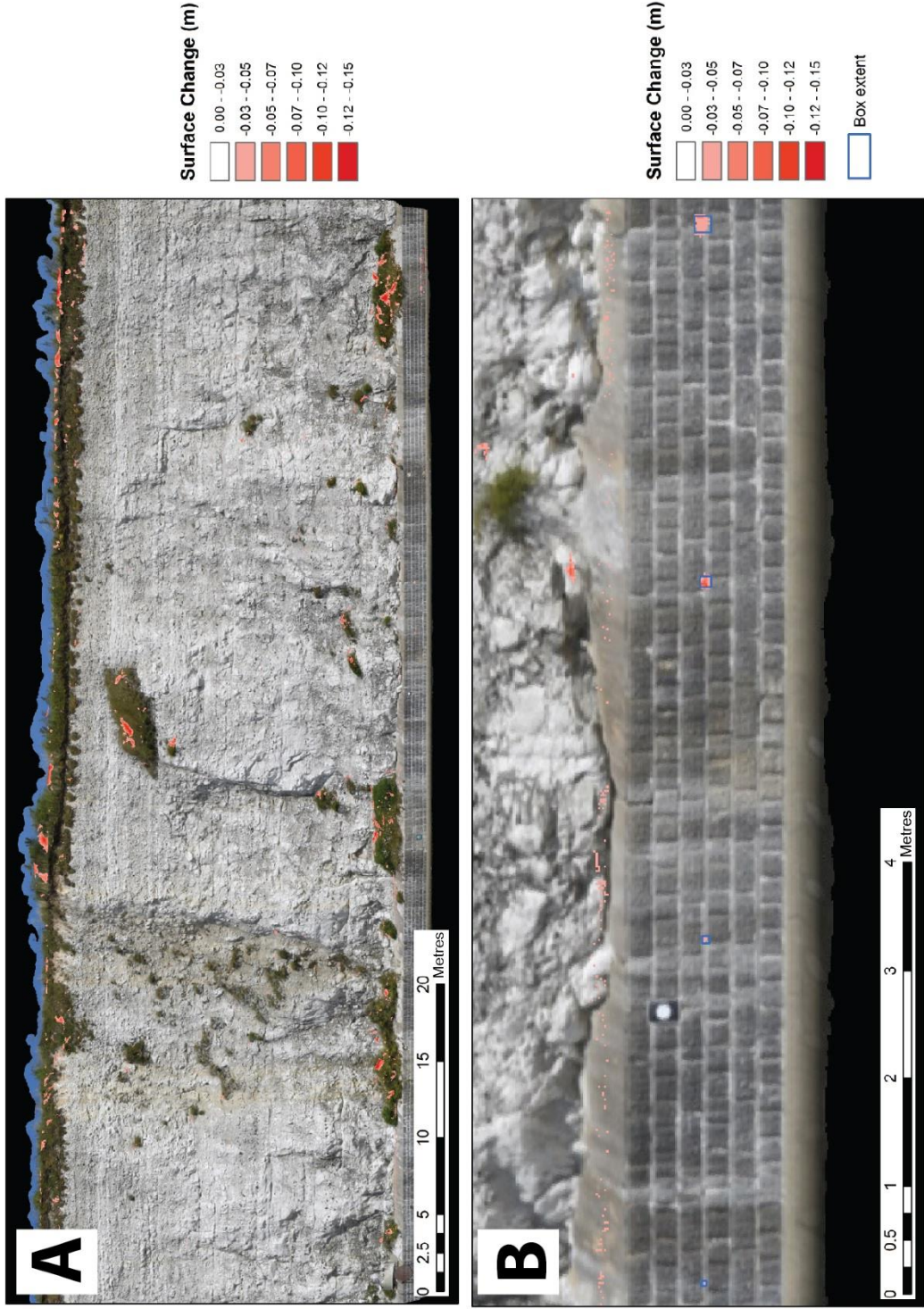


Figure 27: Threshold of change detection for terrestrial photogrammetry, image captured with Nikon D810 35mm prime lens, (A) change detection between datasets captured immediately after each other with boxes fixed and removed and (B) inset showing location and known extent of boxes.

(e.g. Aug-Sep, Sep-Oct). This automated method reduced processing time and meant that only the edge effects and vegetation from the July dataset had to be verified against the images to determine if the change was true, where it was not the false change was reclassified manually. Finally, the mask was trimmed to represent the extent of the cliff face and to remove the shore platform or beach material from the rasters. All surface change below the detectable threshold was removed by masking the rasters for each month and volumetric calculations were undertaken using the cut/fill tool in ArcGIS.

3.3. Environmental investigations – thermal imaging

The effects of thermal weathering processes are well established yet relatively unexplored in the coastal cliff environment (Walder & Hallet, 1985; Robinson & Jerwood, 1987; Griggs & Trenhaile 1994; Greenwood & Orford, 2007). Studies to date have been unable to acquire thermal images at a comparable frequency to meteorological data to assess relationships between air temperature and cliff surface temperature. Although there have been successes in deploying short term thermography within the scientific literature (e.g. Baroň et al., 2014; Mineo et al., 2015). The difficulty in obtaining longevity of data is compounded by the challenge of installing and maintaining equipment (Mortimore & Lawrence, 2008) limiting the ability to determine meaningful temporal relationships. Such datasets are also highly susceptible to external lighting conditions as reported by Mortimore and Lawrence (2008) who captured thermal imagery at Birling Gap, the Newhaven Chalk formation exposed in the cliffs at Brighton and at Black Rock. Their pilot study (Mortimore & Lawrence, 2008) concluded that for optimum images data capture should be at dawn or dusk to minimise shadow on the cliff face, as the aim of the research was to assess the optimum meteorological conditions for failure in the chalk and capture the thermal fingerprint of such failures. This pilot study collected another dataset the following year but there was little data processed and subsequently no further outputs were

supplied from the INTERREG IIIa INFORM project with respect to thermography. This section will present the approach to obtaining an hourly thermal dataset.

3.3.1. Installation and set-up

The site selected for the thermal image capture was at the same location in Brighton Marina where terrestrial photogrammetry was deployed. This enabled the equipment to be installed on a property seaward of the cliff face and was approximately 360 m from a meteorological station (Figure 28) at the cliff top which is maintained by the CCO on behalf of BHCC.

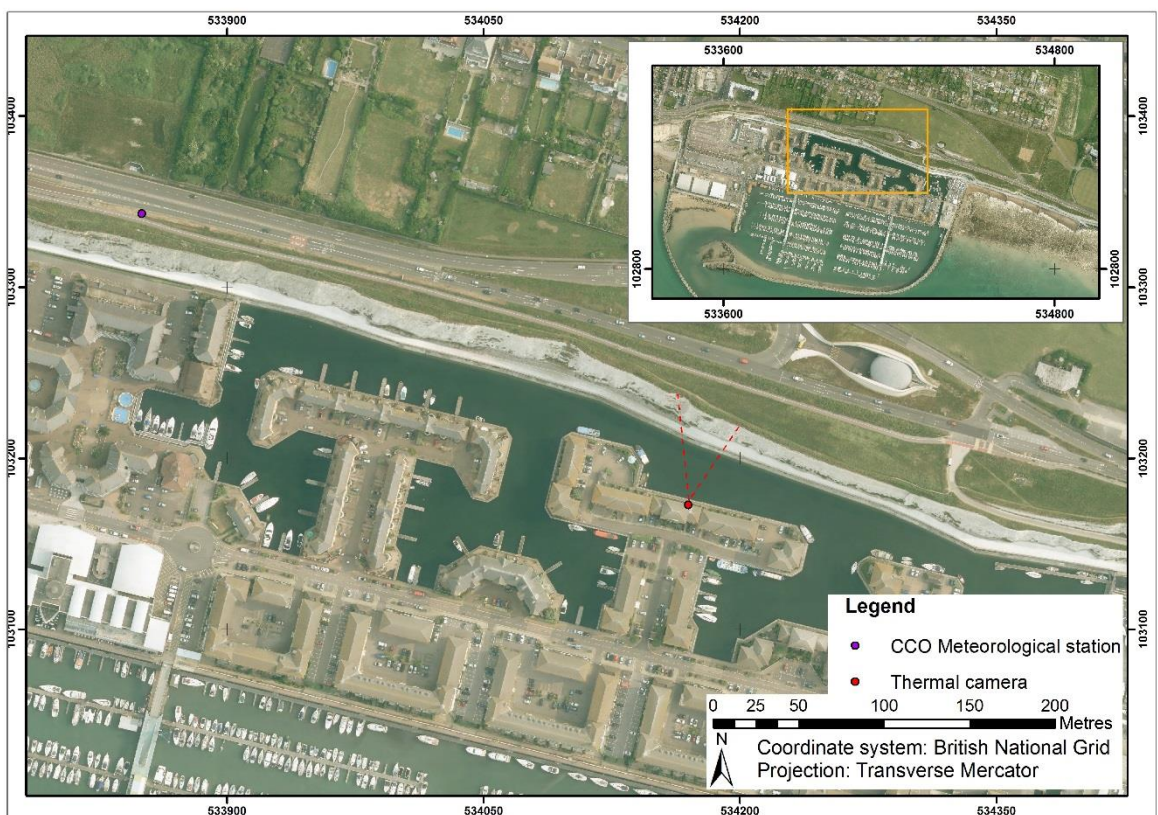


Figure 28: Location of thermal camera and meteorological station at cliffs in Brighton Marina (Red dashed line indicates the approximate field of view of the thermal camera) [2013 imagery downloaded from the CCO].

The thermal camera procured for data capture was a FLIR A35sc which has an operating temperature range of $-40\text{ }^{\circ}\text{C}$ to $550\text{ }^{\circ}\text{C}$, an image frequency of 60 Hz and a pixel matrix of 320 x 256. The FLIR A35sc is a static camera requiring a computer for operation and is fitted with a standard fixed 48° lens. To overcome the difficulties associated with installing sensitive equipment in a coastal environment including; precipitation, salt spray and nesting of wildlife

the thermal camera was housed in a weatherproof box (Figure 29A) and fixed to the wall just below the eaves (Figure 29B). The housing was fitted with a thermal glass inspection window to allow accurate imagery to still be obtained whilst protecting the equipment. The A35sc was mounted on a fully adjustable bracket (Figure 29C) which allowed the camera to be directed and fixed towards the centre of the cliff face before data collection began. The computer required for operation was housed in a service cupboard inside the building in a Peli-case (Figure 29D) which provided both security and ease of access when downloading of data was required. Using the FLIR IR Max software the thermal camera was set to automated capture, taking an image once every hour on the hour. Regular visits were undertaken to download data from the hard drive and check on camera operation. The camera was focussed with the object distance at approximately 50 m.

3.3.2. Thermal image optimisation

Several methods are presented within this section which optimised the thermal imagery to produce accurate absolute temperatures, these include accounting for emissivity, reflectance and image flattening.

Emissivity is quantified as a percentage or decimal of the amount of radiation emitted from an object in comparison to that of a perfect radiation emitter, or black body (Norman & Becker, 1995; FLIR, 2015). Obtaining the correct value for emissivity is critical in obtaining accurate absolute temperature values (FLIR, 2015). FLIR (2015) report that the majority of non-metals have an emissivity value near 0.9. There are many methods to obtain emissivity as detailed by FLIR (2015) however many of these solutions require close range methods and are readily undertaken on electrical products. As a result the spot tool (which locates a pixel and details the recorded temperature) within the FLIR IR Max software was used to extract temperatures from a given location on the cliff face. The extracted temperature was then compared to a surface temperature recorded using a CEM DT-8861 compact dual laser targeting infrared

thermometer. This was undertaken for a number of locations along the base of cliff, as the only accessible location to the chalk. The extracted and measured values were entered into the spot tool analysis menu and the emissivity of 0.95 was calculated. This value was therefore used in all subsequent analysis.

Another important parameter to account for obtaining reliable absolute temperatures is the reflected temperature (Norman & Becker, 1995; Monroe Infrared, 2014; FLIR, 2015). This parameter compensates for temperatures from the surrounding objects within the environment reflecting on the target (Monroe Infrared, 2015), in this case the cliff. To obtain the reflected temperature value the emissivity value has to be set to 1.0 and a piece of crinkled aluminium foil needs to be flattened and placed in the image scene (Monroe Infrared, 2014). Aluminium foil sheets were joined together to produce a piece of foil with dimensions 1.5 m x 2 m. These dimensions were selected to increase visibility in the thermal image (Figure 29D) and provide a greater surface area for an average temperature to be calculated from. The aluminium sheet was temporarily attached to the rear splash wall below the chalk cliff and a polygon drawn around the foil sheet in the FLIR IR Max software (Figure 29E). The average temperature was extracted of 15.3 °C and was used in in the camera data file for the subsequent analysis.

In the early stages of operation, between November and December 2014, there were instances where the temperature in the weatherproof housing was greater than the surface of the cliff. Under this scenario the camera was producing more heat (or energy) than was received through the thermal lens (Figure 30A) and as a result the lens does not receive enough energy to generate an image of the cliff. The result is a thermal image which displays a radial pattern (Figure 30B) which is a reflection of the camera's heat on the thermal window of the housing (Figure 30A). To remove this issue from the imagery, image flattening was undertaken, whereby a matt black surface was placed in front of the thermal lens on the housing and a user calibration was performed using the FLIR IR Max software. This process captures several frames where the

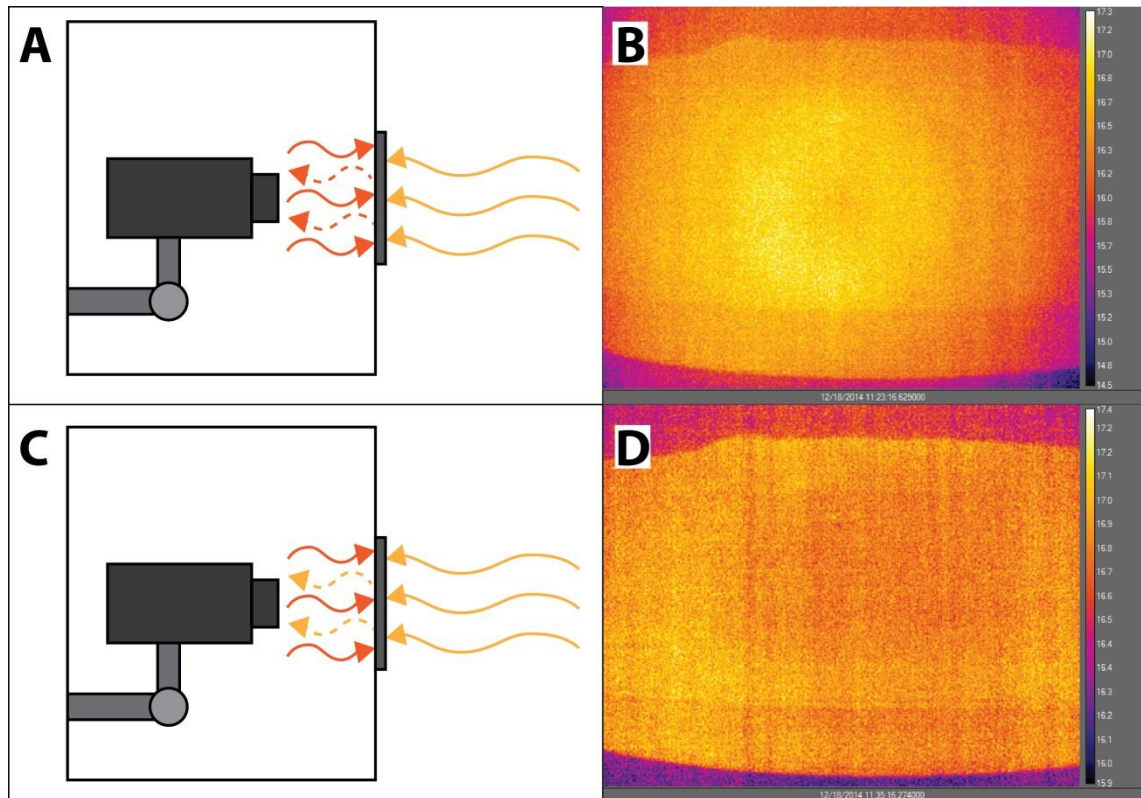


Figure 30: Thermal image flattening undertaken on 18/12/2014 (A) schematic illustrating reflected operating temperature being recorded (B) thermal image illustrating the reflected operating temperature of the camera, (C) schematic illustrating the corrected thermal recording and (D) the corrected thermal imagery (Temperatures on legends in (B) and (D) are in °C).

3.3.3. Data collection issues

A total of 18,204 images were recorded between 06/11/2014 (12:00) and the 31/12/2016 (23:00), this represents 96.45% (18,875) of the total hours between these two dates. Data was lost due to corruption of downloaded files between 9/11/15 (12:00) and 04/12/15 (11:00) which accounts for 89% of the absent data, whilst the remaining files were not recorded between 14/03/2016 (15:00) and 18/03/2016 (11:00) due to a power cut. The automated image capture had to be restarted manually after power loss. In addition to this environmental conditions provide issues when collecting thermal images. Both precipitation and relative humidity cause images to become blurred and unusable. By analysing the thermal images, a relative humidity threshold of 90% was found, above this value images were unusable (Figure 31A). The meteorological station in Brighton Marina recorded 4,686 hours above this threshold approximately 25.8% of the entire dataset and 5.1% (36/703) of the analysed thermal images

when air temperature was below freezing. Precipitation also has an effect on image capture (Figure 31B), although many of the images where precipitation occurs is prevalent relative humidity is high. Figure 31B was captured on 13th August 2015 at 10:00, 4 mm of rain was recorded in the ten minutes prior to capture and 6mm ten minutes post capture. The reasoning for the blur in the images under both of these conditions is that the water absorbs energy from the cliff and the surrounding environment which is read by the thermal camera as the object of interest, this creates a blurred film across the image and therefore the data cannot be used.

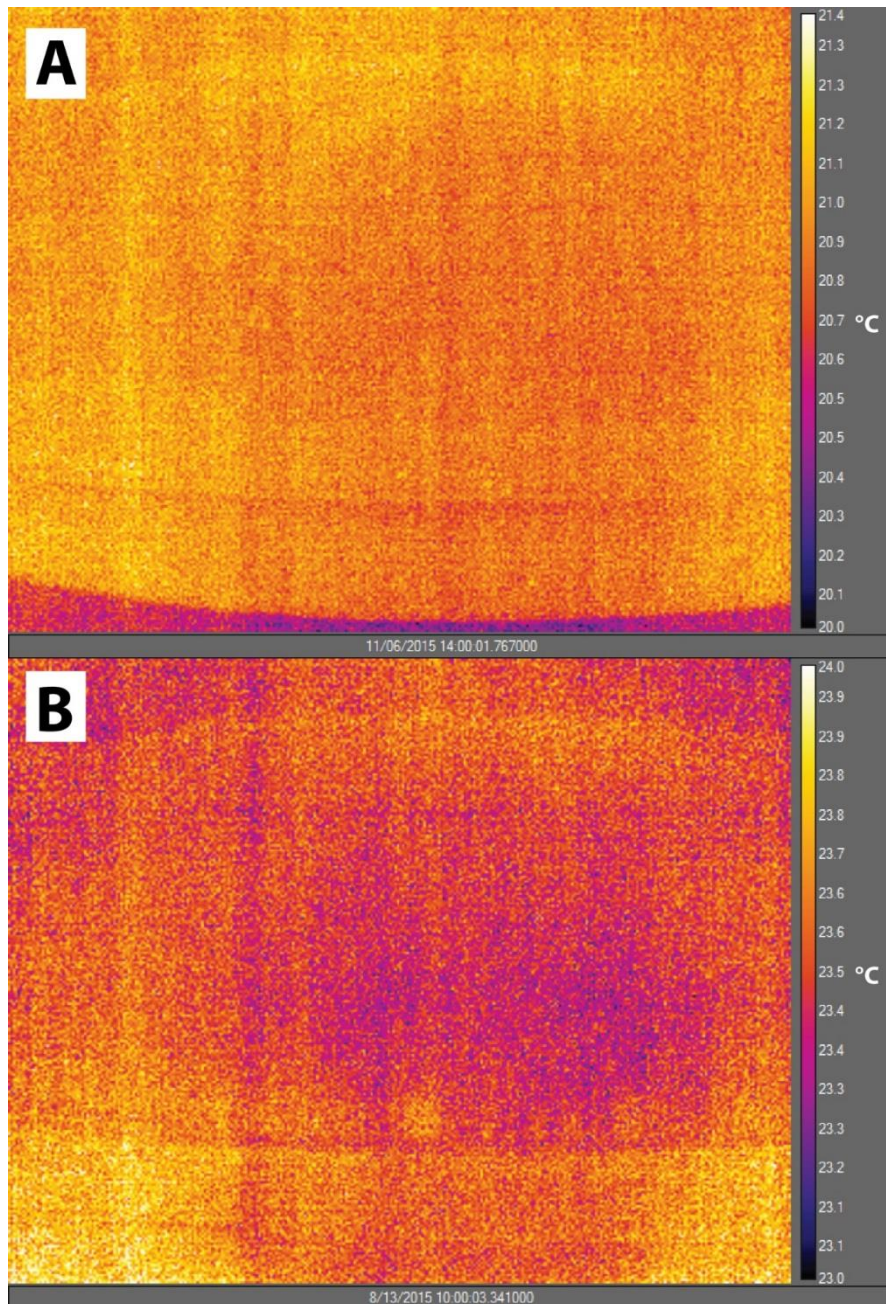


Figure 31: Thermal imagery data capture issues (A) relative humidity exceeding 90% captured on 06/11/2015 at 14:00 and (B) heavy rainfall captured

3.4. Numerical modelling of cliffs – kinematics and limit equilibrium

The deterministic approach to modelling potential rockfalls utilises the obtained geological parameters from the site (Park & West, 2001) in determining risk of failure through the calculated FoS value (Goodman, 1976; Hoek & Bray, 1981). The limit equilibrium method is a justified approach as observations of failure within the Newhaven Chalk tend to be brittle in nature with negligible prior deformation which would be assessed in FEA/FEM. This approach has been applied in engineering of slopes with distributed joint systems, which is characteristic of the Newhaven Chalk formation of the study area. Engineering reports from High-Point Rendel (2002; 2006), for the case of Brighton Marina, model the Newhaven Chalk through limit-equilibrium methods to assess the FoS of slopes through various engineering works including regarding and rock bolting. The kinematic analysis methodology will be presented within this section based on 3D photogrammetric models of the Newhaven Chalk in Telscombe as no model was generated for the entire defended section due to constraints placed on the UAV flight operations by the CAA. The limit equilibrium method used the data obtained from the kinematic analysis to assess the relative stability of the conjugate joint sets within the defended section of cliff line from Brighton Marina to Telscombe. This research therefore builds a much larger database than the previous engineering reports (High-Point Rendel, 2002; 2006) which focus on specific locations.

3.4.1. Discontinuity mapping and kinematic analysis

To obtain the discontinuity database the 3D photogrammetric model was used from 7th September 2016. The generation of the data is explained in this section through the use of the software platforms; ADAM 3DM Analyst (mapping) and Dips 7.0 (kinematics).

Discontinuity mapping involved digitising planes on individual chalk failure surfaces (Figure 32A). Mapping of the discontinuities was completed on the 3D model at approximately 0.5 m from the surface as described by Mathis (2011) and utilised by (Barlow et al., 2017). However due to



Figure 32: Discontinuity mapping illustrating joints and faults digitised on the 3D model generated for Telscombe 07/09/2016 using ADAM 3DM analyst (A) mapping of entire study area, (B) inset of western section showing detail of mapping and (C) identified location of previous wedge failure [Yellow discs – Joint Set 1, Orange discs – Joint Set 2, Blue discs – unidentified joint set, Red discs – faults].

the complex morphology and shadow on the orthoimage this distance varied in some cases. The fresh erosional surfaces were identified by a distinct change in colour, distinguishable in chalk by a bright white surface against surrounding weathered material, and by a smooth non-roughened surface characteristic of failure (Barlow et al., 2017). The dip and dip direction of these digitised surfaces were automatically derived by the software through extraction of the direction cosines with respect to the normals of the digitised plane (Sturzenegger & Stead, 2009; Barlow et al., 2017). A total of 391 discontinuities were digitised, which included 255 joint surfaces, 28 faults and 108 bedding planes. Mapping of bedding planes was more challenging as these features were predominately only etched on the surface of the chalk. As a result, mapping of these planes took advantage of convexities and concavities on the slope surface where exposure of these surfaces in 3D space was achievable, this led to a higher frequency of smaller discs being generated to increase confidence in the data, as much greater discs were not representative of the bedding plane across greater distances. The increased number of bedding planes has little impact on subsequent data analysis through mode of failure as the bedding planes do not form major failure surfaces but are more likely to control the extent of a failure.

The discontinuity database was exported to Dips 7.0 to identify the major joint sets within the Newhaven Chalk at Telscombe. Average cliff parameters required for the analysis were extracted from the 3D model including, the cliff face which was found to strike at 114° or dip direction of 204° and the average slope angle of 76° (Barlow et al., 2017). Joint sets were determined by using the 'set window' tool which generates a user controlled curvilinear four sided window to represent the extent of the cluster. The 'set window' method was selected as it represented the most robust method to obtain the joint set data. Alternative methods included 'free hand' which could lead to user error and 'cluster analysis' which determines an extent from the centre of a defined set in degrees, this also can introduce error by removing data from the same set which lies just outside the buffer generated. The average dip and dip directions were then calculated for the mapped discontinuities which fall within the extent of

the set plots. This process formed the database which was then used in the limit equilibrium analysis.

3.4.2. Limit equilibrium modelling

As the defended section of interest for this section of the study has been protected for over 80 years and has been subject to a variety of engineering measures in an attempt to stabilise the cliff face, very few failure surfaces remain. As a result field measurements were taken to determine conjugate joint set dip values and the dip/slope of the cliff face through the following methods. The dip value of the discontinuity was achieved by standing parallel to the cliff face and measuring the angle of the joint from the horizontal using a clinometer. The angle of the cliff was also measured using a clinometer at each identified conjugate joint set. The dip direction of the cliff face at each identified joint was completed post field visit, the location of each set was mapped in ArcGIS and a transect was cast perpendicular to the cliff face and the angle measured. The limit equilibrium analysis was undertaken in Swedge which is detailed in the following sections.

3.4.2.1. Input data

Input data was required for each of the joints in the wedge analysis. Dip values were obtained from field surveys whilst dip direction values use the average dip direction of the identified joint sets. A joint waviness parameter was also required, for the majority of conjugate sets this was set to 0°. Where there was variation in the joint dip observed in the field both the average and the minimum dip angles were obtained, subtracting these measurements then provides the waviness value. The shear strength model selected for the limit equilibrium analysis was the Mohr-Coulomb:

$$\tau = c' + \sigma'_n \tan \phi'$$

where τ is the shear strength, c' is cohesion, σ'_n is the normal stress and ϕ' is the friction angle.

This model provides a geologically realistic approach to represent the overall strength of the rock mass (Hencher, 2012). The input parameters required for the mohr-coulomb strength model are cohesion and friction angle. A review of literature (Hutchinson, 1972; Lake, 1975; Clayton, 1978; Fletcher & Mizon, 1984; Twine & Wright, 1991; Lord et al., 2002) and geotechnical reports (High-Point Rendel, 2002; 2006) undertaken in the Newhaven Chalk formation provide a range of 34° to 42°, as a result the average friction angle of 38° was used and a sensitivity analysis undertaken to establish the effect of varying this parameter.

As many joints in the Newhaven Chalk formation are sheet-flint filled different shear strengths apply to these surfaces (Mortimore et al., 2004a) through variation in cohesion. To obtain representative cohesion values for the conjugate joint sets identified in the defended cliff line back analysis of identified wedge failures were undertaken from the undefended cliffs at Telscombe. The aforementioned parameters were obtained for the observed wedge failures via digitising of planes in ADAM 3DM analyst with the friction angle set to 38°. Tension cracks parameters of; dip, dip direction and trace length were included in the slope input parameters if required and cohesion was set to 0 kPa. A sensitivity analysis was then undertaken to determine the cohesion value for both joints where the FoS was critical (FoS=1). These values were then used to assess the risk of the identified conjugate joint sets or potential future wedge failures within the defended cliff line. The cohesion values from the analyses range from 9.45 kPa to 27.25 kPa which fall within the ranges reported in the scientific literature (Hoek & Bray, 1981; Lord et al. 2002). To account for conditions which are not represented by the small sample of back analyses the peak cohesion value reported by Barton (1974) of 80 kPa was used as the upper limit value in the wedge analyses. Scaling of the wedge, when required, enabled the size of the wedge to be user controlled to represent the point of intersection on the cliff face.

3.4.2.2. Output data

The generated 3D model of each wedge developed from the input joint parameters evaluates the potential risk of failure through the FoS. The volume, joint area, normal force and stress are calculated along with the shear strength and mode of failure; sliding on joint 1, joint 2, or on both surfaces. The mode of failure is useful as it can be used to determine whether the potential failure on any conjugate joint set lie within the primary or secondary critical zone for wedge failure as reported by Barlow et al. (2017). In addition the landward retreat at the cliff top was extracted from the scaled 3D model to quantify the greatest cliff top erosion from a wedge failure which did not include a tension crack. This represents the worst case scenario for each scaled wedge as the inclusion of a tension crack would reduce the volume of the failure and also the extent of the cliff top recession. This enabled the impact of these potential scenarios on the A259 to be explored.

3.5. Summary

This chapter has presented the methodological approaches used within this research. This includes applying readily accepted methods such as orthorectification of aerial imagery to produce a dataset which has been fully orthorectified for the study area for the first time, to obtain historical recession rates with quantifiable uncertainty. The development of a reliable digital photogrammetric approach for generating high precision models of the chalk sea cliffs was achieved which meets Aim 1, Objective 2 in Section 1.3. The methods for exploring environmental conditions over a much greater timescale and frequency than previously achieved in scientific research was also presented, before kinematic and limit equilibrium methods were outlined to provide an approach to assess greater magnitude failures within protected sections of cliffs. These methods provide the data presented in the following sections of study sites and the results and discussion sections within this research.

Chapter 4 – Study area

Using the knowledge obtained from current research within this field and utilising the methodological approaches, as presented in earlier chapters, this chapter provides the geomorphological setting for the coastal cliffs of East Sussex from Brighton Marina to Belle Tout. The historical recession rates are used to contextualise the cliffs in Brighton and determine the study sites of Brighton Marina (protected) and Telscombe (unprotected), which enabled a comparative assessment of cliff behaviour with cliffs of similar geology to be undertaken. An overview of environmental conditions and kinematics are presented as crucial parameters in assessing retreat for both protected and unprotected cliff lines. Infrastructure at risk of continued cliff recession, namely the A259 coastal road, is then discussed as one of the key aspects of this research. The preliminary findings provide a base for the following chapter to present the key results from this research.

4.1. Geomorphology of the coastal chalk cliffs

The exposure of chalk formations between Brighton and Belle Tout represent the geological strata of the Upper Cretaceous period. They also demonstrate the effects of Quaternary processes (Mortimore et al., 2001). The chalk cliffs are orientated towards the predominant wind and wave direction from the south-west (May, 2003). Figure 33 illustrates both the geology (Figure 33A) and elevation (Figure 33B) of the study site.

At the western extent of the study area is Black Rock, a Site of Special Scientific Interest (SSSI), an ancient (approximately 200,000 year old) cliff platform cut into the chalk which is now overlain by raised beach deposits and a sequence of crudely bedded chalk debris and chalk rubble (Prosser, 2006). The raised beach comprises of relatively well-rounded flint gravel comparable with the present Brighton beach alongside some sand and shell debris, Mortimore and Duperret (2004) report that this unit is in general freely draining.

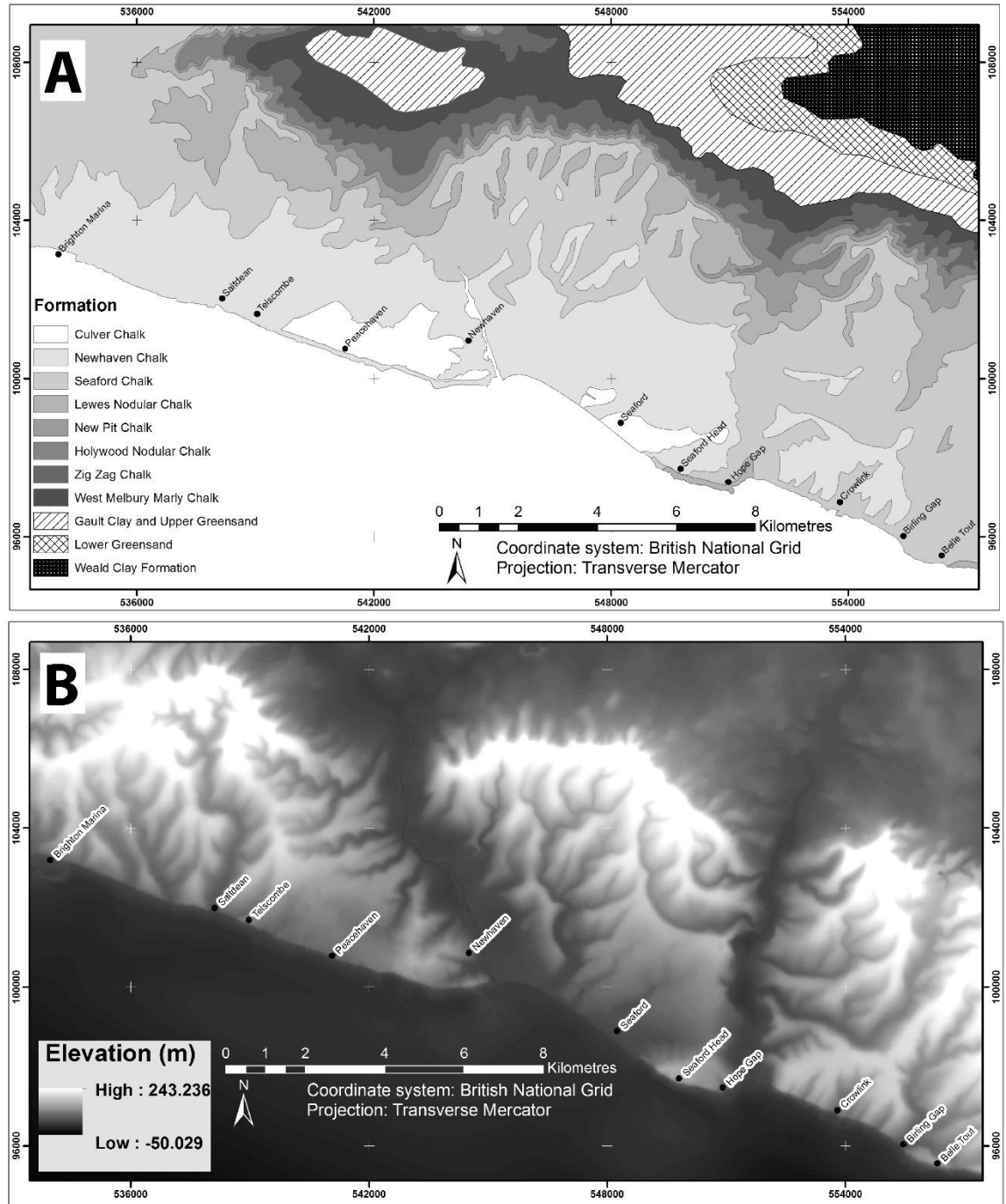


Figure 33: Study area (A) geology (Developed utilising British Geological Survey materials copyright NERC, 2016) and (B) elevation (generated from Ordnance Survey contour data).

To the east, between Brighton Marina and Newhaven there are two main lithological units, the Newhaven and Culver Chalk formations. The Newhaven Chalk is characterised by numerous marl seams (Mortimore, 1983; 1986a; 1986b; Mortimore et al., 2001). The overlying Culver Chalk formation is exposed to the east of this section from Saltdean to Newhaven (Mortimore et al., 2001; 2004a). The variation in elevation is apparent along the entire study site (Figure

33B) with alternating hills and truncated valleys, the latter of which in some cases reach sea-level due to Quaternary weathering and alteration (Mortimore et al., 2004a). Discontinuous fringing shingle beaches exist across the study site fed by the erosion of flints from the cliffs (Orford, 1978; May, 2003), sediment is intercepted by a network of groynes to the west (Brighton to Saltdean) and by the Newhaven breakwater which provides localised cliff protection (Dornbusch et al., 2007). To the east at Seaford, the cliffs rise to 85m and exhibit largely vertical joints as seen at Seaford Head. The dry valley of Hope Gap is formed of weaker chalk beneath the valley floor due to periglacial weathering (May, 2003), which is subject to higher rates of erosion at the cliff edge and shore platform. The dry valley mouths, cliffs and platforms of the Seven Sisters have been cut across the dip of the chalk (May, 2003) and are predominantly formed of the Seaford and Newhaven Chalk Formations which vary in height from 72 m to 12 m at Birling Gap. The valley features at Crowlink and Birling Gap are formed of Coombe Rock (chalk which has been previously been subject to erosion, either scree or solifluction deposits which have cemented) which extends out onto the shore platform and thus the platform is cut lower here than elsewhere along the stretch of coastline. The cliffs at Beachy Head, in excess of 160 m high are formed of the Seaford Chalk and Lewes Nodular Chalk Formations which overlies the New Pit Chalk (all White Chalk subgroup formations). They are raised to this level on the axis of the Beachy Head anticline (Mortimore et al., 2004a), notably the flints at the top of Beachy Head are also located at beach level at Birling Gap in the Birling Gap syncline (Mortimore et al., 2004a). Illustrating the importance of geological tectonic structures (folds and faults) on the contemporary structure of the chalk cliffs.

4.2. Historical recession rates 1957-2013

The historical recession rates illustrate the behaviour of the cliff system within the study area between 1957 and 2013. These results provide a crucial role in contextualising the system and determining comparative sites to be assessed within the research. A total of 1,862 transects

were cast each extracting historical recession data from the digitised cliff lines. The impact of missing imagery (covered in Section 3.1) resulted in 16% of the study area without images from 1957, 9% from 1991 and 7% from both 1957 and 1991. In these cases historical recession rates were undertaken on the remaining available datasets. For the analysis of this dataset the cliff system was divided into cliff behaviour units (CBUs) and the geomorphological characteristics assessed to determine their impact on the rates of recession from 1957 to 2013.

4.2.1. CBUs

Many studies and research programmes have defined CBUs as a way of characterising coastal cliffs, this includes region wide programmes such as Futurecoast (Halcrow, 2002) which was utilised in developing policies in the second round of SMPs. The cliffs within this research were characterised by the following criteria:

- Elevation – which was grouped by 10 metre intervals, the results were reviewed and adjustments made if subsequent sections were only separated by relatively small differences.
- Aspect – the cliff line was characterised by the inter-cardinal or ordinal directions for example, any recorded aspect between 157.5° and 202.5° would be classified as southerly facing.
- Geology – dependent on the earlier presented bedrock map (Figure 12A).
- Defence – was dependent on the type, if any, of coastal protection or cliff stabilisation measures.

4.2.2. Spatial and temporal trends in retreat rates

The characteristics of each CBU were examined for the unprotected cliff line. The defended cliffs which have been decoupled from wave action and stabilised in several sections are addressed separately. Table 10 displays the influence of aspect on the historical recession of the chalk cliffs. The greatest rate of recession was associated with the dominant wind and wave

direction from the south west of 0.33 m yr^{-1} , the south easterly CBUs located between Seaford and Cuckmere Haven exhibit recession at approximately half that rate at 0.17 m yr^{-1} . When examining the dominant geological formation there was little variation between Culver, Newhaven and Seaford Chalk with retreat rates of 0.31 m yr^{-1} , 0.28 m yr^{-1} and 0.32 m yr^{-1} respectively. Retreat rates have remained relatively steady through time (Table 10), but were marginally higher in the period to 1957-73 inferring a slowing in recession as reported by Dornbusch et al. (2008). This higher rate of recession could be directly related to the intervals selected as well as reflecting a series of larger magnitude events which occurred during the 1957-73 period, the relatively constant retreat rate over the 56 year period is a much more reliable inference from the data given the variation is within the subsequent error bands of the data. The greatest retreat rate was located at Birling Gap during 1973-1991 with a retreat rate of 0.84 m yr^{-1} which is in agreement with Moore et al. (2001) who found annual rates varied between 0.64 m yr^{-1} and 1.41 m yr^{-1} for the same location over the period 1874-1999.

Aspect	WLR (m yr^{-1})		LRR (m yr^{-1})			Ave. cliff height (m)
	1957-2013	CI (2σ)	1957-1973	1973-1991	1991-2013	
South East	-0.15	± 0.09	-0.25	-0.15	-0.15	21.16
South	-0.26	± 0.17	-0.37	-0.27	-0.23	52.01
South	-0.30	± 0.20	-0.49	-0.30	-0.26	48.06

Table 10: Cliff retreat rates between 1957 and 2013 grouped by aspect (WLR – Weighted Linear Regression, LRR – Linear Regression Rate, CI – Confidence Interval).

Comparing the recession rates between 1957 and 2013 with those published by Dornbusch et al. (2008) reveals a variation in annual recession. As temporal intervals varied between the studies, with Dornbusch et al. (2008) calculating recession over a much greater period 1873-2001, a subset of the dataset was used for a comparative assessment of these results (Table 11). Both the entire temporal period (56 years) and a 40 year subset from 1973-2013 was compared to Dornbusch et al.'s (2008) 1973-2001. Across the entire study area the figures reported by Dornbusch et al. (2008) are up to 0.05 m yr^{-1} greater than those found in this study. The positional accuracy reported for the images used by Dornbusch et al. (2008) was $\approx \pm 0.30 \text{ m}$ but no uncertainty was reported for each temporal recession period, as presented in this research

($-0.22 \text{ m yr}^{-1} \pm 0.18 \text{ m}$ for the entire study area). Although the differences in recession are within an order of magnitude these results, with quantified error are more reliable for use in predicting future scenarios.

Location	WLR (m yr^{-1})		LRR (m yr^{-1})	Dornbusch et al. (2008)	Difference	
	1957-2013	CI (2σ)	1973-2013(2σ)	1973-2001		
Whole coast	-0.22	± 0.18	-0.22	-0.27	-0.05	-0.05
Black Rock – Rottingdean	-0.03	± 0.05	-0.03	N/A	N/A	N/A
Saltdean – Newhaven	-0.26	± 0.27	-0.28	-0.20	0.06	0.08
S'ford Head – Cuckmere	-0.17	± 0.17	-0.15	-0.21	-0.04	-0.06
Cuckmere – Belle Tout	-0.32	± 0.18	-0.31	-0.35	-0.03	-0.04
Birling Gap	-0.51	± 0.20	-0.54	-0.50	0.01	0.04

Table 11: Comparison of calculated recession rates with Dornbusch et al. (2008).

Saltdean to Newhaven and Birling Gap had comparatively higher recession rates than that reported by Dornbusch et al. (2008) up to 0.08 m yr^{-1} and 0.04 m yr^{-1} respectively. Notably the differences between datasets lies within the error bands of the presented data from this research and within the spatial uncertainty of the images as reported by Dornbusch et al. (2008).

The spatial trends across the entire study area from 1957 to 2013 are presented in Figure 34A. The lowest rates of up to -0.10 m yr^{-1} are located between Brighton Marina and Saltdean (Figure 34B) where the cliff line has been protected since the 1930's. The section of coastline to the east, from Saltdean to Newhaven (Figure 34C), has comparatively high recession rates for the period between 1957 and 2013 for what now is a predominantly protected cliff line, the reasons for this are primarily anthropogenic and are presented in the following section. The coastline around Seaford Head (Figure 34D) exhibit retreat rates between -0.10 m yr^{-1} and -0.30 m yr^{-1} which varies with aspect, although there are pockets of higher recession which represents the episodic nature of failure. The most eastern stretch of cliff line in the study area extends from Seven Sisters to Belle Tout (Figure 34E), the cliffs in this section represent the highest recession rates at Birling Gap. The tallest cliffs of approximately 70 m are also located within this section and during the course of this research a large failure which resulted in landward recession of the cliff edge of several metres occurred demonstrating the continued and relatively high retreat rates observed from the historical data.

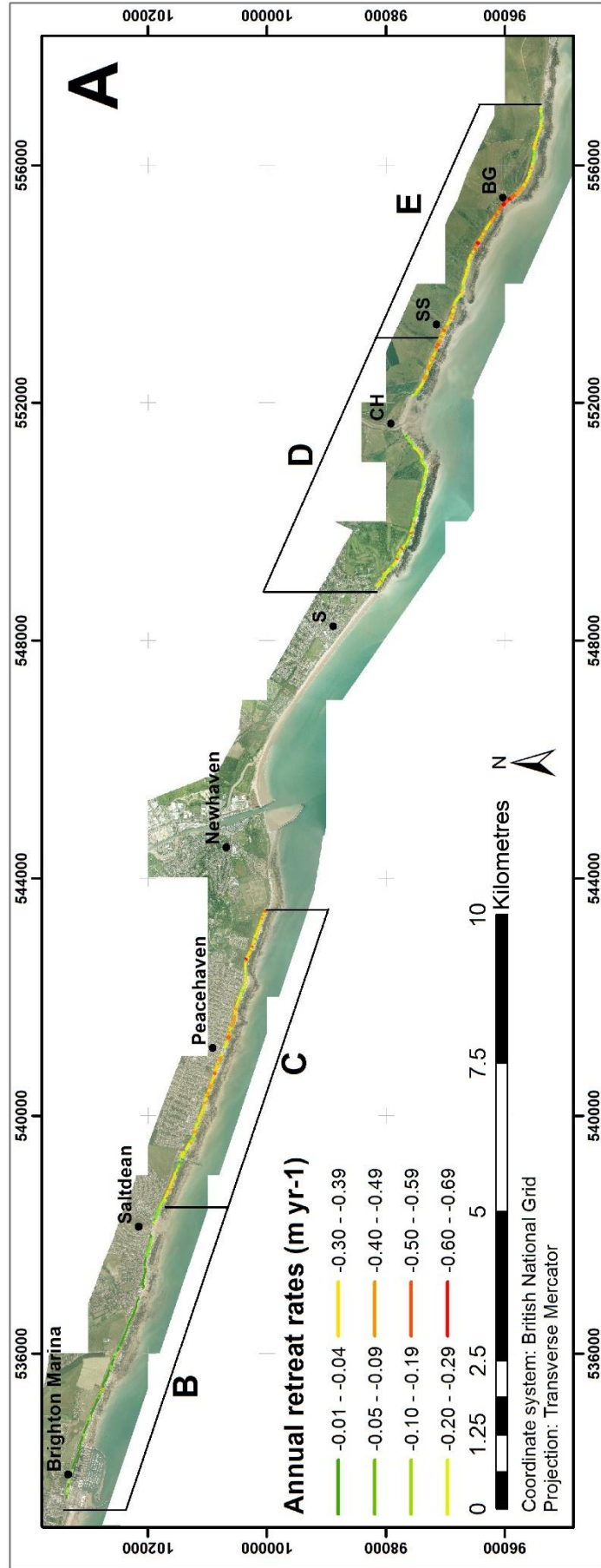


Figure 34: (A) Retreat rates from 1957-2013 for the entire study area of Brighton Marina to Belle Tout (S - Seaford, CH - Cuckmere Haven, SS - Seven Sisters, BG - Birling Gap) - (2013 imagery downloaded from the CCO).

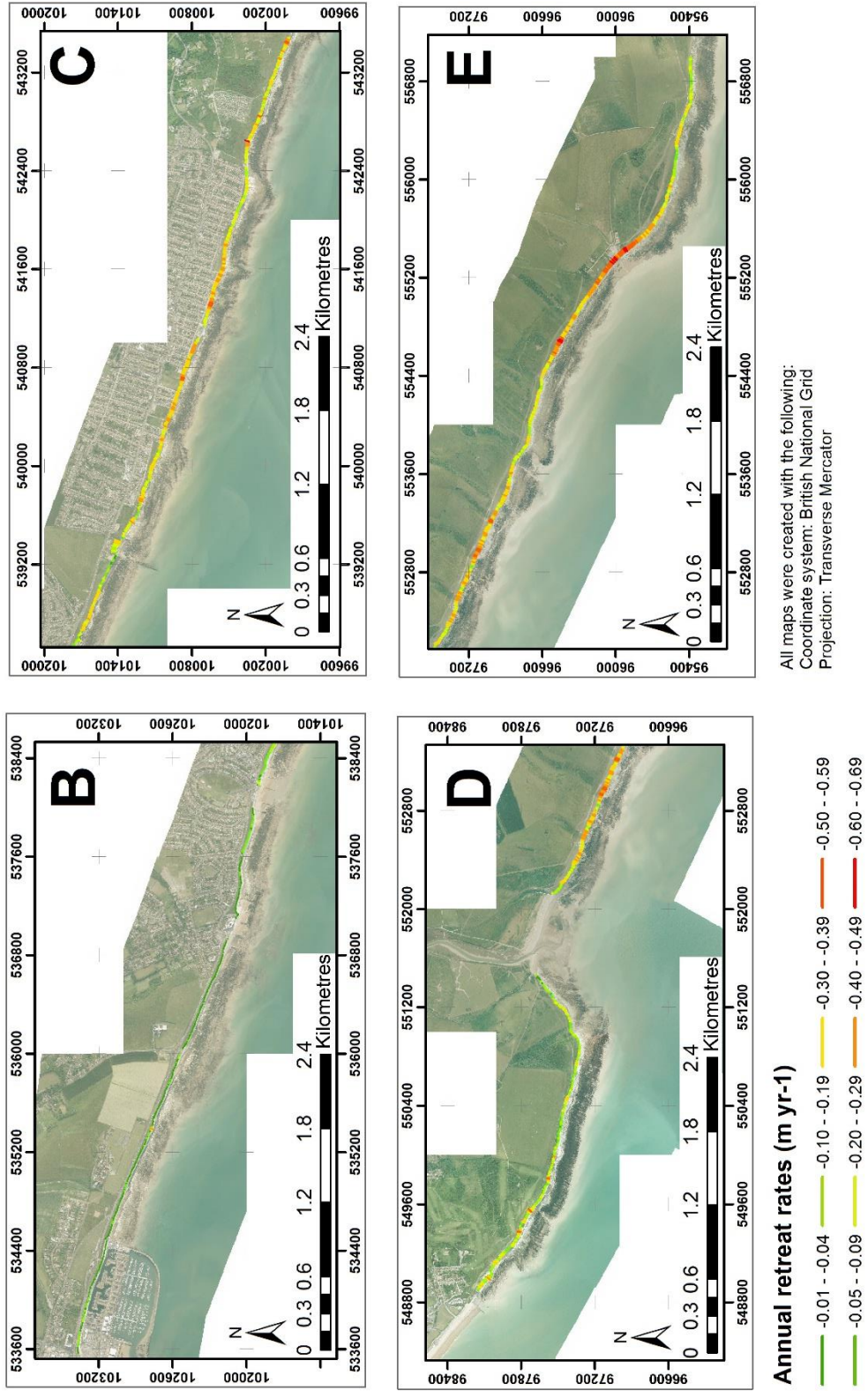


Figure 34: (Continued), (B) Brighton Marina to Saltdean, (C) Saltdean to Newhaven, (D) Seaford to east of Cuckmere Haven, (E) Seven Sisters to Belle Tout (2013 imagery downloaded from the CCO).

4.3. Coastal cliff protection

Between Brighton Marina and Newhaven approximately 8.5 km of the 11.8 km of coastline is protected with sea defences. The majority of these defences are cliff toe protection structures in the form of a sea wall which doubles as a popular promenade known as the Undercliff Walk. This section will outline the details of these defences by Brighton and Hove City Council (BHCC) and Lewes District Council.

4.3.1. Undercliff Walk – sea wall

The most substantial coastal protection within the study area is the Undercliff walk. The longest section of the sea wall extends from Brighton Marina to Telscombe, with a shorter section further east which protects the cliff toe at Peacehaven. Figure 35 details the location and date of installation of the various stages of sea defence. The earliest section of the Undercliff Walk was constructed from Black Rock (now the site of Brighton Marina) to Rottingdean between 1930 and 1933 (Figure 35A) and was built to enhance existing defences and introduce a walkway along the foot of the cliffs (Brighton & Hove City Council, 2013). This was later extended to Saltdean Gap in 1935 due to the continued recession of this section of cliff line which posed significant risk to the road and property. The final couple of hundred metres of the western section of the Undercliff Walk were installed in 1964 (Dornbusch et al., 2007). In the 1980's reconstruction of this section was undertaken due to the end of the existing life of the defences, this included encasement of the old wall and reconstruction of the walk and rear splash wall (Lawrence et al., 2013). The eastern section of the sea wall is located in Peacehaven, here the construction has been sporadic (Figure 35B) defending the cliff due to the proximity of residential properties at the cliff top. There were four stages of construction from 1977 to 1996 (Dornbusch et al., 2007) with this section now spanning the length of Peacehaven. During the construction of the Undercliff walk/sea wall the cliff face was reprofiled, where required, from a near vertical slope to an angle of between 70° and 80° (Cleeve & Williams, 1987).

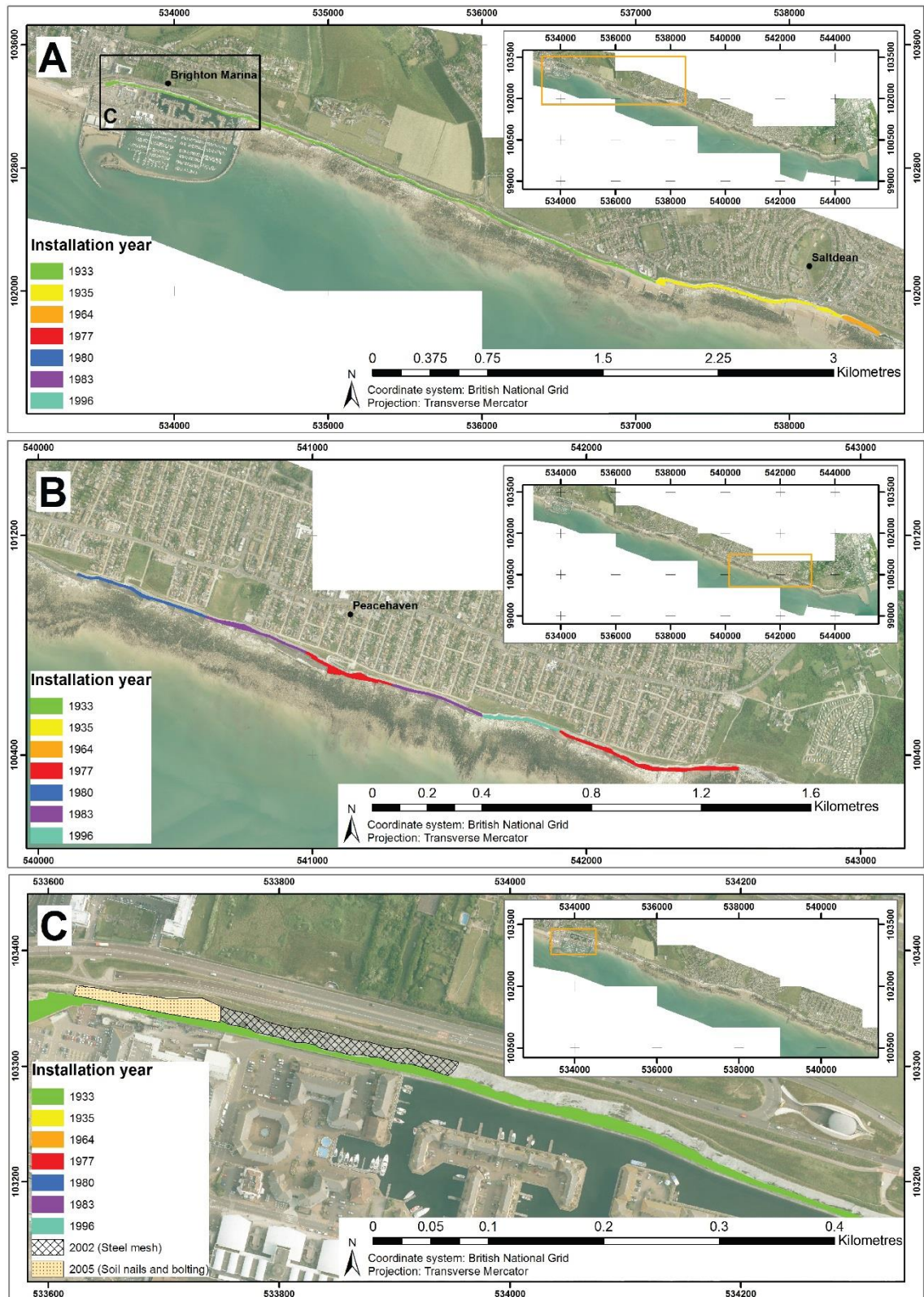


Figure 35: Location and dates for installation of sea defences and cliff stabilisation measures (A) Brighton Marina to Saltdean, (B) Telscombe to east of Peacehaven and (C) detail of Brighton Marina defences.

4.3.2. Cliff face stabilisation

As a result of the failures which occurred in 2000/2001 with a total mass of over 4,000 m³ Brighton and Hove City Council closed the Undercliff walkway behind Brighton Marina where the vast majority of these failures occurred. It was decided that cliff stabilisation measures were needed to reduce the risk of any future failures which could affect the commercial or residential properties within the marina and had the potential to breach the A259 or pose a significant risk to life. As a result a two phase installation project was initiated within Brighton Marina (Figure 35C) to stabilise the cliff face. Stage 1 (2002) required trimming (next section) of the upper portion of the cliff face and installation of rockfall netting. Stage 2 (2005) required regrading and installation of soil nails.

4.3.2.1. Trimming of the cliff face

To reduce the risk of future failures from unstable and over steepened cliff faces the decision was taken to trim back the upper 7 metres of the cliff face from between 70° and 80° to 60° (Figure 36). This was due to be regraded to an angle of 45° however a late objection from English Nature revised this (High-Point Rendel, 2002). This work was undertaken in 2002 (Figure 35C & Figure 36A) for the chalk cliffs at Brighton Marina (High-Point Rendel, 2002).

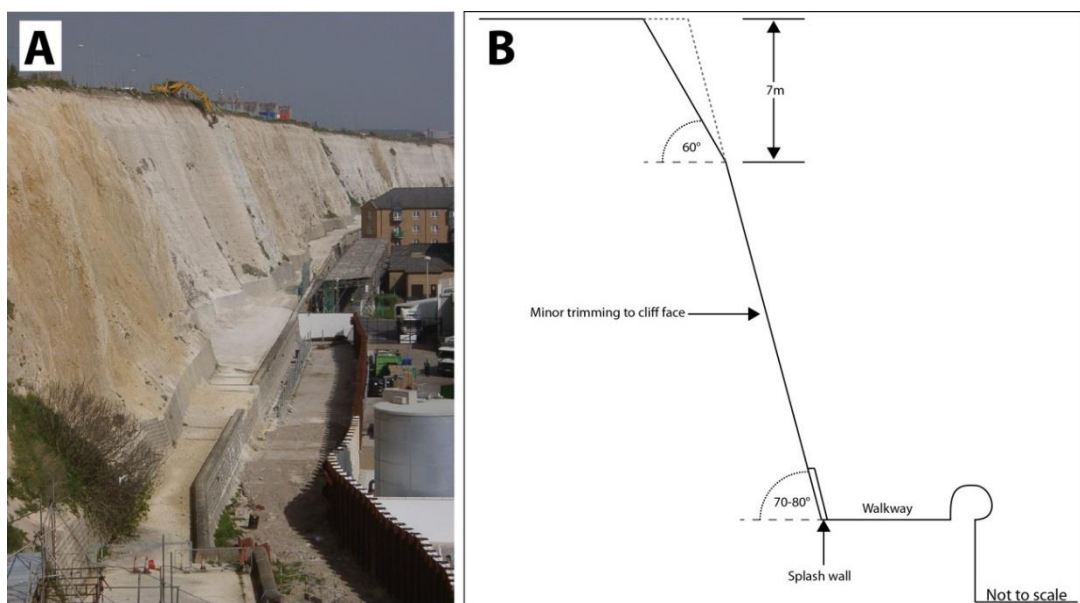


Figure 36: Cliff trimming of the chalk cliffs in Brighton Marina (A) Image of work being undertaken (University of Sussex, 2013) and (B) schematic showing detail of work (High-Point Rendel, 2002; 2006).

4.3.2.2. Rockfall netting

To reduce the impact of regular spalling rock and any small scale rock falls, wire mesh or rock fall netting was installed over the chalk cliff face within Brighton Marina (High-Point Rendel, 2002). The installation of this netting included a matrix of Ischebeck Titan 30/11 6 m rock bolts drilled and fixed into position at 1.5 m vertical and 2 m horizontal intervals (High-Point Rendel, 2002). A variety of 4.5 m and 7.5 m length bolts were installed as required. The rock fall mesh was 6,350 m² with the bolts fixed at an inclination of 30°. The design life of the work has a minimum of 20 years including cliff top fencing but the stabilisation scheme has a design life of 40 years with the bolts of 120 years. Regular maintenance to remove collected material from behind the netting will be required to ensure the stabilisation scheme operates effectively.

4.3.2.3. Soil nails (Black Rock)

The initial proposal was to install the previously outlined stabilisation scheme across the chalk cliffs and at Black Rock. However, this was rejected by English Nature resulting in a public enquiry (Prosser, 2006). Due to the SSSI status of Black Rock an alternative scheme was selected which required similar trimming of the cliff face and a network of soil nails to be installed. These were installed on a grid with a spacing of 2 m (horizontally and vertically) ranging from a length of 6 m to 15 m (High-Point Rendel, 2006). The range in lengths was due to the various depths of material through the cliff face and the proximity to Marine Drive (A259 Road). This scheme was designed to prevent large-scale failures as observed in 2000/2001 but regular spalling is still expected. The stabilisation scheme is to be assessed three times a year (twice in winter and once in summer) and after periods of heavy rainfall or hard frosts (High-Point Rendel, 2006). The scheme has been installed as a 'permanent work' but life expectancy due to corrosion is 5-10 years. If erosion continues behind the soil nail plates packing or repositioning of the plates will be required. The design life of the soil nails are 120 years (High-Point Rendel, 2006).

4.3.2.4. Rock bolting (Chalk)

Rock bolting was installed behind Brighton Marina and also in localised areas identified as high risk between Brighton Marina and Ovingdean (Royal Haskoning, 2005). These locations are primarily where wedge joint sets had been observed and were installed to previously described specifications. Installation of sub-horizontal catch fences on the cliff face have been designed to withstand a 50kg rockfall (Royal Haskoning, 2005). These are installed where the walkway is sufficiently narrow that any spalling debris has a greater risk of striking users of the promenade.

4.3.3. Impact of cliff protection on recession rates

The higher rates of cliff recession along the Peacehaven coastline (Figure 34C) can largely be attributed to the stages of sea defence installation. As detailed previously trimming of the cliff line has taken place to stabilise the cliff where cliff toe protection has already been installed (High-Point Rendel, 2002; 2006; Royal Haskoning, 2005) with the cliff face trimmed back to an angle between 70° and 80° (Cleeve & Williams, 1987). The trimming of the cliff face artificially introduces significant landward recession at the cliff top when dealing with aerial images. To establish how much of the recession was due to anthropogenic influences the average cliff height accounting for the height of the sea wall was extracted from the DEM. The angle of cliff trimming was then varied from 70° to 80° and the landward recession calculated. To account for the recession pre and post installation the temporal period until the defence was installed was multiplied by the preceding retreat rate. The distance remaining, accounting for the trimming, was divided by the years to obtain a post installation recession until the next aerial image dataset for example:

Cliff face installation: 1980

Total recession (1973-91) = 1957-73 RR x yrs between image and installation + effect of trimming + remaining dist.

The results are presented in Table 12. The majority of defences were installed between the 1973 and 1991 aerial image datasets (Figure 35B). The clear acceleration in retreat rates around

the period when the defences were installed skews the results calculated for the entire temporal period (Figure 34A and 34C). On average the recession preceding the installation of the sea wall and the impact of trimming accounts for 93.35% of the recession between the respective historical cliff line locations. The post installation recession rates are similar to those recorded in the subsequent epochs suggesting a relatively stable post-recession rate and in a few cases a slowing of recession. Notably all recession rates post installation decrease by an order of magnitude. The defences installed in 1996 have no post installation retreat rate due to the datasets from 1991 and 2013. However there is a noticeable decrease from -0.54 m yr⁻¹ (1973-1991) to 0.17 m yr⁻¹ (1991-2013). The current recession for the Peacehaven defended section of cliff line would now mirror those from Brighton Marina to Saltdean (Figure 34A & 34B).

Approx. location*	Def. Installed	Retreat rates (m yr ⁻¹)				Trimming angle (°)	Recession due to trimming (m)	Effect of trimming (%)	Calculated retreat rate post installation (m yr ⁻¹)
		1957-73	1973-91	1991-2013	Before installation				
Peacehaven east	1977	-0.38	-0.43	-0.05	-0.38	80	-5.79	95.34	-0.02
Peacehaven west	1980	-0.39	-0.71	-0.07	-0.39	76	-6.32	91.15	-0.06
Peacehaven central	1983	-0.38	-0.8	-0.05	-0.38	76	-6.63	94.41	-0.04
Peacehaven east	1983	-0.4	-0.81	-0.06	-0.4	77	-6.52	92.85	-0.08
Peacehaven east	1996	-0.28	-0.54	-0.17	-0.17	79	-5.73	93.02	-0.03

Table 12: Impact of defences on cliff recession rates.

(*- more detailed location of these defences are presented in Figure 35B)

4.4. Development and assets at risk from continued cliff recession

The risk to population and infrastructure due to cliff retreat is greatest between Brighton Marina and Peacehaven. Although there are coastal towns further east with cliff frontages including Newhaven and Seaford, as well as individual pockets of property at risk for example the coastguard cottages at Cuckmere Haven and commercial and residential properties at Birling Gap.

The main coastal road between Brighton and Newhaven, the A259, is situated at the cliff top and is at risk from future recession of the cliffs. Since 2013 the average daily traffic flow has been monitored (Brighton & Hove City Council - BHCC, 2017) at three locations. These were; approximately 750m east of Brighton Marina, Saltdean Gap and centrally at Telscombe cliffs with average daily traffic flows of 23,082, 25,432 and 21,450 vehicles respectively. The distance between the current cliff edge and the A259 road was measured along 10 m spaced transects (Figure 37A). The transects were cast orthogonal to the road which explains the variation in angle of some of the transects. Several 'pinch-points' were located where the distance between the A259 and cliff edge narrowed. Between Brighton Marina and to the east of Peacehaven the minimum distance from cliff edge to the A259 was 8.77 m, and a maximum of 489.04 m although many of these greater distances occur nearer the eastern boundary (Figure 37A). Three out of the four subsections (Figure 37B, C, D & E) had at least one transect measuring a distance of less than 10 m between the cliff top and A259. Where the cliff is unprotected at Telscombe the minimum distance between the cliff edge and road is approximately 42 metres. The Shoreline Management Plan (SMP) for this stretch of coast (Environment Agency, 2009) notes the potential risks as detailed in this section. The SMP (Environment Agency, 2009) also outlines that with an increasing intensity of rainfall resulting from a changing climate and if weathering of the cliff face increases difficult long term decisions will have to be faced in the future. There has been no detailed cost benefit analysis of the properties and/or infrastructure versus the financial costs of sustaining them (Environment Agency, 2009). The SMP concludes that a programme to monitor manage and review is required for the future risk management of this frontage.

In addition, the stretch of coastline between Brighton Marina and Peacehaven has seen extensive development of residential property to within 11 metres of the cliff edge, with access roads and gardens significantly closer to the cliff edge. These sections of coastline are now protected by a sea wall however continued recession due to sub-aerial weathering means

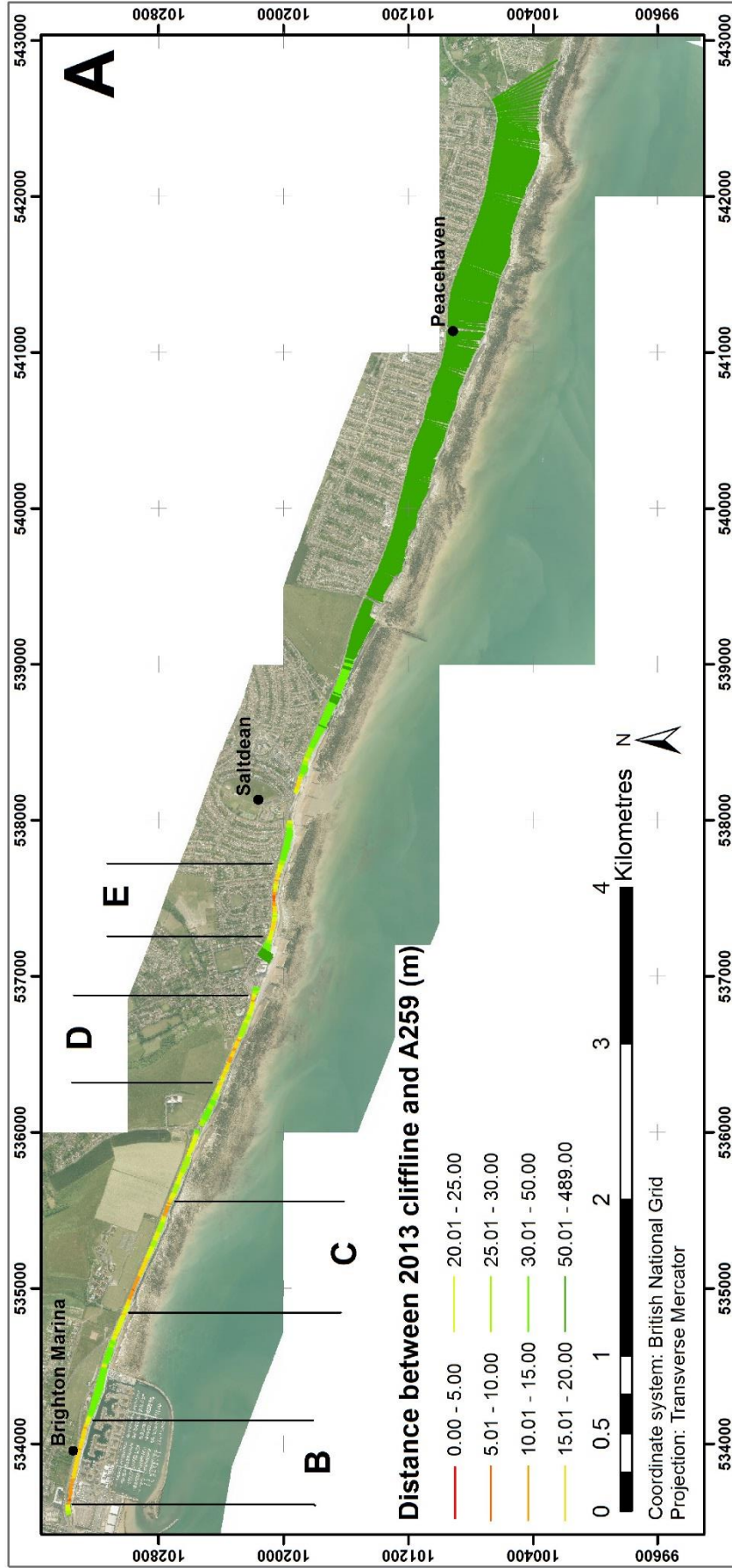
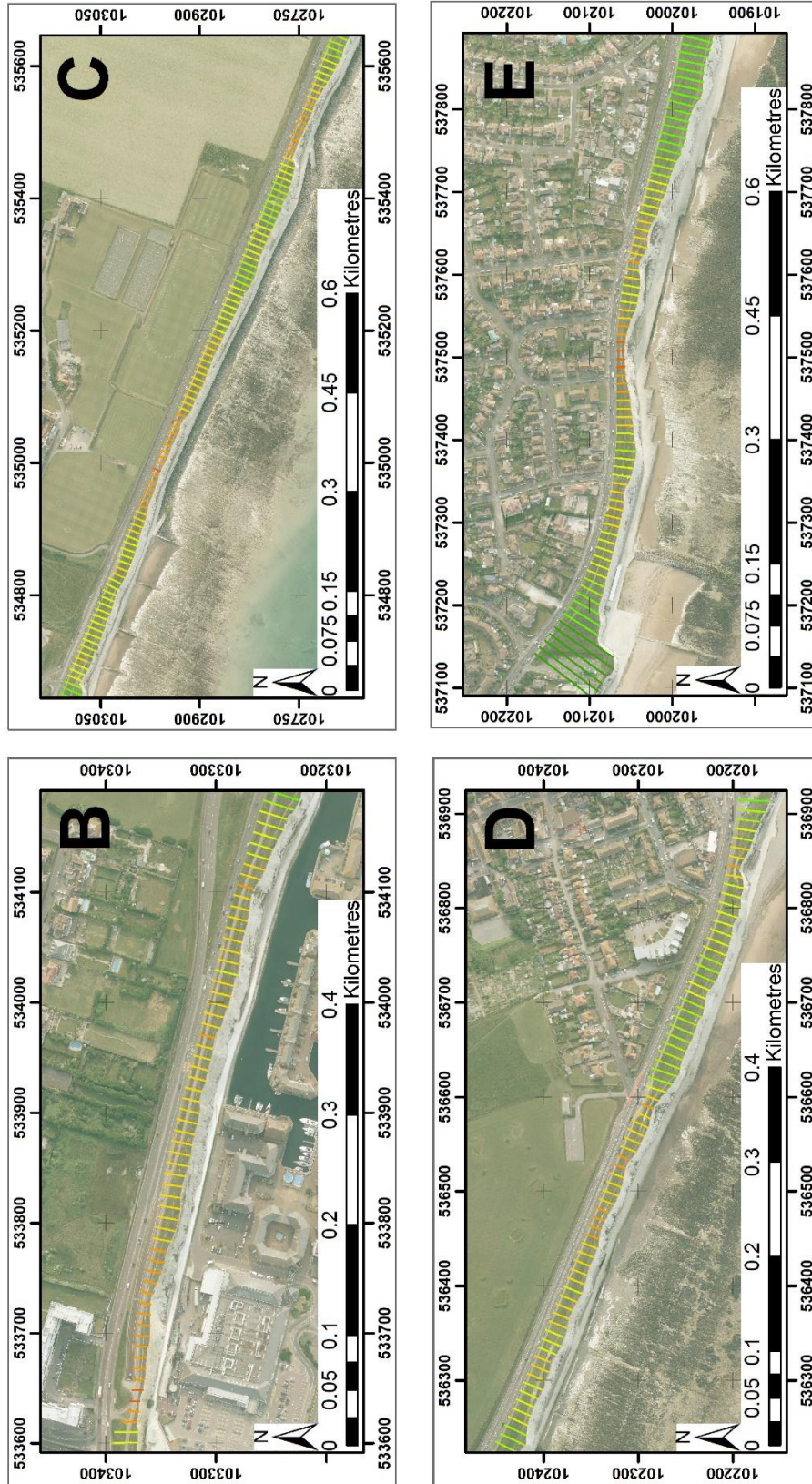


Figure 37: (A) Distance between 2013 cliff top edge and A259 (2013 imagery downloaded from the CCO).



Distance between 2013 cliffline and A259 (m)

0.00 - 5.00 10.01 - 15.00 20.01 - 25.00 30.01 - 50.00
 5.01 - 10.00 15.01 - 20.00 25.01 - 30.00 50.01 - 489.00

Figure 37: (Continued) Distance between 2013 cliff top edge and A259 (B) Brighton Marina, (C) East of the marina, (D) Rottingdean and (E) Saltdean (2013 imagery downloaded from the CCO).

All maps were created with the following:
 Coordinate system: British National Grid
 Projection: Transverse Mercator

recession will continue with risk to these properties. The development of Brighton Marina provides another substantial risk at the cliff toe to people and infrastructure. Figure 38A illustrates the damage to commercial property during the winter of 2000/2001 and 38B the proximity of another rockfall during the same period which almost reached the nearby residences (left of image). Fortunately, there were no injuries or loss of life from these events. However, the walkway was breached by approximately 2,000 m³ of Quaternary sediments and chalk debris from Black Rock (Figure 38A) and several hundred cubic metres (Figure 38B) of Newhaven Chalk debris.



Figure 38: Cliff failures in Brighton Marina during the winter of 2000/2001 (A) Black Rock affecting commercial properties (B) in Newhaven Chalk which almost hit the residential properties. (Image source: University of Sussex, 2013).

4.5. Environmental conditions

The environmental conditions for the study site are presented through a series of datasets, the Brighton Marina meteorological station (CCO, 2017a) recorded annual precipitation of 347 mm, 444 mm, 314 mm and 349 mm for 2013, 2014, 2015 and 2016 respectively. The minimum air temperature recorded from the same station was -2.1 °C, -0.3 °C, -2.0 °C and -1.2 °C for 2013, 2014, 2015 and 2016 respectively. The UKCP09 (Murphy et al., 2009) predict that temperatures are likely to rise with rainfall increasing in the winter and decreasing in the summer. Two well-known precursors to failures within chalk cliffs are; heavy rainfall, which leads to saturation and

therefore a weakening of the chalk, and freezing temperatures, which results in pressure being exerted within fractures and along discontinuities. The precipitation recorded during this study is significantly less than that recorded in 2000/2001 (approximately 30% less comparing the Ditchling Road met station data for the relevant time periods) when the largest failures within the protected sections occurred. This signifies that this research has been undertaken in relatively dry conditions.

The following section details the results of the thermal imaging to assess the impact of freezing air temperatures on the surface of the chalk cliffs. The data from the Brighton Marina meteorological station enabled periods of freezing air temperatures to be identified (Figure 39) which significantly reduced the processing of the thermal image dataset. Seven periods were highlighted (Table 13) with the greatest duration lasting eight days between 31st January and the 7th February 2015. During the thermal data capture a total of 12 days recorded temperatures at or below freezing (0 °C); two in 2014, eight in 2015 and two in 2016. The lowest recorded temperature during data collection was -1.7 °C at 07:00 on the 2nd February 2015. The minimum air temperatures recorded between November 2014 and December 2016 are significantly warmer and are much shorter in duration than previous years. The meteorological station which was installed in 2012 recorded 20 days of below freezing temperatures in 2012 and 32 in 2013. The coldest temperature recorded during these years was -5.3 °C (03/02/12) which occurred during a period of seven days where night temperatures were consistently below freezing. The longest duration of nights recording below freezing temperatures was in 2013

No.	Period of interest	Days	Consecutive nights with below freezing temperatures	Minimum air temperature (°C)	Wind direction (°) at min temp
1	28 – 29/12/2014	2	1	-0.2	355 (N)
2	17 – 23/01/2015	7	1	-1.1	350 (N)
3	31/01 – 07/02/2015	8	2	-1.7	275 (W)
4	16 – 20/01/2016	5	1	-1.2	7 (N)
5	15 – 16/02/2016	2	0*	0.4	321 (NW)
6	24 – 25/2/2016	2	0*	0.4	358 (N)
7	05 – 07/03/2016	3	0*	0.2	300 (NW)

Table 13: Meteorological data from identified periods of freezing air temperatures between November 2014 and December 2016 (*periods in 2016 where temperature was recorded below 0.5°C for further comparison between cliff surface temperatures).

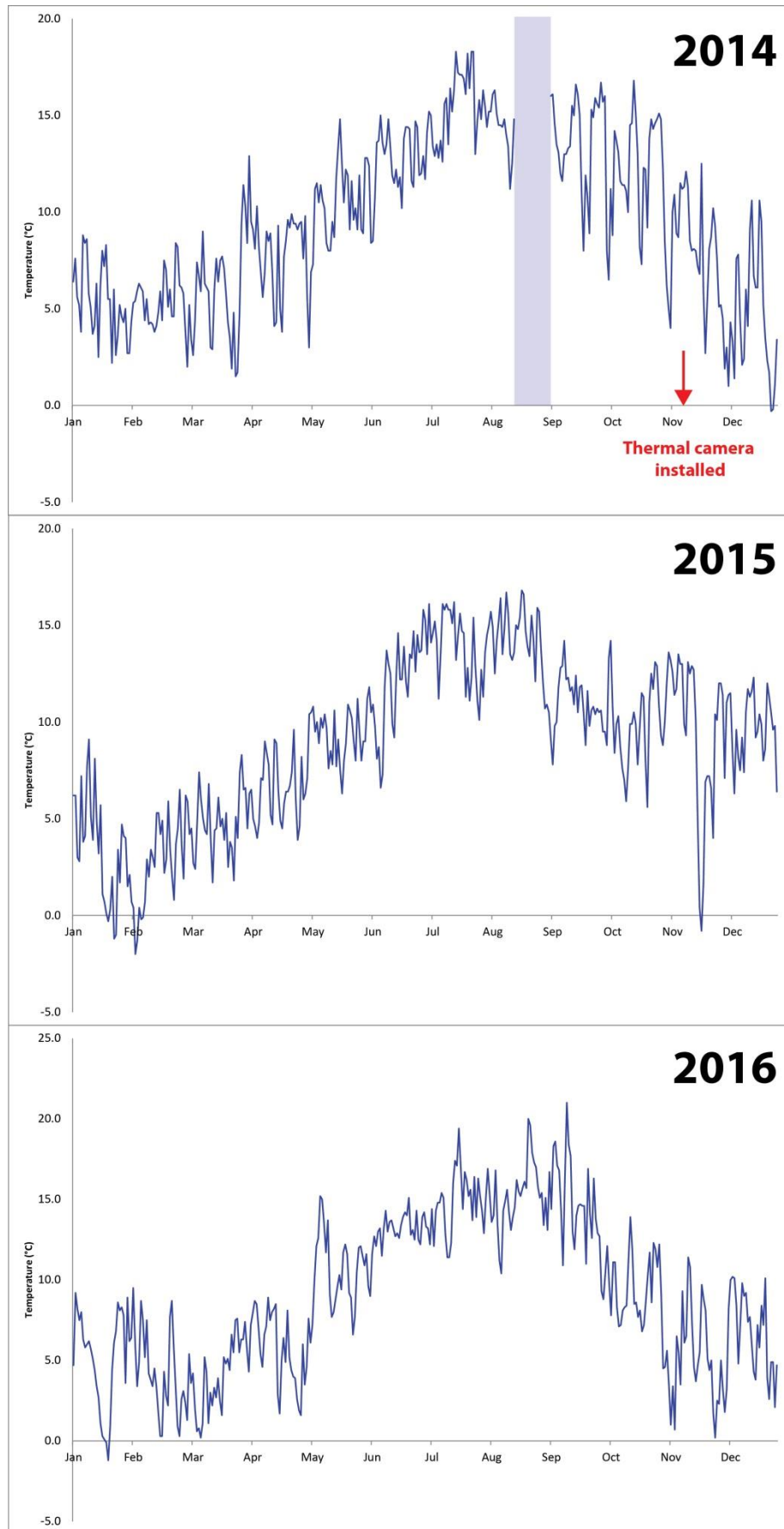


Figure 39: Minimum daily air temperature between 2014 and 2016 recorded by met station in Brighton Marina (blue highlighted area is where met station was not recording air temperature).

between 14th January and the 22nd January (9 consecutive nights). Thus the environmental conditions to assess the effect of freezing air temperatures on chalk cliff surface temperatures have been limited during this research.

A total of 703 thermal images were examined from the seven identified periods of interest (Table 14). The mean, standard deviation, maximum and minimum values were extracted from each image for the entire cliff face. The cliff was also sub divided into four zones to determine temperature variation with cliff height. Figure 40 illustrates the thermal imagery collected between 28th and 29th December 2014 using a linear scale which is bound by the minimum and maximum cliff surface temperatures recorded during this period of 3.5 °C and 19.6 °C respectively. The minimum cliff surface temperature was recorded at 00:00 on 29th December 2014, the wind direction was from the north (355°) and the air temperature was -0.2 °C. The minimum cliff surface temperatures recorded (Table 14) for each of the identified periods reveal a buffer between air temperature and minimum cliff face temperature. The buffer for freezing air temperatures (No. 1-4 in Table 14) averaged at 3.8 °C.

No.	Period of interest	Date and time of recording	Min. air temp (°C)	Min. cliff surface temp (°C)	Ave. cliff surface temp (°C)
1	28 – 29/12/2014	29/12/14 00:00	-0.2	3.5	5.9
2	17 – 23/01/2015	22/01/15 23:00	-1.1	2.5	5.3
3	31/01 – 07/02/2015	02/02/15 07:00	-1.7	1.1	4.2
4	16 – 20/01/2016	19/01/16 07:00	-1.2	3.9	5.3
5	15 – 16/02/2016	16/02/16 06:00	0.4	4.2	5.8
6	24 – 25/2/2016	25/02/16 05:00	0.4	4.1	5.6
7	05 – 07/03/2016	06/03/16 06:00	0.2	4.6	6.1

Table 14: Minimum and average cliff surface temperature recordings with time and date of capture.

The lowest cliff surface temperature, of 1.1 °C, was recorded on the 2nd February 2015 at 07:00 which coincided with the coldest air temperature recorded during the research of -1.7 °C. The buffer between air temperature and surface temperature was the smallest at this time with a margin of 2.8 °C (Figure 41). Interestingly the following night recorded an air temperature of -1.3 °C however the minimum cliff surface temperature was much higher than the previous night

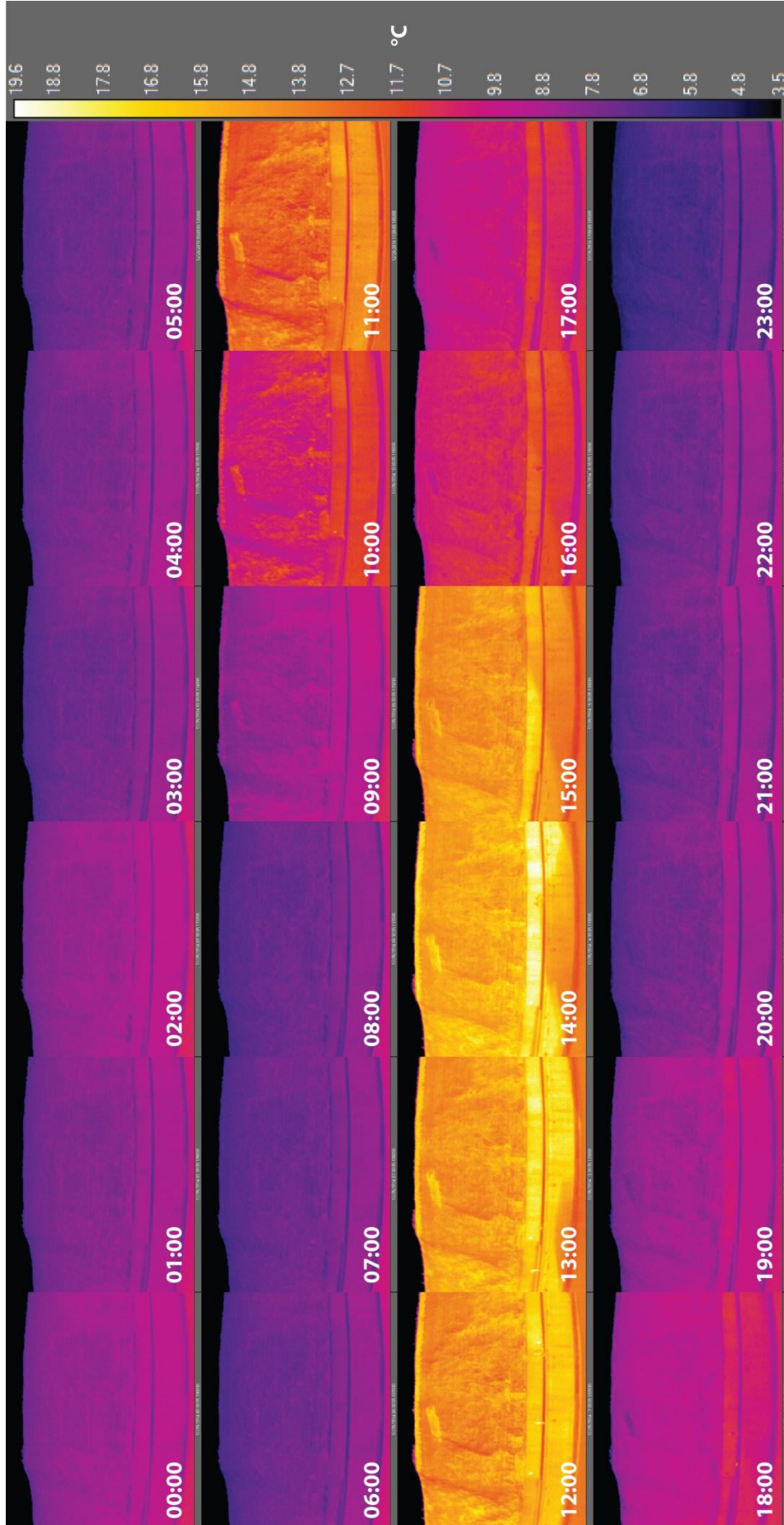


Figure 40: Hourly thermal imagery captured in Brighton Marina between 28-29/12/2014 (tiled imagery above only shows 28/12/14, continued on next page).

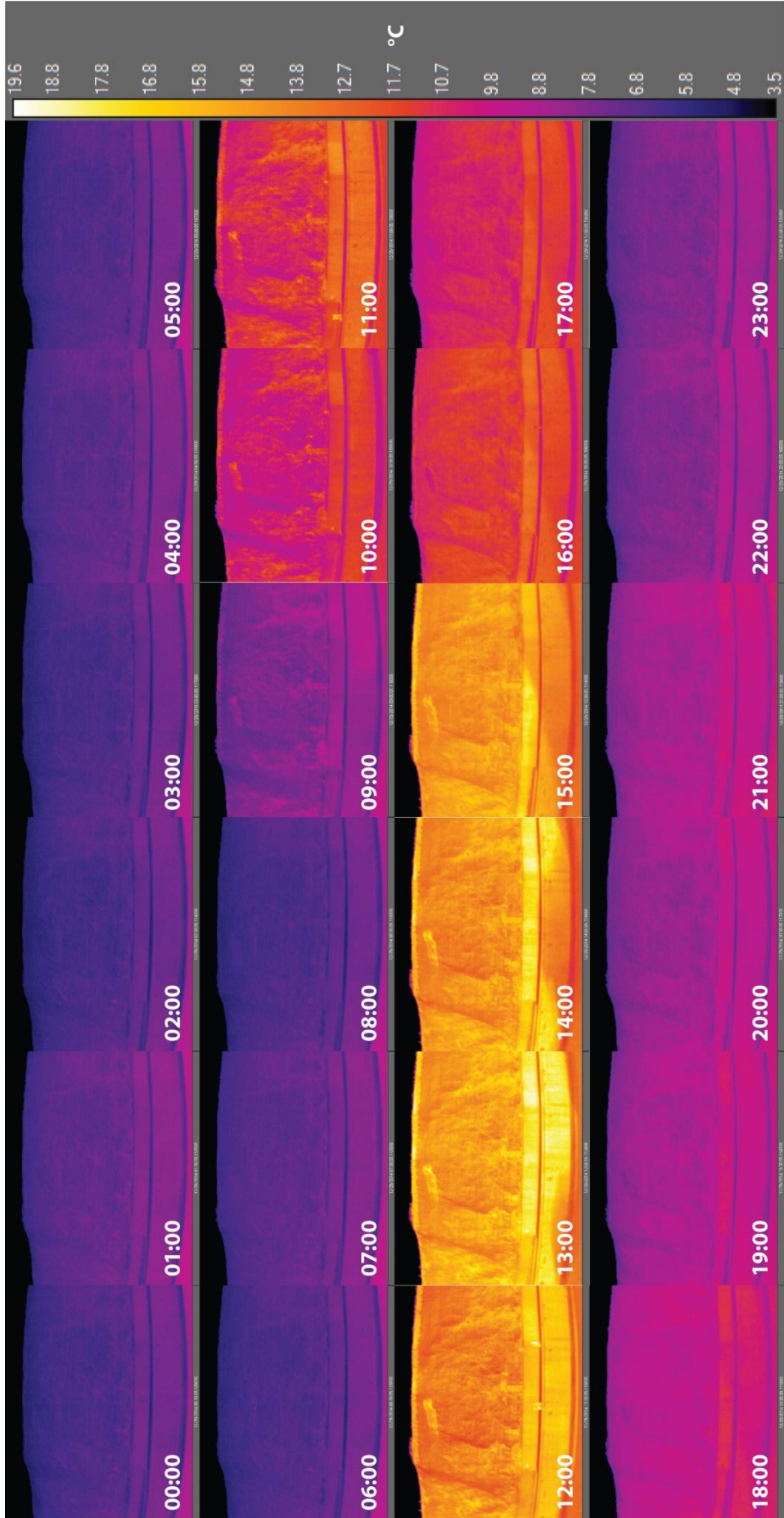


Figure 40 (continued): Hourly thermal imagery captured in Brighton Marina between 28-29/12/2014 (tiled imagery above only shows 29/12/14).

at 3.8 °C. This variation is most likely explained with reference to the dominant wind direction. The wind direction on the morning of the 2nd of February was from the west which would have driven the cold air into the cliff face which is orientated to the south-west. Whereas the following night, and for all other below freezing air temperatures recorded, the wind was predominantly from the north. The absence of below freezing cliff surface temperatures can be hypothesised using the findings from this research. Firstly, the duration of periods when the air temperature was below freezing on consecutive nights was limited within the study, with a maximum of two. Irrespective of wind direction a sustained period of night temperatures below 0 °C, as recorded in February 2012 and January 2013, would likely result in freezing cliff surface temperatures. Conversely a shorter period of below freezing temperatures which were accompanied by winds from the south, south-west or west could lead to freezing surface temperatures as suggested by the results presented in this section. Evidently any severe frosts similar to the February 2012, of -5.3 °C would likely induce freezing of the cliff surface as evidenced by the average buffer of 3.8 °C.

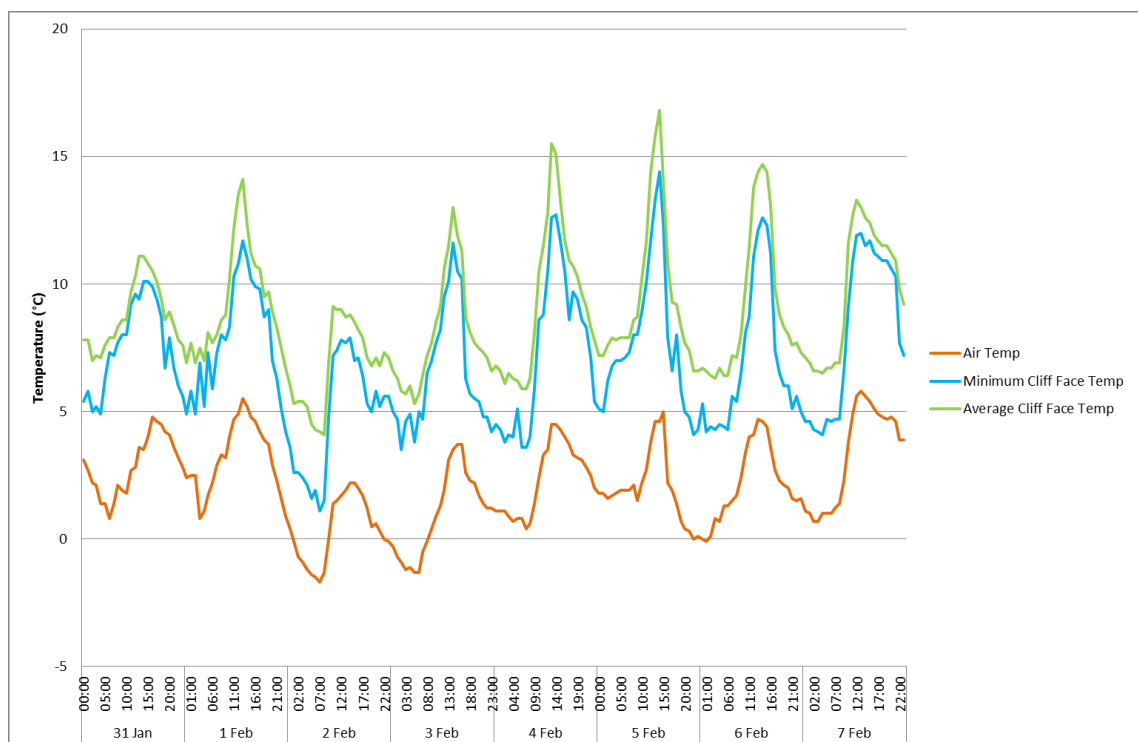


Figure 41: Air temperature, average cliff face temperature and minimum cliff face temperature between 31/01/2015 and 07/02/2015.

Spatial trends were also found using the thermal imaging data, this was achieved by subdividing the surface into quarters each representing a different elevation of the cliff from the base (splash wall) to the cliff top, excluding the vegetation at the top of the cliff. This analysis found that the upper quarter of the cliff was significantly cooler than the lower three quarters. For the periods identified with air temperatures below freezing (No. 1-4 in Tables 13 & 14) the cliff top was on average 0.8 °C colder than the rest of the cliff, this reduced to 0.5° for the other three periods (No. 5-7 in Tables 13 & 14) as expected due to slightly higher air temperatures. Figure 42 illustrates this relationship between 31st January and the 7th February 2015 whilst Figure 43 presents the thermal imagery demonstrating the top-down cooling from 1st February to the 2nd February 2015. There are several explanations for this finding. Firstly, as exemplified in the thermal image at 20:00 in Figure 43 the promenade and sea wall are warmer than the cliff face and as a result heat is emitted from these surfaces during the night. This replicates the impact that the sea would have in an undefended coastline. Secondly the marina buildings are approximately 50m from the cliff and so heat from the buildings can be transferred towards the lower sections of cliff face which are of similar height to the residential properties.

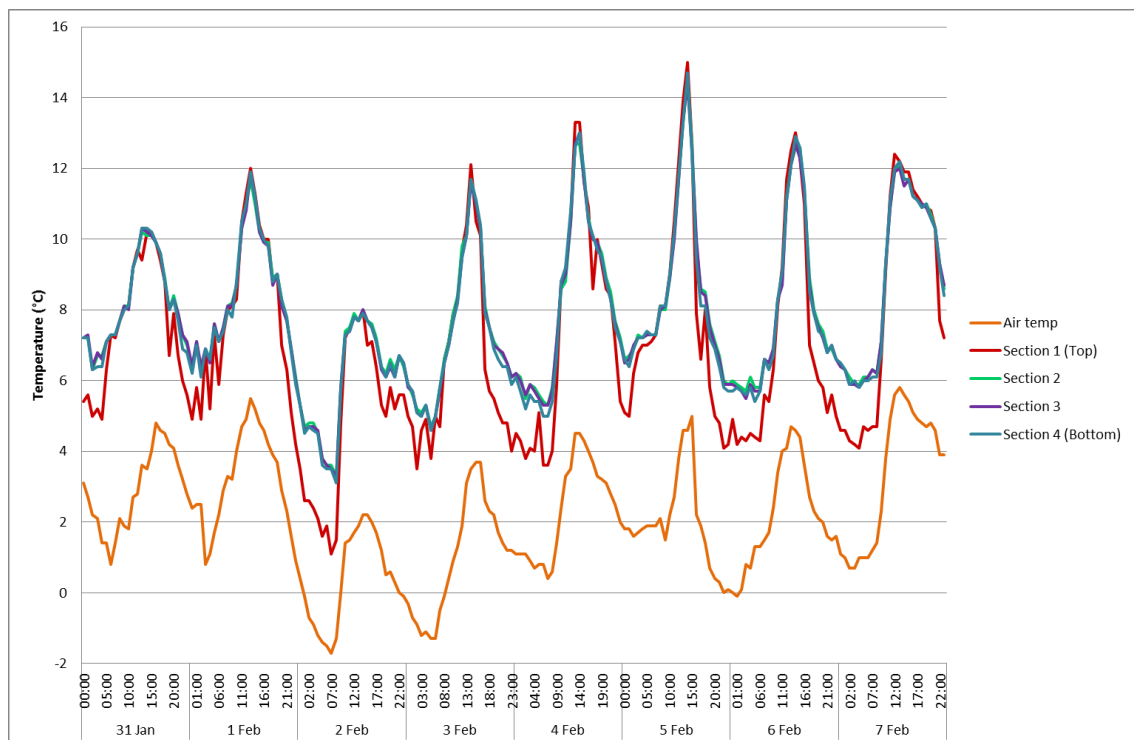


Figure 42: Air temperature and minimum cliff surface temperature by section between 31/01/2015 – 07/02/2015.

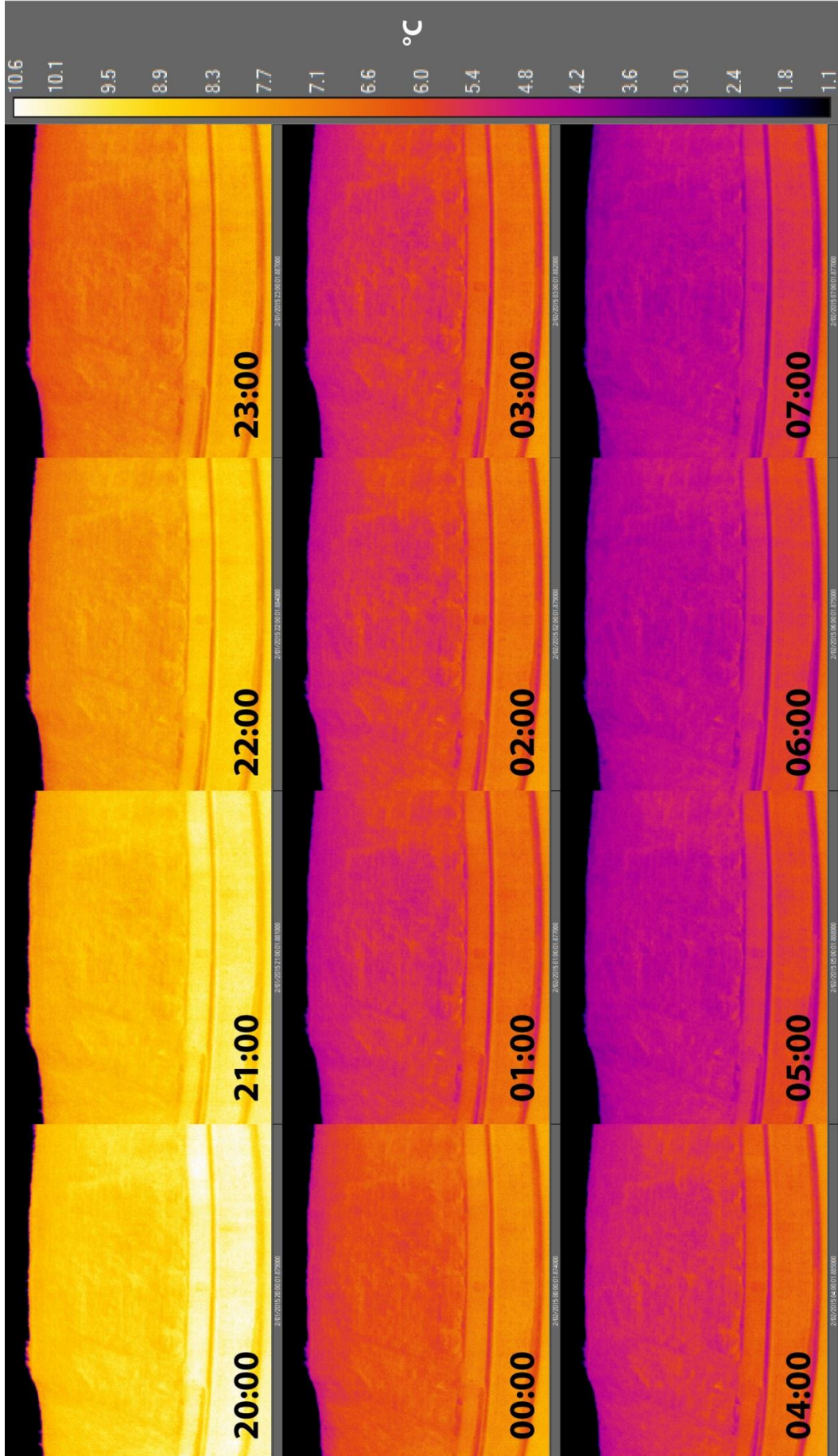


Figure 43: Hourly thermal imagery captured in Brighton Marina showing top-down cooling of the cliff face (between 20:00 on 01/02/2015 and 07:00 on 02/02/2015).

The results presented with respect to the environmental conditions at the site during the period of data collection infer minimal activity, due to the relative dry conditions and very few periods of below freezing temperatures which did not induce surface freezing within the protected section of cliff line at Brighton Marina. Analysis of change detection through photogrammetry at the site is presented in the next chapter.

4.6. Kinematic analysis – Newhaven Chalk geological controls

The kinematic analysis completed on the photogrammetric models from Telscombe provide details on the dominant joint sets within the broader study area of the same geological formation. Figures 44A and 44B illustrate the density pole and contour plots for the mapped discontinuities including and excluding bedding planes respectively. The bedding planes were removed from Figure 44B to better visualise the density concentrations of the joints and faults. The two identified joint sets; Joint Set 1 (JS1) and Joint Set 2 (JS2) were located towards the north and north east of the plot respectively (Figure 44C), whilst the fault set (FS) were located to the south east of the plot (Figure 44C). Table 15 details the identified joint sets.

Set	Number mapped	Dip (°)	Dip direction (°)
JS1	76	75	169
JS2	98	78	233
FS	14	59	288
Bedding planes	108	1	87
Unidentified joints	81	-	-
Unidentified faults	14	-	-

Table 15: Identified sets from discontinuity analysis using Dips 7.0 (Data extracted from Figure 44C).

The kinematic analysis undertaken identifies the feasibility of the different modes of failure for the chalk cliffs at Telscombe. This analysis found that wedge failure, with 39.97% of all mapped intersections favourable to this mode, is the most likely method of failure (adapted from Barlow et al., 2017). This is split 27.82% and 12.15% for sliding on both planes (the primary critical zone) and sliding on one plane (secondary critical zone) respectively (Figure 45). The percentage of intersections falling within the favourable region for the other modes of failure are; 7.16% of planar, 4.24% flexural toppling and 0.31% direct toppling (adapted from Barlow et al., 2017). As

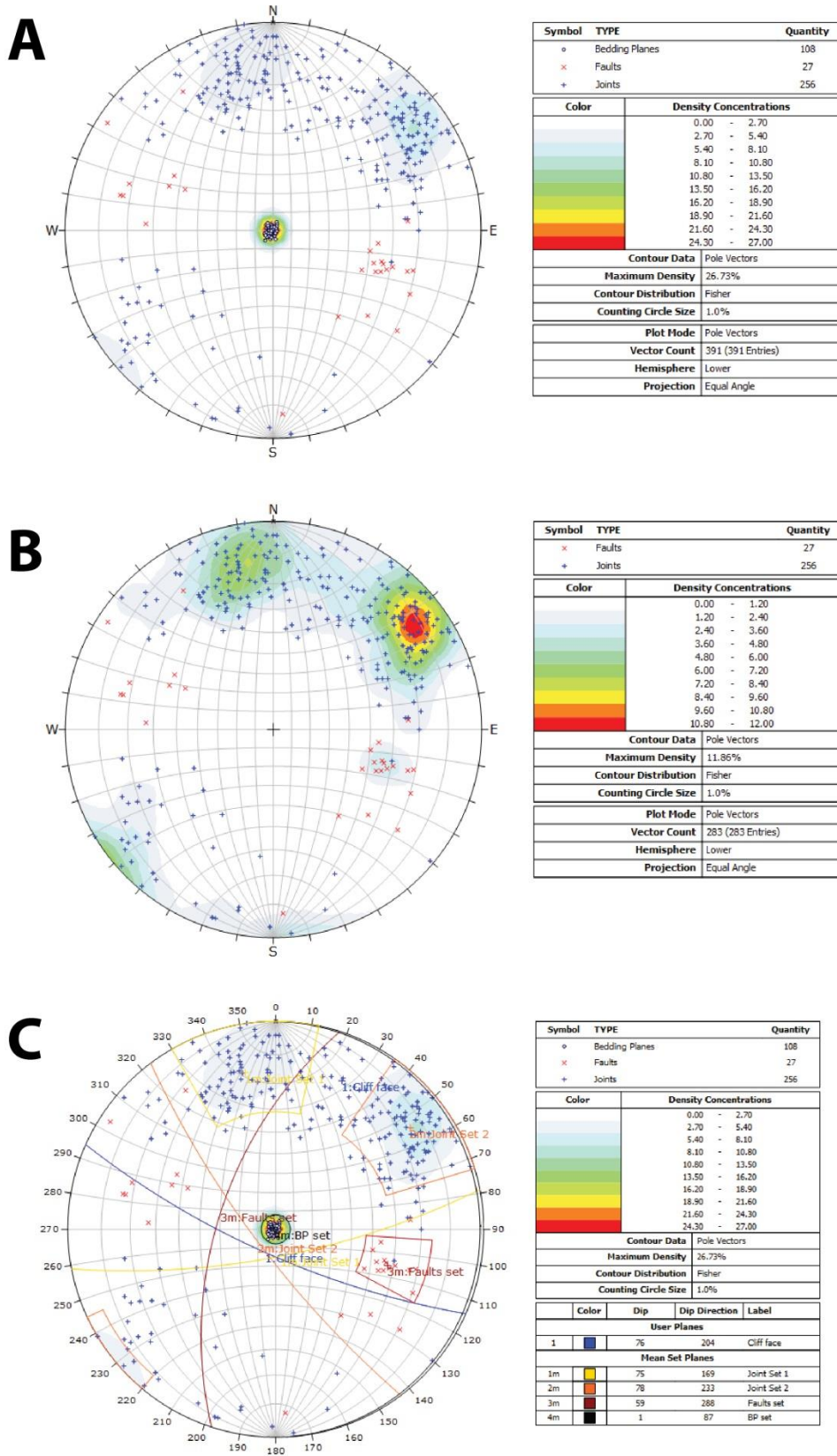


Figure 44: Wolf equal angle stereographic projection of discontinuity data from Telscombe cliffs, (A) pole plot densities of all mapped discontinuities, (B) pole plot densities of mapped joints and faults, and (C) pole plot densities of all mapped discontinuities with identified joint and fault sets with great circles.

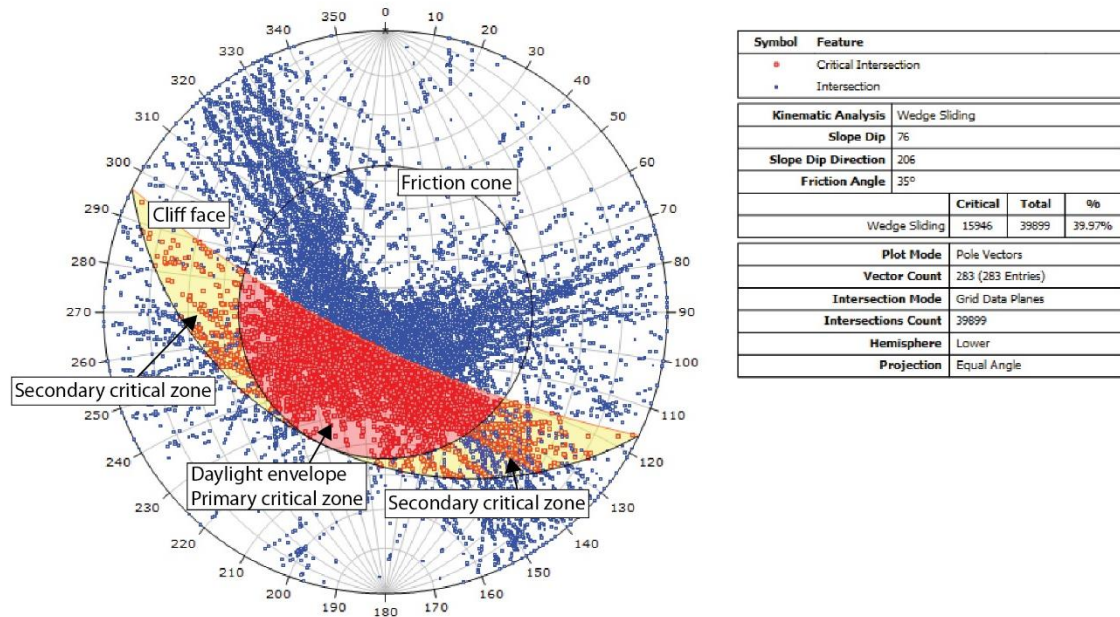


Figure 45: Stereographic representation of discontinuity data for points of intersection between joints and faults for wedge failure.

a result wedge failure analysis was undertaken through the limit-equilibrium analysis of rock falls in the defended section of cliff line formed of Newhaven Chalk where identifiable conjugate joint sets (Mortimore et al., 2004a) are evident. The averaged joint set parameters displayed in Table 15 are consistent with the scientific literature (Mortimore et al., 2004a; 2004b; Lawrence, 2007; Barlow et al., 2017) and will form the basis for the limit equilibrium analysis for wedge failures presented in the following chapter.

4.7. Marine conditions

With the cliffs orientated to the south-west they are exposed to Atlantic swell and storm waves generated within the English Channel (May, 2003; Dornbusch et al., 2008). Data examined from January 2008 to July 2017 from the Seaford wave buoy provided by the CCO (Amos, 2008; Bovington, 2009; Bovington & Amos, 2010; Bovington et al., 2011; Amos, 2013; Bovington et al., 2014; Bovington et al., 2015; CCO, 2016; CCO; 2017b) reveals 76% of the monthly averaged wave directions are from the south-west. The approximate spring tidal range is 6.1 metres (CCO, 2015) which submerges the shore platform, and the significant wave height ranges from 0.56 m in the

summer months to 1.1 m in the winter. Notably 72% of storm H_s greater than 4 m in height were south-westerly driven with the largest recorded on the 14th February 2014, 5.34 m. The data derived from the Seaford wave buoy demonstrates that the south-westerly orientated coastline is exposed to a greater period of wave attack both in calm and storm conditions which is known to be the one of the drivers of cliff failure (Mortimore et al., 2004a).

4.8. Study sites – Brighton Marina and Telscombe

This chapter has provided a geomorphological background to the chalk cliffs of East Sussex, an understanding of the current system behaviour is developed through assessing the historical recession rates and anthropogenic influences on the cliffs through toe protection structures and cliff face stabilisation measures. This provided the opportunity to undertake a comparative assessment of the behaviour between the protected and unprotected sections of cliff line. Figure 46 illustrates the location of these two sites; Brighton Marina (the protected site) and Telscombe (the unprotected site) which are approximately 4.5 km apart where terrestrial and UAV photogrammetry were deployed respectively as well as assessing the drivers to recession which have been referred to in this chapter. The site at Brighton Marina was chosen as it provided good access seaward of the cliff face and notably recorded the highest volume of chalk debris from the pathway in comparison to the sections with cliff face stabilisation measures,

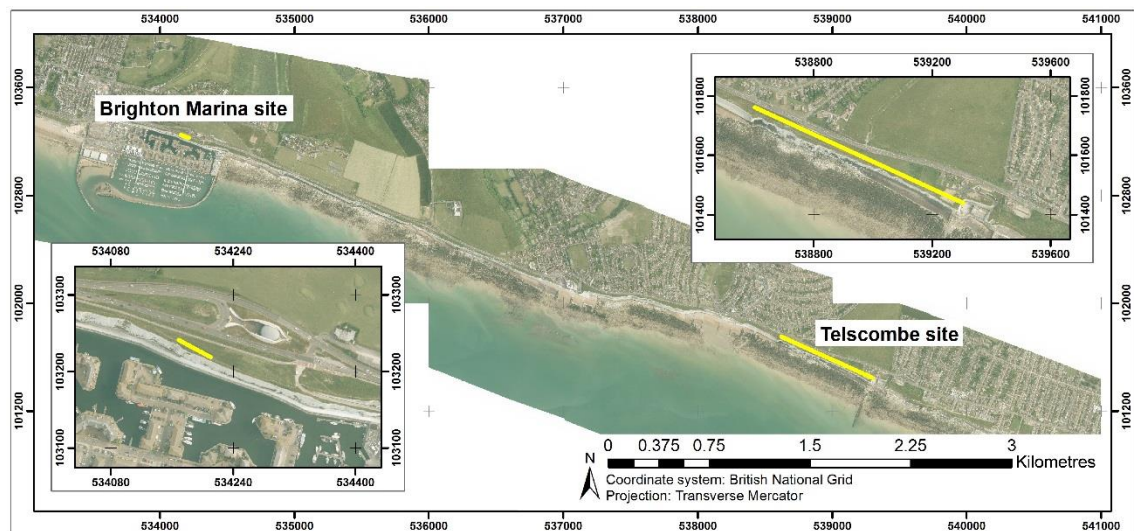


Figure 46: Location of photogrammetry study sites (2013 imagery downloaded from the CCO).

during the closure of the Undercliff walk between December 2012 and May 2013. The site at Telscombe forms one of the few unprotected cliff lines between Brighton and Newhaven and is approximately 750 m in length with a maximum elevation of 49 m. Due to the concrete groyne which protects the sewage outfall pipe to the east of the site a substantial shingle beach which tapers over 300 metres provides natural defence to the eastern extent of the cliff line. The western 50 m of the site is protected at the toe by rock armour to prevent outflanking of the Undercliff walk/sea wall cliff toe protection structure. The following results and discussion chapter will present the outcomes of this comparative assessment and the impact that continued recession will have on infrastructure through probabilistic modelling.

Chapter 5 – Results and discussion

This chapter presents the key findings from the research and assesses the risk to the A259 coastal road. High frequency collection of photogrammetric datasets enabled surface change detection to be quantified and a rockfall inventory produced. Through negative power law scaling of rockfalls and statistical correlations found between the scaling parameters and significant wave height, a key contribution of this research, a probabilistic recession model was developed to estimate recession of the unprotected cliff line under current and future conditions. Deterministic modelling was completed using data from the kinematic analysis, back analysis of observed wedge failures and field measurements to determine the potential impact that one of these larger scale failures would have within the defended section of cliff line between Brighton Marina and Saltdean. A traditional probabilistic method following industry best practice is then presented to assess the recession of this section of cliff line. This provides the opportunity to assess the key contribution of this research against the methodological approach currently used in the absence of such data.

5.1. Change detection

The rationale for developing a reliable photogrammetric model for high precision monitoring of coastal cliffs was presented in Section 3.2.7. The salient points from this section (3.2.7) are reported below as they detail the resolution of the 3D models used to undertake the 2.5D surface change detection. Both the terrestrial and UAV photogrammetry models increased on the current point densities achieved of 25 pts/m² (Bovington, 2010; 2012; 2013a; 2013b) for the site. The terrestrial datasets captured at Brighton Marina recorded a point density of 1,323 pts/m² for the Sony DSC-H300 and 3,832 pts/m² for the Nikon D810 35mm prime lens using the convergent image capture method. The UAV photogrammetry at Telscombe recorded a point density 351 pts/m² this represents an increase in the resolution of the photogrammetry methodology against those currently deployed at the site and are comparable to other TLS

deployments at alternative coastal cliff sites (Lim et al., 2005; Barlow et al., 2012). Importantly the point density recorded for the UAV photogrammetry is developed from one strip due to restrictions on processing capability. Increasing this to several passes at different elevations, which would produce a convergent strip model would increase the point density similar to that produced by the terrestrial photogrammetry method.

5.1.1. Terrestrial photogrammetry – Brighton Marina

Due to the development of the methodological approach, datasets from the higher resolution models were rasterised at both 0.02 m and 0.03 m cell size for comparison with the models generated from the Sony DSC-H300 imagery. Comparison of models at each stage of method development (Figures 47, 48 & 49) were undertaken to determine if any rockfall had occurred between these data captures. Figure 47 illustrates a surface change raster between models captured from November 2014 and January 2016 from the Sony DSC-H300 and Nikon D810 35 mm varied lens respectively, the cell size of these rasters was 0.03 m. The only change which was detected in this 15 month period was within vegetated areas. Figure 48 is representative of surface change between January 2016 and March 2017 captured from the Nikon D810 35 mm varied lens and the Nikon D810 35 mm prime lens respectively. This surface change raster has a cell size of 0.02 m. The majority of surface change is, again, due to vegetation however there are clusters of 'change' detected along the edges of the cliff where aspect changes abruptly. The imagery was examined within these areas to determine whether this was representative of spalling rockfall. This revealed that no rockfall had occurred, this may be as a result of a reduced cell size which enabled small edge effects to be falsely identified as surface change. Equally, this issue may be due to the change in image capture method as the true strip method may introduce greater uncertainty in the placement of the 'edges' as opposed to the convergent method which utilises greater distance to base ratios and therefore increases depth accuracy. Figure 48 illustrates surface change between models that were both captured using the convergent strip

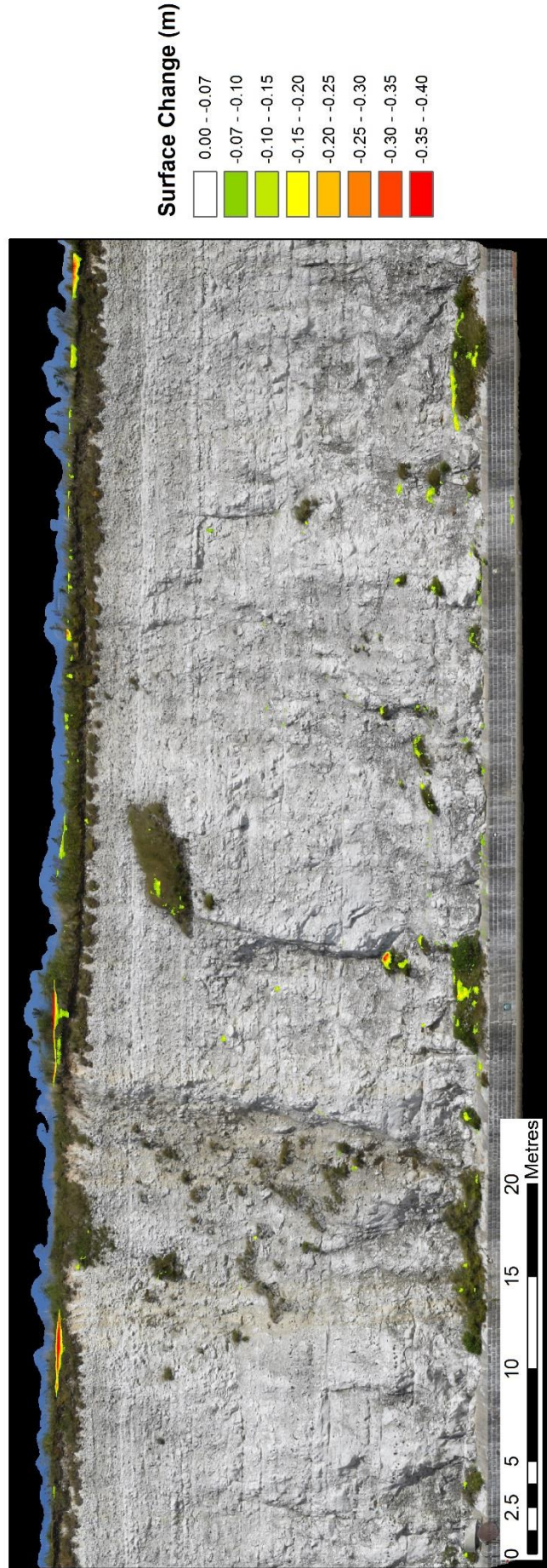


Figure 47: Surface change between November 2014 and January 2016 at Brighton Marina using terrestrial photogrammetry captured from the Sony DSC-H300 and Nikon D810 35mm varied lens respectively, raster cell size=0.03m.

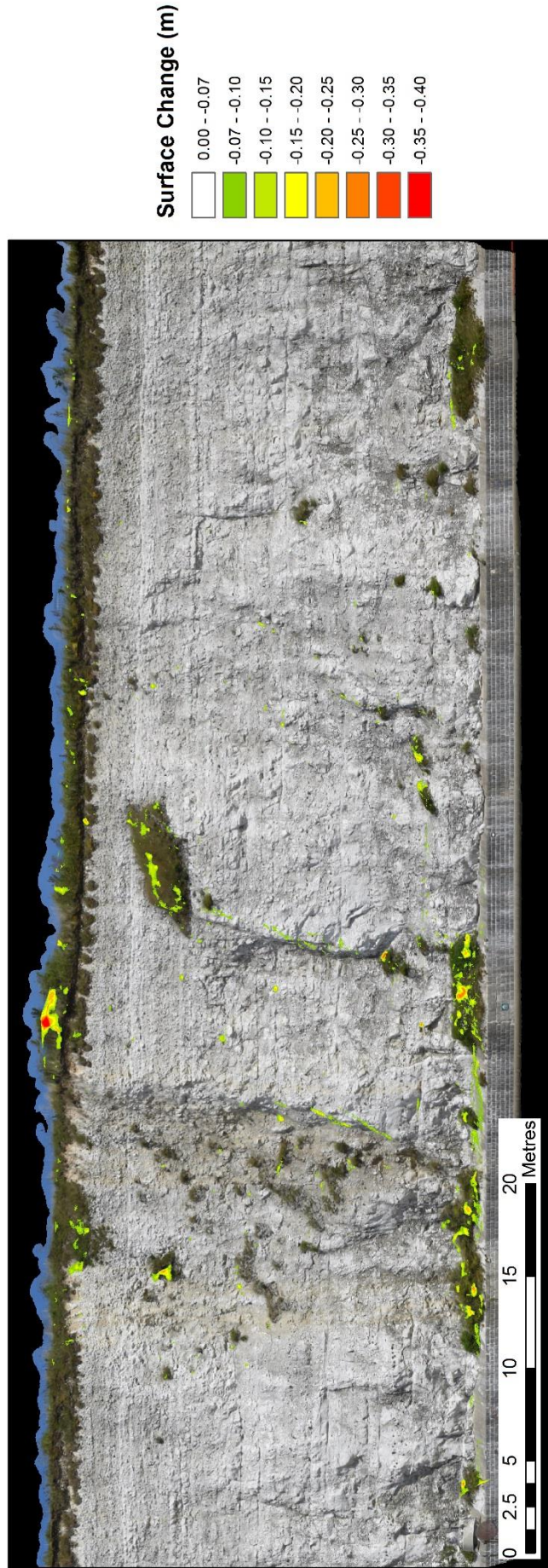


Figure 48: Surface change between January 2016 and March 2017 at Brighton Marina using terrestrial photogrammetry captured from the Nikon D810 35mm varied lens and prime lens respectively, raster cell size=0.02m.

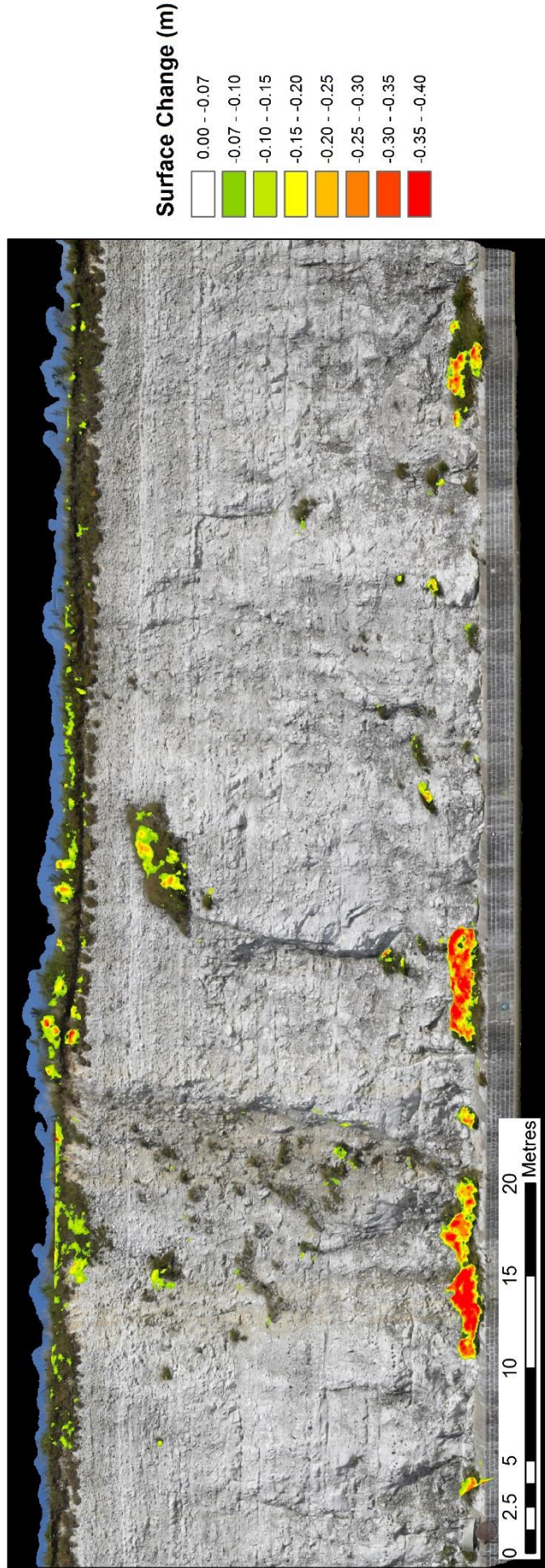


Figure 49: Surface change between July 2016 and March 2017 at Brighton Marina using terrestrial photogrammetry captured from the Nikon D810 35mm prime lens, raster cell size=0.02m.

method and the Nikon D810 35 mm prime lens (June 2016-March 2017). Similarly the only surface change is detected within vegetated areas. Importantly however the edge effects previously found (Figure 47) are no longer identified whilst the cell size remained at 0.02 m. This provides evidence to support the earlier hypothesis that the edge effects were most likely introduced by the non-convergent image set.

The key finding from the terrestrial photogrammetry is that no detectable rockfall (spalling) has occurred between November 2014 and March 2017 in the study area at Brighton Marina. Weekly field visits to the site suggest small rockfalls have occurred but have not exceeded the detectable threshold. This result shows that cliff regrading has, in the short term, stabilised the cliff with regards to sub-aerial weathering so that small magnitude high frequency rockfalls have not totalled more than 0.07 m in surface change. Importantly during the data collection period environmental conditions (Section 4.5) have been favourable to a low activity of rockfalls in protected cliff sections. As surface freezing temperatures were not detected which would initiate expansion of water within discontinuities and average precipitation recorded throughout the research resulted in the chalk retaining its material strength.

5.1.2. UAV photogrammetry – Telscombe

The UAV photogrammetry collected monthly between August 2016 and July 2017 in the undefended section of cliff line at Telscombe detected successive block failures in the Newhaven Chalk as presented by Mortimore et al. (2004a) and also supplied evidence of the known process of toe erosion in inducing failure in coastal cliffs. The threshold of change detection for the UAV photogrammetry as explained in Table 7 (Section 3.2.6.2) was set to 0.10 m and the cell size of the rasters used for surface change detection 0.10 m. A total volumetric flux of 3,889.4 m³ was detected during the twelve month period of data collection with the largest failure between February and March 2017 at 2,546.8 m³, although this figure does not account for erosion in the lower section of cliff which is obscured by debris (up to 10 m high and 30 m wide). The total

number of failures observed was 10,085 with all of the larger failures occurring west of central in the study area (Figure 50), this is unsurprising due to the shingle beach that acts as natural toe protection to the eastern section of the site.

5.1.2.1. Successive block failures (August – December 2016)

The successive block failures identified in the cliffs at Telscombe occurred centrally within the study area. Between August and December 2016 a total erosional mass flux of 788.2 m³ was recorded. The first failure that was detected occurred between data collection on the 5th August and 7th September 2016. Additional field visits during this period enabled the date of failure to be identified between the 17th and 24th August. This window coincided with a two day period (20-21 August 2016) of strong south-westerly winds averaging 8.45 ms⁻¹, with average peak gusts of 11.29 ms⁻¹ and 19.2 ms⁻¹ recorded respectively from the Brighton Marina meteorological station (Barlow et al., 2017). These strong winds coincided with the high tide, between 6.3 m and 6.9 m CD (Chart Datum) resulting in substantial wave attack of the cliff toe (Barlow et al., 2017). The wedge failure, located centrally in Figure 51A, failed on a conjugate joint set intersecting near the base of cliff. The failure was bound at the top by a band of more resistant nodular flint. The wedge failure volume was measured at 152.7 m³. To the west of this failure the arch of a small cave failed (Figure 51A) during the same month with a volume of 47.2 m³. The following month only revealed a relatively small amount of material, totalling 2.2 m³, removed from the cliff toe (Figure 51B) before a block failed in the upper cliff between 10th October and the 11th November, with a volume of 37.7 m³ (Figure 51C). The preceding wedge failure led to an overhang of material (Figure 52) for the upper two thirds of the cliff. This failed between the 11th November and the 6th December 2016 and was the largest of the failure blocks with a volume of 512.2 m³ (Figure 51D). Further rockfall was identified around the arch, on the western side with a volume of 38.5 m³. The progressive nature of these failures within the Newhaven Chalk was previously presented as a series of blocks which may fail either top down

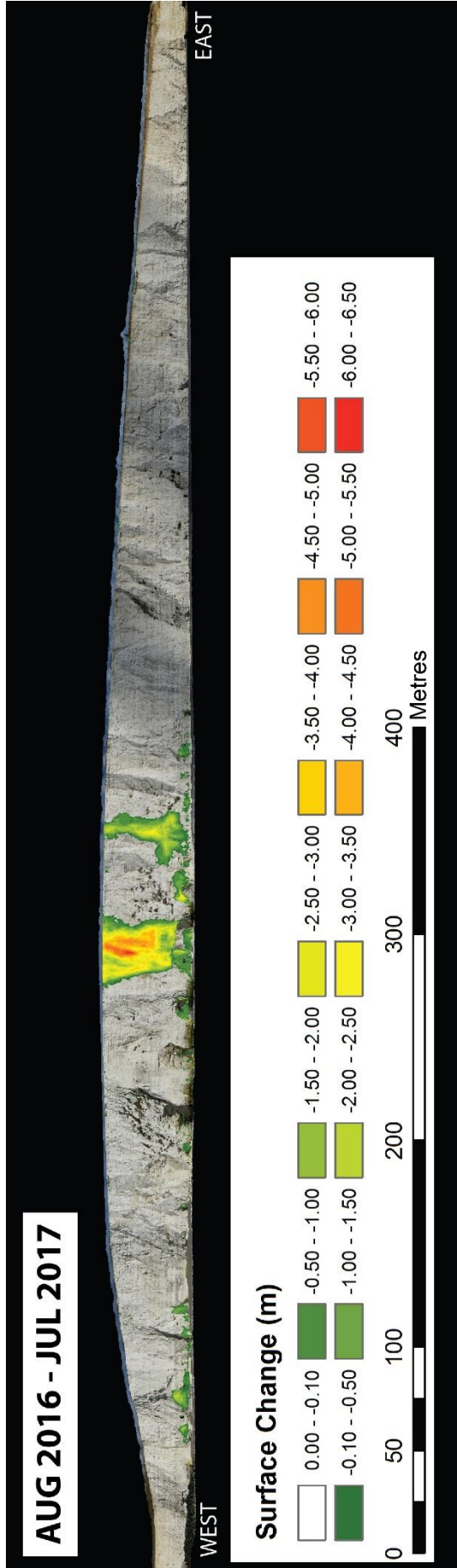


Figure 50: Surface change between August 2016 and March 2017 at Telscombe using UAV photogrammetry captured from the Nikon D810 24mm prime lens, raster cell size=0.10m.

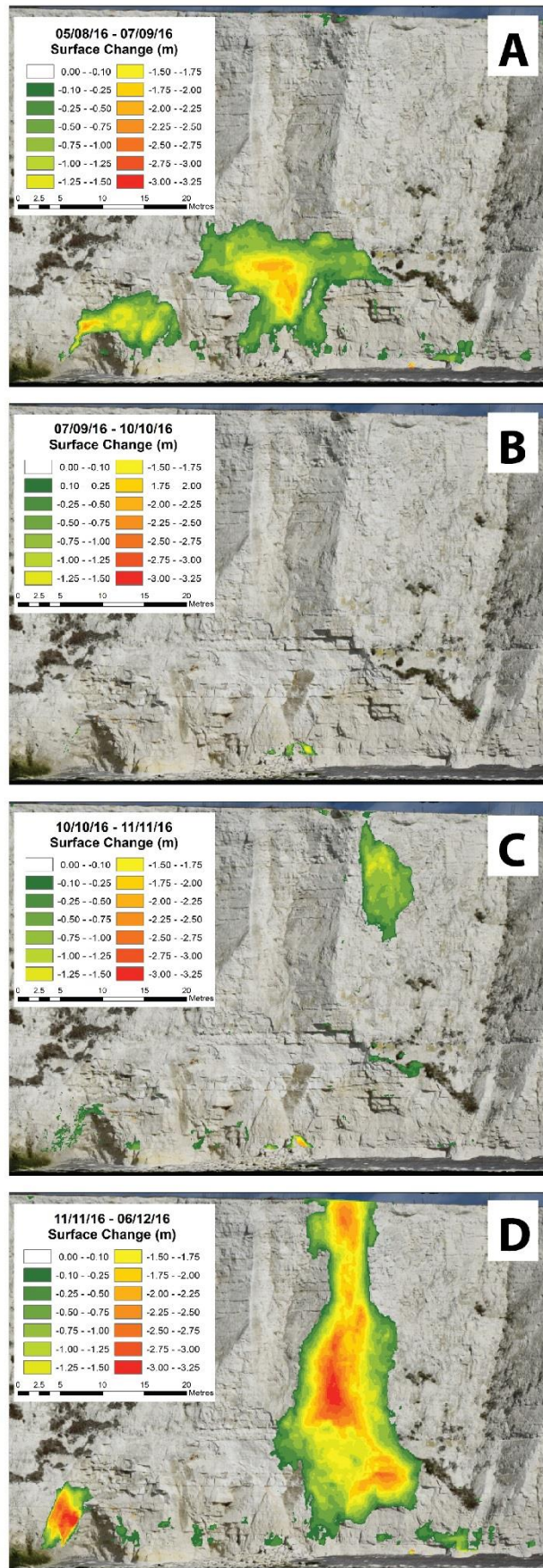


Figure 51: Surface change monitoring successive failures in the Newhaven Chalk at Telscombe between 05/08/16 and 06/12/16, cell size=0.10m (A)Aug-Sep 2016, (B)Sep-Oct 2016, (C) Oct-Nov 2016 & (D) Nov-Dec 2016.

or bottom up on a series of conjugate shear surfaces by Mortimore et al. (2004a). Mortimore et al.'s (2004a) findings were based on a wealth of observations and knowledge acquired on the chalk coasts of Sussex, the results presented in Figure 51 offer the first remotely sensed dataset which offers clear supporting evidence illustrating this accepted process.

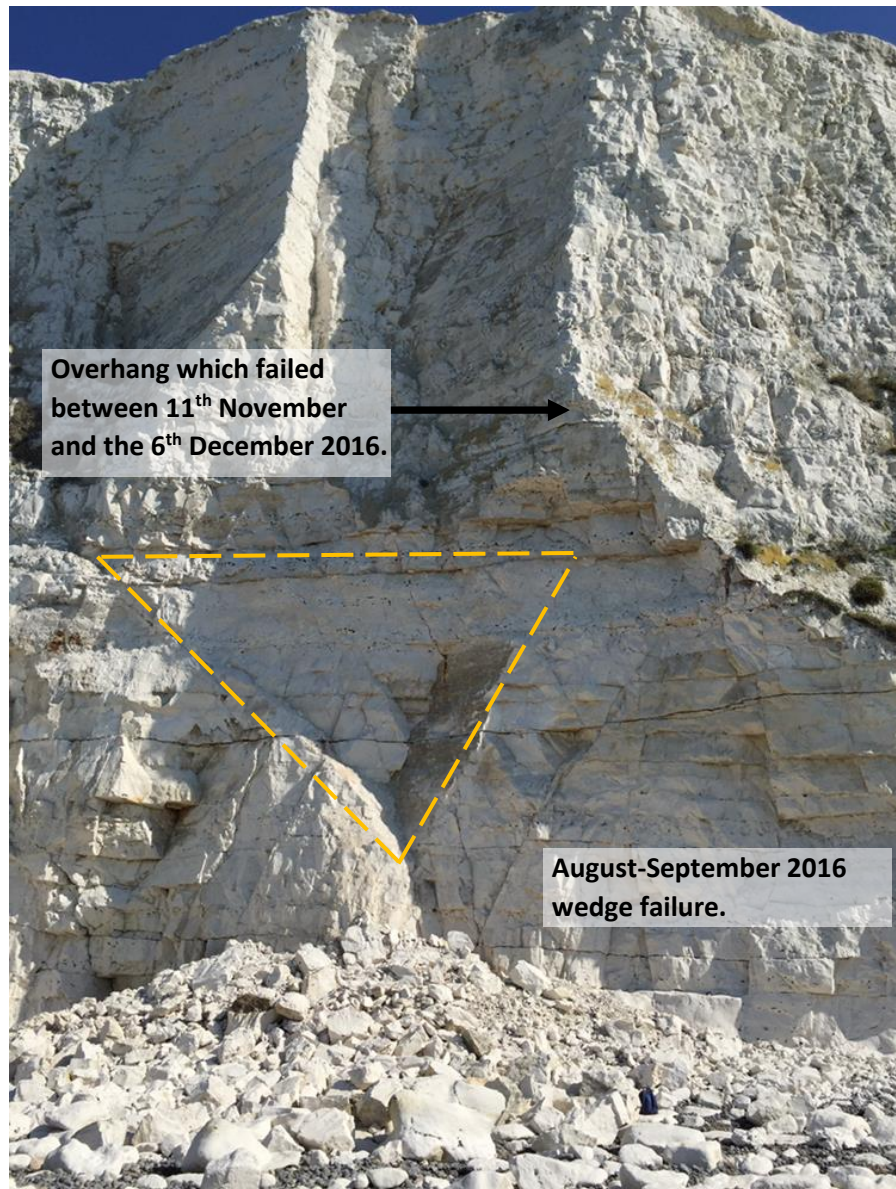
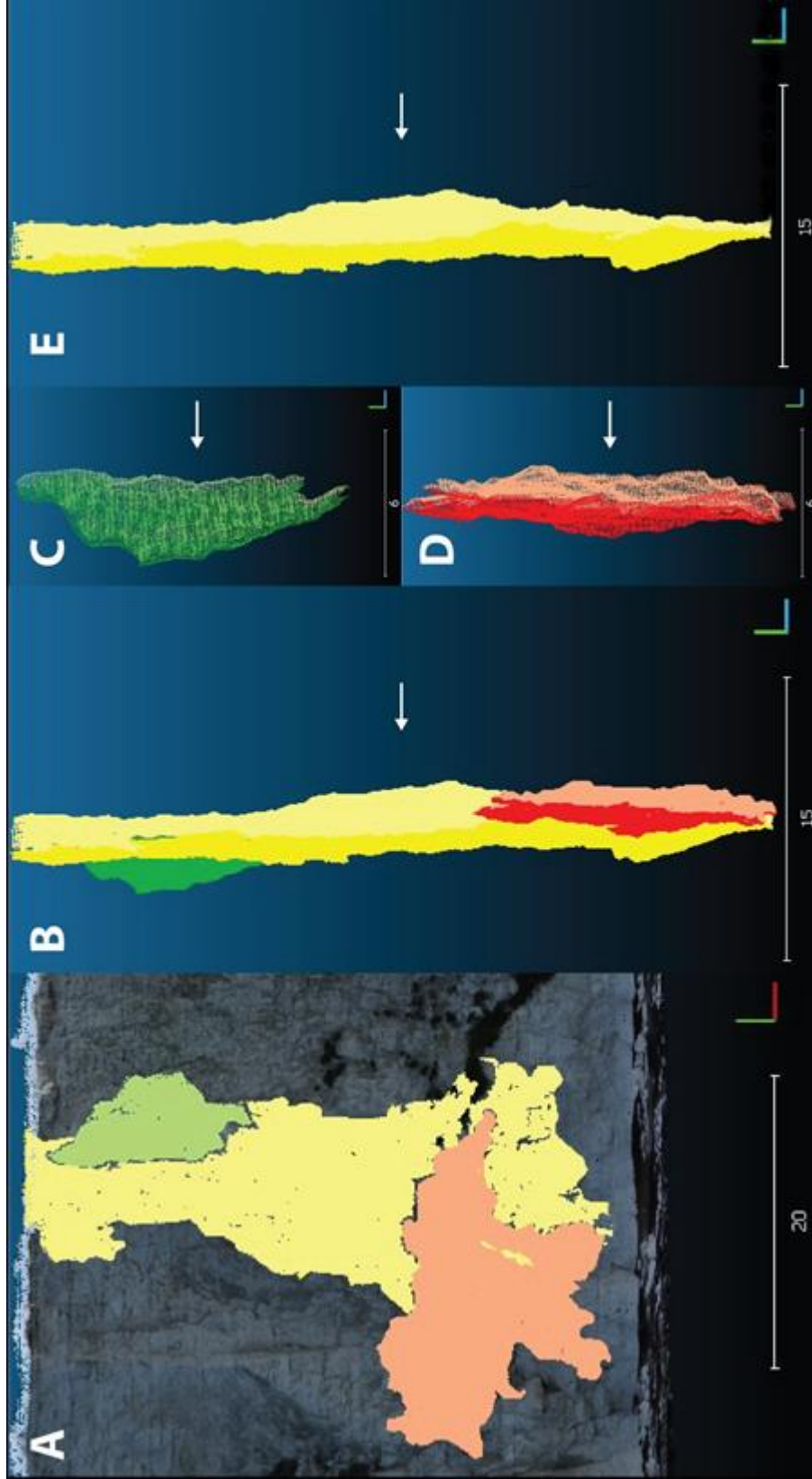


Figure 52: Wedge failure at Telscombe cliffs leaving overhanging cliff material which failed between the 11th November and the 6th December 2016, image taken on 24/08/2016.

Figures 53A and 53B illustrate the interaction between the successive failures observed in Figure 51. Using Cloud Compare (Cloud Compare v2.6.3, 2016) these blocks were isolated to provide a 3D presentation of each failure (Figures 53C, 53D & 53E). The visualisation of these blocks can be compared to that presented by Mortimore et al. (2004a) in Figure 54. The initial wedge failure



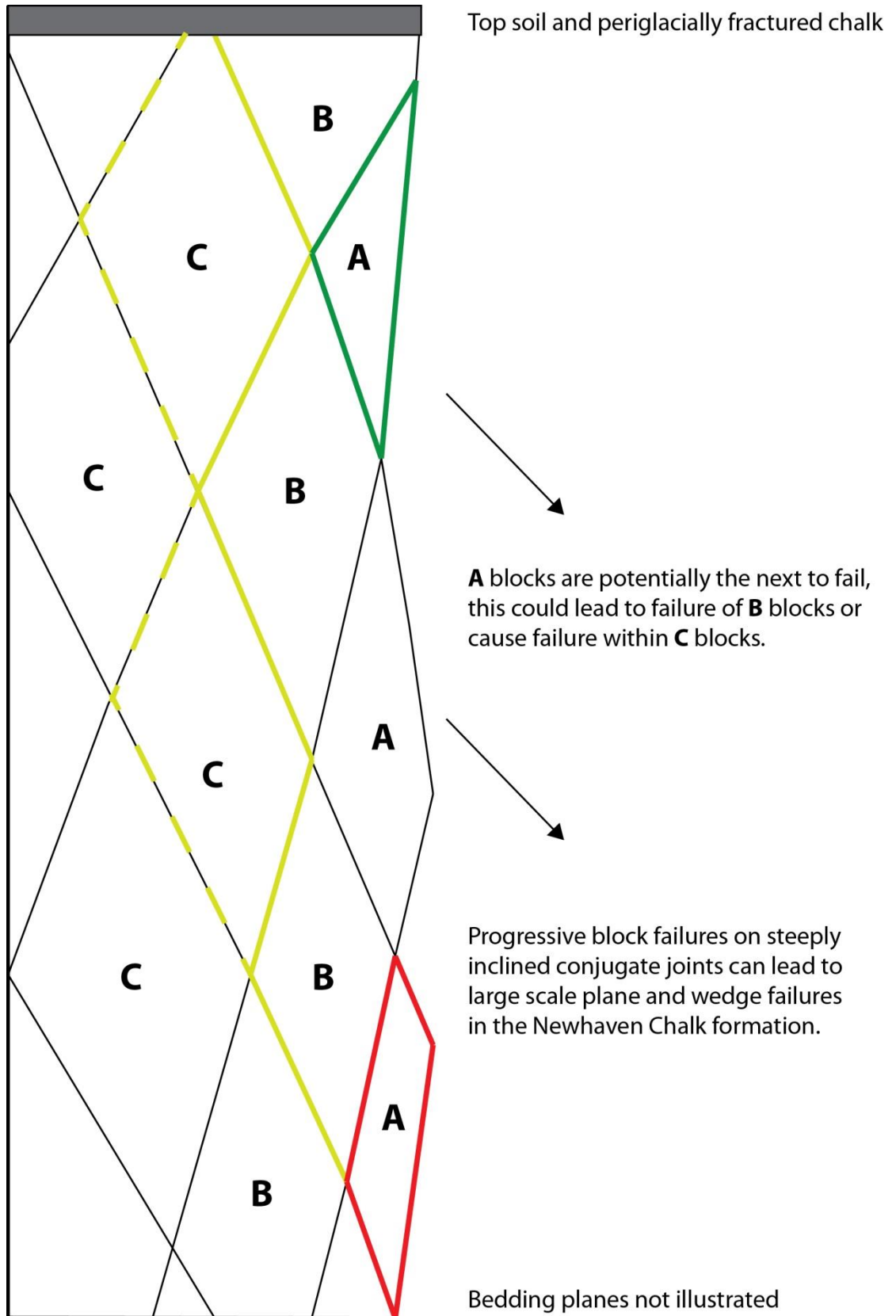


Figure 54: Peacehaven type failure in the Newhaven Chalk (Adapted from Mortimore et al., 2004a, p.15) illustrating the progressive nature of failures observed at Telscombe between August and December 2016 (Red – Aug-Sep, Green – Oct-Nov and Yellow – Nov-Dec).

is represented by block 'A' (red) which, as Mortimore et al. (2004a) state could lead to further failures in blocks 'B' and/or 'C'. The failure in the upper cliff in November represents another 'A' block (green) using Mortimore et al.'s (2004a) schematic. The following failures culminating with the largest rockfall for this site in November (Figure 51D and Figure 53E) represent 'B' blocks or 'C' blocks, confirming that the initial failures lead to a destabilisation in the cliff along the planes of weakness as presented by Mortimore et al. (2004a).

5.1.2.2. Toe erosion and subsequent failure (August 2016 – March 2017)

Approximately 55 m to the west of the presented successive failures monthly toe erosion was detected totalling 104.9 m³ between August 2016 and February 2017. This well-established process of cliff failure led to the largest observed failure in February-March 2017 of 2,546.8 m³. This figure is most likely an underestimate of the true volume due to the substantial debris which obscures the lower quarter of the cliff. Table 16 and Figure 55 provide a monthly and spatial breakdown of the observed erosion, the erosion to the right of the images (east) is not included in these totals as it is representative of the arch erosion quantified in the previous section.

Month	Total volume of erosion within area of interest (m ³)
August – September 2016	2.8
September – October 2016	0.6
October – November 2016	54.0
November – December 2016	26.5
December 2016 – January 2017	22.7
January – February 2017	2.7
February – March 2017	2546.8
TOTAL	2656.1

Table 16: Volume of monthly toe erosion and the subsequent failure between August 2016 and March 2017.

Analysis of the 3D model following the largest failure revealed a conjugate joint set (Figure 56A) intersecting at the base of cliff which formed a wedge. As the kinematic analysis identified (after Barlow et al., 2017), this is the most likely mechanism of failure within the Newhaven Chalk at

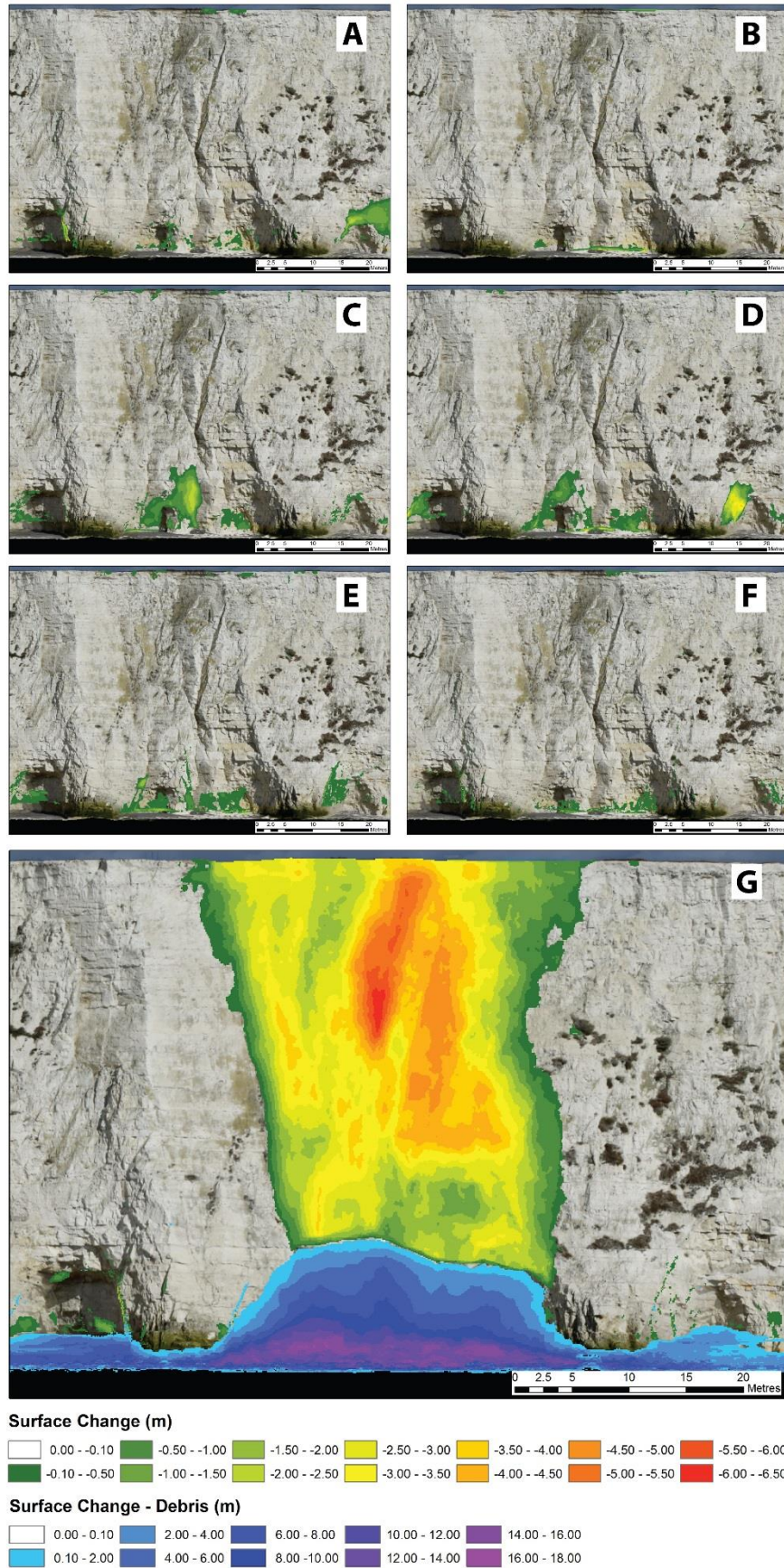


Figure 55: Surface change monitoring toe erosion and subsequent failure in the Newhaven Chalk at Telscombe between 05/08/16 and 07/03/17, cell size=0.10m (A)Aug-Sep 2016, (B)Sep-Oct 2016, (C) Oct-Nov 2016, (D) Nov-Dec 2016, (E) Dec 2016-Jan 2017, (F) Jan-Feb 2017 and (G) Feb-Mar 2017.

Telscombe. A limit equilibrium analysis (Figure 56B) was completed in the software Swedge to assess the impact of the steepening cliff face due to toe erosion. Figure 56C details the input parameters used for this analysis. The Factor of Safety (FoS) reduced from 1.51 to 1.00 between August 2016 and March 2017 (Figure 57) under these conditions (Figure 56C). The greatest reduction in FoS, as expected, coincided with the largest preceding failure of 54.0 m³, this increased the cliff face angle by 2.74° to 78.77°. This failure along with those observed between August and February were focussed at the toe of the cliff where the conjugate joints intersected. The steepening of the cliff face would have increased the stress network along these planes of weakness within the chalk which primed this location to failure. During the 18 days between the February and March surveys there were several periods of strong winds that coincided with high tides. The Brighton Marina meteorological station recorded the peak gust 21.6 ms⁻¹ on the 23rd February 2017, and recorded the highest average wind speed and average gust for the duration between surveys of 5.4 ms⁻¹ and 7.245 ms⁻¹ respectively. This would have led to substantial wave attack at the cliff toe which had been significantly eroded over the previous months.

5.2. Using negative power law scaling of rockfalls to develop a probabilistic recession model

One of the conventional methods to assess erosion within geomorphic environments is through magnitude-frequency analysis (Wolman & Miller, 1960; Stark & Guzzetti, 2009; Barlow et al., 2012; Lim, 2014). The modelling of erosion through the use of negative power laws (Bak, 1996) is evidenced by Brunetti et al. (2009) in assessing the probability distributions of landslide volumes, whilst Lim et al. (2010) and Barlow et al. (2012) have applied the methodology to the study of sea cliffs. As part of this research, volumetric estimations were calculated from the monthly surface models with a minimum reliable detectable rockfall size of 1 x 10⁻³ m³. The following section applies negative power law scaling of rockfall magnitude-frequency distributions to the rockfall inventory obtained between August 2016 and July 2017.

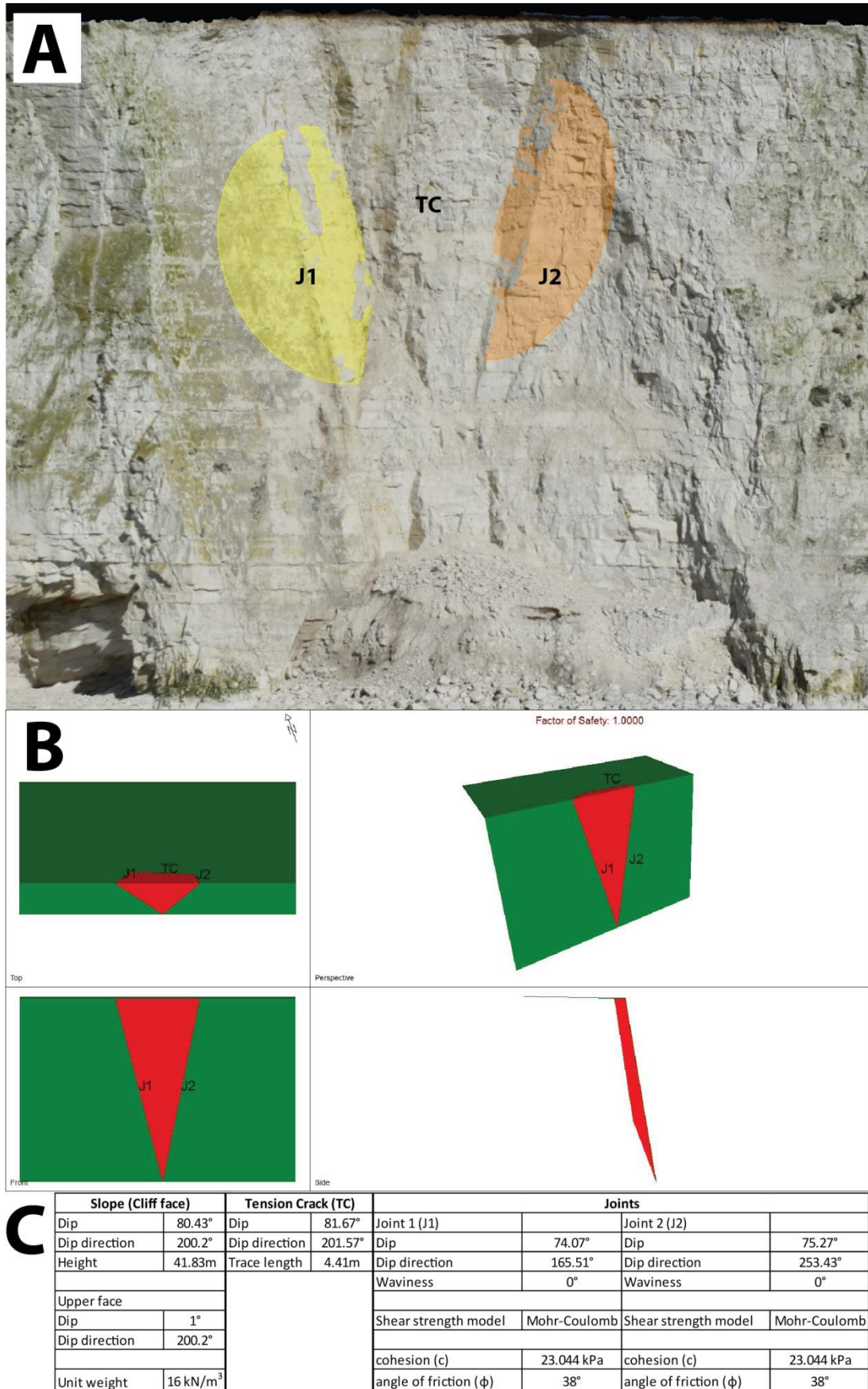


Figure 56: Limit equilibrium model of wedge failure between February and March 2017 using Swedge, (A) 3D model in ADAM 3DM Analyst detailing the joint surfaces, (B) Model output from Swedge, (C) Tabulated input parameters for Swedge analysis.

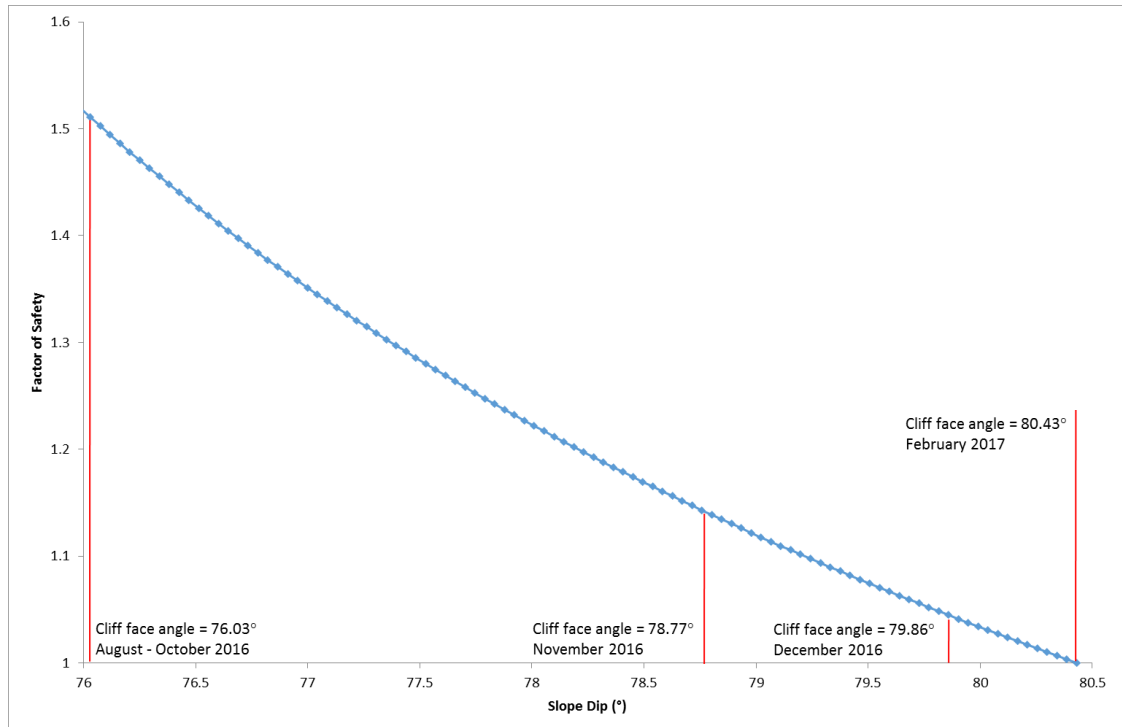


Figure 57: Limit equilibrium analysis of wedge failure in Newhaven Chalk, Telscombe effect of toe erosion in steepening of cliff face on Factor of Safety (FoS) using Swedge between August 2016 and February 2017.

5.2.1. Negative power law parameter estimation

The negative power law scaling of rockfall magnitude-frequency distributions was modelled using (Brunetti et al., 2009):

$$f(V_R) = sV_R^{-\beta} \quad (1)$$

where $f(V_R)$ is the frequency density, V_R is the magnitude of a given event and s and β are empirically derived constants. This method has been readily used in the scientific literature (Stark & Hovius, 2001; Dussauge et al., 2003; Brardinoni & Church, 2004; Guthrie & Evans, 2004; Malamud et al., 2004; Dong & Guzzetti, 2005; Van Den Eeckhaut et al., 2007; White et al., 2008; Marques, 2008; Brunetti et al., 2009; Rossi et al., 2010) and has been found to be statistically robust over the volumetric range found in the rockfall inventory from Telscombe (Malamud et al., 2004; Barlow et al., 2012).

Rockfall magnitude-frequencies were plotted on logarithmic axes (Figure 58A) using traditional logarithmic binning methods (Guzetti et al., 2002; White et al., 2008; Barlow et al., 2012), the frequency densities were calculated for each of the classifications of rockfall magnitudes by using the formula (Malamud et al., 2004):

$$f(V_R) = \frac{\delta N_R}{\delta V_R} \quad (2)$$

where $f(V_R)$ is the frequency density of a rockfall with magnitude V_R , δN_R is the number of rockfalls within the specified volume range of δV_R , and δV_R corresponds to the width of the bin. The power law parameters are usually found using a least squares regression (LSR) method on logarithmically transformed data (Hovius et al., 1997; Korup, 2005; Barlow et al., 2012). The accuracy of the power law estimations were tested, following Barlow et al. (2012) using the integral of Equation 1:

$$\delta N_R = \int_{\min}^{\max} s V_R^{-\beta} dV_R \quad (3)$$

$$\delta N_R = \frac{s V_{R \max}^{1-\beta}}{1-\beta} - \frac{s V_{R \min}^{1-\beta}}{1-\beta} \quad (4)$$

By using Equation 4 and setting the $V_{R \max}$ and $V_{R \min}$ to the respective bin widths it is possible to assess the accuracy of the estimated power law parameters against the actual observations (Barlow et al., 2012), an example taken from the month August to September 2016 is provided in Figure 58B. The R^2 value of 0.9981 shows definitive agreement between the observations and the power law model. This provides confidence that the estimations reliably predict the frequency of the various magnitudes of failure. As the period between surveys varied the frequency densities were normalized by time and area ($\text{km}^{-2} \text{ month}^{-1}$), with a month represented by 30.4375 days (365.25 days per year / 12 months). The study area was subdivided into two cliff behaviour units of 'unprotected' and 'naturally protected' to account for the impact of the shingle beach on the power law estimations (Figure 58C & 58D) and subsequent analyses. The R^2 values for the power law estimation parameters (Eg. Figure 58A) varied from 0.9697 to 0.9947

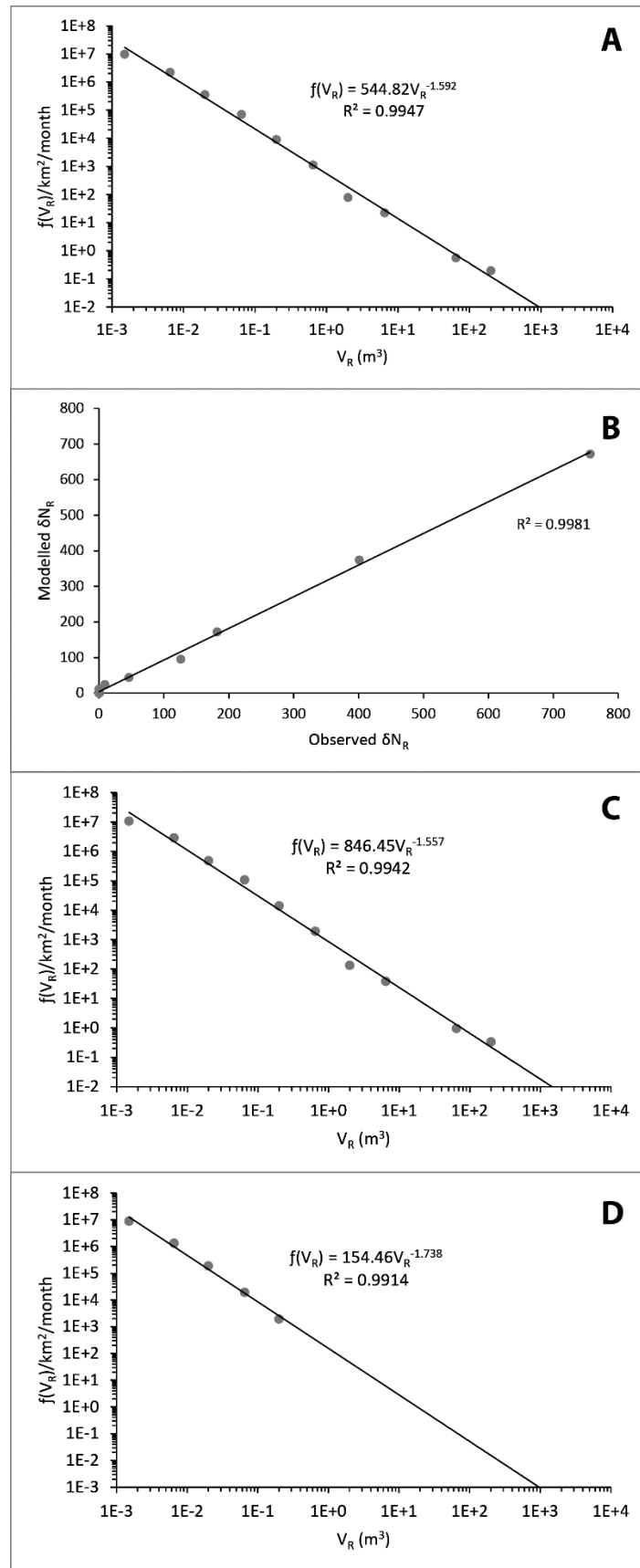


Figure 58: Power law estimation parameters for August to September 2016 (A) frequency density and magnitude of failures for the entire study area, (B) the predicted vs. observed frequency of failures for all binned data, (C) frequency density and magnitude of failures for the unprotected section and (D) frequency density and magnitude of failures for the naturally protected section (shingle beach) [black lines depict best fit models].

for the entire study area, 0.9693 to 0.9942 for the unprotected section and 0.9042 to 0.9979 for the naturally protected section.

5.2.2. Modelling cliff erosion with H_s and sea level rise (SLR)

The erosional flux can be calculated for a given magnitude of event by multiplying the frequency density of the event by the magnitude, the result of applying this to the power law equation is (Barlow et al. (2012):

$$V_{RC} = sV_R^{-\beta} V_R \quad (5)$$

$$V_{RC} = sV_R^{-\beta+1} \quad (6)$$

where V_{RC} is the volume in $m^3 km^{-2} month^{-1}$ for an event of magnitude V_R . Thus, the total volumetric erosional flux (V_T) of rock between a minimum and maximum magnitude can be calculated by (Barlow et al., 2012):

$$V_T = \int_{min}^{max} sV_R^{-\beta+1} dV_R \quad (7)$$

$$V_T = \frac{sV_{Rmax}^{2-\beta}}{2-\beta} - \frac{sV_{Rmin}^{2-\beta}}{2-\beta} \quad (8)$$

The maximum volume (V_{Rmax}) for Equation 8 can be easily extracted from the rockfall inventory, the minimum value can be more difficult to determine. A rollover in the distribution is often found with low magnitude events when modelling the magnitude-frequency of rockfalls, this forms the data censoring threshold (Barlow et al., 2012) at which rockfall volumes can be accurately modelled using the negative power law method. To avoid negating erosion of smaller volumes which still occur a minimum value of $1 \times 10^{-6} m^3$ was used in the modelling of erosion to account for the erosion below the detectable threshold of using the UAV photogrammetry methodology ($1 \times 10^{-3} m^3$).

Investigations to ascertain whether the power law estimations could be constrained by environmental (H_s – CCO, 2017c) or atmospheric conditions (temperature, precipitation and wind speed – CCO, 2017a) were undertaken. The wave data was downloaded from the nearby

wave buoy at Seaford provided by the Channel Coastal Observatory (CCO, 2017c). To determine the waves which interact with the base of cliff the minimum elevation of the cliff toe was extracted from the photogrammetry models. Tidal data downloaded from the British Oceanographic Data Centre (BODC, 2017) for Newhaven enabled a binary classification of tidal interaction with the base of cliff. This classification was then applied to the dataset so only waves which interacted with the cliff were considered in the analysis. Significant linear regression correlations were found between H_s and the β and s values with R^2 values of 0.3936 and 0.5793 respectively for the entire study area (Figure 59A & 59B). These improved, as expected, for the unprotected section of cliff to R^2 values of 0.4971 for β and 0.5902 for s (Figure 59C & 59D). The linear regression relationships between s and H_s intersect the x axis at 0.614 m and 0.602 m for the entire study area (Figure 59B) and unprotected section (Figure 59D) respectively. When comparing the erosion activity to the H_s values from the observation dataset it was considered appropriate to determine that if the value of H_s in the model was below this threshold the erosion activity would be set to zero. A dataset with a greater spatial extent would likely increase the strength of these relationships as the site has a limited number of conjugate joint sets where wedge failures occur, each at a different stage of the failure cycle. Reoccurring failures are therefore temporally limited by the cycle, with a greater sample of conjugate joint sets the likelihood that delivery of high energy waves would lead to failure is increased thus strengthening the relationships between H_s and the power law parameters. Either weak or no correlation was found between atmospheric conditions and the unprotected section, likewise there were no significant correlations found for the naturally protected beach section for any atmospheric or environmental variables considered. As a result the subsequent analyses was focused on the unprotected section of cliff line considering marine conditions.

The projections of future wave climate are presented by the UKCP09 (Lowe et al., 2009) and were generated using the medium emission scenario (IPCC scenario A1B, Leake et al., 2009).

The wave model was run for the UK continental shelf and meteorological parameters of wind

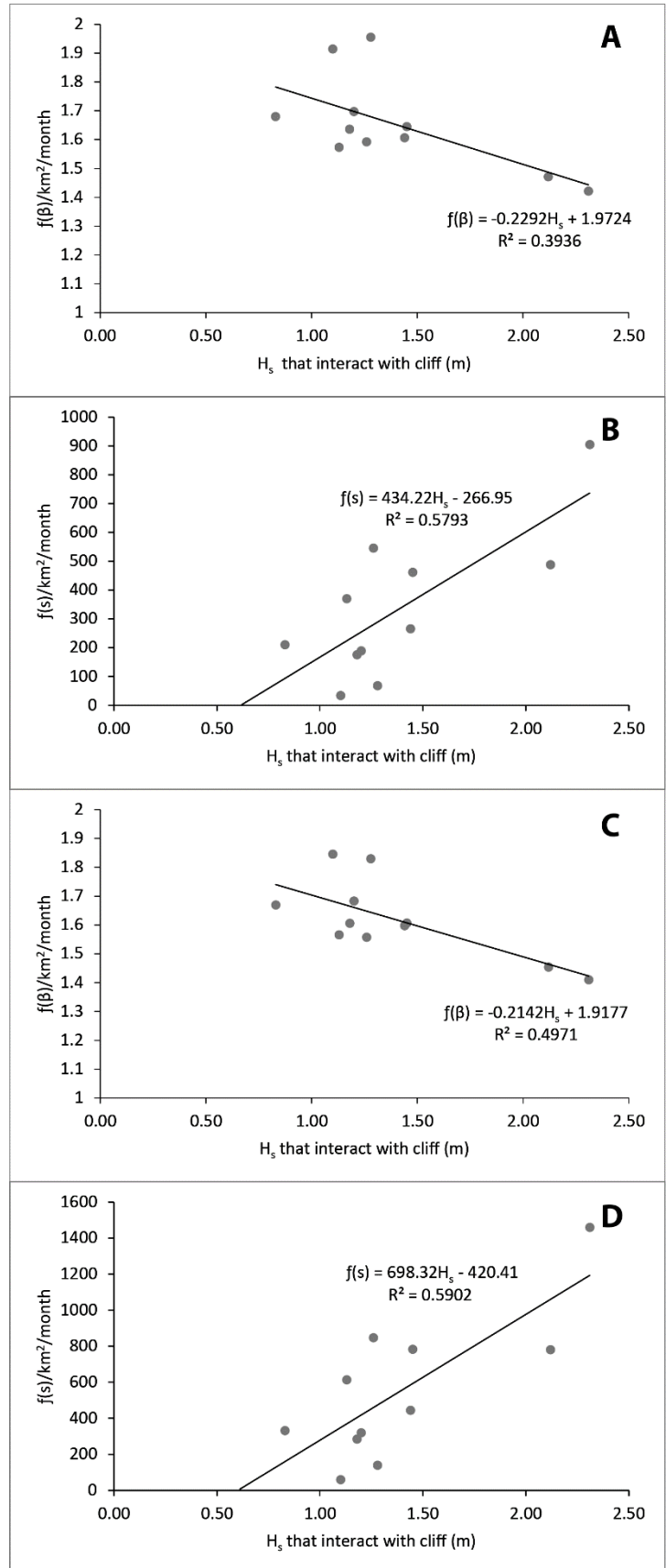


Figure 59: Normalised power law estimation parameters β and s vs. H_s (A) β vs. H_s for entire study area, (B) s vs. H_s for entire study area, (C) β vs. H_s for the unprotected section of cliff and (D) s vs. H_s for the unprotected section of cliff (black lines indicate best fit models).

and pressure obtained from the Hadley Centre Met Office were used to force the wave and surge models (Brown et al., 2012). The regional model was divided into approximate 12 km grid cells, with the nearest to the study site selected for data extraction. A detailed explanation of the wave model and data generation is provided by (Brown et al., 2012). The 6-hour time series dataset was grouped by month and averaged over 20 years to obtain each decade (e.g. 2010-2029 generates the decade 2020) as is the case with all UKCP09 environmental and atmospheric projections. Probability plots were obtained for each month in each decade between January 2020 and December 2089 (e.g. Figure 60) and a relationship between probability and H_s was found for each month. Random number generation between 0 and 1 could then be used to obtain a H_s value which would calculate β and s using the equations presented in Figure 59. To account for SLR a time of exposure method was utilised, the percentage of the tidal cycle that interacts with the base of cliff was recorded. Under present conditions 28.58% of the tidal cycle is at or above the minimum cliff height. Using the relative sea level (RSL) rise data presented by the UKCP09 (Lowe et al., 2009), which was downloaded for the study site from the UKCP09 user interface (UKCP, 2009) under the medium emission scenario the 50th percentile (most likely scenario) was extracted for each year. This increase in sea level was added to the observed data

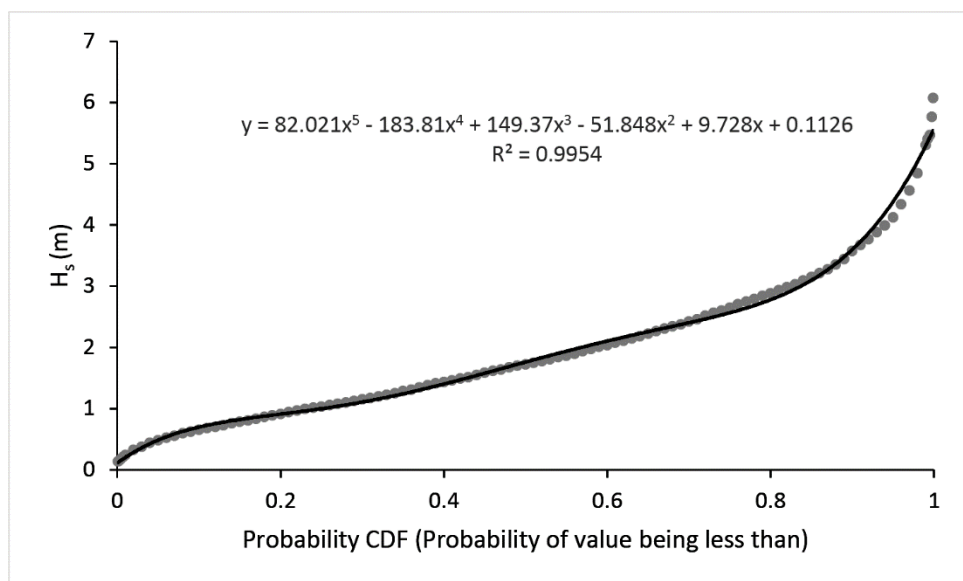


Figure 60: Example of H_s vs. cumulative distribution probability (CDF).

and reflected as a percentage of the tidal cycle which interacted with the cliff. From the current observations to 2089 there is a predicted increase from 28.58% to 33.85%. To reflect this in the model the total volume (V_T) calculated from Equation 8 under current conditions whereby 28.58% of the tidal cycle interacts with the cliff was given a scaling factor of 1. The yearly increase in sea level was then given a scaling factor relative to this base level. Therefore by 2089 when there is a predicted increase of 5.27% in the percentage of the tidal cycle interacting with the cliff, the scaling factor applied to V_T for that year was 1.0527.

For the $V_{R\max}$ values a cumulative probability plot was generated (Figure 61) from the inventory so that a random number between 0 and 1 could generate a max failure volume to be used in Equation 8. As no single model accurately expressed the relationship between cumulative probability and max failure two logarithmic relationships were selected (intersect when cumulative probability = 0.8216159).

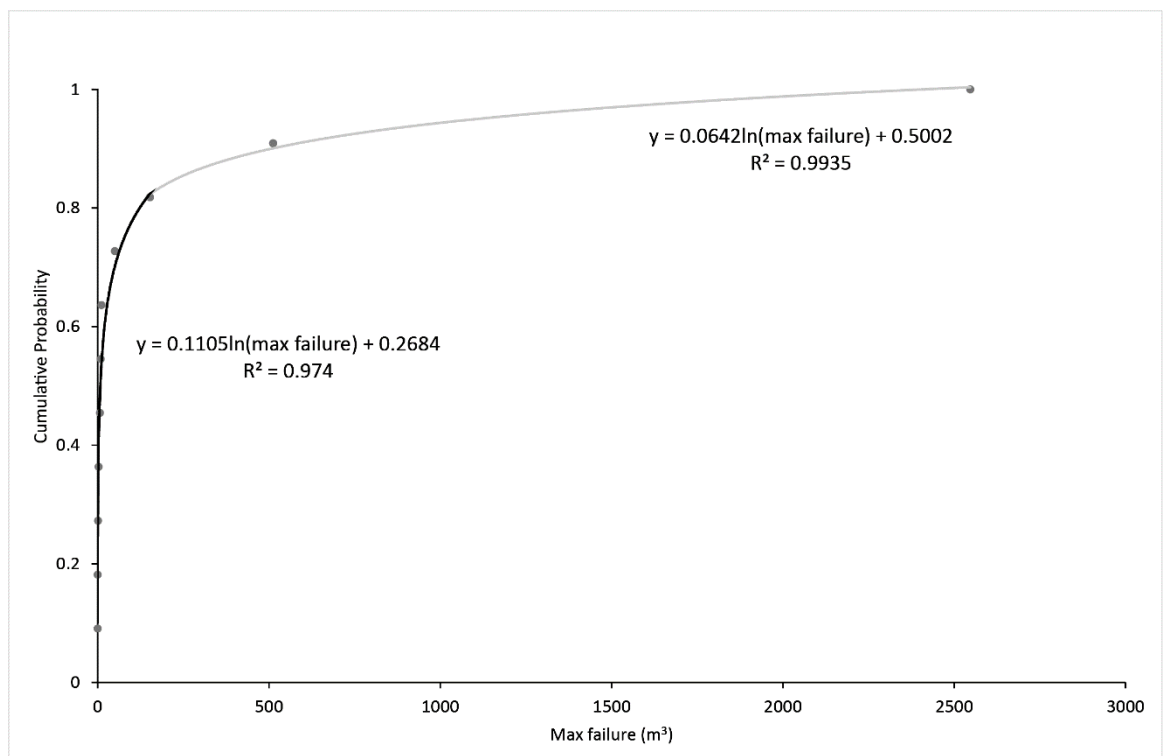


Figure 61: Cumulative probability plot for max failure (black and grey lines indicate best fit models).

Using the numerical relationships presented and the random number generation which drives the model a Monte Carlo simulation model was run based on Equation 8 (Barlow et al., 2012). To determine the most likely erosion scenario, 10,000 iterations of the model were run from

2020-2089 (70 years). Comparisons between the model outputs and historical recession rates generated from orthorectified aerial imagery from 1957, 1973, 1991 and 2013 for the study area were undertaken to assess model reliability. The V_T for 2020-2089 under current conditions, maintained for the entire temporal period, and future conditions (UKCP09 medium emission scenario) as discussed were then used to calculate cliff top recession which enabled an assessment of the risk to the A259 coastal road for this time period.

5.2.3. Model validation

Model validation was undertaken by plotting the observed V_T against the modelled V_T (Figure 62). The R^2 value for the unprotected section was very strong at 0.9918 (Figure 62) and predicted 97% of the observed V_T . The model performs well with respect to the months with the largest failures and overestimates V_T when the total volumetric flux for a given month is less than approximately 10 m^3 as Barlow et al. (2012) found.

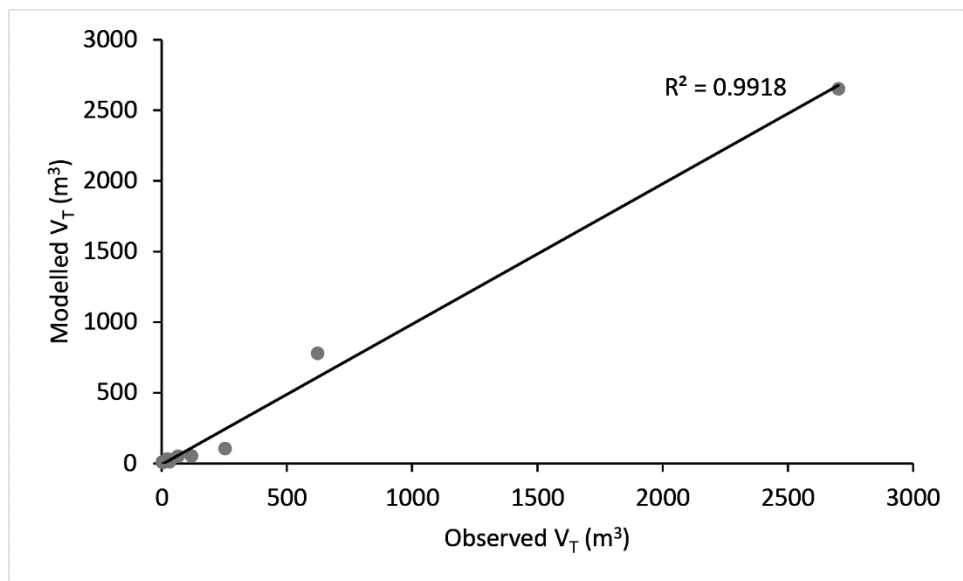


Figure 62: Modelled V_T vs observed V_T for the undefended (no beach) section of Telscombe cliffs.

The model predicts average annual recession under current conditions of 0.29 m yr^{-1} , the historical recession rate obtained from the orthorectified imagery between 1957 and 2013 for the same area was $0.31 \text{ m yr}^{-1} \pm 0.16 \text{ m}$ (2σ) which is similar to other published retreat rates for

the site in the scientific literature (Dornbusch et al., 2008). The similarity of these results provides confidence that the model will accurately predict future change.

5.2.4. Erosion modelling results

Mass movements were recorded over seven orders of magnitude, the largest event in the inventory involved the entire cliff face at the highest point which provides confidence that the data collected covers the entire range of failure magnitudes that are possible at the site. The 12 month inventory is comprised of 10,085 mass movements with a total volumetric flux of 3,889.35 m³. The surface area for the entire study area of Telscombe cliffs was 23,597.45 m², this was subdivided into the unprotected section and the naturally protected beach section with surface areas of 13,890.46 m² and 9,706.99 m² respectively. Although accounting for approximately 59% of the study area, the unprotected section had a total volumetric flux of 3,872.62 m³, representing 99.57% of the entire study area total. The monthly inventories are listed in Table 17 and comparisons made between the total volumes (V_T) for the unprotected (no beach) and naturally protected (beach) sub-sections. The largest failure was observed between February and March 2017 with an estimated volume of 2,546.8 m³, although this is likely to be an underestimate as the lower quarter of the cliff was obscured by debris which has remained through the summer months. Other notable failures occurred between November

Month	V_T Observed (m ³)	
	Unprotected (no beach)	Naturally protected (beach)
Aug – Sep 2016	252.6	2.8
Sep – Oct 2016	22.1	1.2
Oct – Nov 2016	119.2	0.8
Nov – Dec 2016	622.0	1.0
Dec – Jan 2017	64.4	0.5
Jan – Feb 2017	31.4	1.8
Feb – Mar 2017	2702.0	1.6
Mar – Apr 2017	20.1	0.7
Apr – May 2017	32.0	3.8
May – Jun 2017	4.6	1.8
Jun – Jul 2017	2.2	0.7

Table 17: Monthly observed V_T for the unprotected and naturally protected cliff line at Telscombe (correct to 1 d.p.).

and December 2016 and in the late summer of 2016 (August – September 2016) with estimated volumes of 512.2 m³ and 152.7 m³ respectively. Correlations can be drawn between these larger failures and the wave environment of the period between surveys. The average H_s for Aug-Sep, Nov-Dec and Feb-Mar were 1.26 m, 2.12 m and 2.31 m respectively. Furthermore the percentage of waves which interacted with the cliff that were classified as storm waves, H_s > 3.85 m (Bovington et al., 2015) were 6% (Aug-Sep), 9% (Nov-Dec) and 14% (Feb-Mar), the highest percentage in the remainder of the dataset was 3% between May and June. Waves, as the most likely mechanism to initiate failure (Mortimore et al., 2004a; Mitchell & Pope 2004; Barlow et al., 2012) due to erosion of the cliff toe and delivery of energy to the base of cliff where conjugate joint sets readily converge form a crucial parameter in predicting future erosion scenarios. These results indicate a minimal lag time between delivery of high energy waves and greater magnitude events, either through toe erosion or a significant increase in the stress environment propagating along conjugate joints (Sunamura, 2015).

5.2.5. Scaling parameters

As detailed by Barlow et al. (2012) the s value provides an indication on the level of activity within a given dataset whereas β describes the contribution of each magnitude of rockfall to the total volume. For example as β increases the smaller magnitude rockfalls contribute a greater amount to the total volume than the larger magnitude failures. The normalised scaling parameters for the undefended section of cliff vary between 1.409 to 1.829 for β and from 59.36 to 1459.50 for s . The range in β values is consistent with those presented in other scientific research (Van Den Eeckhaut et al., 2007; Brunetti et al., 2009; Barlow et al., 2012). The smaller β and larger s values are generally found in the winter months (winter ave. β =1.537, ave. s =895.51, summer ave. β =1.744, ave. s =348.38) when an increase in erosion would be expected due to the frequency of storms, with the exception of the August to September record (β =1.557, s =846.45). With regards to the maximum failure volume (V_{max}), this is primarily controlled by the slope morphology (Martin et al., 2002). This is evidenced by the wedge failures at the site

(Mortimore et al., 2004a; 2004b; Barlow et al., 2017) which constrain the magnitude of the observed larger failures in the inventory presented. By finding statistically significant relationships between the scaling parameters (β & s) and H_s , the power law model can be constrained to provide a useful predictive capability for future coastal management which is presented in the following section.

5.2.6. Erosion scenarios – probabilistic recession model

To investigate the implications of future erosion at Telscombe a Monte Carlo simulation was developed. This enabled a comparison of current versus future marine conditions, under the medium emissions scenario for the period 2020-2089, to be undertaken. However the model is based on a 12 month inventory which may or may not be indicative of cliff behaviour over greater temporal scales. The simulation was generated using Equation 8 and was driven through the generation of random numbers and was subject to 10,000 iterations. The scaling parameters were controlled through the derived relationships with H_s (Figures 59C & 59D) and the max failure volume calculated using the cumulative probability relationships found from the inventory (Figure 61). An example simulation is illustrated in Figure 63 (black line indicates

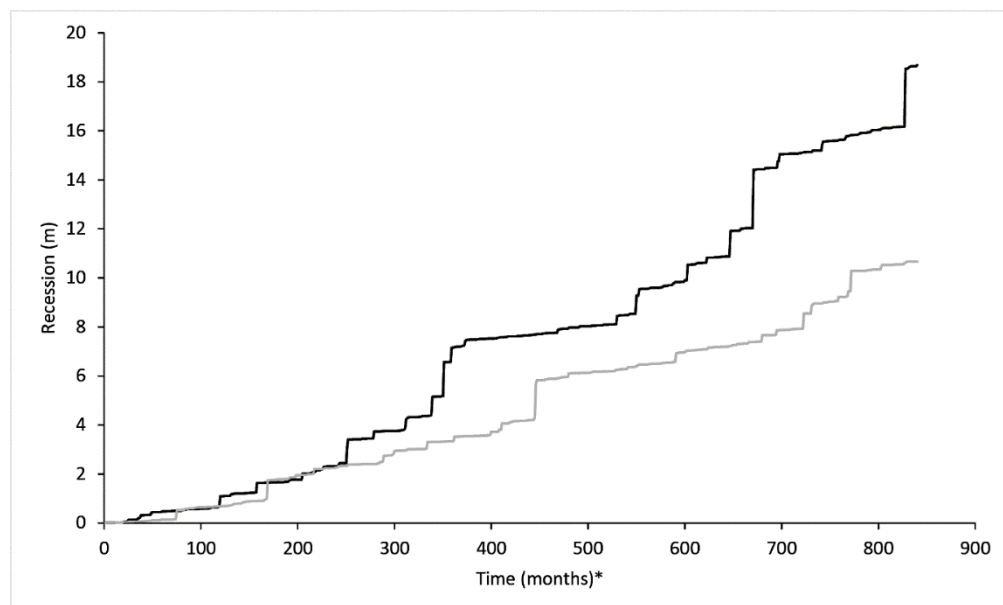


Figure 63: Example of a simulated erosion model for Telscombe run for 840 months (70 years) between 2020 and 2089 (black line indicates future conditions (UKCP09 medium emission scenario, grey line indicates current conditions, *- time in months from January 2020).

future conditions under medium emissions scenario and grey line current conditions maintained between 2020 and 2089). The sporadic nature of cliff failure is evidenced in both plots through the noticeable large magnitude events which occur throughout the 70 year period.

The results of the Monte Carlo simulation are provided in Figure 64 and Table 18. The mean total recession increases by 1.31 m (approx.+6%) over the 70 year period between the future and current conditions (Table 18), highlighting the impact of future sea level rise and an increase in significant wave height. The results of the Monte Carlo simulation were normally distributed with a strong positive skew due to the influence of extreme events. In order to apply parametric statistics, the skew was eliminated using a \log_{10} transformation as shown in Figure 64. The maximum recession distances predicted by the model were 121.97 m and 143.56 m under current and future conditions (UKCP09 medium emission scenario) respectively. The reason for these extremes values are twofold, firstly due to the high magnitude failure (2,546.8 m³) observed in the February to March 2017, this magnitude of failure can be generated in any month of the simulation due to the cumulative probability relationship (Figure 61) which controls the maximum failure volume from randomly generated numbers. This in combination

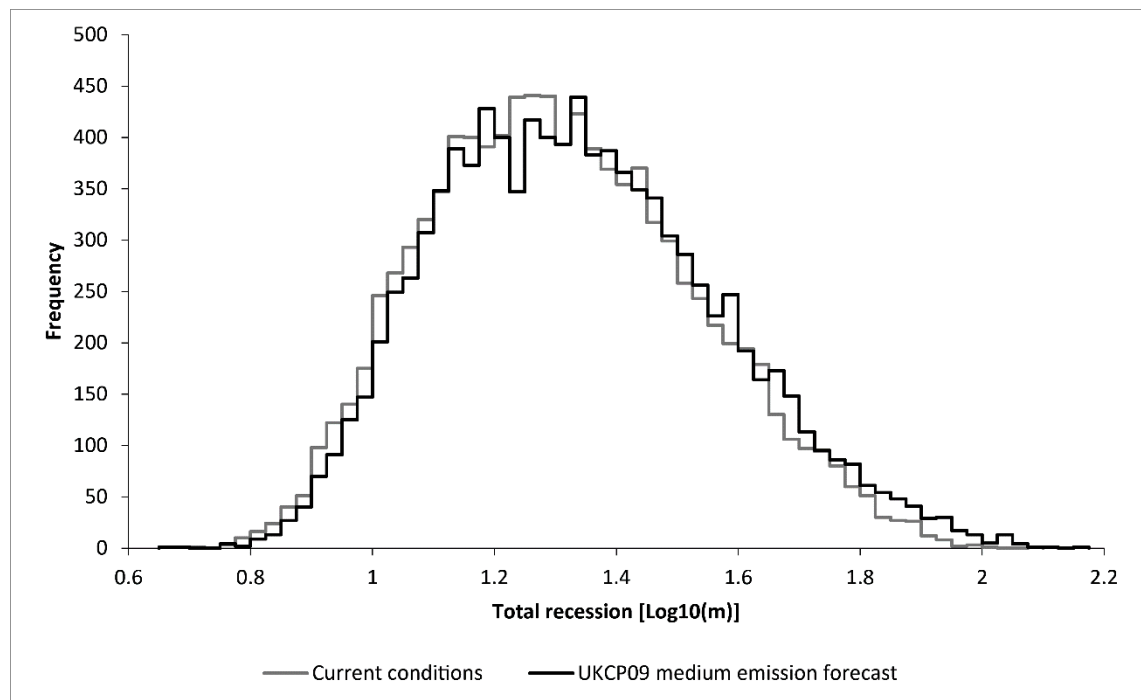


Figure 64: Monte Carlo simulation histogram of Log10 transformation of total recession between 2020 and 2089.

with future significant wave heights that control the scaling parameters, which are greater than those observed during the data collection period enable the model to predict a monthly V_T several orders of magnitude greater than observed in the inventory during the 840 month simulation. However it should be noted that for this extreme case the frequency of occurrence was reported as 1/10,000, as the model was run over a 70 year period the chance of this extreme event occurring is one in 700,000 years. This corresponds to over three standard deviations from the mean under current and future conditions, reaffirming the statistical unlikelihood of occurrence.

	Recession - current conditions			Recession - future conditions		
	Log10*	Total** (m)	Annual** (m yr ⁻¹)	Log10*	Total** (m)	Annual** (m yr ⁻¹)
Mean	1.311	20.45	0.29	1.338	21.76	0.31
Standard deviation	0.219	-	-	0.229	-	-
Maximum	2.086	121.97	1.74	2.157	143.56	2.05
Minimum	0.714	5.18	0.07	0.659	4.56	0.07

Table 18: Results of Monte Carlo simulation (*correct to 3d.p. and **correct to 2d.p.)

Figure 65 illustrates the mean and 95.5% confidence interval (2σ) for the recession under current and future conditions from the 2013 cliffline (the most recent aerial imagery available) to assess the risk to the A259 coastal road. The distance between the cliff edge (Figure 65) and the A259 ranges between 42.07 m to 52.75 m with an average of 46.62 m. Under the most likely erosion scenario (mean in Table 18) approximately 48.6% and 51.7% of the area between the cliff line and minimum distance to the road could be lost by 2089 for current and future conditions respectively. Under both modelled scenarios the 95.5% certainty limit breaches the A259 coastal road and therefore highlights the potential risk to infrastructure if recession exceeds the modelled average. To determine the probability that the road would be breached by future recession decadal Monte Carlo simulations were run. The minimum distance between the current cliff edge and road was located within each model and the probability calculated using the standard score (z-score) found by:

$$\text{standard score } (z) = \frac{X - \mu}{\sigma} \quad (9)$$

where X is the minimum distance between the cliff edge and road, μ is the mean recession distance calculated for each decade. Figure 66 presents the results of this analysis. Best fit

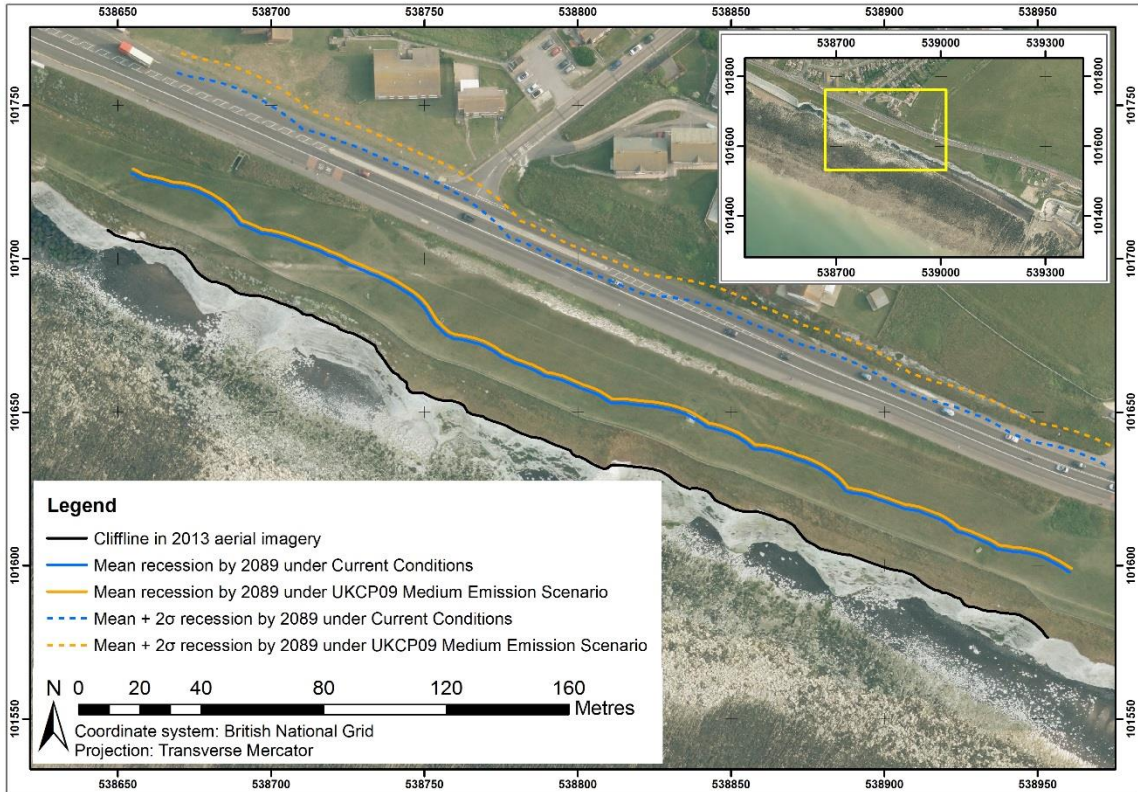


Figure 65: Model predictions of Telscombe cliffline position by 2089.

polynomials were applied to the data with strong R^2 values of 0.9989 and 0.9981 under current conditions and future conditions (UKCP09 medium emission scenario) respectively. The probability is relatively similar over the first three decades from 2020-2050 whether under current or future (UKCP09 medium emission scenario) conditions. The probability that the A259 is breached in the unprotected section of cliff line at Telscombe by 2050 is relatively low at 0.0073 and 0.0129 under current and future (UKCP09 medium emission scenario) conditions respectively. This increases to a substantial risk of 0.0778 and 0.1056 by 2090 under current and future (UKCP09 medium emission scenario) conditions respectively. The impact of future H_s (UKCP09 medium emission scenario) combined with SLR increases the probability by 0.0278

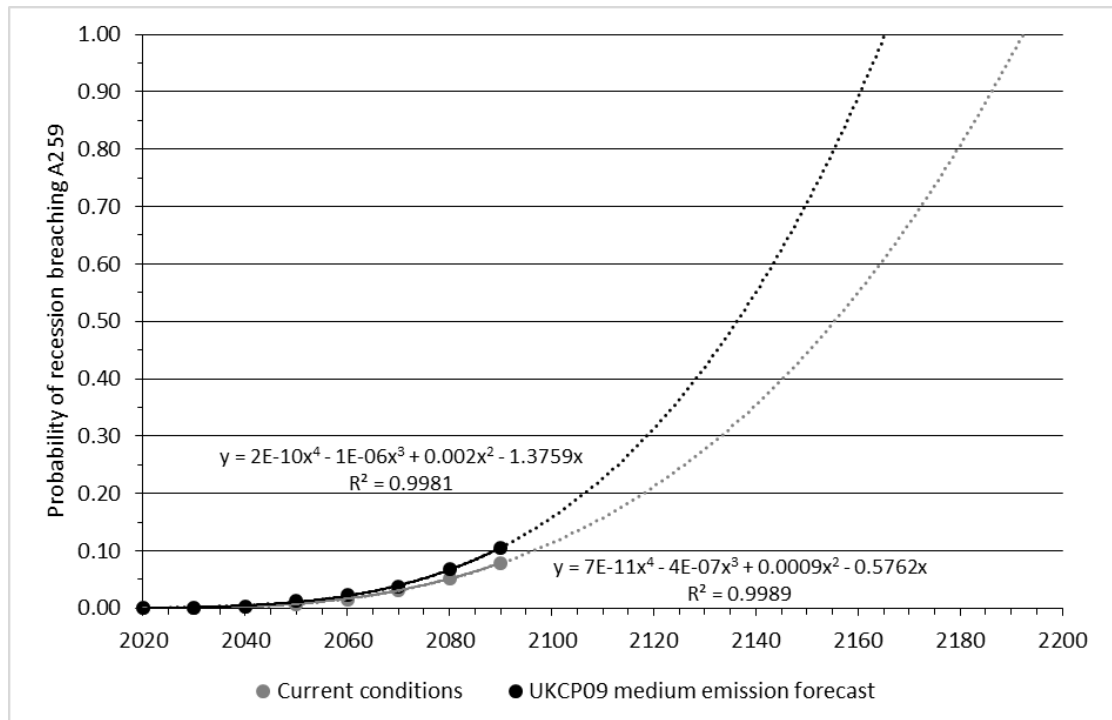


Figure 66: Decadal probability of recession breaching the A259 along the unprotected section of cliff line at Telscombe (dashed lines represent extrapolation beyond model predictions).

of the A259 being breached by 2090. Alternatively the risk to the road by 2090 under current conditions is almost equal to that of the risk by 2083 under future conditions (UKCP09 medium emission scenario). By extrapolating the observed trend further through time cliff recession would breach the A259 in 2165, when probability that recession reaches the road is equal to 1, assuming the UKCP09 medium emission scenario holds for this duration. This scenario is reached approximately 27 years earlier due to influences of a changing climate.

The results from this analysis indicate that coastal management decisions may need to be taken to preserve the coastal road in its current position. As evidenced with neighbouring sections of cliff line when defences have been installed the annual recession rate has decreased by an order of magnitude. The model assumes the current unprotected state of the cliff remains throughout for the modelled 70 year period from 2020-2089. As recession continues system feedbacks may alter the cliff environment. For example beach growth, which is a negative feedback to cliff erosion where recession results in delivery of flint from the cliff to the beach. Alternatively accelerated recession within the undefended section could create an embayment and lead to

the formation of a pocket beach. The effectiveness of a beach at the cliff toe is evident from the naturally protected section with a significant reduction in erosion (Table 18).

This model represents the first process driven probabilistic model of sea cliff recession developed through observations of rockfalls and marine conditions. The outputs from this model provide decision makers, in this case the local councils with a timescale and associated probability to assess the risk to the main coastal road in Brighton the A259. This enables appropriate time for decisions and any subsequent planning and/or installation of cliff toe protection measures to be completed.

5.3. Deterministic modelling of wedge failures (limit equilibrium analysis)

This section presents the results of the limit equilibrium analysis on potential wedge failures within the protected section of cliff line from Brighton Marina to Saltdean, the location of the observed joints are illustrated in Figure 67. A total of 114 joints were measured with 108 forming 54 conjugate joint sets (e.g. Figure 68). The joints observed in the cliff at Brighton Marina are weathered to a greater extent than those further east towards Saltdean which are much clearer. The potential wedge failures within Brighton Marina are, on average, of much smaller magnitude (Figure 69) ranging from 0.252 m³ to 21.221 m³ with an average volume of 3.871 m³ in comparison to the dataset to the east which range from 0.13 m³ to 194.704 m³ with an average of 30.083 m³. The largest of these potential wedge failures has been stabilised by Brighton and Hove City Council through rock bolting (Royal Haskoning, 2005).

5.3.1. Factor of Safety (FoS) outputs

The factor of safety for each identified potential wedge failure was calculated based on the cohesion of the back analysis of wedge failures and the peak cohesion as reported by Barton (1974). As all of the observed joint sets were stable at the time of measurement and no subsequent failure (to May 2017) had occurred along these joint surfaces the FoS values should

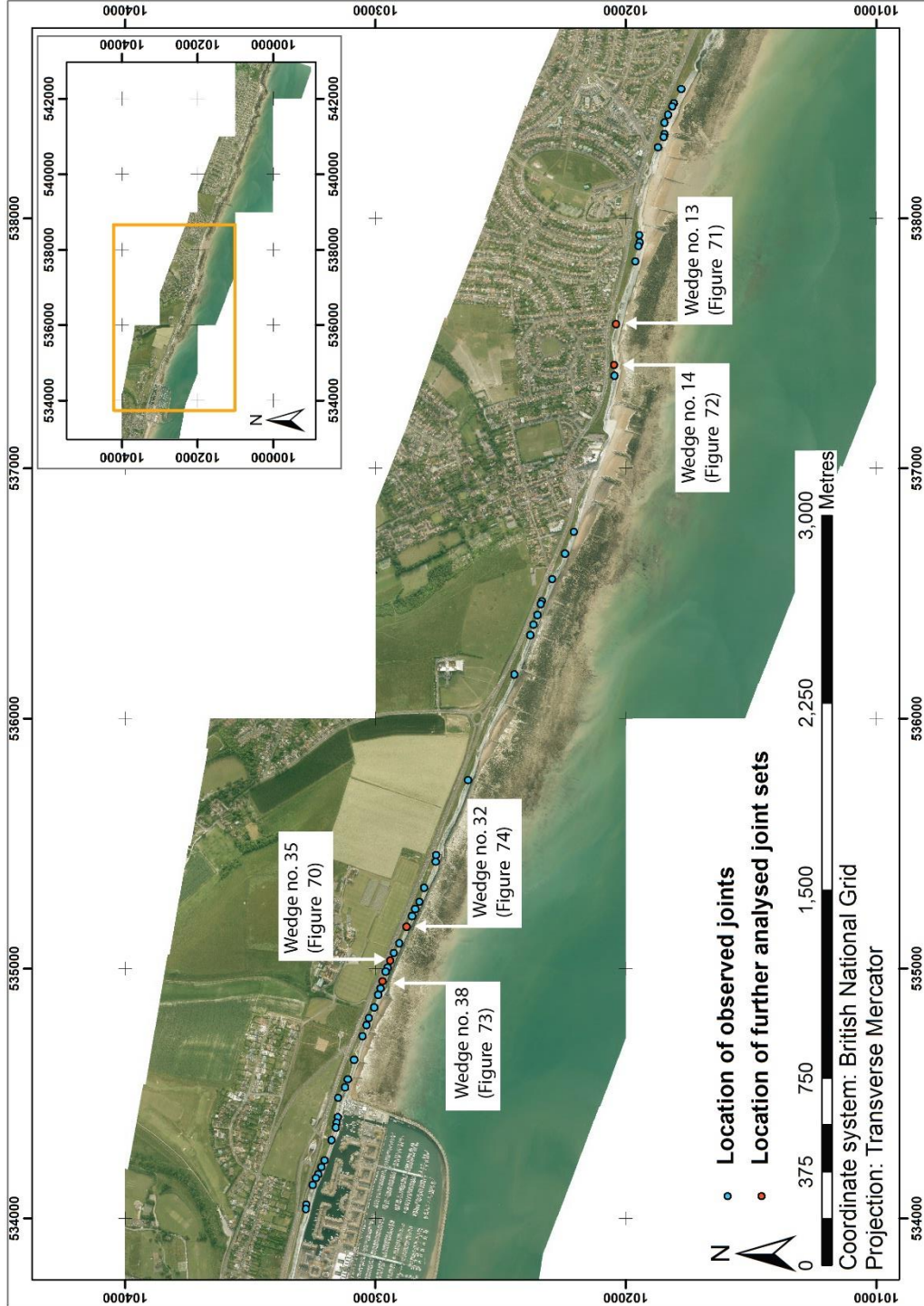


Figure 67: Location of observed conjugate joint sets in the defended section of cliff line from Brighton Marina to Saltdean (2013 imagery downloaded from the CCO).



Figure 68: Example of conjugate joint set in protected Newhaven Chalk cliffs between Brighton Marina and Saltdean.

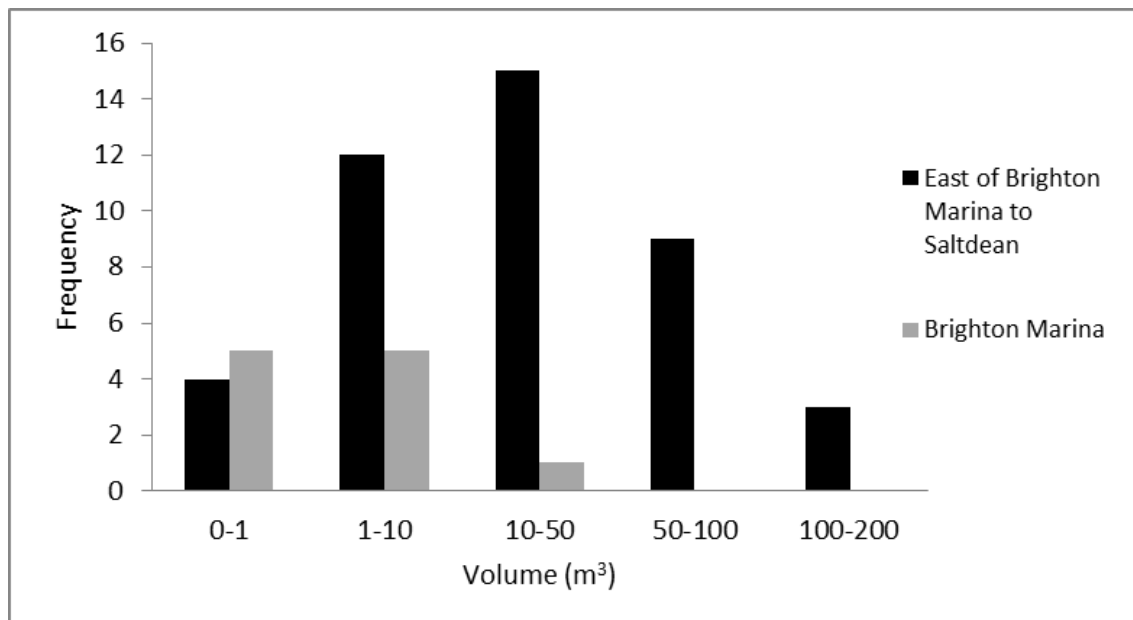


Figure 69: Frequency of different volumes for potential wedge failures generated from observed conjugate joint sets between Brighton Marina and Saltdean.

reflect the current stable nature of these wedges. By using the lowest cohesion value of 9.45 kPa 'wedge 14' reports a FoS of 0.967 with an estimated volume of 3.809 m³. This value was discounted as a FoS below 1.0 is unrealistic and signifies that the slope is unstable and failure is likely or should already have occurred. The cohesion value for this wedge joint set is therefore greater than the minimum cohesion value of 9.45 kPa. A similar outcome was found for 'wedge 65' however this reflects the wedge of greatest volume which as mentioned has been stabilised. All other conjugate joint sets were stable although 57.4% (31/54) recorded a FoS between 1.0 and 2.0. This result indicates that either, many of the wedge failures are nearing instability and are likely to fail in the future or that the cohesion value for many of the identified wedges is greater than this minimum value. The latter of these explanations is more likely due to the low frequency of observed failures, six rockfalls between 1999 and 2012 ranging from estimated volumes of 2 m³ to 20 m³ (Brighton & Hove City Council - BHCC, 2012), within the defended section of cliff line. No modelled wedge failures were below the critical FoS when the cohesion value was increased to 10.24 kPa (the second found through back analysis of observed wedge failures in Telscombe) and there was a reduction in the FoS between 1.0 and 2.0 to 44.4% (24/54). As expected due to the relationship between cohesion and shear strength in the Mohr-Coulomb equation, this decreased further to 1.9% (1/54) when cohesion was increased to 27.25 kPa. This result, based on observed rockfalls (Brighton & Hove City Council - BHCC, 2012) is more likely to be representative of the true state of these modelled wedge failures. As the back analysis dataset is limited to the few cohesion values presented the FoS calculated through the wedge analyses comes with an apparent caveat. Future wedge failures that can be recorded will provide greater confidence to the cohesion values used in these analyses and thus provide greater confidence in the FoS outputs.

5.3.2. Impact of potential failures

One of the advantages of using the deterministic limit-equilibrium modelling approach is the ability to scale the wedge to produce an estimation of the cliff top retreat following failure. The modelling does not include the influence of any tension crack so the estimations are made on the assumption that the average joint dip directions from JS1 and JS2 intersect to form a 'textbook' wedge and so represents the worst-case cliff top recession scenario for failure along these averaged joint sets. To illustrate the workflow and impact of potential failures a series of the modelled wedges are presented to represent the greatest cliff top retreat (Figures 70 & 71), the lowest FoS (Figure 72) and the failures which occur closest to the A259 (Figures 73 & 74). These examples include the modelling of the wedge through the observed conjugate joint sets in Swedge (A – in Figures 70-74), an image with the identified conjugate joint set (B – in Figures 70-74) and the estimated cliff top retreat (C – in Figures 70-74).

The wedge modelled in Figure 70 near to Roedean School has the greatest cliff top retreat of 3.66 m, approximately a third of the distance between the cliff edge and the A259. Although relatively stable as expressed in the FoS value of 2.607 when cohesion was set to 27.25 kPa, failure would not threaten the A259 directly but would pose significant risk. Restrictions on traffic movement may have to be considered or stabilisation of the cliff face may be required following such failure. Figure 71 represents a wedge identified approximately 500m west of central Saltdean and has an estimated cliff top retreat of 3.16 m. This potential retreat is 14.8% of the distance between cliff edge and the A259 and although representing a significant distance poses no direct threat to the road. The FoS for this wedge, 2.613, suggests relative stability, with the higher cohesion value of 27.25 kPa. This in combination with significant vegetation in the lower to mid slope (Figure 71B & C) highlights stability within this cliff section over a number of years.

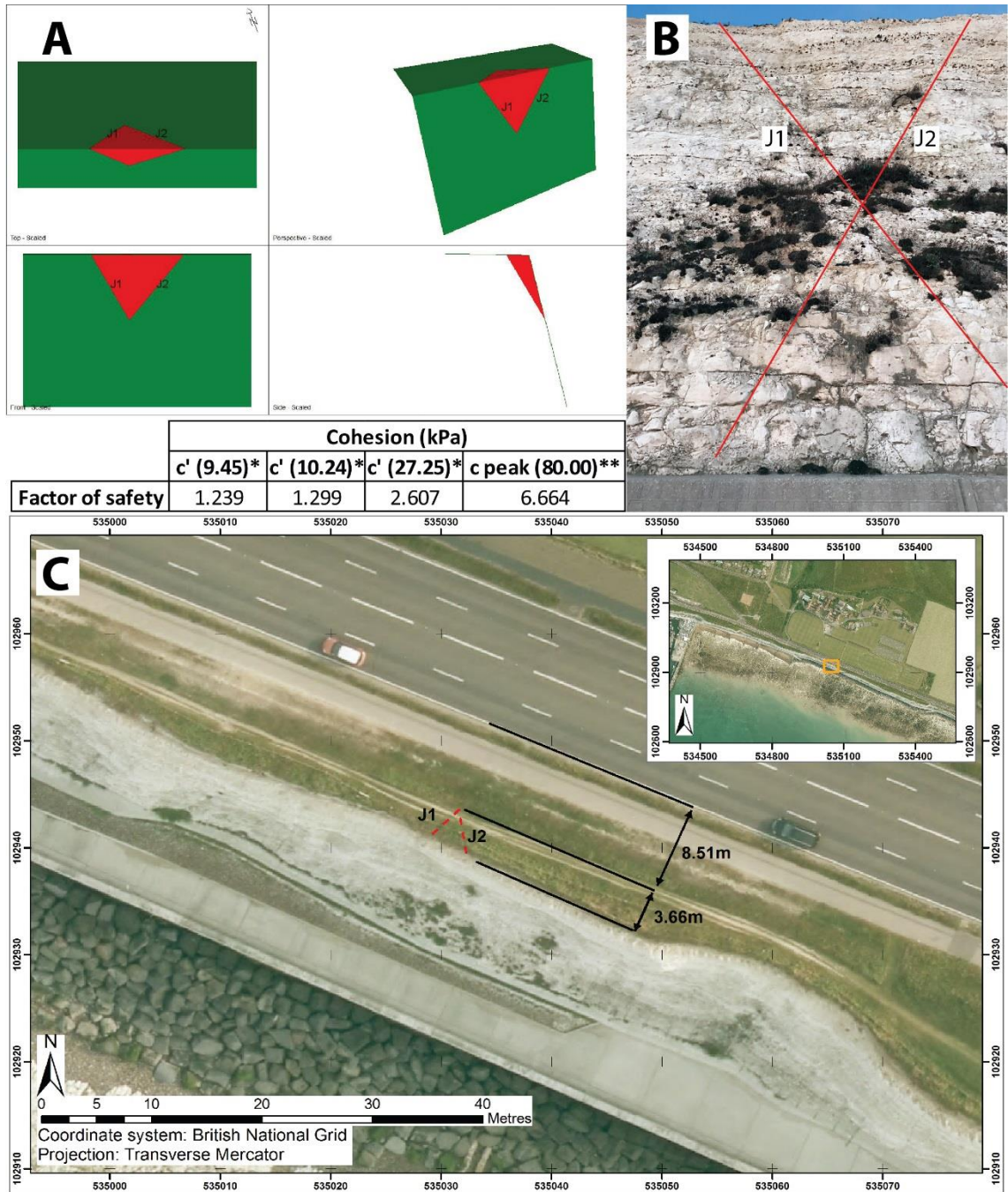


Figure 70: Wedge failure modelling in defended cliffs near Roedean School (A) limit-equilibrium modelling in Swedge, (B) field observation with conjugate set identified and (C) cliff top retreat and distance to road (2013 imagery in 'C' downloaded from the CCO) [*cohesion derived from back analysis **cohesion from Barton (1974)].

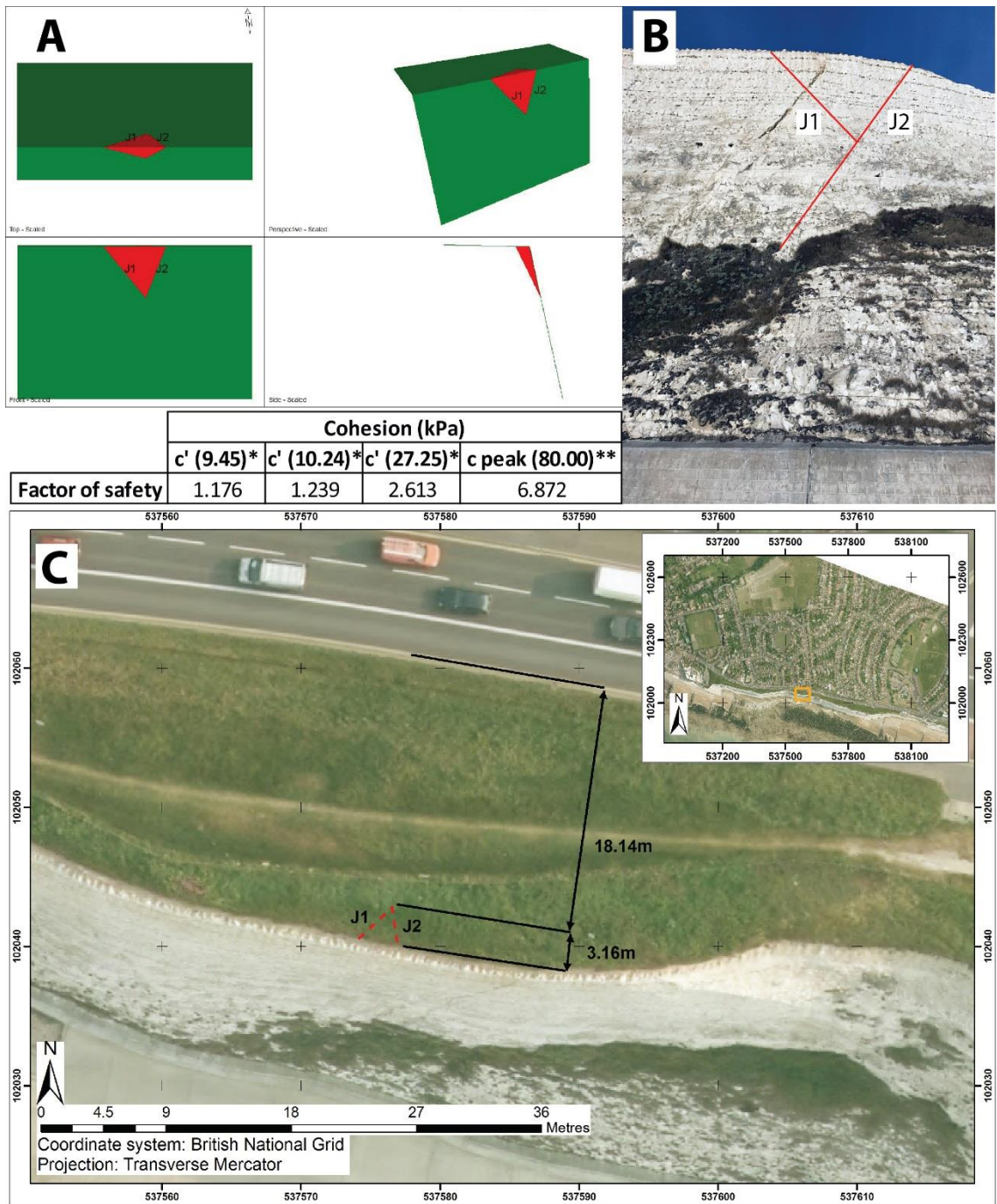


Figure 71: Wedge failure modelling in defended cliffs 500m west of Saltdean (A) limit-equilibrium modelling in Swedge, (B) field observation with conjugate set identified and (C) cliff top retreat and distance to road (2013 imagery in 'C' downloaded from the CCO) [*cohesion derived from back analysis **cohesion from Barton (1974)].

The wedge identified with the lowest FoS (Figure 72) was approximately 700m to the west of Saltdean and was mentioned previously in Section 5.3.1 as the FoS for the lowest cohesion value was less than 1.0. Even when modelled with the maximum cohesion value reported by Barton (1974) of 80 kPa the FoS is relatively low at 4.819 in comparison to the other wedges identified when modelled under the same conditions. The cliff recession associated with the failure of this wedge is calculated to be 0.46 m.

The two analysed wedge failures which were ranked second and third with respect to distance to road after the wedge presented in Figure 70 are presented in Figures 73 and 74. Both of these potential failures are located in the same 'pinch-point' section of cliff line near Roedean School. The distance between cliff edge and the A259 in Figure 56 is 13.02 m and the potential wedge failure exhibits a recession of 2.38 m approximately 18.3% of this distance. Failure of this wedge would require relocation of the cliff top fencing but would not breach the current desire line. The failure of the wedge in Figure 74 representing 14.6% of the distance from cliff edge to road would breach the current cliff top fencing and so would need to be replaced further landward. In both cases there is no imminent threat to the A259, in addition the FoS results indicate stability with the current cohesion values.

5.3.3. Sensitivity analysis

As reported by Park and West (2001) the difficulty in rock slope engineering surrounding the use of deterministic models is found in the inherent variability in both the orientation and strength of discontinuities. To overcome this issue and to increase confidence in the presented wedge failure analyses a sensitivity analysis was undertaken to determine the effect of cohesion, the material friction angle and the joint (discontinuity) dip direction. For the sensitivity analyses presented the aforementioned variables were varied from the minimum recorded value to the maximum recorded value in either the database or from the reviewed literature in the case of friction angle, whilst all other parameters remained constant. The wedge models were ordered

by the calculated FoS and the 25th, 50th and 75th percentile were used as the representative sample for the dataset. A summary of these identified wedges is presented in Table 19.

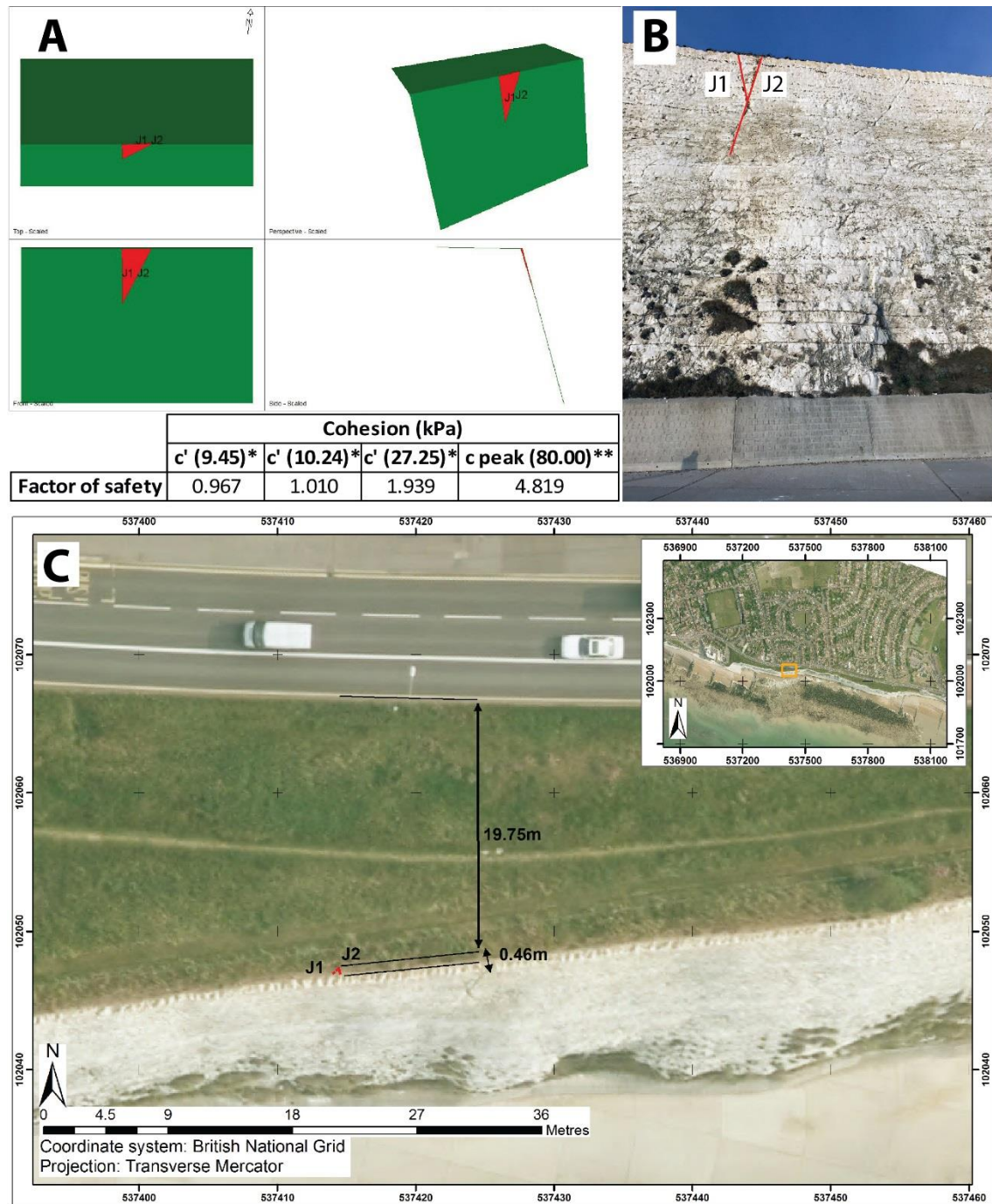


Figure 72: Wedge failure modelling in defended cliffs 700m west of Saltdean (A) limit-equilibrium modelling in Swedge, (B) field observation with conjugate set identified and (C) cliff top retreat and distance to road (2013 imagery in 'C' downloaded from the CCO) [*cohesion derived from back analysis **cohesion from Barton (1974)].

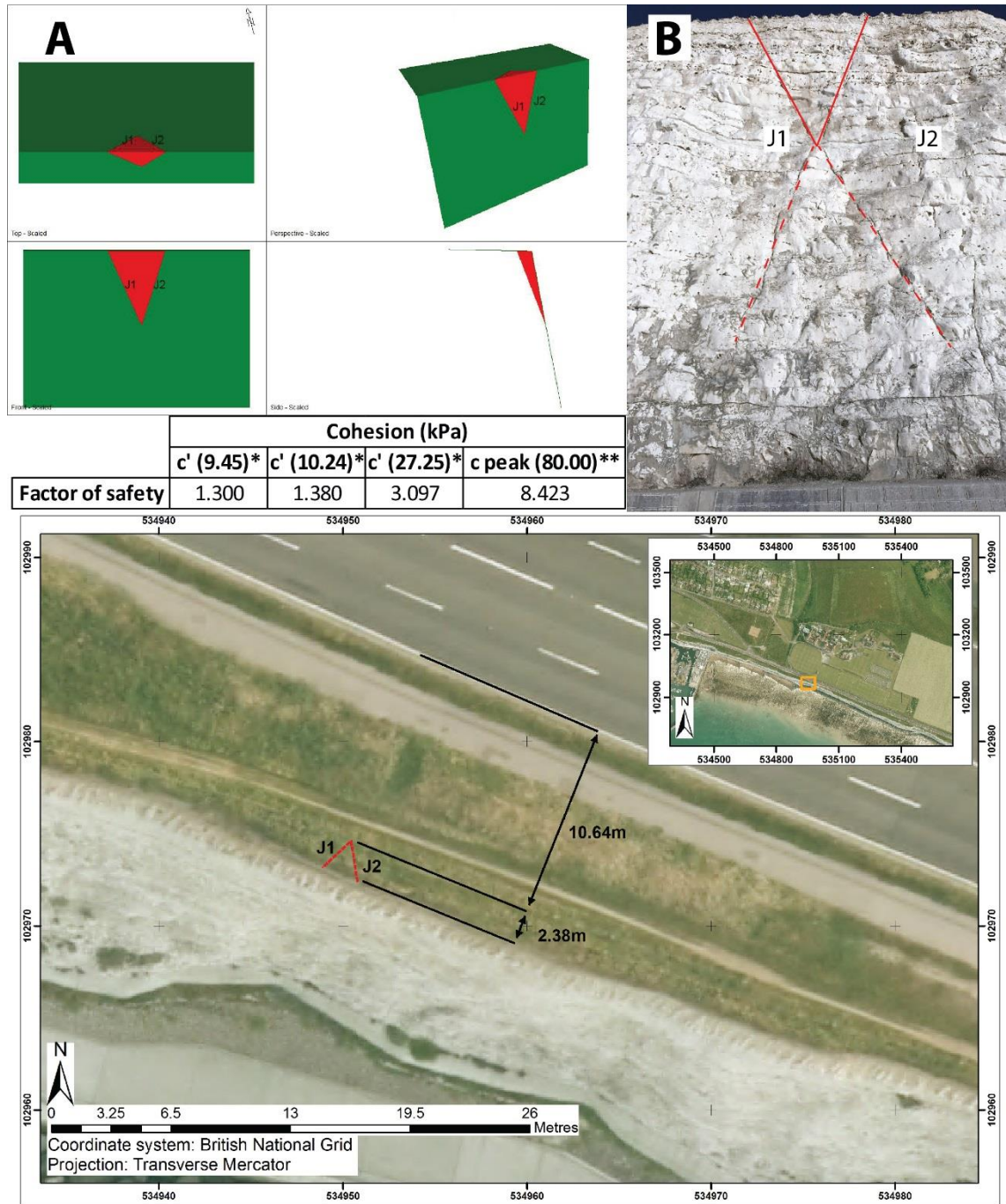


Figure 73: Wedge failure modelling near Roedean School representing the second closest distance from cliff edge to A259 (A) limit-equilibrium modelling in Swedge, (B) field observation with conjugate set identified and (C) cliff top retreat and distance to road (2013 imagery in 'C' downloaded from the CCO) [*cohesion derived from back analysis **cohesion from Barton (1974)].

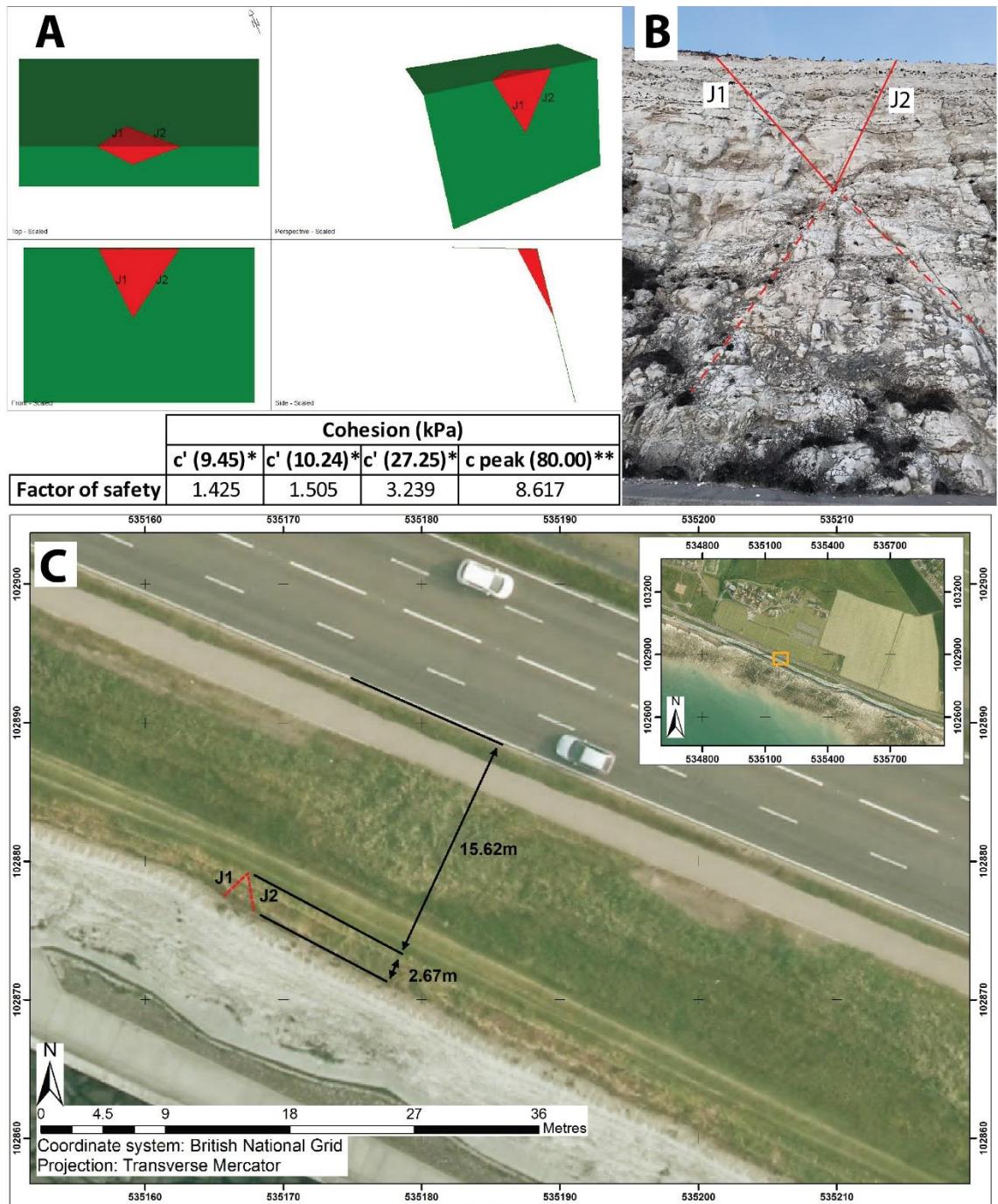


Figure 74: Wedge failure modelling near Roedean School representing the third closest distance from cliff edge to A259 (A) limit-equilibrium modelling in Swedge, (B) field observation with conjugate set identified and (C) cliff top retreat and distance to road (2013 imagery in 'C' downloaded from the CCO) [*cohesion derived from back analysis **cohesion from Barton (1974)].

Quartile	25	50	75
Wedge ID	36	39	20
Height (m)	24.58	24.22	26.95
Cliff face dip (°)	77	75	75
Cliff face dip direction (°)	202	196	203
Critical cohesion (kPa)	6.01	3.86	3.03
Volume (m ³)	44.175	14.041	8.276

Table 19: Summary of representative wedge analysis sample for sensitivity analysis.

The joint cohesion in the sensitivity analysis ranged from 0 kPa to 27.25 kPa the highest recorded value from the back analyses of wedge failures in Telscombe. Figure 75A illustrates the expected effect of an increase in cohesion leading to an increase in FoS, the greatest range in FoS is observed in the more stable slopes inferring a reduction in cohesion in the 75th percentile wedge would have much more of an effect on the FoS values. Conversely any reduction in cohesion on the 25th and 50th percentile modelled wedges could lead to imminent failure under the range of cohesion values presented. As all modelled wedges were set to critical (FoS = 1.0) Figure 75B shows FoS below this threshold.

The relationship in Figure 75B between friction angle applied to the joint surfaces and FoS find a subtle influence on the modelled wedges. The greatest FoS range was found on the 25th percentile of 0.118, this decreased to 0.115 and 0.092 for the 50th and 75th percentile wedges respectively. This result infers that the range of friction angles reported in the literature for friction angle of Newhaven Chalk only has a slight impact on the FoS for wedge failures in the defended cliff section.

Analysis was also undertaken to determine the impact of joint dip direction. As the average joint dip directions had been used in all modelled wedges, the sensitivity of this parameter was tested by exploring the full range of values in the joint sets identified. The opposing joint remained constant, using the average dip direction. Figures 76A, B and C illustrate the impact of varying the average joint dip direction for the 25th, 50th and 75th percentile modelled wedge respectively. The range for JS1 was 150.6°-191.4° and for JS2 214.5°-251.5°. To display both ranges on the same chart (Figures 76A, B & C) the x-axis is presented as a percent of the range of input values

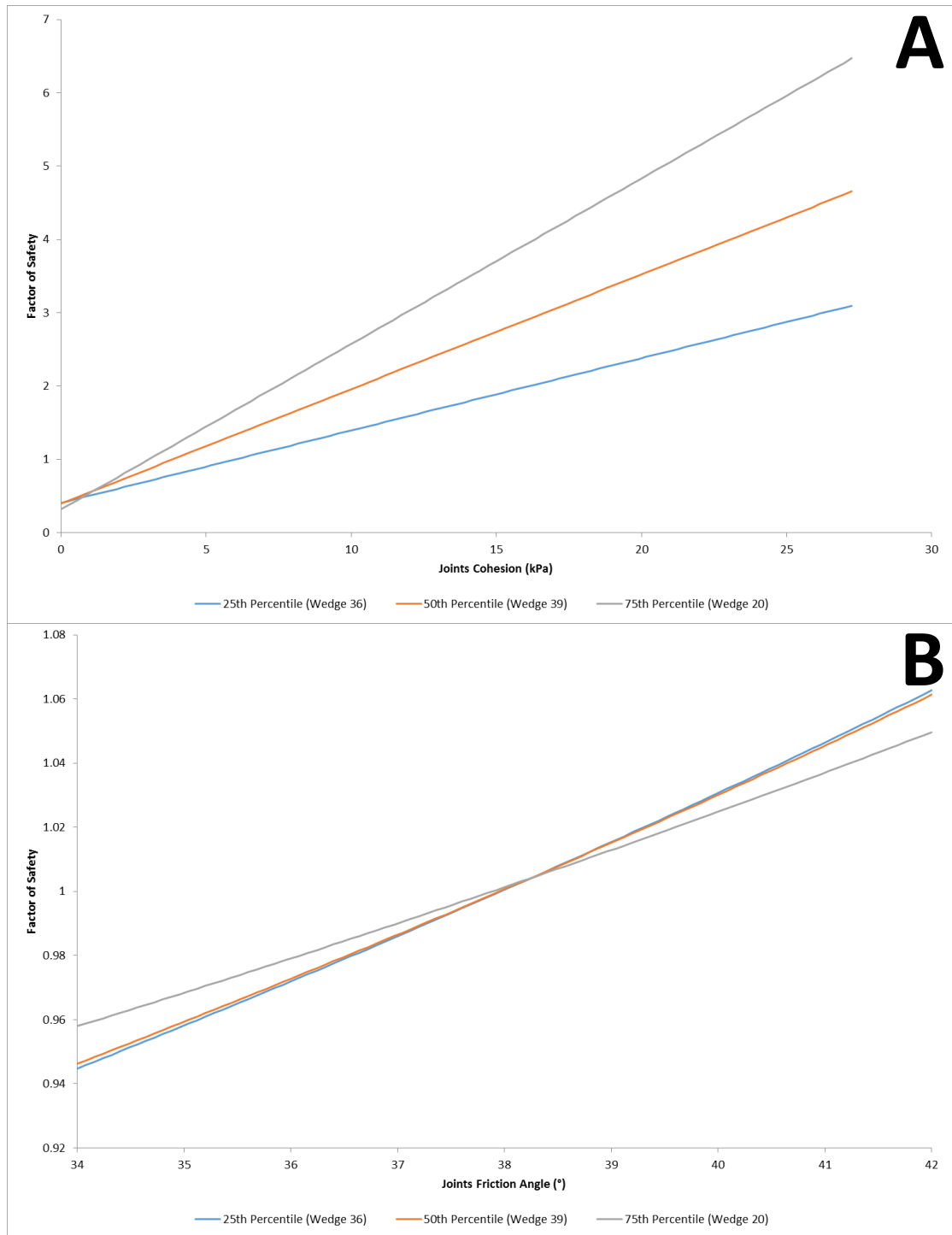


Figure 75: Sensitivity analysis of modelled wedge failures along defended cliff lines in Brighton using the 25th, 50th and 75th percentile of wedges with reference to FoS value, (A) joint cohesion varied from 0-27.25 kPa and (B) joint friction angle varied from 34°-42° [Note differing scales on y axis].

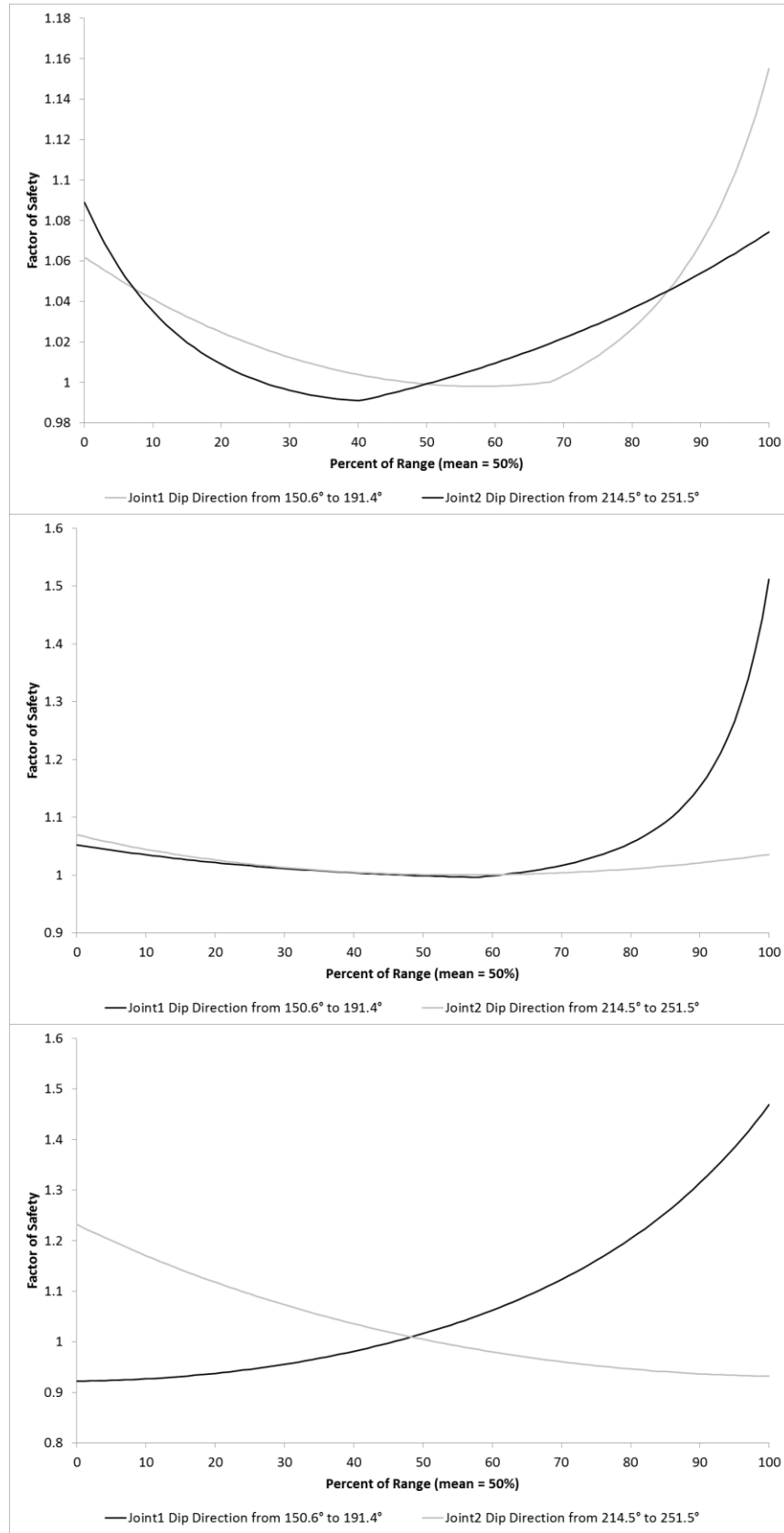


Figure 76: Sensitivity analysis of modelled wedge failures along the defended cliff line in Brighton showing the impact of the range of dip direction for JS1 and JS2 for (A) the 25th percentile, (B) the 50th percentile and (C) the 75th percentile [Note differing scales on y axis].

as is accustomed in the Swedge analysis for multi-variable sensitivity analysis. The impact of the variation in joint dip direction was greatest with respect to the FoS with JS1 across all wedges analysed in the sensitivity analysis (Table 20). The greatest variation was observed in the 75th percentile wedge with a range in FoS of 0.547 and 0.301 for JS1 and JS2 respectively.

Wedge percentile	Set	Max FoS*	Min FoS*	FoS range*
25	JS1	1.155	0.998	0.157
25	JS2	1.089	0.991	0.098
50	JS1	1.512	0.996	0.516
50	JS2	1.070	1.000	0.070
75	JS1	1.469	0.922	0.547
75	JS2	1.233	0.932	0.301

Table 20: Sensitivity analysis of dip direction for JS1 and JS2 versus FoS (*- correct to 3d.p.).

As expected, the relationships found between FoS and joint dip direction are not comparable between models (Figure 76) unlike with cohesion and friction angle. This is because joint dip direction is used directly to generate the wedge instead of determining the driving and resisting forces. By undertaking a sensitivity analysis on cohesion, friction angle and joint dip direction the relative importance of these parameters was demonstrated. Greater confidence in the modelled wedge results can be construed as the average values used from the literature for friction angle have a limited impact on the FoS. The critical cohesion values for all wedges modelled, excluding the two examples discussed earlier, are less than those found through the back analysis of wedge failures (Figure 75) inferring current stability across identified conjugate sets in the defended cliff line between Brighton Marina and Saltdean.

5.4. Probabilistic recession model for the protected section of cliff line between Brighton Marina and Saltdean

As the terrestrial photogrammetry for Brighton Marina, a site which represents the protected sections of cliff, was unable to detect any rock fall (>0.07 m in surface change) over the research period alternative methodological approaches are required to develop a probabilistic model to assess the risk to infrastructure. A variety of approaches to predict cliff recession have been presented, as summarised by Lee et al. (2001). These include simple extrapolation of historical

recession rates to those which account for impacts of future climate. Applications of probabilistic methods of cliff recession are presented by Lee et al. (2001) and implemented in national projects as reported by Moore et al. (2010b) such as the Risk Assessment of Coastal Erosion (RACE) (Halcrow, 2006). This section will develop the industry best practice method for the site between Brighton Marina and Telscombe to produce a probabilistic model of recession for this section. Comparisons can then be made between this method and the negative power law methodology presented earlier.

5.4.1. Observed recession rates and associated spatial probability

This alternative probabilistic modelling method utilised the recession rates calculated for the period between 1957 and 2013 from 10 m spaced transects as presented in Chapter 4. The cliff between Brighton Marina and Saltdean was subdivided into road units (Figure 77), which were

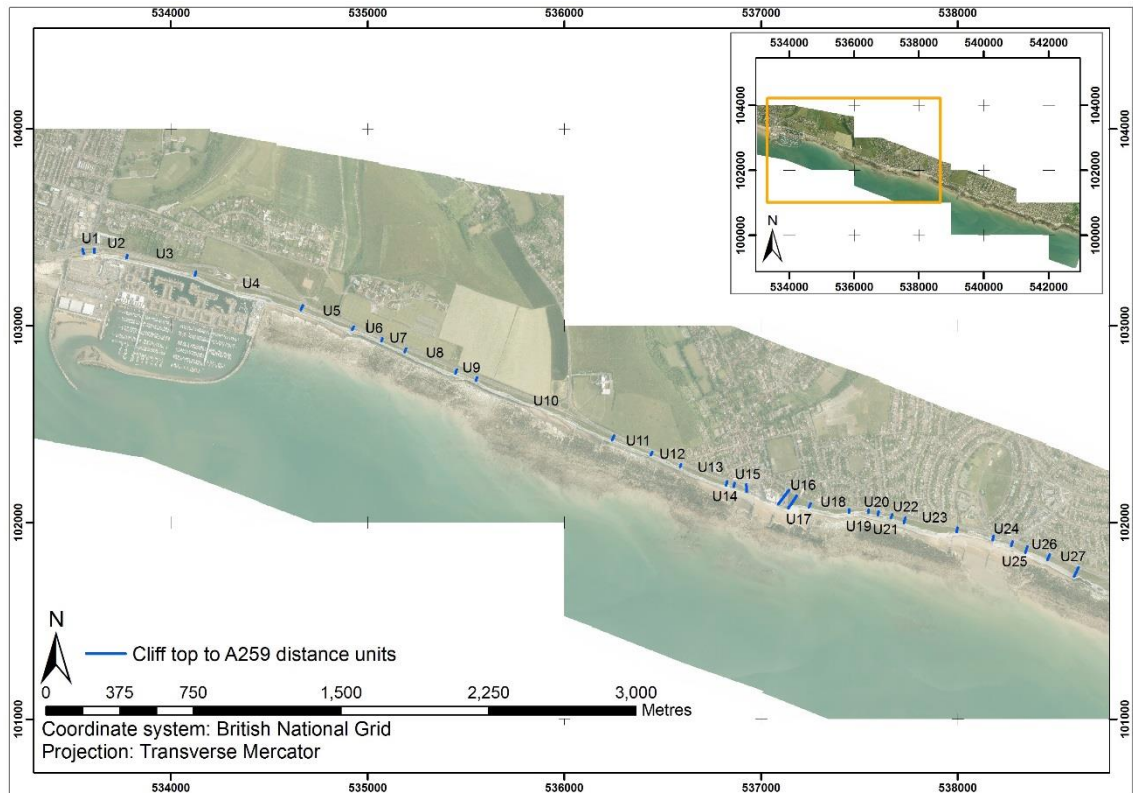


Figure 77: Brighton Marina to Saltdean road units, classified by distance from cliff edge to A259 (2013 imagery downloaded from the CCO).

classified based on distance between cliff edge and the seaward edge of the A259 road. To obtain a spatial probability for recession rates across the entire site, between Brighton Marina and Saltdean, the historical recession data from the 540 transects was averaged per road unit (Figure 77). This resulted in a range of annual retreat rates from 0.01 m yr^{-1} to 0.07 m yr^{-1} with the higher rates associated with the large failures in Brighton Marina in 2000/2001 as discussed in Chapter 4. The final stage of the spatial probability calculation was to divide the frequency of the average road unit retreat rate by the total number of road units. For example 15 of the road units recorded an average historical recession rate of 0.02 m yr^{-1} , this resulted in a spatial probability of 0.56 (15/27 units). For analysis of specific sites identified as 'pinch-point' units the probability for retreat rates was adjusted to reflect that unit. In the majority of cases in the defended cliff section there was very little variation in retreat rates measured within the specified road units.

5.4.2. Impact of potential wedge failures

The potential impact of the modelled wedge failures was assessed. To account for this mode of failure within units (Figure 77) where no observation, between 1999 and 2012 (Brighton & Hove City Council - BHCC, 2012), has been recorded but conjugate joint sets have been observed the following method was applied when assessing individual units identified as 'pinch-points'. To determine a recession rate and associated probability several datasets were assimilated. Firstly, the potential wedge failures include both a wedge width and cliff top retreat value so a spatial probability can be calculated of an observed wedge occurring within a given unit. For example, the cliff top width of a hypothesised wedge is 4 m and is observed in a unit 200 m wide, this accounts spatially for 0.02% of the unit and thus can be termed the spatial probability of that wedge occurring within the given unit. This is a similar calculation to how the retreat rate probability is calculated. The next stage requires a retreat rate to be assigned to the spatial probability, this is achieved by utilising the observed rockfall inventory maintained by Brighton

and Hove City Council (2012) which identified the location and volumes of previous failures in the defended cliff section. The observed failures (Brighton & Hove City Council - BHCC, 2012) were classified into four volumetric groups (Table 21) and the historical recession rate assigned to each magnitude of rockfall. These rates were then included in the probabilistic analysis for the unit under investigation with the aforementioned spatial probability.

Classified volume of failure (m³)	Assigned recession rate (m yr⁻¹)*
1 – 10	0.025
10 – 50	0.035
50 – 100	0.050
100 – 500	0.070

Table 21: Classified volume of failures observed in BHCC rockfall inventory assigned an annual recession rate (* determined by locating the failures and identifying the historical recession rates - presented in Chapter 4).

5.4.3. Impact of future climate

The impact of future climate is likely to impact annual temperatures as well as winter rainfall, wave direction and sea level rise (Moore et al., 2010b). For the cliffs between Brighton Marina and Saltdean which have been decoupled from marine erosion the key drivers which will influence recession are subaerial, thus rainfall and temperature are of greater significance to this model. The UKCP09 (Murphy et al., 2009) present the modelled changes in mean seasonal precipitation and temperature (Table 22). The average winter precipitation at 90% probability is predicted to increase by 52.7% and by 8.3% for the summer in approximately 60 years to 2080. In this same period mean winter temperatures are set to increase by 4.8°C and 6.6°C in the winter and summer respectively with 90% probability. It is important to note that no empirical relationship is found between these climate scenarios and cliff recession. Moore et al. (2010b) report that the impact of these projections cannot be reliably quantified in determining impact on coastal cliff recession. As a result judgement decisions can be made which represent the best available estimates of the impact of such future climatic conditions, these are based on site specific knowledge, an understanding of the system, and currently available but limited

	Emissions	Change at 10% probability	Change at 50% probability	Change at 90% probability
Mean winter precipitation change (%)	Low	4	18	40
	Medium	4	22	51
	High	7	30	67
	(Average)	5.0	23.3	52.7
Mean summer precipitation change (%)	Low	-39	-15	13
	Medium	-48	-23	7
	High	-57	-29	5
	(Average)	-48	-22.3	8.3
Mean winter temperature change (°C)	Low	2.0	2.6	4.0
	Medium	1.6	3.0	4.7
	High	2.0	3.7	5.7
	(Average)	1.9	3.1	4.8
Mean summer temperature change (°C)	Low	1.4	3.0	5.1
	Medium	2.0	3.9	6.5
	High	2.6	4.9	8.1
	(Average)	2.0	3.9	6.6

Table 22: UKCP09 winter and summer changes in precipitation and temperature for south-east England under different emission scenarios and varying probabilities (Murphy et al., 2009) [Note averages are calculated and not representative of any emission scenario].

empirical data (Lee, 2005; Moore et al., 2007; Moore et al., 2010b). A series of scaling or adjustment factors were determined which were used to increase or decrease the historical recession rates whilst applying a probability to each of these scenarios. As Moore et al. (2010) report the impact of future climate on 'low' sensitivity cliffs, which this research has deemed an appropriate classification for the defended cliffs in Brighton, is between 0% (minimum) and 20% (maximum) for an increase in cliff instability and recession. Therefore, no adjustment factor exceeded 1.2, as 1.0 represent current conditions. Table 23 presents the scaling factors and probabilities which were used in the probabilistic recession model. As there is a distinct lack of empirical data to base these values on this methodological approach presented to develop a probabilistic recession model of the cliffs in Brighton is through a sensitivity analysis due to a change in climatic conditions and does not represent an absolute condition.

Winter rainfall	Estimated probability	Scaling/adjustment factor	Temperature	Estimated probability	Scaling/adjustment factor
Increase	0.7	1.2	Increase	0.7	1.05
No change	0.2	1	No change	0.2	1
Decrease	0.1	0.9	Decrease	0.1	1.1

Table 23: Probability and scaling/adjustment factors for winter rainfall and temperature used in the probabilistic recession model for Brighton cliffs between Brighton Marina and Saltdean.

The probabilities were estimated by reviewing the UKCP09 projections which report that an increase in temperature and winter rainfall is the most likely scenario. The scaling factor for an increase in rainfall was set to increase but not exceed a 20% increase in recession, as retreat rates observed in Brighton Marina during the wettest winter on record led to significant cliff falls in the defended section (Chapter 4) so were assigned the greatest increase in cliff instability (up to 20%) as noted by Moore et al. (2010b). Likewise, the probabilities for an increase in temperature were estimated using the most likely scenarios reported by the UKCP09. The scaling adjustment for an increase in temperature was set to a maximum recession increase of 5%, as an increase in temperatures could lead to drying and fracturing of the chalk face and an increase in spalling rockfall. For context, entering this scaling factor into the sensitivity analysis for the dominant annual recession rate within the defended cliffs of 0.02 m y^{-1} and projecting this for 100 years leads to a total increase in recession of 0.1 m. A decrease in temperature was estimated to increase the rate of retreat by up to 10%, this is due to an increase in freeze thaw weathering which leads to an increase in fracturing and spalling of rock. Continued thermal monitoring as presented in Chapter 4 can be used in future research to provide confidence to this factor.

5.4.4. Projecting historical recession data using a probabilistic model

As the empirical adjustments are based on judgement decisions a probabilistic model was developed to show future recession between Brighton Marina and Saltdean where all adjustment factors were set to 1.0. Therefore the following models assume no change in climatic conditions over the projected temporal period. Figure 78 presents a probabilistic recession model for a 50 year projection between Brighton Marina and Saltdean. The minimum distance from cliff edge to the A259 is currently 8.77 m. The 50 year projection model records a probability of 96.3% (to 1d.p.) for a recession of 0.75 m which accounts for continued gradualistic spalling of rockfall or a more significant wedge failure in the order of $1\text{-}10 \text{ m}^3$. This

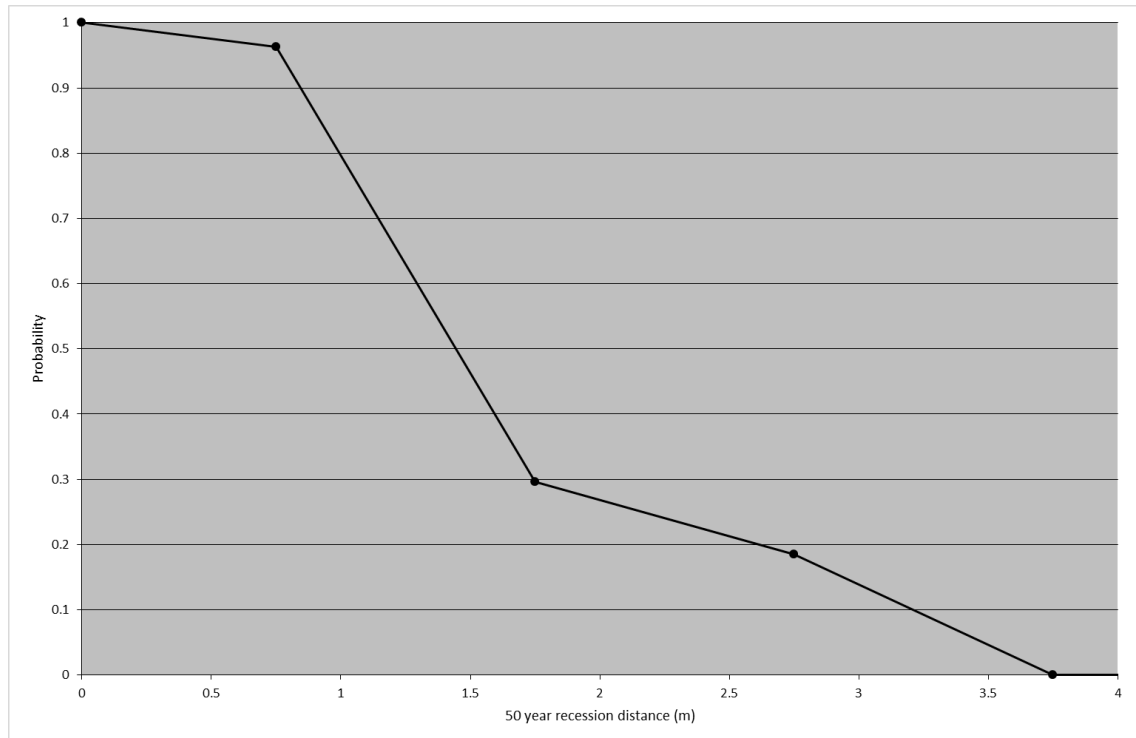


Figure 78: Probabilistic recession model with present climatic conditions projected for 50 years for the defended cliff line between Brighton Marina and Saltdean.

model also predicts that no section of the A259 is at threat due to cliff recession. Although historical recession data is only available for the 56 year period between 1957 and 2013 (Chapter 4) and projection over greater temporal scales can be less reliable, in the absence of any other empirical dataset the historical recession rates were projected over 100, 200 and 400 years to assess the impact of continued recession over much greater temporal periods. Figure 79 presents the probabilistic recession model for these three epochs. Similarly to the 50 year projection the 100 year projection does not predict the A259 to be at risk if climate conditions remain the same as the present day. As expected there is a notable increase in the probability of greater cliff top recession with a probability of 0.963 that recession reaches 1.5 m over 100 years and a probability of 0.296 that recession reaches 3.5 m within the protected cliff line. The recession rate doubles with the same probability for the 200 year projection with the first substantial threat to the road highlighted within this temporal projection. With an estimated probability of 0.25 that the A259 coast road will be breached in 200 years where the minimum distance between cliff edge and the road currently stands at 8.77 m. This increases significantly

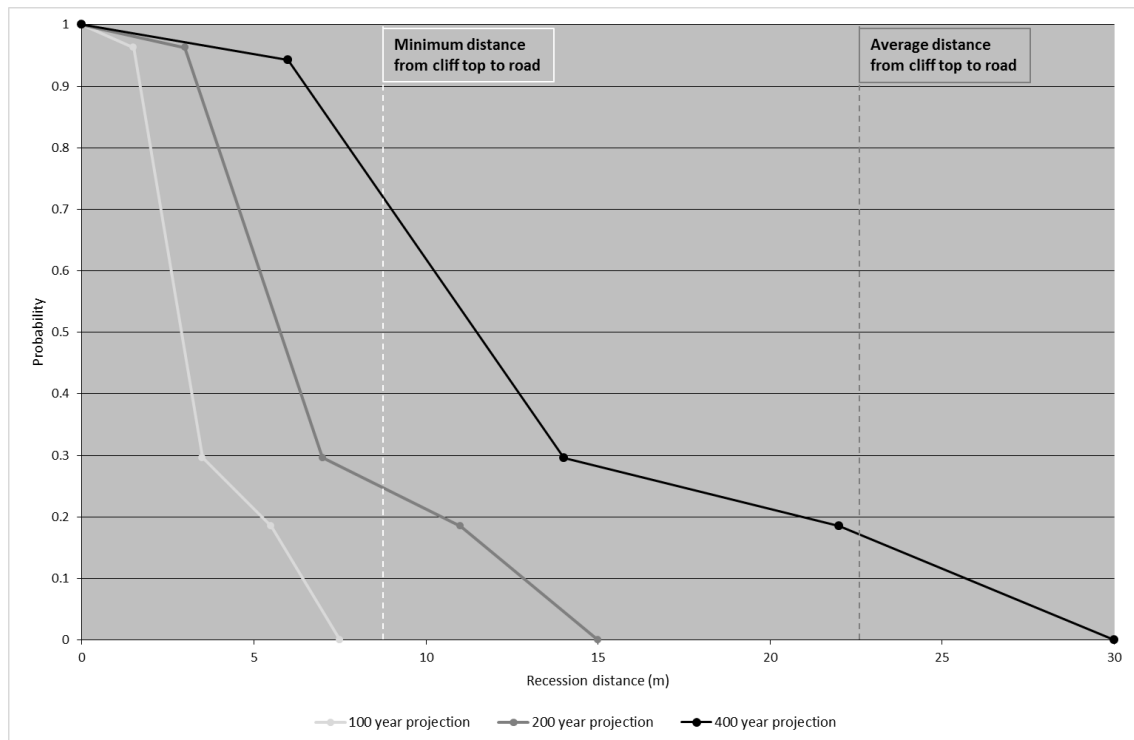


Figure 79: Probabilistic recession model with present climatic conditions projected for 100, 200 and 400 years for the defended cliff line between Brighton Marina and Saltdean (Minimum and average distance from cliff edge to road identified).

to approximately 72% probability over 400 years, whilst the probability that recession meets the average distance between cliff top edge and the road (22.57 m) between Brighton Marina and Saltdean is just below 20% in the event that current climatic conditions prevail.

5.4.5. Probabilistic recession model – sensitivity analysis

The adjustment or scaling factors as detailed in Table 23 form the basis for the probabilistic recession model (Appendix E) accounting for future climatic change. As there is no empirical process-response data available between future climate projections and the recession of cliffs the results presented are in the form of a sensitivity analysis, versus current conditions. The climatically adjusted recession rates were calculated by multiplying the observations by the scaling factors:

$$\text{Recession Rate}_{\text{climate}} = \text{HRR} \times \text{SF}_{\text{rainfall}} \times \text{SF}_{\text{temperature}}$$

where HRR is the historical recession rate and SF represents the scaling or adjustment factors.

Conditional probabilities were calculated for each of the climatically adjusted recession rates:

$$\text{Probability}_{RR \text{ climate}} = \text{HRR probability}_{\text{spatial}} \times \text{Probability}_{\Delta \text{ rainfall}} \times \text{Probability}_{\Delta \text{ temperature}}$$

The recession data was then binned using a series of minimum and maximum recession rates optimised for the dataset. The conditional probabilities for each bin width, or range of recession rates, were totalled. The midpoint of each bin was then multiplied by the projection period to ascertain a recession distance over time (Appendix E). The associated probabilities were then used to plot the cumulative probability of recession per epoch.

Figure 80 presents this model for projections over 50, 100, 200 and 400 years as presented in the previous sections under current climatic conditions. The general trend observed in the probabilistic model accounting for a change in future climate is an increase in cliff top recession. The model predicts a reduction in probability of slower recession whilst increasing both the range of recession values and associated probabilities at greater rates. Under contemporary conditions the A259 was not at risk when projecting recession rates 100 years into the future

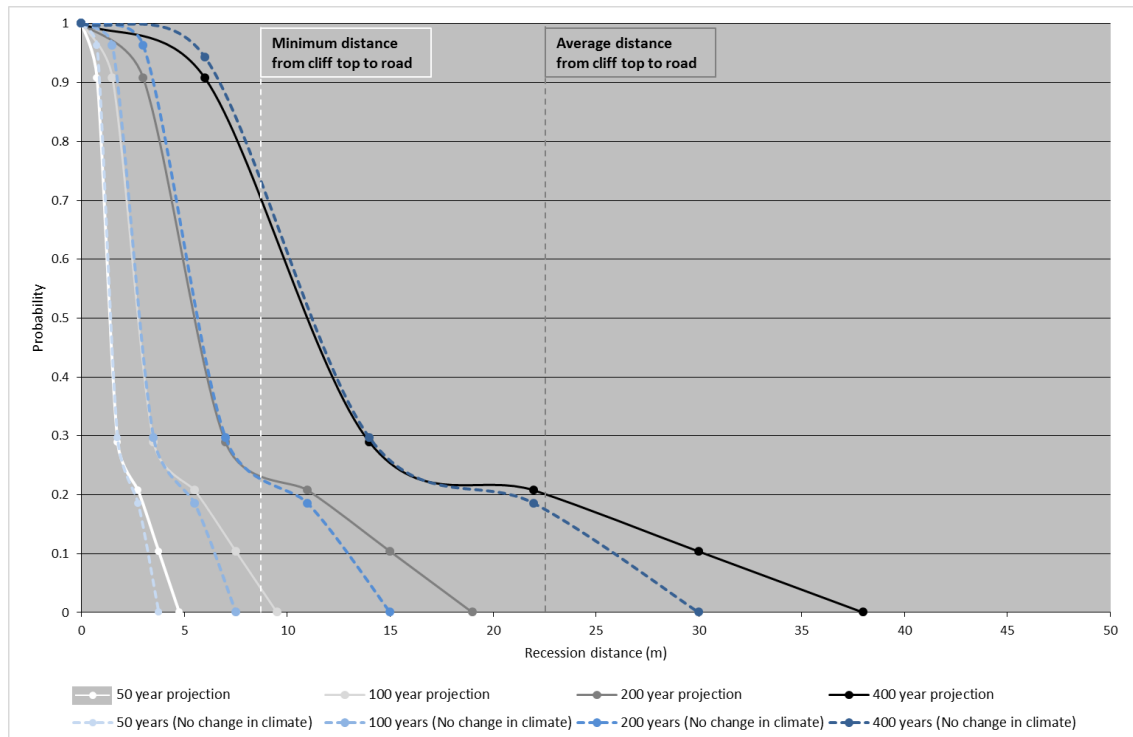


Figure 80: Probabilistic recession model sensitivity analysis accounting for change in future climatic conditions projected for 50, 100, 200 and 400 years for the defended cliff line between Brighton Marina and Saltdean (Minimum and average distance from cliff edge to road identified).

however for the same period using the climate sensitivity analysis model a probability of 0.04 is reported for recession to meet the A259 at the minimum distance of 8.77 m. The narrowest cliff edge to road distance is located in Black Rock, Brighton Marina which has since been stabilised with a matrix of soil nails (Chapter 4) to reduce the likelihood of failure within this zone. The rate of recession which would lead to the breach of the A259 under the 100 year projection is as a result of the greatest average recession rate of 0.07 m yr^{-1} recorded for the site which is increased by a maximum of 20% due to an increase in winter rainfall and an increase of up to 10% in response to temperature decreases leading to an increase freeze thaw action. This collective increase in recession rate due to climatic influences results in a calculated maximum recession rate of 0.10 (to 2d.p.). This annual recession rate would require a failure within the 'pinch-points' identified between the cliff edge and A259 of greater magnitude to the largest observed in Brighton Marina in the winter of 2000/2001.

5.4.6. Impact on the A259 – recession model at identified 'pinch-points'

The analysis of two individual units, U9 and U16 (Figure 77), assess the probability of recession reaching the A259 where the distance between the cliff edge and road represents the smallest distance. Furthermore, this analysis provides a more detailed site specific approach to these units which only include recession distances measured within the unit of interest whilst accounting for the potential impact of observed wedge failures, and not the greatest recession rates of the entire site as presented in the sensitivity analysis model for the entire site (Figure 74).

Unit 19 (U19 in Figure 77) is located approximately 600 m west of central Saltdean. Within this unit the minimum cliff edge to road distance is 9.1 m. The minimum distance as mentioned previously is 8.77 m and is located in the stabilised cliffs at Black Rock, Brighton Marina between the cliff edge and the access road from the A259 to the Marina. The average historical recession rate calculated for unit 19 was 0.02 m yr^{-1} and there were no conjugate joint sets observed, a

default probability of 0.01 was applied to all potential medium to large scale failures, which represents wedge failures on joints that are not visible due to weathering, and the retreat rates as presented in Table 21 were used for this calculation. Figure 81 illustrates the probabilistic recession model under current climatic and future climatic conditions for 50, 100 and 200 year epochs. Under the 100 year projection, accounting for the maximum impact of climate change from the sensitivity analysis, there is a calculated probability of 0.0014 that recession in U19 reaches the road at the minimum distance of 9.1 m. This probability is almost 29 times less than predicted by the model for the entire area for a similar recession distance (Figure 80). This infers that the study area model overestimates the probability of recession and thus individual units should be used for greater reliability, as they reflect the narrower range of unit specific historical recession rates. For the 200 year projection for U19 this increases to a probability of cliff recession reaching the A259 of 2.17% accounting for maximum impact of climate influences. As a result the likelihood of cliff recession impacting the A259 in U19 within readily applied management epochs, of 50 – 100 years is unlikely.

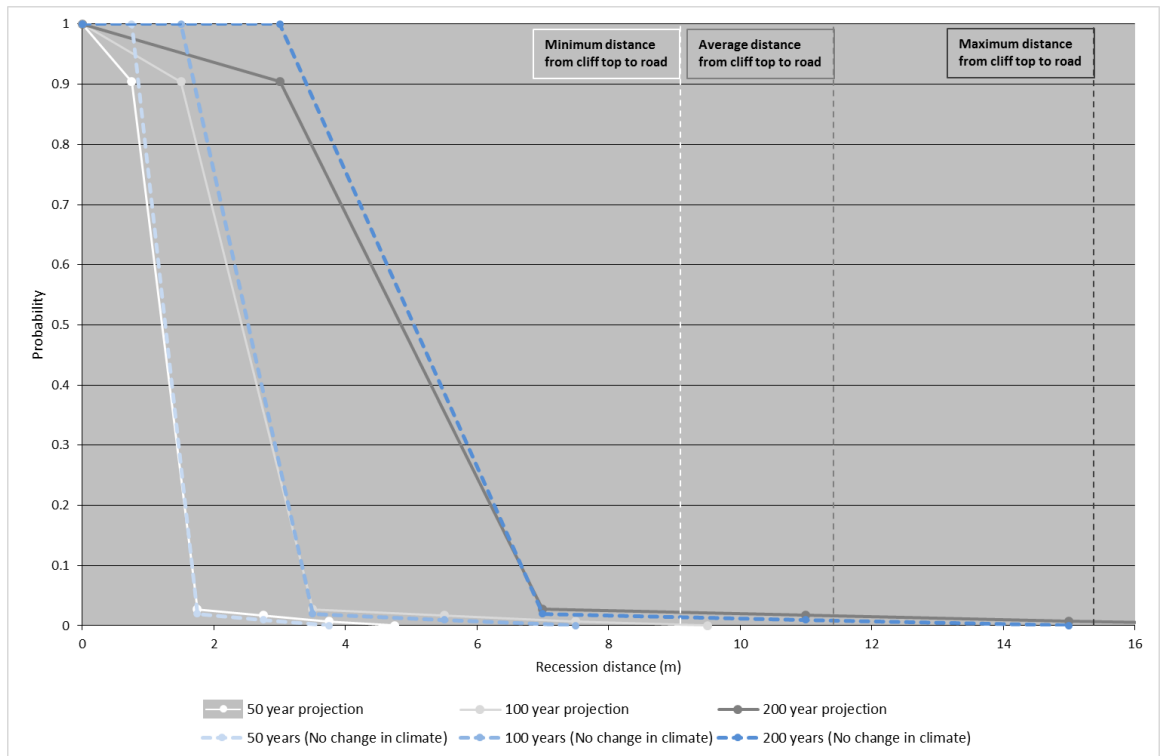


Figure 81: Probabilistic recession model sensitivity analysis accounting for change in future climatic conditions projected for 50, 100, and 200 years for unit 19 (Figure 77) of the defended cliff line between Brighton Marina and Saltdean (Minimum and average and maximum distance from cliff edge to road identified for the unit).

The other 'pinch-point' which was identified and analysed was unit 6 (U6 in Figure 77) which is located approximately 500 m east of the eastern breakwater at Brighton Marina. The minimum distance between cliff edge and the A259 is currently 9.97 m and the average historical recession rate for this unit was 0.02 m yr^{-1} . A total of four potential wedge failures were identified within this unit on conjugate joint sets, one within the $1\text{-}10 \text{ m}^3$, two within the $10\text{-}50 \text{ m}^3$ and one within the $50\text{-}100 \text{ m}^3$ classifications. The spatial impact of these potential wedge failures accounted for 3%, 7% and 9% of the total cliff top width for the unit. The wedge failures identified were assigned a recession rate as presented in Table 21 and included in the probabilistic modelling. Figure 82 presents the probabilistic recession model under current climatic and future climatic conditions for 50, 100 and 200 year epochs. The minimum distance from cliff edge to road is not reached in the 50 or 100 year projections for this unit under current or future climatic conditions. However, there is a noticeable increase in probability for recession between unit 19 and unit 6. For example, the probabilistic models, which account for future climate change, record for unit 19 a probability of 0.027 for recession to reach 3.5 m over 100 years this is 0.149 in unit 6 for the same distance due to the increase likelihood of larger scale failure through the observed wedges. When unit 6 is modelled over 200 years, under the maximum modelled impact from climate change, there is a significant risk to the A259 with a calculated probability of 0.092 that recession will reach the road. This finding is a direct result of an increase in recession through greater magnitude events. For the road to be breached in 200 years several medium ($1\text{-}10 \text{ m}^3$) to large ($10\text{-}50 \text{ m}^3$) scale magnitude events would have to occur in the same location over this time period. However under current climatic conditions the probability of the road being breached is significantly less at 0.0325. The risk of recession in this unit is greater than in unit 19 but requires further monitoring to determine the likelihood of future failure. If one of the modelled wedge failures occurred within this section further cliff face stability measures would likely be considered, as has been the case with other large conjugate joint sets

within the defended cliff line in Brighton, to prevent risk to the A259 over greater temporal periods as presented in Figure 82.

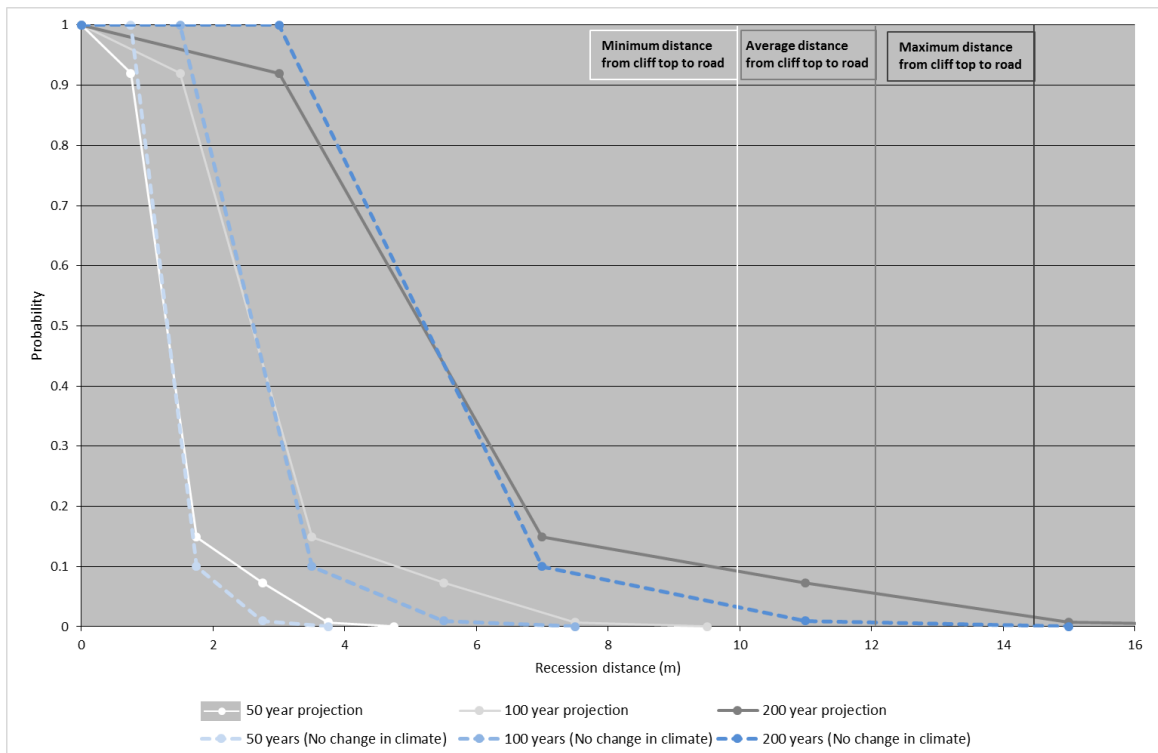


Figure 82: Probabilistic recession model sensitivity analysis accounting for change in future climatic conditions projected for 50, 100, and 200 years for unit 6 (Figure 77) of the defended cliff line between Brighton Marina and Saltdean (Minimum and average and maximum distance from cliff edge to road identified for the unit).

5.4.7. Comparison of methodological approaches

Two methods of probabilistic recession modelling of sea cliffs have been presented within this research; the negative power law scaling of rockfalls which were constrained by H_s and accounted for SLR for the unprotected cliffs at Telscombe and a judgement based approach using historical recession rates and scaling factors for future climate along the protected cliff line. The former method is statistically robust and utilises the most current predictions of future climate, under the UKCP09 medium emission scenario, and is statistically the more reliable method. However when such rockfall inventories and process-response relationships are unavailable, the alternative method which represents the industrial best practice may be used. The scaling factors are determined through a knowledge of the system and future climate

predictions, but as no numerical relationship has been derived the only appropriate presentation of results are through a sensitivity analysis. This enables projections over greater temporal scales to be assessed accounting for a variety of scenarios from no change (current) to worst case where recession increases due to an increase in precipitation and fracturing of the rock through freezing or drying.

5.5 Summary of results

Through the use of digital photogrammetry, 2.5 D change detection revealed no rockfalls at the protected site in Brighton Marina between November 2014 and March 2017, above the detection threshold of 0.07m. The unprotected site at Telscombe recorded a total of 10,085 mass wasting events with an estimated total volumetric flux of 3,889.35 m³. This monitoring revealed progressive failures on conjugate joint sets which totaled 702.6 m³. Evidence of toe erosion, totalling 104.9 m³ between August 2016 and February 2017, due to wave action and steepening of the cliff face resulted in the largest single failure of 2,546.8 m³. Each of the larger events recorded correlated with storm events within the period between data capture.

Frequency-magnitude analysis of the monthly rockfall inventories demonstrated negative power law scaling over seven orders of magnitude. For the first time, statistically significant correlations were found between significant wave height (H_s) and the power law scaling coefficients, β and s with R^2 values of 0.4971 and 0.5793 respectively. Using these relationships and the prediction of wave climate and sea level forecasts under the UKCP09 medium emission climate model (A1B) a Monte Carlo simulation of potential erosion scenarios between 2020 and 2089 was established. The model predicted an approximate 6% increase in recession between the current and future (UKCP09 medium emission scenario) conditions from 20.45 m to 21.76 m and estimated the probability of recession breaching the A259 coastal road by 2089 as 0.0778 under current conditions and 0.1056 due to the influence of future climate.

Limit equilibrium analysis undertaken on the observed conjugate joint sets within the defended section of cliffs between Brighton Marina and Telscombe revealed that the coastal road would not be at immediate threat (breach) due to any of the modelled wedge failures occurring. However measures would need to be put in place to maintain the road in its current location were any of these failures to occur. In the absence of a rockfall inventory for this section of cliff line, a probabilistic recession model using current industry best practice was used to predict future recession for the defended section of cliffs. Within identified 'pinch-points' where the distance between the road and cliff edge was less than 10 m the probability of recession reaching the road over the next 100 years did not exceed 0.0014.

The following chapter provides conclusions to the research and highlights the benefits which this research could have for both scientific research and the industrial sector, before presenting opportunities for further research.

Chapter 6 – Conclusions

This chapter provides conclusions to the research by revisiting the aims and objectives outlined in Chapter 1, Section 1.3.

(A1) The primary aim was to characterise and quantify the recession of defended and undefended chalk cliffs between Brighton Marina and Telscombe.

This was achieved through the deployment of terrestrial and UAV photogrammetry. The developed models enabled mapping in 3D space of the discontinuities within the study site at Telscombe which enabled a kinematic analysis to be undertaken (Chapter 4, Section 4.6, after Barlow et al., 2017). This was the first time such analysis had been undertaken using UAV photogrammetry models for chalk sea cliffs, with the results agreeing with that presented in the scientific literature using more traditional approaches (Mortimore et al., 2004a; 2004b; Lawrence, 2007). Weekly and monthly surveys for the terrestrial and UAV photogrammetry models respectively enabled surface change detection to be completed to quantify rockfall events and cliff recession at the sites.

The primary aim was achieved through the completion of the following objectives:

(O1) Determine the historical rates of recession for defended and undefended chalk cliffs of similar characteristics and exposure in the area.

The fully orthorectified dataset for aerial images from 1957, 1971, 1993 and 2013 provided a more reliable dataset for measuring historical recession rates for the study area. This method enabled the inclusion of uncertainty and thus produces error bands for the measured recession rates, something which previous studies published in the scientific literature had not been able to provide (e.g. Dornbusch et al., 2008). Nevertheless the results provided from this analysis were very similar to that published by Dornbusch et al. (2008) for the section of coastline between Black Rock and Belle Tout, of $-0.22 \text{ m yr}^{-1} \pm 0.18 \text{ m}$ (this study) and -0.27 m yr^{-1} (Dornbusch et al., 2008).

(O2) Develop a reliable methodology using photogrammetry for high precision monitoring of sea cliffs.

One of the contributions to research within this field was the development of a reliable photogrammetry methodology which could be used for both terrestrial and UAV deployments. The relative affordability of photogrammetry versus TLS systems provide a greater opportunity for procurement of DSLR cameras and UAVs which can be used within a range of geomorphological contexts. Through the development of the methodology this research concludes that full frame cameras with fixed focal length lenses provide the optimal configuration for obtaining the most accurate photogrammetry models with the greatest point density. The accuracy of the optimum terrestrial models, which were obtained using convergent strip photography, was 0.02 m (3DSE) with an average point spacing of 0.016 m. The optimum UAV models recorded 3DSE values which ranged between 0.03 m and 0.06 m. The variation was due to environmental conditions, mainly wind, which affected the amount of images captured between surveys, with the larger 3DSE values correlating with those dataset with less images captured. The point spacing was 0.05 m for the UAV photogrammetry models due to processing capability restrictions. The threshold of surface change detection was found to be 0.07 m and 0.10 m for the terrestrial and UAV models respectively.

(O3) Quantify the erosional mass flux from defended cliffs in Brighton Marina and undefended cliffs in Telscombe using terrestrial and UAV photogrammetry respectively.

Although the terrestrial photogrammetry in Brighton Marina provided a 'no-change' (>0.07 m) result during the period of data collection this is due to the performance of the cliff stabilisation and toe protection measures previously installed. The 12 month dataset obtained from the UAV photogrammetry in Telscombe enabled quantification of rockfalls and the erosional mass flux between August 2016 and July 2017 of 3,889.4 m³. The largest failure during any monthly period was 2,546.8 m³ observed between February and March 2017. By capturing datasets at monthly intervals, an improved understanding of the spatial and temporal development of the

unprotected chalk cliffs at Telscombe was obtained. This informed 3D modelling of successive block failures (Chapter 5, Section 5.1.2.1), surface change and 3D models of the characteristic rock cliff wedge failure within the Newhaven formation previously observed and illustrated by Mortimore et al. (2004a). Rockfall failure sequences were observed through toe erosion leading to the largest failure observed within the rockfall inventory (Chapter 5, Section 5.1.2.2) which enabled subsequent analysis of the effect of the steepening of the cliff face on the FoS.

(O4) Develop a probabilistic model of chalk cliff erosion using negative power law scaling of rockfalls.

The key contribution to scientific research within this field was the development of the probabilistic recession model of sea cliffs through the use of UAV photogrammetry and negative power law scaling of rockfalls (Chapter 5, Section 5.2). By constraining the power law scaling parameters, β and s with significant wave height (H_s) through linear regression relationships with R^2 values of 0.4971 and 0.5793, a model was developed which accurately predicted the observed monthly failures with an R^2 of 0.9981 for the unprotected section of cliff line at Telscombe. This model was then used to predict recession through a Monte Carlo simulation of 10,000 iterations to establish the most likely cliff recession scenarios under current and future conditions using the UKCP09 Medium Emission Scenario for H_s and accounting for SLR between 2020 and 2089. For the most likely cliff recession scenario the model predicts an approximate 6% increase in recession due to future conditions under the UKCP09 Medium Emission Scenario from 20.45m to 21.76 m between 2020 and 2089. The model also determines the probability of the A259 coastal road being breached by 2089 as 0.0778 (approx. 1 in 12) and 0.1056 (approx. 1 in 9) for current and future conditions respectively. This is the first time that power law scaling parameters have been constrained by marine conditions in developing a probabilistic model which will be useful in determining future management decisions for the site.

(A2) The secondary aim of the research was to establish the effectiveness of current mitigation approaches.

This was achieved through calculating cliff recession rates prior to and post installation of toe protection structures (Chapter 4, Section 4.3.3). As installation of toe protection measures coincides with regrading of the cliff face, artificial recession is introduced into the historical recession rates obtained from aerial images. An investigation into this issue revealed on average 93.35% of the recession observed between aerial imagery before and after installation of toe protection is accounted for through regrading of the cliffs. As a result recession rates reduce by an order of magnitude following the installation of toe protection. No assessment could be made on the effectiveness of cliff stabilisation measures as these were implemented post 2002 and the aerial image datasets used were from 1993 and 2013. It is very likely that the reduction in cliff recession due to these stabilisation measures would have been undetected due to the error bands of the orthorectified aerial images.

(O5) Determine the dominant mechanism of failure for the chalk cliffs in Brighton and the impact of these failures within defended cliff sections.

Through kinematic analysis (Chapter 4, Section 4.6, after Barlow et al., 2017) the relative likelihood of each mechanism of rockfall/cliff failure was quantified. Wedge failure was found to be the most likely, with 39.97% of all mapped intersections favourable to this mode. The percentage of intersections falling within the favourable region for the other modes of failure are; 7.16% of planar, 4.24% flexural toppling and 0.31% direct toppling (adapted from Barlow et al., 2017). Through back analysis of observed wedge failures at Telscombe and a review of literature to obtain input parameters, a limit equilibrium analysis was undertaken on the observed conjugate joint sets in the protected stretch of cliffs between Brighton Marina and Saltdean. None of the modelled wedge failures led to a breach of the A259 road, therefore it can be concluded that the coastal road is not at immediate threat due to failure of this mode with the magnitude of wedge failures modelled in this research. However subsequent intervention would be required through cliff stabilisation measures if such failures occurred in identified pinch points. The A259 coastal road is still at threat due to continued recession,

whether it be as a result of high frequency low magnitude events or low frequency high magnitude events.

(O6) Estimate the time for cliff recession to impact infrastructure, namely the A259 road for defended and undefended cliffs in Brighton.

Through the probabilistic modelling approaches presented a time scale can be presented for recession to breach the A259. It must be noted that the model developed through the negative power law scaling of rockfalls which is driven by observations and future climate prediction models for the unprotected cliffs at Telscombe is statistically more reliable than the judgement based approach for the protected section. However, the traditional expert judgement approach provides a crucial role where data uncertainties are not quantifiable or unknown. Along the unprotected coastline the probability of the road being breached before 2050 is low with a probability of 0.0073 (approx. 1 in 137) and 0.0129 (approx. 1 in 77) under current and future (UKCP09 medium emission scenario) conditions respectively. This does increase substantially to 0.0778 (approx. 1 in 12) and 0.1056 (approx. 1 in 9) by 2089 for current and future conditions respectively. For the alternative method presented for the protected cliff line a probability of 0.04 (1 in 25) is calculated for recession to breach the road within 100 years (from 2013, the latest aerial imagery). For the identified 'pinch-point' of Unit 6 the model predicts no risk to the road under the 50 or 100 year projections. The probability that recession reaches the A259 within this unit increases to 0.0325 (approx. 1 in 30) and 0.092 (approx. 1 in 10) for current and future climate respectively when modelled over 200 years. For the other 'pinch-point' Unit 19 there was no risk found over the 50 year projection. This increased to 0.0014 (approx. 1 in 714) over 100 years and 0.0217 (approx. 1 in 46) over 200 years accounting for future climate. These models provide useful data to decision makers including the local councils in determining the best strategy for future management of the site.

6.1. Benefits for the industrial sector

This research was funded through an EPSRC iCase (Engineering and Physical Sciences Research Council industrial Co-operative Award in Science and Technology) studentship, and many of the methodological approaches could be used to benefit the industrial sector.

The use of UAVs in capturing high-resolution data provides a saving in both cost and time. The 750m section of cliff line surveyed at Telscombe required field visits between 30 and 45 minutes, which included a flight time of approximately eight minutes. Ground control points were surveyed once at the site, coordinates were then extracted from the flints in the first 3D model which were used as the control network in subsequent model generation. This reduced the time in the field and most importantly reduces the risk to the individual, employee or surveyor who would have to capture the ground control on all site visits.

Another benefit of capturing high resolution data using photogrammetry is the ability to digitally identify discontinuities within the rock mass. Traditionally, this would have been undertaken with a compass and clinometer at the base of cliff. By moving this process to the office exposure to risk is reduced and a much greater surface area of the rock mass can be used for data analysis. This provides a more representative sample as opposed to the two metres at the base of cliff which could be mapped in the field.

The ability to capture high resolution data at high frequency with a significant cost reduction, as opposed to laser scanning alternatives, not only makes this technology more accessible but also increases the opportunities for deployment. As with this study, analysis can then be undertaken to improve our understanding of the monitored environment and build models to predict future change at the site which would have previously been more challenging or unachievable.

6.2. Recommendations for further research

Following the conclusions of this study it is possible to make recommendations for further research and practice within the field of coastal cliff instability and erosion management. One of the limitations to the probabilistic model developed for the unprotected section of cliff at Telscombe was the relatively short period of data collection, of 12 months, from which the model was extrapolated between 2020 and 2089. By continuing to build this monthly inventory this will enable; the relationships between the power law scaling parameters and significant wave height to be assessed to determine whether these relationships hold over greater temporal periods, an assessment of the relationships between erosion and environmental conditions and to determine whether the magnitude frequency distributions reflect are representative of annual rockfalls. These measures may further strengthen the model through an increase in the R^2 values between the power law scaling parameters and the marine or environmental variables assessed.

Continued monitoring of the protected cliff line through terrestrial photogrammetry can be undertaken to quantify rockfalls within this section. The likelihood is under environmental conditions of greater precipitation and harder or longer duration of frosts the frequency of rockfalls within the protected cliff line will increase. By obtaining a rockfall inventory under these conditions a similar numerical model, to that developed for Telscombe, could be developed which would provide greater confidence in a probabilistic model for the protected section of cliff line.

Further research into the thermal behaviour of the chalk cliffs is possible. One option for this dataset is the development of a model which can determine the cliff surface temperature from environmental parameters including air temperature, wind direction, and relative humidity. The high frequency database which exists can be used to achieve this along with continued monitoring of the study site within Brighton Marina. This will enable any future frost events

which lead to freezing temperatures recorded on the cliff face to be examined against any possible failures.

One limitation to the photogrammetric models developed using UAV photogrammetry was the lower point density/point spacing. The raw DTMs had almost double the points than the final merged DTMs for each month, this was due to processing restrictions. However with acquisition of hardware capable of processing such datasets models with greater resolution may be developed. In addition future improvements may be made to the accuracy of these models through multiple strip captures which would enable vertical as well as horizontal overlap of the images. As presented within this research for the terrestrial photogrammetry through the convergent strip, images taken with a different view point increase the point matching in 3D space and therefore the overall accuracy of the model. These models should be able to be processed with more capable hardware as referred to previously.

This study has provided contribution to the ongoing research into the nature of coastal cliff behaviour through the means of data acquisition and modelling. It has developed a reliable methodology for deploying photogrammetry for both terrestrial and UAV applications in the coastal environment. This study presents the first time that probabilistic recession modelling of sea cliffs has been developed through negative power law scaling of rockfalls constrained by driving forces to erosion, in this case waves through the significant wave height. This enabled probabilities to be assigned to recession impacting infrastructure over the next 70 years. The applications of these models may ultimately provide a new methodological approach for assessing risk of future coastal cliff recession.

References

- Abellán, A., Jaboyedoff, M., Oppikofer, T., & Vilaplana, J. M. (2009). Detection of millimetric deformation using a terrestrial laser scanner: experiment and application to a rockfall event. *Natural Hazards and Earth System Sciences*, 9, pp. 365-372. [Online] DOI: 10.5194/nhess-9-365-2009
- ADAM Technology. (2004). *Image Capturing Recommendations*. Belmont, Australia: ADAM Technology.
- ADAM Technology. (2010a). *3DM Analyst Mine Mapping Suite: 3D Measurement, Camera Calibration and Block Adjustment Software (First Edition, revision 1.0.137)*. Belmont, Australia: ADAM Technology.
- ADAM Technology. (2010b). ADAM Technology Team Blog – How accurate is photogrammetry? – Part 2 (19th October 2010). Retrieved from <https://www.adamtech.com.au/Blog/?p=167>
- Adams, J., & Chandler, J. (2003). Evaluation of Lidar and medium scale photogrammetry for detecting soft-cliff coastal change. *The Photogrammetric Record*, 17(99), pp. 405-418. [Online] DOI: 10.1111/0031-868X.00195
- Allison, R. J. (1989). Rates and mechanisms of change in hard rock coastal cliffs. *Zeitschrift für Geomorphologie*, 73, pp. 125-138.
- Amos, D. (2008) – *Annual Report 2008 – Beachy Head to Selsey Bill*. Retrieved from <http://www.channelcoast.org/reports/>
- Amos, D. (2013) – *Annual Report 2013 – Beachy Head to Selsey Bill*. Retrieved from <http://www.channelcoast.org/reports/>
- Anders, F. J., & Byrnes, M. R. (1991). Accuracy of shoreline change rates as determined from maps and aerial photographs. *Shore and Beach*, 59(1), pp. 17-26.
- Ashton, A., Walkden, M., & Dickson, M. (2011). Equilibrium responses of cliffed coasts to changes in the rate of sea level rise. *Marine Geology*, 284(1-4), pp. 217-229. [Online] DOI: 10.1016/j.margeo.2011.01.007
- Attewell, P. B., & Farmer, I. W. (1976). *Principles of Engineering Geology*. New York: John Wiley & Sons.
- Awange, J. (2012). *Environmental Monitoring using GNSS, Global Navigation Satellite System*. Berlin: Springer.
- Awange, J., & Kiema, J. B. K. (2013). *Environmental Geoinformatics: Monitoring and Management*. Berlin: Springer.
- Bak, P. (1996). *How nature works: the science of self-organized criticality*. New York: Springer
- Barlow, J., Gilham, J., & Cofrã, I. I. (2017). Kinematic analysis of sea cliff stability using UAV photogrammetry. *International Journal of Remote Sensing*, 38(8-10), pp. 2464-2479. [Online] DOI: 10.1080/01431161.2016.1275061

- Barlow, J., Lim, M., Rosser, N., Petley, D., Brain, M., Norman, E., & Geer, M. (2012). Modelling cliff erosion using negative power law scaling of rock falls. *Geomorphology*, 139-140, pp. 416-424. [Online] DOI: 10.1016/j.geomorph.2011.11.006
- Baroň, I., Bečkovský, D., & Míča, L. (2014). Application of infrared thermography for mapping open fractures in deep-seated rockslides and unstable cliffs. *Landslides*, 11(1), pp. 15-27. [Online] DOI: 10.1007/s10346-012-0367-z
- Barton, N. R. (1974). *A review of shear strength of filled discontinuities in rock*. Norwegian Geotechnical Institute Publication Number 105. Oslo, Norway: Norwegian Geotechnical Institute.
- Betts, H. D., & DeRose, R. C. (1999). Digital elevation models as a tool for monitoring and measuring gully erosion. *Journal of Applied Earth Observation and Geoinformation*, 1(2), pp. 91-101. [Online] DOI: 10.1016/S0303-2434(99)85002-8
- Bialek, J. (1969). *Le recul des falaises du cap d'Antifer au Tréport, entre 1830 et 1966*. Arrondissement de Dieppe: Direction Départementale de l'Équipement de Seine-Maritime.
- Birch, J.S. (2009). *3DM Analyst Mine Mapping Suite Training* [ADAM Technology Presentation]. Retrieved from: <http://slideplayer.com/slide/6869698/>
- Bird, E. (2007). *Coastal Geomorphology An Introduction* (2nd edn.). Chichester: John Wiley and Sons.
- Bird, E. C. F. (1969). *Coasts*. Massachusetts: MIT Press Cambridge.
- Bird, E. C. F. (2000). *Coastal Geomorphology: An introduction*. Chichester: John Wiley & Sons.
- Bishop, M. P., James, L.A., Shroder Jr, J. F., & Walsh, S. J. (2011). Geospatial technologies and digital geomorphological mapping: concepts, issues and research. *Geomorphology*, 137(1), pp.5-26. [Online] DOI: 10.1016/j.geomorph.2011.06.027
- Bovington, J. (2009) – *Frontage Review Report 2009 – Beachy Head to Selsey Bill*. Retrieved from <http://www.channelcoast.org/reports/>
- Bovington, J. (2010). *Report of Survey – Brighton Marina to Saltdean, Management Unit 4DSU11 - 20/05/2010*. Worthing Borough Council: Worthing.
- Bovington, J. (2012). *Report of Survey – Brighton Marina to Newhaven Harbour, Management Units 4d-SU08, 4d-SU09, 4d-SU08, 4d-SU010, 4DSU11, 4d-SU12 - 24/07/2012*. Worthing Borough Council: Worthing.
- Bovington, J. (2013a). *Brighton Cliff Survey Report May 2010 – July 2012, Strategic Regional Coastal Monitoring*. Shoreham, West Sussex: Adur & Worthing Councils
- Bovington, J. (2013b). *Report of Survey – Brighton Marina to Newhaven Harbour, Management Units 4d-SU08, 4d-SU09, 4d-SU08, 4d-SU010, 4DSU11, 4d-SU12 - 26/07/2013*. Worthing Borough Council: Worthing.

- Bovington, J., & Amos, D. (2010) – *Annual Report 2010 – Beachy Head to Selsey Bill*. Retrieved from <http://www.channelcoast.org/reports/>
- Bovington, J., Amos, D., & Ford, L. (2011) – *Annual Report 2011 – Beachy Head to Selsey Bill*. Retrieved from <http://www.channelcoast.org/reports/>
- Bovington, J., Amos, D., & Warman, L. (2014) – *Annual Report 2014 – Beachy Head to Selsey Bill*. Retrieved from <http://www.channelcoast.org/reports/>
- Bovington, J., Amos, D., & Warman, L. (2015) – *Annual Report 2015 – Beachy Head to Selsey Bill*. Retrieved from <http://www.channelcoast.org/reports/>
- Brardinoni, F., & Church, M. (2004). Representing the landslide magnitude–frequency relation: Capilano River Basin, British Columbia. *Earth Surface Processes and Landforms*, 29(1), pp. 115–124. [Online] DOI: 10.1002/esp.1029
- Bray, M. J., & Hooke, J. M. (1997). Prediction of soft-cliff retreat with accelerating sea-level rise. *Journal of Coastal Research*, 13(2), pp. 453-467. [Online] URL: <http://www.jstor.org/stable/4298640>
- Brighton and Hove City Council – BHCC. (2012). Observed rockfalls, cliff stabilisation measures and defences installed between 1999 and 2012 (annotated maps). Brighton & Hove City Council: Brighton
- Brighton and Hove City Council – BHCC. (2013). *The historical development of coast defence in Brighton & Hove*. Retrieved from <https://www.brighton-hove.gov.uk/content/environment/coast-defence-and-flood-management/historical-development-coast-defence-brighton>
- Brighton and Hove City Council – BHCC. (2017). *Travel, transport and road safety: Counting traffic in Brighton and Hove*. Retrieved from <http://www.brighton-hove.gov.uk/content/parking-and-travel/travel-transport-and-road-safety/counting-traffic-brighton-and-hove>
- British Oceanographic Data Centre (BODC). (2017). *BODC – NERC UK Tide Gauge Network Download Data*. Retrieved from https://www.bodc.ac.uk/data/hosted_data_systems/sea_level/uk_tide_gauge_network/processed_customise_time_selection/
- Brooks, S. M., & Spencer, T. (2010). Temporal and spatial variation in recession rates and sediment release from soft rock cliffs, Suffolk coast, UK. *Geomorphology*, 124(1-2), pp. 26-41. [Online] DOI: 10.1016/j.geomorph.2010.08.005
- Brown, J. M., Wolf, J., & Souza, A. J. (2012). Past to future extreme events in Liverpool Bay: model projections from 1960-2100. *Climatic Change*, 111(2), pp. 365-391. [Online] DOI: 10.1007/s10584-011-0145-2
- Brunetti, M. T., Guzzetti, F., & Rossi, M. (2009). Probability distributions of landslide volumes. *Nonlinear Processes in Geophysics*, 16(2), pp. 179-188. [Online] DOI: 10.5194/npg-16-179-2009

- Brunsdon, D, & Lee, E. M. (2004). Behaviour of coastal landslide systems: an inter-disciplinary view. *Zeitschrift für Geomorphologie*, 134, pp. 1-112.
- Brunsdon, D, & Lee, E. M. (2000). 'Understanding the behaviour of coastal landslide systems: an inter-disciplinary view', in Bromhead, E. N., Dixon, N., & Ibsen, M. L. (Eds.) *Landslides: in research, theory and practice proceedings of the 8th International Symposium on Landslides*. Cardiff, Wales.
- Buckley, S. J., Howell, H. D., Enge, H. D., & Kurz, T. H. (2008). Terrestrial laser scanning in geology: data acquisition, processing and accuracy considerations. *Journal of the Geological Society*, 165, pp. 625-638. [Online] DOI: 10.1144/0016-76492007-100
- Busby, J. P., Senfaute, G., Gourry, J. C., Lawrence, J. A., Pedersen, S. A. S., & Mortimore, R. N. (2004). Developing tools for the prediction of catastrophic coastal cliff collapse. *Proceedings of Littoral. 7th International Symposium: Delivering Sustainable Coasts: Connecting Science and Policy*. Aberdeen, Scotland, UK, pp. 597–602.
- Cambers, G. (1976). Temporal scales in coastal erosion systems. *Transactions of the Institute of British Geographers*, 1(2), pp. 246-256. [Online] URL: <http://www.jstor.org/stable/621987>
- Carter, B. J., & Lajtai, E. Z. (1992). Rock slope stability and distributed joint systems. *Canadian Geotechnical Engineering Journal*, 29(1), pp.53-60. [Online] DOI: 10.1139/t92-006
- Chandler, J. H., Ashmore, P., Paola, C., Gooch, M., & Varkaris, F. (2002). Monitoring river channel change using terrestrial oblique digital imagery and automated digital photogrammetry. *Annals of the Associated American Geographers*, 92(4), pp. 631-644. [Online] DOI: 10.1111/1467-8306.00308
- Channel Coastal Observatory (CCO). (2015). *Channel Coastal Observatory - Regional Coastal Monitoring Programmes Seaford Wave Buoy*. Retrieved from http://www.channelcoast.org/data_management/real_time_data/charts/?chart=81&tab=info&disp_option=
- Channel Coastal Observatory (CCO). (2016). *Channel Coastal Observatory - Regional Coastal Monitoring Programmes Annual Wave Report 2016 Seaford Wave Buoy*. Retrieved from <https://www.channelcoast.org/reports/>
- Channel Coastal Observatory (CCO). (2017a). *Realtime Data - Brighton Met Station*. Retrieved from http://www.channelcoast.org/data_management/real_time_data/charts/?chart=88&tab=met&disp_option=1
- Channel Coastal Observatory (CCO). (2017b). *Channel Coastal Observatory - Regional Coastal Monitoring Programmes Annual Wave Report 2017 Seaford Wave Buoy*. Retrieved from <https://www.channelcoast.org/reports/>

- Channel Coastal Observatory (CCO). (2017c). *Realtime Data – Seaford wave buoy*. Retrieved from http://www.channelcoast.org/data_management/real_time_data/charts/?chart=81&tab=waves&start=1493285400&end=1493371800&disp_option=1&datum=chart
- Chmiel, J., Kay, S., & Spruyt, P. (2004). 'Orthorectification and geometric quality assessment of very high spatial resolution satellite imagery for Common Agricultural Policy purposes', in *Proceedings of XXth International Archives of the Photogrammetry, Remote Sensing and Spatial Information Sciences, 35(Part B4)*,. Istanbul: ISPRS. 12–23 July 2004. Istanbul, Turkey: ISPRS, pp. 1-6.
- Clarke, D., & Smethurst, J. A. (2010). Effects of climate change on cycles of wetting and drying in engineered clay slopes in England. *Quarterly Journal of Engineering Geology and Hydrogeology*, 43, pp.473-486. [Online] DOI: 10.1144/1470-9236/08-106
- Clayton, C. R. (1978). *Chalk as fill* (Unpublished doctoral thesis). University of Surrey, UK.
- Cleeve, J., & Williams, R. B. G. (1987). *Cliff erosion in East Sussex*. Brighton: University of Sussex.
- Clifford, J. M., Förstner, W., Bernhard, W., Paderes, F., & Munjy, R. (2004). The mathematics of photogrammetry. In J. McGlone, E. Mikhail, & R. Mullen (Eds.), *Manual of photogrammetry* (pp. 181-316) (5th ed.). Maryland: American Society of Photogrammetry and Remote Sensing.
- Cloud Compare v2.6.3. (2016). *CloudCompare 3D point cloud and mesh processing software Open Source Project*. Retrieved from <http://www.cloudcompare.org/>
- Costa, S., Delahaye, D., Freiré-Díaz, Di Nocera, L., Davidson, R., & Plessis, E. (2004). 'Quantification of the Normandy and Picardy Chalk cliff retreat by photogrammetric analysis', in Mortimore, R. N., & Duperret, A. (Eds.) *Coastal Chalk Cliff Instability*. London: Geological Society, Engineering Geology Special Publications, pp. 139-147.
- Crisp, S. (2013). *Camera sensor size: Why does it matter and exactly how big are they?* Retrieved from <http://newatlas.com/camera-sensor-size-guide/26684/>
- Cruden, D. M., & Varnes, D. J. (1996). 'Landslide types and processes', in Turner. A. K., & Schuster, L. R. (Eds.) *Landslides: Investigation and Mitigation*. Washington: Transportation Research Board Business Office, pp. 36-75.
- d'Oleire-Oltmanns, S., Marzloff, I., Peter, K. D., & Ries, J. B. (2012). Unmanned Aerial Vehicle (UAV) for Monitoring Soil Erosion in Morocco. *Remote Sensing*, 4(11), pp. 3390-3416. DOI: 10.3390/rs4113390
- Davidson-Anrott, R. (2010). *Introduction to Coastal Processes and Geomorphology*. Cambridge: Cambridge University Press.
- Davies, G. L. H., & Stephens, N. (1978). *Geomorphology of the British Isles*. London: Methuen.
- Davies, J. L. (1972). *Geographical variation in coastal development*. New York: Oliver and Boyd.

- Davies, P., Williams, A. T., & Bomboe, P. (1998). Numerical analysis of coastal cliff failure along the Pembrokeshire Coast National Park, Wales, UK. *Earth Surface Processes and Landforms*, 23(12), pp. 1123-1134. [Online] DOI: 10.1002/(SICI)1096-9837(199812)23:12<1123::AID-ESP945>3.0.CO;2-F
- De Freitas, M. H. (1972). Some examples of cliff failure in South West England. *Proceedings of the Ussher Society*, 2(5), pp. 388-397.
- De Freitas, M. H., & Watters, R. J. (1973). Some field examples of toppling failure. *Géotechnique*, 23(4), pp. 495-513. [Online] DOI: 10.1680/geot.1973.23.4.495
- Department of Environment, Food and Rural Affairs - DEFRA. (2007). *Environment Agency Strategic Overview for Flood and Coastal Erosion Risk Management*. England: Crown Copyright.
- Department of Environment, Food and Rural Affairs – DEFRA. (2009a). Appraisal of flood and coastal erosion risk management: a Defra policy statement. London: Crown Copyright.
- Department of Environment, Food and Rural Affairs - DEFRA. (2009b). *A Strategy for Promoting an Integrated Approach to the Management of Coastal Areas in England*. England: Crown Copyright.
- Department of Environment, Food and Rural Affairs – DEFRA. (2010). Adapting to coastal change: developing a policy framework. London: Crown Copyright.
- Department of Environment, Food and Rural Affairs –DEFRA. (2006). Shoreline management plans guidance. London: Crown Copyright.
- Dijkstra, T., & Dixon, N. (2010). Climate change and slope stability in the UK: challenges and approaches. *Quarterly Journal of Engineering Geology and Hydrogeology*, 43, pp. 371-385. [Online] DOI: 10.1144/1470-9236/09-036
- Dikau, R., Brunsden, D., Schrott, L., & Ibsen, M. (Eds.). (1996). *Landslide Recognition: Identification, movement and causes*. Chichester: Wiley & Sons.
- Dong, P., & Guzzetti, F. (2005). Frequency-size statistics of coastal soft-cliff erosion. *Journal of Waterway, Port, Coastal, and Ocean Engineering*, 131(1), pp. 37-42.
- Dornbusch, U. (2015). Comment on: Lawrence, J.A., Mortimore, R.N., Stone, K.J., Busby, J.P., 2013. Sea saltwater weakening of chalk and the impact on cliff instability. *Geomorphology*, 191, 14–22. *Geomorphology*, 231, pp. 390-392. [Online] DOI: 10.1016/j.geomorph.2014.10.038
- Dornbusch, U., Robinson, D. A., Moses, C. A., & Williams, R. B. G. (2008). Temporal and spatial variations of Chalk cliff retreat in East Sussex, 1873 to 2001. *Marine Geology*, 249(3-4), pp. 271-282. [Online] DOI: 10.1016/j.margeo.2007.12.005
- Dornbusch, U., Robinson, D. A., Williams, R. B. G., & Moses, C. A. (2007). Chalk shore platform erosion in the vicinity of sea defence structures and the impact of construction methods. *Coastal Engineering*, 54(11), pp.801-810. [Online] DOI: 10.1016/j.coastaleng.2007.05.012

- Dornbusch, U., Robinson, D., Moses, C., & Williams, R. B. (2006a). Chalk coast erosion and its contribution to the shingle budget in East Sussex. *Zeitschrift für Geomorphologie*, 144, pp. 215-230.
- Dornbusch, U., Robinson, D., Moses, C., Williams, R. B., & Costa, S. (2006b). Retreat of chalk cliffs in the eastern English Channel during the last century. *Journal of Maps*, 2(1), pp. 71-78. [Online] DOI: 10.4113/jom.2006.46
- Duperret, A., Taibi, S., Mortimore, R. N., & Daigneault, M. (2005). Effect of groundwater and sea weathering cycles on the strength of chalk rock from unstable coastal cliffs of NW France. *Engineering Geology*, 78(3-4), pp. 321-343. [Online] DOI: 10.1016/j.enggeo.2005.01.004
- Dussauge, C., Grasso, J.-R., & Helmstetter, A. (2003). Statistical analysis of rock fall volume distributions: implications for rock fall dynamics. *Journal of Geophysical Research*, 108(B6), 2286. [Online] DOI: 10.1029/2001JB000650
- Eisenbeiß, H. (2009). *UAV Photogrammetry* (Unpublished doctoral Thesis). University of Technology Dresden, Zurich. Retrieved from www.igp-data.ethz.ch/berichte/blaue_berichte_pdf/105.pdf
- Emery, K. O., & Kuhn, G. G. (1980). Erosion of rock shores at La Jolla, California. *Marine Geology*, 37(3-4), pp.197-208.
- Emery, K. O., & Kuhn, G. G. (1982). Sea cliffs: their processes, profiles, and classification. *Geological Society of America Bulletin*, 93, pp.644-654.
- Environment Agency – EA. (2009). Beachy Head to Selsey Bill Shoreline Management Plan. [Online] URL: <https://www.gov.uk/government/publications/shoreline-management-plans-smmps/shoreline-management-plans-smmps>
- Eos Systems. (2017). Photo Modeler: Are parameter correlation warnings in the Project Status Report after a calibration something that needs further action? Retrieved from http://info.photomodeler.com/blog/kb/are_parameter_correlation_warnings_in_th/
- Fahey, B. D. (1985). Salt weathering as a mechanism of rock breakup in cold climates: An experimental approach. *Zeitschrift für Geomorphologie*, 29(1), pp. 99-111.
- Fell, R., Ho, K. K. S., Lacasse, S., & Leroi, E. (2005). A Framework for Landslide Risk Assessment and Management, in Hungr, O., Fell, R., Couture, R., & Eberhardt, E. (eds.) *Landslide Risk Management*. Canada: Balkema.
- Fletcher, M. S., & Mizon, D. H. (1984). 'Piles in Chalk for Orwell Bridge', in Proceedings Institution of Civil Engineers Conference. *Piling and Ground Treatment*. London: Thomas Telford, pp.203-209.
- FLIR. (2015). *FLIR Research and Science: Use low-cost materials to increase target emissivity*. Retrieved from <http://www.flir.com/science/blog/details/?ID=71556>

- Fookes, P. G., & Hawkins, A. B. (1988). Limestone weathering: its engineering significance and a proposed classification. *Quarterly Journal of Engineering Geology*, 21, pp. 7-31.
- Fookes, P. G., Lee, E. M., & Griffiths, J. S. (2012). *Engineering Geomorphology Theory and Practice*. Dunbeath: Whittles Publishing.
- Fraser, C. S., & Cronk, S. (2009). A hybrid measurement approach for close-range photogrammetry. *ISPRS Journal of Photogrammetry and Remote Sensing*, 64(3), pp. 328-333. [Online] DOI: 10.1016/j.isprsjprs.2008.09.009
- Fuller, R. M. (1983). 'Aerial photographs as records of changing vegetation patterns', in Fuller, R. M. (Ed.) *Ecological mapping from ground, air and space. (ITE Symposium, 10)*. UK: NERC/ITE, pp.57-68.
- Genz, A. S., Fletcher, C. H., Dunn, R. A., Frazer, L. N. & Rooney, J. J. (2007). The predictive accuracy of shoreline change rate methods and alongshore beach variation on Maui, Hawaii. *Journal of Coastal Research*, v. 23(1), pp.87-105. [Online] DOI: 10.2112/05-0521.1
- Geomorphological Services Limited. (1986). *Review of Landsliding in Great Britain*. Reports to the Department of the Environment.
- Gonçalves, J. A., & Henriques, R. (2015). UAV photogrammetry for topographic monitoring of coastal areas. *ISPRS Journal of Photogrammetry and Remote Sensing*, 104, pp. 101-111. DOI: 10.1016/j.isprsjprs.2015.02.009
- Goodman, R. E. (1976). *Methods of Geological Engineering in Discontinuities Rocks*. Mennnesota: West Publishing Company.
- Goodman, R. E. (1989). *Introduction to Rock Mechanics*. New York: John Wiley and Sons.
- Goudie, A. S. (1974). Further experimental investigation of rock weathering by salt crystallisation and other mechanical processes. *Zeitschrift für Geomorphologie*, 21, pp.1-12.
- Graham, R., & Koh, A. (2002). *Digital Aerial Survey: Theory and Practice*. Caithness, Scotland: Whittles Publishing.
- Greenwood, R. O., & Orford, J. D. (2007). Factors controlling the retreat of Drumlin coastal cliffs in a low energy marine environment – Strangford Lough, Northern Ireland. *Journal of Coastal Research*, 23(2), 285-297. [Online] DOI: 10.2112/04-0417.1
- Griggs, G. B., & Trenhaile, A. S. (1994). 'Coastal cliffs and platforms', in Carter, R. W. G., & Woodroffe, C. D. (eds.) *Coastal Evolution Late Quaternary shoreline morphodynamics*. Cambridge: Cambridge University Press, pp. 425-450.
- Guilcher, A. (1958). *Coastal and Submarine Morphology*. London: Methuen.
- Guthrie, R., & Evans, S. (2004). Analysis of landslide frequencies and characteristics in a natural system. Coastal British Columbia. *Earth Surface Processes and Landforms*, 29(11), pp. 1321–1339. [Online] DOI: 10.1002/esp.1095

- Guzzetti, F., Malamud, B., Turcotte, D., & Reichenbach, P. (2002). Power-law correlations of landslide areas in central Italy. *Earth and Planetary Science Letters*, 195(3-4), pp. 169–183. DOI: 10.1016/S0012-821X(01)00589-1
- Haala, N., & Rothermel, M. (2012). Dense Multi-Stereo Matching for High Quality Digital Elevation Models. *PFG Photogrammetrie-Fernerkundung-Geoinformation*, 2012(4), pp. 331-343. DOI: 10.1127/1432-8364/2012/0121
- Hackney, C., Darby, S. E., & Leyland, J. (2013). Modelling the response of soft cliffs to climate change: A statistical, process-response model using accumulated excess energy. *Geomorphology*, 187, pp. 108-121. [Online] DOI: 10.1016/j.geomorph.2013.01.005
- Halcrow Group Ltd. (2002). *'Futurecoast' study for DEFRA*. Crown Copyright.
- Halcrow Group Ltd. (2006). *Risk Assessment of Coastal Erosion (RACE)*. Technical report (2 volumes) to DEFRA.
- Hales, T. C., & Roering, J. J. (2007). Climatic controls on frost cracking and implications for the evolution of bedrock landscapes. *Journal of Geophysical Research Earth Surface*, 112(F2). [Online] DOI: 10.1029/2006JF000616
- Hall, J. W., Meadowcroft, I. C., Lee, E. M., & van Gelder, P. H. A. J. M. (2002). Stochastic simulation of episodic soft coastal cliff recession. *Coastal Engineering*, 46(3), pp. 159-174. [Online] DOI: 10.1016/S0378-3839(02)00089-3
- Hallet, B. (1983). The breakdown of rock due to freezing: a theoretical model. *Proceedings of the 4th International conference on Permafrost*, pp. 433-438. Washington D.C.: National Academy Press.
- Hancock, P. L. (1985). Brittle microtectonics: principles and practice. *Journal of Structural Geology*, 7(3-4), pp.437-457. [Online] DOI: 10.1016/0191-8141(85)90048-3
- Hantz, D., Vengeon, J. M., & Dussage-Peisser, C. (2003). An historical, geomechanical and probabilistic approach to rock-fall hazard assessment. *Natural Hazards and Earth System Science*, 3, pp. 693-701. [Online] DOI: 10.5194/nhess-3-693-2003
- Hencher, S. (2012). *Practical Engineering Geology*. London: CRC Press – Taylor & Francis Group.
- Hencher, S. R., Liao, Q.H., & Monaghan, B. G. (1996). Modelling of slope behaviour for open pits. *Transactions of the Institution of Mining and Metallurgy – Section A*, 105, pp. A37-A47.
- High-Point Rendel. (2002). *Brighton Marina Cliff Stabilisation As Built Report – Report No. R/001331/AB/1*. London: High-Point Rendel.
- High-Point Rendel. (2005). *Black Rock Stage 2 Cliff Stabilisation, Brighton Marina Quantitative Risk Assessment: Black Rock*. Brighton and Hove City Council: Brighton.
- High-Point Rendel. (2006). *Black Rock Stage 2 Cliff Stabilisation Works – Report No. R/2419/03*. London: High-Point Rendel.

- Himmelstoss, E. A. (2009) – ‘DSAS 4.0 Installation Instructions and User Guide’ in Thieler, E. R., Himmelstoss, E. A., Zichichi, J. L., & Ayhan, E. *Digital Shoreline Analysis System (DSAS) version 4.0 — An ArcGIS extension for calculating shoreline change*. U.S. Geological Survey Open-File Report 2008-1278 updated for version 4.3.
- Hoek, E., & Bray, J. W. (1981). *Rock Slope Engineering* (3rd Ed.). London: Institute of Mining and Metallurgy.
- Honkavaara, E., Ahokas, E., Hyyppä, J., Jaakkola, J., Kaartinen, H., Kuitinen, R., & Nurminen, K. (2006). Geometric test field calibration of digital photogrammetric sensors. *ISPRS Journal of photogrammetry and Remote Sensing*, 60(6), 387-399. [Online] DOI: 10.1016/j.isprsjprs.2006.04.003
- Hooke, J. M. (1999). Decades of change: contributions of geomorphology to fluvial and coastal engineering and management. *Geomorphology*, 31(1-4), pp. 373-389. [Online] DOI: 10.1016/S0169-555X(99)00083-5
- Hopson, P. M. (2005). A stratigraphical framework for the Upper Cretaceous Chalk of England and Scotland, with statements on the Chalk of Northern Ireland and the UK offshore sector. *British Geological Survey Research Report*, RR/05/01.
- Hovius, N., Stark, C., & Allen, P. (1997). Sediment flux from a mountain belt derived by landslide mapping. *Geology*, 25(3), pp. 231–234. [Online] DOI: 10.1130/0091-7631(1997)025<0231:SFFAMB>2.3.CO;2
- Huang, Y. D. (2000). Evaluation of information loss in digital elevation models with digital photogrammetric systems. *The Photogrammetric Record*, 16(95), pp. 781-791. [Online] DOI: 10.1111/0031-868X.00151
- Hughenoltz, C. H., Whitehead, K., Brown, O. W., Barchyn, T. E., Moorman, B. J., LeClair, A., Riddell, K., & Hamilton, T. (2013). Geomorphological mapping with a small unmanned aircraft system (sUAS): Feature detection and accuracy assessment of a photogrammetrically-derived digital terrain model. *Geomorphology*, 194, pp. 16-24. DOI:10.1016/j.geomorph.2013.03.023
- Hungr, O., Leroueil, S., & Picarelli, L. (2014) The Varnes classification of landslide types, an update. *Landslides*, 11(2), pp. 167-194. [Online] DOI: 10.1007/s10346-013-0436-y
- Hurst, M. D., Rood, D. H., Ellis, M. A., Anderson, R. S., & Dornbusch, U. (2016). Recent acceleration in coastal cliff retreat rates on the south coast of Great Britain. *Proceedings of the National Academy of Sciences of the United States of America*, 113(47), pp. 13336-13341. [Online] DOI: 10.1073/pnas.1613044113
- Hutchinson, J. N. (1972). ‘Field and laboratory studies of a fall in Upper Chalk cliffs at Joss Bay, Isle of Thanet’, in Parry, R. H. G (Ed.) *Stress-Strain Behaviour of Soils, Proceedings of the Roscoe Memorial Symposium*, pp. 692-706. Henley-on-Thames: G.T. Foulis.
- Hutchinson, J. N. (1975). *The response of London Clay cliffs to differing rates of toe erosion. Building Research establishment Paper CP27/75*. Watford.

- Hutchinson, J. N. (2002). 'Chalk flows from the coastal cliff or northwest Europe', in Evans, S. G., & DeGraff, J. V. (Eds.) *Catastrophic Landslides: Effects, Occurrences and Mechanisms*. Boulder, Colorado: Geological Society of America Reviews in Engineering Geology, pp. 257-302.
- Jaeger, J. C. (1971). Friction of rocks and stability of rock slopes. *Geotechnique*, 21(2), pp.97-134.
- James, M. R., & Robson, S. (2012). Straightforward Reconstruction of 3D Surfaces and Topography with a Camera: Accuracy and Geoscience Application. *Journal of Geophysical Research: Earth Surface*, 117(F3), pp.1-17. [Online] DOI:10.1029/2011JF002289
- Jerwood, L. C., Robinson, D. A., & Williams, R. B. G. (1990). Experimental frost and salt weathering of Chalk-II. *Earth Surface Process and Landforms*, 15(8), pp. 699-708. [Online] DOI: 10.1002/esp.3290150804
- Katz, O., & Mushkin, A. (2013). Characteristics of sea-cliff erosion induced by a strong winter storm in the eastern Mediterranean. *Quaternary Research*, 80(1), pp. 20-32. [Online] DOI: 10.1016/j.yqres.2013.04.004
- Kazhdan, M., & Hoppe, H. (2013a). *Screened Poisson Surface Reconstruction (Version 6.13a)*. Retrieved from <http://www.cs.jhu.edu/~misha/Code/PoissonRecon/Version6.13a/>
- Kazhdan, M., & Hoppe, H. (2013b). Screened poisson surface reconstruction. *ACM Transactions on Graphics (TOG)*, 32(3), pp. 1-13. [Online] DOI: 10.1145/2487228.2487237
- Kazhdan, M., Bolitho, M., & Hoppe, H. (2006). Poisson surface reconstruction. In K. Polthier, & A. Sheffer (Eds.), *Eurographics Symposium on Geometry Processing (SGP)* (pp. 61-70). Airela-Ville, Switzerland : Eurographics Association.
- Kennedy, D. M. (2014). 'The rock coast of Australia', in Kennedy, D. M., Stephenson, W. J., & Naylor, L. A. (Eds.) *Rock Coast Geomorphology: A Global Synthesis*. London: Geological Society Memoirs, 40, pp. 235-246
- Kennedy, D. M., Stephenson, W. J., & Naylor, L. A. (Eds.). (2014). *Rock Coast Geomorphology: A Global Synthesis*. London: Geological Society Memoirs, 40, pp. 1-6
- Keutterling, A., & Thomas, A. (2006). Monitoring glacier elevation and volume changes with digital photogrammetry and GIS at Gepatschferner glacier, Austria. *International Journal of Remote Sensing*, 27(19), pp. 4371-4380. [Online] DOI: 10.1080/01431160600851819
- Kimber, O. G., Allison, R. J., & Cox, N. J. (1998). Mechanisms of failure and slope development in rock masses. *Transactions of the Institute of British Geographers*, 23(3), pp. 353-370. [Online] DOI: 10.1111/j.0020-2754.1998.00353.x
- King, C. A. M. (1972). *Beaches and Coasts* (2nd edn.). London: Edward Arnold.
- Kliche, C.A. (1999). *Rock Slope Stability*. Littleton, Colorado: Society for Mining Metallurgy and Exploration (SME).

- Kline, S. W., Adams, P. N., & Limber, P. W. (2014). The unsteady nature of sea cliff retreat due to mechanical abrasion, failure and comminution feedbacks. *Geomorphology*, 219, pp. 53-67. [Online] DOI: 10.1016/j.geomorph.2014.03.037
- Kloehn, K. K., Beechie, T. J., Morely, S. A., Coe, H. J., & Duda, J. J. (2008). Influence of dams on river-floodplain dynamics in the Elwha River, Washington. *Northwest Scientific Association*, 82, (Special Issue), pp.224-235. [Online] DOI: 10.3955/0029-344X-82.S.I.224
- Konecny, G. (2003). *Geoinformation: remote sensing, photogrammetry and geographic information systems* (1st ed.). London: Taylor & Francis.
- Konecny, G. (2014). *Geoinformation: Remote Sensing, Photogrammetry and Geographic Information Systems* (2nd ed.). London: CRC Press.
- Korup, O. (2005). Distribution of landslides in southwest New Zealand. *Landslides*, 2(1), pp. 43–51. [Online] DOI: 10.1007/s10346-004-0042-0
- Krosley, L. K., Shaffner, P. T., Oerter, E., & Ortiz, T. (2006). *Digital ground-based photogrammetry for measuring discontinuity orientations in steep rock exposures*. Proceedings of the 41st US Symposium of Rock Mechanics, pp. 1-13. Colorado: Golden.
- Kutter, H. K. (1974). 'Analytical methods for rock slope analysis', in Muller, L. (Ed.) *Rock Mechanics*. New York: Springer, pp.198-211.
- Lageat, Y., Hénaff, A., & Costa, S. (2006). The retreat of the chalk cliffs of the Pays-de-Caux (France): erosion processes and patterns. *Zeitschrift für Geomorphologie*, 144, pp. 183-197.
- Lake, L. M. (1975). *The engineering properties of chalk with special reference to foundation design and performance* (Unpublished doctoral thesis). University of Surrey, UK.
- Lane, S. N. (2000). The measurement of river channel morphology using digital photogrammetry. *The Photogrammetric Record*, 16(96), pp. 937-961. [Online] DOI: 10.1111/0031-868X.00159
- Lawrence, J. A. (2007). *Engineering properties of Chalk in relation to coastal cliff slope stability* (unpublished doctoral thesis). University of Brighton: Brighton, UK.
- Lawrence, J. A., & Mortimore, R. N. (2015). Reply to comment on: Lawrence, J.A., Mortimore, R.N., Stone, K.J., and Busby, J.P., 2013. Sea saltwater weakening of chalk and the impact on cliff instability. *Geomorphology* 191, 14–22. *Geomorphology*, 231, pp. 393-394. [Online] DOI: 10.1016/j.geomorph.2014.10.031
- Lawrence, J. A., Mortimore, R. N., Stone, K. J., & Busby, J. P. (2013). Sea salt weakening of Chalk and the impact of cliff instability. *Geomorphology*, 191, pp. 14–22. [Online] DOI: 10.1016/j.geomorph.2013.02.022
- LCHF. (1972). *Etude de la production des galets sur le littoral haut-normand*. France: Laboratoire Central d'Hydraulique.

- Leake, J., Wolf, J., Lowe, J., Hall, J., & Nicholls, R. (2009). 'Response of marine climate to future climate change: application to coastal regions.' in McKee Smith, J. (Ed.) *Proceedings of the 31st International Conference on Coastal Engineering*, pp. 4354-4364.
- Lee, E. M. (1997). The investigation and management of soft rock cliffs. *Proceedings of MAFF conference for Rivers and Coastal Engineers*, B.1.1-B.1.12.
- Lee, E. M. (2005). Coastal cliff recession risk: a simple judgement-based model. *Quarterly Journal of Engineering Geology and Hydrogeology*, 38, pp.89-104. [Online] DOI: 10.1144/1470-9236/04-055
- Lee, E. M., & Clark, A. R. (2002). *Investigation and Management of soft rock cliffs*. London: Thomas Telford.
- Lee, E. M., & Jones, D. K. C. (2004). *Landslide Risk Assessment*. London: Thomas Telford Publishing.
- Lee, E. M., & Jones, D. K. C. (2014). *Landslide Risk Assessment* (2nd edn.). London: ICE Publishing.
- Lee, E. M., Hall, J. W., & Meadowcroft, I. C. (2001). Coastal cliff recession: the use of probabilistic prediction methods. *Geomorphology*, 40(3-4), pp. 253-269. [Online] DOI: 10.1016/S0169-555X(01)00053-8
- Lim, M. (2006). *Coastal cliff evolution with reference to Staithes, North Yorkshire*. (Unpublished doctoral Thesis). Durham University, Durham, UK. URL: <http://etheses.dur.ac.uk/1809/>
- Lim, M. (2014). 'The rock coast of the British Isles: cliffs', in Kennedy, D. M., Stephenson, W. J., & Naylor, L. A. (Eds.) *Rock Coast Geomorphology: A Global Synthesis*. London: Geological Society Memoirs, 40, pp. 19-38.
- Lim, M., Petley, D. N., Rosser, N. J., Allison, R. J., Long, A. J., & Pybus, D. (2005). Combined digital photogrammetry and time-of-flight laser scanning for monitoring cliff evolution. *The Photogrammetric Record*, 20(110), pp.109-129. [Online] DOI: 10.1111/j.1477-9730.2005.00315.x
- Lim, M., Rosser, N. J., Allison, R. J., & Petley, D. N. (2010). Erosional processes in the hard rock coastal cliffs at Staithes, North Yorkshire. *Geomorphology*, 114(1-2), pp. 12-21. [Online] DOI: 10.1016/j.geomorph.2009.02.011
- Lim, M., Rosser, N. J., Petley, D. N., & Keene, M. (2011). Quantifying the controls and influence of tide and wave impacts on coastal rock cliff erosion. *Journal of Coastal Research*, 27(1), 46-56. [Online] DOI: 10.2112/JCOASTRES-D-09-00061.1
- Linder, W. (2003). *Digital Photogrammetry. Theory and Applications*. Berlin: Springer.
- Lord, J. A., Clayton, C. R. I., & Mortimore, R. N. (2002). *Engineering in Chalk*. London: CIRIA.

- Lowe, J. A., Howard, T. P., Pardaens, A., Tinker, J., Holt, J., Wakelin, S., Milne, G., Leake, J., Wolf, J., Horsburgh, K., Reeder, T., Jenkins, G., Ridley, J., Dye, S., & Bradley, S. (2009). *UK Climate projections science report: Marine and coastal projections*. Exeter, UK: Met Office Hadley Centre.
- Luhman, T., Fraser, C., & Maas, H-G. (2016) Sensor modelling and camera calibration for close-range photogrammetry. *ISPRS Journal of Photogrammetry and Remote Sensing*, 115, pp. 37-46. [Online] DOI: 10.1016/j.isprsjprs.2015.10.006
- Luhman, T., Robson, S., Kyle, S., & Harley, I. (2011). *Close Range Photogrammetry: Principles, techniques and applications*. Scotland: Whittles Publishing.
- Luhmann, T., Robson, S., Kyle, S., & Boehm, J. (2013). *Close Range Photogrammetry and 3D Imaging* (2nd ed.). Berlin: De Gruyter.
- Malamud, B., Turcotte, D., Guzzetti, F., & Reichenbach, P. (2004). Landslide inventories and their statistical properties. *Earth Surface Processes and Landforms*, 29(6), pp. 687–711. [Online] DOI: 10.1002/esp.1064
- Mandl, G. (2005). *Rock Joints The mechanical genesis*. New York: Springer.
- Marques, F. M. S. F. (2008). Magnitude–frequency of sea cliff instabilities. *Natural Hazards and Earth System Sciences*, 8(5), pp. 1161–1171. [Online] DOI: 10.5194/nhess-8-1161-2008
- Marzloff, I., & Poesen, J. (2009). The potential of 3D gully monitoring with GIS using high-resolution aerial photography and digital photogrammetry system. *Geomorphology*, 111(1-2), pp. 48-60. [Online] DOI: 10.1016/j.geomorph.2008.05.047
- Matthews, N. A. (2008). *Aerial and close-range photogrammetric technology: providing resource documentation, interpretation, and preservation*. Technical Note 428. Denver, Colorado: Bureau of Land Management. Retrieved from www.blm.gov/nstc/library/pdf/TN428.pdf
- May, V. J. (1971). The retreat of chalk cliffs. *The Geographical Journal*, 137(2), pp. 203-206. [Online] URL: <http://www.jstor.org/stable/1796740>
- May, V. J. (2003) – ‘Beachy Head – Seaford Head Chapter 4: Soft Rock Cliffs’ in May, V. J., & Hansom, J. D. *Coastal Geomorphology of Great Britain. Geological Conservation Review Series, No. 28*. Peterborough: Joint Nature Conservation Committee, 10.
- May, V. J., & Heeps, C. (1985). The nature and rates of change of Chalk coastlines. *Zeitschrift für Geomorphologie, Supplementband*, 57, pp. 81-94.
- McGreevy, J. P. (1982). Frost and salt weathering: further experimental results. *Earth Surface Processes and Landforms*, 7(5), pp. 475-488. [Online] DOI: 10.1002/esp.3290070508
- McInnes, R. G. (2009). *A Non-Technical Guide to Coastal Risk Management*, Report for SCOPAC.
- McInnes, R. G., & Moore, R. (2011). *Cliff instability and erosion management in Great Britain – A Good Practice Guide*. Birmingham: Halcrow Group Ltd.

- Met Office. (2016). *UK climate – Historic station data*. Retrieved from <http://www.metoffice.gov.uk/public/weather/climate-historic/#?tab=climateHistoric>
- Mineo, S., Pappalardo, G., Rapisarda, F., Cubito, A., & Di Maria, G. (2015). Integrated geostructural, seismic and infrared thermography surveys for the study of an unstable rock slope in the Peloritani Chain (NE Sicily). *Engineering Geology*, 195, pp. 225-235. [Online] DOI: 10.1016/j.enggeo.2015.06.010
- Mitchell, S.B., & Pope, D.J. (2004). 'Prediction of nearshore wave energy distribution by analysis of numerical wave model output: East Sussex coastline, UK', in Mortimore, R. N., & Duperret, A. (Eds.) *Coastal Chalk Cliff Instability*. London: Geological Society, Engineering Geology Special Publications, pp. 99-108.
- Monroe Infrared. (2014). *Monroe Infrared Knowledgebase: A guide to thermal imaging cameras: How do I take a good infrared thermal image?* Retrieved from <http://monroeinfrared.com/knowledgebase/a-guide-to-thermal-imaging-cameras/how-do-i-take-a-good-infrared-thermal-image>
- Moore, J. R., Sanders, J. W., Dietrich, W. E., & Glaser, S. D. (2009). Influence of rock mass strength on the erosion rate of alpine cliffs. *Earth Surface Processes and Landforms*, 34(10), pp. 1339-1352. [Online] DOI: 10.1002/esp.1821
- Moore, L. J. (2000). Shoreline mapping techniques. *Journal of Coastal Research*, 16(1), pp. 111-124. [Online] URL: <http://www.jstor.org/stable/4300016>
- Moore, R., & Davis, G. (2015) – Cliff instability and erosion management in England and Wales. *Journal of Coastal Conservation*, 19(6), pp. 771-784. DOI: 10.1007/s11852-014-0359-3
- Moore, R., Carey, J., & McInnes, R. (2010a). Landslide Behaviour and Climate Change: Predictable consequences for the Ventnor Undercliff, Isle of Wight. *Quarterly Journal of Engineering Geology*, 43, pp. 447-460.
- Moore, R., Carey, J., McInnes, R. G., & Houghton, J. (2007). Climate change, so what? Implications for ground movement and landslide event frequency in the Ventnor Undercliff, Isle of Wight. *Proceedings of the International Conference on Landslides and Climate Change*, Ventnor, Isle of Wight, pp. 335-344.
- Moore, R., Clark, A. R., & Lee, E. M. (1998). 'Coastal cliff behaviour and management: Blackgang, Isle of Wight', in Maund, J. G., & Eddleston, M (Eds.) *Geohazards and engineering geology*. London: Geological Society, Engineering Geology Special Publications, 15, pp. 49-59.
- Moore, R., Fish, P., Glennerster, M., & Bradbury, A. (2003) – *Cliff behaviour assessment: a quantitative approach using digital photogrammetry and GIS*. 38th DEFRA Flood and Coastal Management Conference, 1-11.
- Moore, R., Rogers, J., Woodget, A., & Baptiste, A. (2010b). *Climate change impact on cliff instability and erosion in the UK*. In Proceedings of the Environment Agency Annual Conference of River and Coastal Engineers, Telford International Centre.

- Morgan, J. L., Gergek, S. E., & Coops, N. C. (2010) – Aerial Photography: A rapidly evolving tool for ecological management. *BioScience*, 60(1), 47-59. DOI: 10.1525/bio.2010.60.1.9
- Moritmore, R., & Lawrence, J. (2008). *Long-term monitoring programme for the cliffs between Black Rock and Saltdean, INFORM PROJECT – Annual Report 1, 2007*. Brighton: University of Brighton Civil Engineering and Geology Division.
- Mortimore, R. N. (1983). The stratigraphy and sedimentation of the Turonian–Campanian in the Southern Province of England. *Zitteliana*, 10, pp.27–41. [Online] URL: https://www.zobodat.at/pdf/Zitteliana_10_0027-0041.pdf
- Mortimore, R. N. (1986a) Stratigraphy of the Upper Cretaceous White Chalk of Sussex. *Proceedings of the Geologists' Association*, 97(2), pp.97–139. [Online] DOI: 10.1016/S0016-7878(86)80065-7
- Mortimore, R. N. (1986b) 'Controls on Upper Cretaceous sedimentation in the South Downs with particular reference to flint distribution', in Sieveking, G., & Hart, M. B. (Eds.) *The Scientific Study of Flint and Chert*. Cambridge: Cambridge University Press, pp.21–42.
- Mortimore, R. N., Lawrence, J., Pope, D., Duperret, A., & Genter, A. (2004a). 'Coastal cliff geohazards in weak rock: the UK Chalk cliffs of Sussex', in Mortimore, R. N., & Duperret, A. (Eds.) *Coastal Chalk Cliff Instability*. London: Geological Society, Engineering Geology Special Publications, pp. 3-32.
- Mortimore, R. N., Stone, K. J., Lawrence, J., & Duperret, A. (2004b). 'Chalk physical properties and cliff instability', in Mortimore, R. N., & Duperret, A. (Eds.) *Coastal Chalk Cliff Instability*. London: Geological Society, Engineering Geology Special Publications, pp. 75-88.
- Mortimore, R., & Duperret, A. (Eds.). (2004). *Coastal Chalk Cliff Instability*. London: Geological Society, Engineering Geology Special Publications.
- Mortimore, R., & Duperret, A. (Eds.). (2004). *Coastal Chalk Cliff Instability*. London: Geological Society, Engineering Geology Special Publications.
- Mortimore, R., Wood, C., & Gallois, R. (2001). *Geological Conservation Review, Volume 23: British Upper Cretaceous Stratigraphy, Chapter 3: Southern Province England, Site: Newhaven to Brighton*. Available from: <http://jncc.defra.gov.uk/default.aspx?page=4174&gcr=216> (Accessed 10 November 2013).
- Moses, C. A. (2014). 'The rock coast of the British Isles: shore platforms', in Kennedy, D. M., Stephenson, W. J., & Naylor, L. A. (Eds.) *Rock Coast Geomorphology: A Global Synthesis*. London: Geological Society Memoirs, 40, pp. 39-56.
- Murphy, J.M., Sexton, D.M.H., Jenkins, G.J., Boorman, P.M., Booth, B.B.B., Brown, C.C., Clark, R.T., Collins, M., Harris, G.R., Kendon, E.J., Betts, R.A., Brown, S.J., Howard, T. P., Humphrey, K. A., McCarthy, M. P., McDonald, R. E., Stephens, A., Wallace, C., Warren, R., Wilby, R., & Wood, R. A. (2009). *UK Climate Projections Science Report: Climate change projections*. Exeter, UK: Met Office Hadley Centre.

- Natural Environment Research Council – NERC (2016). British Geological Onshore Digital Maps (WMS service). Retrieved from: <http://bgs.ac.uk/data/services/digmap50wms.html>
- Paine, D. P., & Kiser, J. D. (2003) – *Aerial Photography and Image Interpretation* (2nd Ed.) – New Jersey: Wiley & Sons.
- Nex, F., & Remondino, F. (2014). UAV for 3D mapping applications: a review. *Applied Geomatics*, 6(1), pp. 1-15. DOI: 10.1007/s12518-013-0120-x
- Niethammer, U., Rothmund, S., James, M. R., Traveletti, J., & Joswig, M. (2010). UAV-based remote sensing of landslides. *International Archives of Photogrammetry, Remote Sensing and Spatial Information Sciences, Vol. XXXVIII, Part 5 Commission V Symposium, Newcastle upon Tyne, UK*, pp. 496-501.
- Norman, J. M., & Becker, F. (1995). Terminology in thermal infrared remote sensing of natural surfaces. *Remote Sensing Reviews*, 12(3-4), pp. 159-173. [Online] DOI: 10.1080/02757259509532284
- Orford, J. D. (1978). *Methods of identifying and interpreting the dynamics of littoral zone facies using particle size and form, with special reference to beach gravel sedimentation* (Unpublished doctoral thesis). University of Reading, Reading, UK.
- Oyedotun, T. D. T. (2014). 'Section 3.2.2. Shoreline Geometry: DSAS as a tool for historical trend analysis', in Clarke, L., & Nield, J. M. (Eds.) *Geomorphological Techniques* (Online Edition). London: British Society for Geomorphology. [Online] URL: http://geomorphology.org.uk/sites/default/files/geom_tech_chapters/3.2.2_ShorelineGeometry.pdf
- Park, H., & West, T. R. (2001). Development of a probabilistic approach for rock wedge failure. *Engineering Geology*, 59(3-4), pp.233-251. [Online] DOI: 10.1016/S0013-7952(00)00076-4
- Pethick, J. (1984). *An Introduction to Coastal Geomorphology*. London: Edward Arnold.
- Phillips, B. (1969). *Cliff and Shore Platform Development in the Isle of Man* (Unpublished doctoral Thesis). University of Wales, Aberystwyth, Wales.
- Pierre, G., & Lahousse, P. (2006). The role of groundwater in cliff instability: an example at Cap Blanc-Nez (Pas-de-Calais, France). *Earth Surface Processes and Landforms*, 31(1), pp. 31-45. [Online] DOI: 10.1002/esp.1229
- Prêcheur, C. (1960). Le littoral de la Manche: de Saint-Adresse à Ault. *Etude morphologique, Norois*, n° hors-série, pp. 1–138.
- Pritchard, M. A., & Savigny, K. W. (1990). Numerical modelling of toppling. *Canadian Geotechnical Journal*, 27(6), pp. 823-834. [Online] DOI: 10.1139/t90-095
- Quinn, J. D., Rosser, N.J., Murphy, W., & Lawrence, J. A. (2010). Identifying the behavioural characteristics of clay cliffs using intensive monitoring and geotechnical numerical modelling. *Geomorphology*, 120(3-4), pp. 107-122. [Online] DOI: 10.1016/j.geomorph.2010.03.004

- Rehak, M., Mabillard, R., & Skaloud, J. (2013). A Micro-Uav with the Capability of Direct Georeferencing. *ISPRS - International Archives of the Photogrammetry, Remote Sensing and Spatial Information Sciences*, 40(1), pp.317-323. [Online] DOI: 10.5194/isprsarchives-XL-1-W2-317-2013
- Remondino, F., & El-Hakim, S. (2006). Image-based 3D modelling: a review. *The Photogrammetric Record*, 21(115), pp. 269-291. [Online] DOI: 10.1111/j.1477-9730.2006.00383.x
- Remondino, F., Barazzetti, L., Nex, F., Scaioni, M., & Sarazzi, D. (2011). UAV Photogrammetry for mapping and 3D modelling – current status and future perspectives. *International Archives of the Photogrammetry, Remote Sensing and Spatial Information Sciences, Volume XXXVIII-1/C22, 2011 ISPRS Zurich 2011 Workshop, 14-16 September 2011, Zurich, Switzerland*.
- Rendel Geotechnics. (1995). *Prediction of rates of recession of soft cliffs*. Interim Report to MAFF.
- Rio, L. D., & Gracia, J. F. (2009). Erosion risk assessment of active coastal cliffs in temperate environments. *Geomorphology*, 112(1-2), pp. 82-95. [Online] DOI: 10.1016/j.geomorph.2009.05.009
- Robinson, D. A., & Jerwood, L. C. (1987). Sub-aerial weathering of chalk shore platforms during harsh winters in southeast England. *Marine Geology*, 77(1-2), pp. 1-14.
- Robinson, L. A. (1974). *Towards a process response model of cliff retreat – the case of North East Yorkshire* (Doctoral thesis). University of Leeds, Leeds, UK
- Rocscience. (2011). Rocscience Software Products, Products including DIPS, Rocplane, Swedge, Slide, Phase 2. Rocscience Inc. [available at www.rocscience.com]
- Rosser, N. J., Lim, M., Petley, D. N., & Dunning, S. A. (2007). Patterns of precursory rockfall prior to slope failure. *Journal of Geophysical Research: Earth Surface*, 112(F04014), pp. 1-14. [Online] DOI: 10.1029/2006JF000642
- Rosser, N. J., Petley, D. N., Lim, M., Dunning, S. A., & Allison, R. J. (2005). Terrestrial laser scanning for monitoring the process of hard rock coastal cliff recession. *Quarterly Journal of Engineering Geology and Hydrogeology*, 38, pp. 363-375. [Online] DOI: 10.1144/1470-9236/05-008
- Rossi, M., Witt, A., Guzzetti, F., Malamud, B., & Peruccacci, S. (2010). Analysis of historical landslide time series in the Emilia-Romagna region, northern Italy. *Earth Surface Processes and Landforms*, 35(10), pp. 1123–1137. [Online] DOI: 10.1002/esp.1858
- Royal Haskoning. (2005). *Health and Safety File Brighton Marina to Ovingdean Coast Protection Works – Report No. 3H6762/02/309*. Haywards Heath, West Sussex: Royal Haskoning.
- Salvini, R., Francioni, M., Riccucci, S., Voncini, F., & Callegari, I. (2013). Photogrammetry and laser scanning for analyzing slope stability and rock fall runout along the Domodossola–Iselle railway, the Italian Alps. *Geomorphology*, 185, pp. 110-122. DOI: 10.1016/j.geomorph.2012.12.020

- Schenk, T. (2005). *Introduction to photogrammetry*. Columbus: Ohio State University.
- Selby, M. J. (Ed.) (1993). *Hillslope materials and processes* (2nd edn.). Oxford: Oxford University Press.
- Selby, M. J., Augustinus, P., Moon, V. G., & Stevenson, R. J. (1988). 'Slopes on strong rock masses: modelling and influences of stress distributions and geomechanical properties', in Anderson, M. G. (Ed.) *Modelling Geomorphological Systems*. Chichester: John Wiley & Sons, pp. 341-374.
- Sissons, J. B. (1976). *The Geomorphology of the British Isles: Scotland*. London: Methuen.
- Sjöberg, J. (1997). *Estimating rock mass strength using the Hoek-Brown failure criterion and rock mass classification – a review and application to the Aznalcollar open pit (Internal Report BM 1997:02)*. Sweden: Luleå University of Technology.
- Slatton, K. C., Carter, W. E., Shrestha, R. L., & Dietrich, W. (2007). Airborne laser swath mapping: achieving the resolution and accuracy required for geosurficial research. *Geophysical Research Letters*, 34, p. L23S10. DOI: 10.1029/2007GL031939
- Stark, C., & Guzzetti, F. (2009). Landslide rupture and probability distribution of mobilized debris volumes. *Journal of Geophysical Research*, 114(F2), pp. F00A02. [Online] DOI: 10.1029/2008JF001008
- Stark, C., & Hovius, N. (2001). The characterization of landslide size distributions. *Geophysical Research Letters*, 28(6), pp. 1091–1094. [Online] DOI: 10.1029/2000GL008527
- Stavrou, A., Lawrence, J. A., Mortimore, R. N., & Murphy, W. (2011). A geotechnical and GIS based method for evaluating risk exposition along coastal cliff environments: a case study of the Chalk cliffs of southern England. *Natural Hazards and Earth System Sciences*, 11(11), pp. 2997-3011. [Online] DOI: 10.5194/nhess-11-2997-2011
- Stead, D., & Coggan, J. (2012). 'Numerical modelling of rock-slope instability', in Clague, J. J., & Stead, D. (Eds.) *Landslides: Types, Mechanisms and Modelling*. Cambridge: Cambridge University Press, pp. 144-158.
- Stead, D., Coggan, J. S., & Eberhardt, E. (2004). Realistic simulation of rock slope failure mechanisms: the need to incorporate principles of fracture mechanics. *International Journal of Rock Mechanics and Mining Sciences*, 41(1), pp. 563-568. [Online] DOI: 10.1016/j.ijrmms.2004.03.100
- Stead, D., Eberhardt, E., & Coggan, J. S. (2006). Developments in the characterization of complex rock slope deformation and failure using numerical modelling techniques. *Engineering Geology*, 83(1-3), pp.217-235. [Online] DOI: 10.1016/j.enggeo.2005.06.033
- Steers, J. A. (1962). Coastal cliffs: report of a symposium. *The Geographical Journal*, 128(3), pp. 303-307. [Online] URL: <http://www.jstor.org/stable/1794044>
- Steers, J. A. (1973). *The Coastline of Scotland*. Cambridge: Cambridge University Press.
- Stephenson, W. J. (2000). Shore platforms: remain a neglected coastal feature? *Progress in Physical Geography*, 24(3), pp. 311-327. DOI: 10.1177/030913330002400301

- Stephenson, W. J., & Kirk, R. M. (2000a). Development of shore platforms on Kaikoura Peninsula, South Island, New Zealand. Part one: the role of waves. *Geomorphology*, 32(1-2), pp. 21-41. [Online] DOI: 10.1016/S0169-555X(99)00061-6
- Stephenson, W. J., & Kirk, R. M. (2000b). Development of shore platforms on Kaikoura Peninsula, South Island, New Zealand. II: the role of subaerial weathering. *Geomorphology*, 32(1-2), pp. 43-56. [Online] DOI: 10.1016/S0169-555X(99)00062-8
- Sturznegger, M, & Stead, D. (2009). Close-range terrestrial digital photogrammetry and terrestrial laser scanning for discontinuity characterisation on rock cuts. *Engineering Geology*, 106(3-4), pp. 163-182. [Online] DOI: 10.1016/j.enggeo.2009.03.004
- Sunamura, T. (1992). *Geomorphology of Rocky Coasts*. Chichester: John Wiley and Sons.
- Sunamura, T. (2015). Rocky coast processes: with special reference to the recession of soft rock cliffs. *Proceedings of the Japan Academy, Series B*, 91(9), pp. 481-500. [Online] DOI: 10.2183/pjab.91.481
- Tabba, M. M. (1984). Deterministic versus risk analysis of slope stability. *Proceedings of Fourth International Symposium on Landslides*. Toronto, Canada, pp. 491-498.
- Teixeira, S. B. (2006). Slope mass movements on rocky sea-cliffs: A power-law distributed natural hazard on the Barlavento Coast, Algarve, Portugal. *Continental Shelf Research*, 26(9), pp. 1077-1091. [Online] DOI: 10.1016/j.csr.2005.12.013
- Thébaudeau, B., Trenhaile, A. S., & Edwards, R. J. (2013). Modelling the development of rocky shoreline profiles along the northern coast of Ireland. *Geomorphology*, 203, pp. 66-78. [Online] DOI: 10.1016/j.geomorph.2013.03.027
- Thieler, E. R., & Danforth, W. W. (1994). Historical shoreline mapping (I): improving techniques and reducing position errors. *Journal of Coastal Research*, 10(3), pp. 549-563. [Online] URL: <http://www.jstor.org/stable/4298252>
- Thieler, E. R., Himmelstoss, E. A., Zichichi, J. L., & Ergul, A. (2009). *Digital Shoreline Analysis System (DSAS): An ArcGIS extension for calculating shoreline change (Version 4.0) [Computer software]*. U.S. Geological Survey Open-File Report 2005-1304. Retrieved from: <https://woodshole.er.usgs.gov/project-pages/DSAS/version4/index.html> (link may change with updates to software – link to all versions is <https://woodshole.er.usgs.gov/project-pages/DSAS/>)
- Thorburn, A. (1977). *Report on the problems of coastal erosion*. Lewes: East Sussex County Council.
- Trenhaile, A. S. (1974). The geometry of shore platforms in England and Wales. *Transactions of the Institute of British Geographers*, 62, pp. 129-142. [Online] DOI: 10.2307/621519
- Trenhaile, A. S. (1980). Shore platforms: a neglected coastal feature. *Progress in Physical Geography*, 4(1), pp. 1-23. [Online] DOI: 10.1177/030913338000400101
- Trenhaile, A. S. (1987). *The Geomorphology of Rock Coasts*. Oxford: Oxford University Press.
- Trenhaile, A. S. (1997). *Coastal dynamics and Landforms*. Oxford: Oxford University Press.

- Trenhaile, A. S. (2001). Modelling the effect of weathering on the evolution and morphology of shore platforms. *Journal of Coastal Research*, 17(2), pp. 398-406. [Online] URL: <http://www.jstor.org/stable/4300191>
- Trenhaile, A. S. (2002). Rock coasts, with particular emphasis on shore platforms. *Geomorphology*, 48(1-3), pp. 7-22. [Online] DOI: 10.1016/S0169-555X(02)00173-3
- Trenhaile, A. S. (2008). Modelling the role of weathering on shore platform development. *Geomorphology*, 94(1-2), pp. 24-39. [Online] DOI: 10.1016/j.geomorph.2007.04.002
- Trenhaile, A. S. (2009). Modelling the erosion of cohesive clay coasts. *Coastal Engineering*, 56(1), pp. 59-72. [Online] DOI: 10.1016/j.coastaleng.2008.07.001
- Trenhaile, A. S. (2014). 'Climate change and its impact on rock coasts', in Kennedy, D. M., Stephenson, W. J., & Naylor, L. A. (Eds.) *Rock Coast Geomorphology: A Global Synthesis*. London: Geological Society Memoirs, 40, pp. 8-14.
- Triggs, B., McLauchlan, P. F., Hartley, R. I., & Fitzgibbon, A. W. (2000). *Bundle Adjustment – A Modern Synthesis*. In B. Triggs, A. Zisserman, R. Szeliski (eds.) *Vision Algorithms: Theory and Practice*. International Workshop on Vision Algorithms – IWVA 1999. Lecture Notes in Computer Science, vol. 1883 (pp.298-372). Berlin, Heidelberg: Springer. [Online] DOI: 10.1007/3-540-44480-7_21
- Twine, D., & Wright, R. H. (1991). 'Farmers Avenue road crossing, Castle Mall development, Norwich', in *Proceedings of the 4th International Deep Foundations Conference, Stresa*. Rotterdam: AA Balkema, pp. 147-155.
- United Kingdom Climate Projections (UKCP). (2009). *UK Climate Projections User Interface*. Retrieved from: <http://ukclimateprojections-ui.metoffice.gov.uk/ui/start/start.php>
- University of Sussex. (2013). *Cliff falls at Brighton Marina 2000-2002*. Retrieved from: http://www.sussex.ac.uk/geography/researchprojects/coastview/Brighton_to_Saltdean/brighton_marina/cliff_fall_brighton_marina_main.htm
- Van Den Eeckhaut, M., Poesen, J., Govers, G., Verstraeten, G., & Demoulin, A. (2007). Characteristics of the size distribution of recent and historical landslides in a populated hilly region. *Earth and Planetary Science Letters*, 256(3-4), pp. 588–603. [Online] DOI: 10.1016/j.epsl.2007.01.040
- Vosselman, G., Sester, M., & Mayer, H. (2004). Basic computer vision techniques. In J. McGlone, E. Mikhail, & R. Mullen (Eds.), *Manual of Photogrammetry* (pp. 455-504) (5th ed.). Maryland: American Society of Photogrammetry and Remote Sensing.
- Walder, J. S., & Hallet, B. (1986). The physical basis of frost weathering: toward a more fundamental and unified perspective. *Arctic and Alpine Research*, 18(1), pp. 27-32. [Online] DOI: 10.2307/1551211

- Walder, J., & Hallet, B. (1985). A theoretical model of the fracture of rock during freezing. *Geological Society of America Bulletin*, 96(3), pp. 336-346. [Online] DOI: 10.1130/0016-7606(1985)96<336:ATMOTF>2.0.CO;2
- Walkden, M. J. A., & Hall, J. W. (2005). A predictive mesoscale model of the erosion and profile development of soft rock shores. *Coastal Engineering*, 52(6), pp. 535-563. [Online] DOI: 10.1016/j.coastaleng.2005.02.005
- Walkden, M., & Dickson, M. (2008). Equilibrium erosion of soft rock shores with a shallow or absent beach under increased sea level rise. *Marine Geology*, 251(1-2), pp. 75-84. [Online] DOI: 10.1016/j.margeo.2008.02.003
- Walkden, M. (2010). *The use of UKCP09 projections to inform coastal erosion modelling in Cumbria*. Exeter, Devon: Royal Haskoning.
- Walkden, M. J. A., & Hall, J. W. (2011). A mesoscale predictive model of the evolution and management of a soft-rock coast. *Journal of Coastal Research*, 27(3), pp. 529-543. [Online] DOI: 10.2112/JCOASTRES-D-10-00099.1
- Westoby, M. J., Brasington, J., Glasser, N. F., Hambrey, M. J., & Reynolds, J. M. (2012). 'Structure-from-Motion' photogrammetry: A low-cost, effective tool for geoscience applications. *Geomorphology*, 179, pp. 300-314. [Online] DOI: 10.1016/j.geomorph.2012.08.021
- White, E. P., Enquist, B. J., & Green, J. L. (2008). On estimating the exponent of power law frequency distributions. *Ecology*, 89(4), pp. 905-912. [Online] DOI: 10.1890/07-1288.1
- Williams, R. B. G., & Robinson, D. A. (1981). The weathering of sandstone by the combined action of frost and salt. *Earth Surface Processes and Landforms*, 6(1), pp. 1-9. [Online] DOI: 10.1002/esp.3290060102
- Williams, R. B. G., & Robinson, D. A. (2006). Frost weathering of rocks in the presence of salts—a review. *Permafrost and Periglacial Processes*, 2(4), pp. 347-353. [Online] DOI: 10.1002/ppp.3430020410
- Wolman, M. G., & Miller, J. P. (1960). Magnitude and frequency of forces in geomorphic processes. *Journal of Geology*, 68(1), pp. 54-74. [Online] DOI: 10.1086/626637
- Wolters, G., & Müller, G. (2008). Effect of cliff shape on internal stresses and rock slope stability. *Journal of Coastal Research*, 24(1), pp. 43-50. [Online] DOI: 10.2112/05-0569.1
- Wyllie, D. C., & Mah, C. W. (2004). *Rock Slope Engineering* (4th ed.). London: Spon Press – Taylor & Francis Group.
- Young, A. P., Flick, R. E., O'Reilly, W. C., Chadwick, D. B., Crampton, W. C., & Helly, J. J. (2014). Estimating cliff retreat in southern California considering sea level rise using a sand balance approach. *Marine Geology*, 348, pp. 15-26. [Online] DOI: 10.1016/j.margeo.2013.11.007

Young, E. J. (2012). dGPS. In S. J. Cook, L. E. Clarke, & J. M. Nield (Eds.), *Geomorphological Techniques* (ISSN 2047-0371, pp.1-10). Retrieved from:
http://www.geomorphology.org.uk/geomorph_techniques

Zenkovic, V. P. (1967). *Processes of coastal development*. London: Oliver and Boyd.

Annex and Appendices

Annex A – Orthorectification of aerial imagery procedure details

The orthorectification process was undertaken using the geospatial imagery software package ENVI 4.8. The following subsections describe the processes undertaken which are basics of digital photogrammetric processing.

Computing rational polynomial coefficients (RPCs)

As there was no accompanying ancillary data to the aerial imagery the orthorectification workflow was completed through generating rational polynomial coefficients (RPCs). The RPCs are required to build a correlation between the image pixels and the ground locations based on a ratio of two cubic polynomial functions (Chmiel et al., 2004). The ENVI platform requires input data for the camera model and the interior and exterior orientation. The camera model type was set to 'frame camera', the focal length of the camera was required, which was researched for the RAF dataset from 1957 (Fuller, 1983) and the principal point coordinates extracted from the raw image.

Interior orientation

The interior orientation requires digitisation of the fiducial marks, these are commonly located in the corners or as tick marks located at the midpoint of the boundaries of the image. These points were refined using the 8X zoom window. This stage provides the software with the spatial extent of the pixels to be utilised in the orthorectification process.

Exterior orientation

To complete the exterior orientation the raw image file, pre-orthorectified image and DEM are all required. The pre-orthorectified image and the DEM must be geographically linked within the software so that the coordinate extracted from the image relates to the same location within the DEM. Chmiel et al. (2004) report that up to 20 ground control points (GCPs) may be required when building RPCs. GCPs should be spread across the image to reduce any warping and should

try to include a variety of elevations. The selection of GCPs is critical to the result, features constructed on the surface should be treated with caution, as buildings, bridges or channels will have significant displacement which will not be replicated within the DEM (Chmiel et al., 2004). Figure 16 (Section 3.1.2) displays an example of the located GCPs in an image from 1957 of Saltdean. The spatial extent of the historical aerial image is much greater than that of the pre-orthorectified imagery and DEM. It was decided to select GCPs spread across the image which were located around the feature of interest, the cliff line, as much of the inland imagery would be cropped in the final processing stages.

Refining process and RMSE

Once the GCPs have been selected the software will report a root mean square error (RMSE), this is a measure of how accurately the GCPs that were digitised in the historical image reflect the spacing in the coordinate system they were extracted from. All reported RMSE values were examined and only accepted if they were less than half the pixel value of the historical image. If the RMSE value was greater than this threshold GCP refinement was undertaken, which required removing 'bad points' or optimising the digitised points. This procedure improves the co-registration between the image and the DEM this ensuring a more accurate geometric rectification (Chmiel et al., 2004).

Orthorectification parameters and processing of images

The final stage of processing requires data input with reference to image processing. Background data values are required alongside providing the software with details of the minimum and maximum elevation recorded in the DEM file. The output projection and map extent are also required before processing of the image. ENVI then completes the processing and generates an orthorectified image from the aerial image. This method was completed for each of the images within the database.

Appendix A – ADAM 3DM Object-Distance Spreadsheet



TECHNOLOGY

Object Distance Calculation Spreadsheet

Camera Name:

Nikon D810

Camera Details	Width	Height
Number of pixels:	7360 x 4912	
Image sensor dimensions:	35.9 x 24 mm	
Actual focal length of lens x adapter:	35 mm	
Actual aperture:	f/8	
Focus distance:	50.00 m	
Desired circle of confusion (diameter):	5 pixels	
Size of each pixel in CCD array:	4.88 x 4.89 um	
Image size:		36.2 megapixels
Field of View Crop/Lens multiplier:		1.0 x 1.0
Equivalent 35mm camera focal length:		35 mm
Equivalent 35mm camera aperture:		f/8.0
Depth of field:		5.58m - Infinity
Hyperfocal distance:		6.31 m

Required Conversion:

Distance -> Pixel Size

Project Type:

Terrestrial Strips

Model Details	Accuracy Estimates
Desired object distance:	Estimated image accuracy: 0.5 pixels
Ground coverage of each Image:	Distance between camera stations: 25.0 m
Ground pixel size:	Object distance/base ratio: 2.00 : 1
Desired target size:	Estimated plan accuracy: 3.5 mm
Desired target + border size:	Estimated distance accuracy: 7 mm
Nominal DTM point density:	Estimated overall accuracy: 8.5 mm
Photoscale:	

Area Details for Strip Planning	
Width and height of area:	100 x 60 m
Desired horizontal overlap:	60% = 30.8 m
Desired vertical overlap:	35% = 12 m
Desired driving speed:	5 m/s
Max. movement during exposure:	0.3 pixels
Min. required shutter speed:	1/2400 seconds
Capture interval:	4.1 seconds
Distance between camera stations:	20.5 m
Distance between strips:	22.3 m
Number of images per strip:	5
Number of strips:	3
Total number of images:	15

Appendix B(i) – Sony DSC-H300 Interior Orientation

3DM CalibCam Adjustment Results
Interior Orientation – Free Network

Project Details

Project Name:	Fullon1-HT
Last Solved:	30/03/2015 at 10:49
Active Images:	DSC00480.JPG; DSC00481.JPG; DSC00483.JPG; DSC00484.JPG; DSC00485.JPG; DSC00487.JPG; DSC00488.JPG; DSC00495.JPG; DSC00496.JPG; DSC00497.JPG; DSC00498.JPG
Number of Active Images:	12
User-Specified Image Accuracy:	X = 0.44 pixels, Y = 0.44 pixels
Units:	Unknown

Results

Bundle Adjustment Performed:	31/03/2015 at 11:02 by jgg385
Status:	Successful
Posterior Variance Factor:	0.97
Computed Image Accuracy:	0.43 pixels (X = 0.44 pixels, Y = 0.43 pixels)
Number of Degrees of Freedom:	10.703

Camera Details

Camera Name	Camera		Lens		Sensor Size	Pixel Size	Image Size (pixels)
	Type	Serial Number	Type	Serial Number			
SONY DSC-H300	H300		1		6.2 mm x 4.5 mm	1.20 µm x 1.18 µm	5,152 x 3,664 (19 MP)

Image Residuals

Image	RMS Error (pixels)			Number of Active Points			
	X	Y	Total	X	Y	Total	
DSC00480.JPG	0.443	0.411	0.604	388	0.394	0.505	743
DSC00481.JPG	0.384	0.428	0.575	324	0.346	0.502	670
DSC00483.JPG	0.393	0.390	0.554	542	0.395	0.591	709
DSC00484.JPG	0.364	0.414	0.552	574	0.332	0.486	697
DSC00485.JPG	0.421	0.403	0.583	543	0.344	0.474	798
DSC00486.JPG	0.374	0.393	0.543	528	0.333	0.483	801

Camera Calibration: Parameter Correlation Matrix

Camera: "SONY DSC-H300"

Parameter	C	X _c	Y _c	K ₁	K ₂	K ₃	P ₁	P ₂	B ₁	B ₂	Max
C	1.00	-0.05	0.12	0.17	0.23	0.03	-0.07	-0.01	-0.01	-0.01	-0.59
X _c		1.00	0.21	-0.02	0.01	-0.01	-0.30	-0.13	-0.08	0.32	-0.90
Y _c			1.00	0.06	-0.04	0.02	-0.13	-0.50	0.08	-0.90	-0.90
K ₁				1.00	-0.94	0.87	-0.01	-0.02	-0.01	-0.05	-0.94
K ₂					1.00	-0.98	0.00	0.04	-0.00	0.04	-0.88
K ₃						1.00	0.00	-0.03	0.01	-0.04	-0.98
P ₁							1.00	0.06	-0.02	-0.27	-0.90
P ₂								1.00	0.35	-0.10	-0.90
B ₁									1.00	0.02	-0.42
B ₂										1.00	0.32

Camera Calibration: Interior Orientation Results

Camera Name	Parameter	Final Value		σ _{Final Value}	σ _{Final Value}	
		(pixels)	(pixels)		(pixels)	(pixels)
SONY DSC-H300	C	4.51			6.66e-004	0.47
	X _c	-1.56e-002	-13.01		3.14e-004	0.16
	Y _c	1.85e-002	15.42		3.26e-004	0.27
	K ₁	2.87e-003	135.13		2.70e-005	1.27
	K ₂	-3.76e-004	-299.71		5.16e-006	3.56
	K ₃	1.13e-005	114.75		3.17e-007	3.22
	P ₁	9.91e-005	3.95		5.05e-006	0.20
	P ₂	1.29e-004	4.29		5.33e-006	0.18
	B ₁	-1.89e-002	-47.13		1.20e-005	0.03
	B ₂	1.79e-004	0.35		1.19e-005	0.02

Exterior Orientations

Image	Location			Rotation (°)					
	X	Y	Z	ω	φ	κ	Bearing	Tilt	
D5C00480.JPG	65.42 ± 0.00	-0.84 ± 0.00	-180.34 ± 0.00	5.54 ± 0.00	2.82 ± 0.00	93.68 ± 0.00	332.97	-83.78	
D5C00481.JPG	66.68 ± 0.02	-3.03 ± 0.02	-183.30 ± 0.01	5.43 ± 0.01	3.51 ± 0.01	2.35 ± 0.00	327.65	-83.53	
D5C00483.JPG	40.13 ± 0.02	41.80 ± 0.03	-108.21 ± 0.01	-5.58 ± 0.00	3.33 ± 0.00	90.71 ± 0.00	210.89	-88.50	
D5C00484.JPG	40.56 ± 0.02	41.42 ± 0.03	-108.05 ± 0.01	-1.88 ± 0.01	4.38 ± 0.01	0.47 ± 0.00	246.77	-85.23	
D5C00485.JPG	36.44 ± 0.02	-56.10 ± 0.02	-88.43 ± 0.02	7.63 ± 0.00	3.82 ± 0.00	94.42 ± 0.00	333.33	-81.47	
D5C00486.JPG	37.36 ± 0.02	-54.32 ± 0.03	-92.59 ± 0.02	10.63 ± 0.01	2.95 ± 0.01	4.67 ± 0.00	344.40	-78.97	
D5C00487.JPG	7.52 ± 0.02	-119.63 ± 0.03	-6.63 ± 0.02	12.68 ± 0.00	3.80 ± 0.00	92.77 ± 0.00	343.17	-76.77	
D5C00488.JPG	7.98 ± 0.02	-119.12 ± 0.03	-6.18 ± 0.03	15.85 ± 0.02	-1.63 ± 0.01	2.38 ± 0.02	5.95	-74.07	
D5C00489.JPG	8.23 ± 0.03	-18.74 ± 0.04	-5.74 ± 0.02	2.43 ± 0.01	0.92 ± 0.00	0.49 ± 0.00	339.23	-87.40	
D5C00495.JPG	8.80 ± 0.03	83.09 ± 0.04	-6.96 ± 0.02	-4.74 ± 0.01	-1.53 ± 0.01	0.48 ± 0.00	162.06	-85.01	
D5C00497.JPG	8.47 ± 0.03	85.27 ± 0.04	-7.90 ± 0.02	-9.16 ± 0.00	-0.45 ± 0.00	90.00 ± 0.00	177.20	-80.83	
D5C00498.JPG	7.74 ± 0.03	-15.49 ± 0.03	-4.69 ± 0.02	-1.67 ± 0.00	-3.07 ± 0.00	92.21 ± 0.00	118.56	-85.51	

Appendix B(ii) – Nikon D810 35mm Varied Lens Interior Orientation

3DM CalibCam Adjustment Results
Interior Orientation – Control Network

3DM Analyst Mine Mapping Suite

Project Details

Project Name:	Nikon D810 35mm (Adj) Lens) ISO 100 AP (1)
Last Saved:	05/07/2016 at 10:08
Control Point File:	Nikon D810 35mm (Adj) Lens) ISO 100 AP.xyz
Number of Control Points:	12
Active Images:	DSC_4317.TIF; DSC_4319.TIF; DSC_4314.TIF; DSC_4315.TIF; DSC_4312.TIF; DSC_4313.TIF; DSC_4309.TIF; DSC_4310.TIF; DSC_4307.TIF; DSC_4308.TIF; DSC_4304.TIF; DSC_4305.TIF
Number of Active Images:	12
User-Specified Image Accuracy:	X = 0.14 pixels, Y = 0.53 pixels
Units:	Metre

Results

Bundle Adjustment Performed:	05/07/2016 at 12:18 by JG:885
Status:	Successful
Posteriori Variance Factor:	0.97
Computed Image Accuracy:	0.49 pixels (X = 0.44 pixels, Y = 0.53 pixels)
Number of Degrees of Freedom:	6,507

Camera Details

Camera Name	Camera		Lens		Sensor Size	Pixel Size	Image Size (pixels)
	Type	Serial Number	Type	Serial Number			
Nikon D810 Adj 35mm (ISO 100 - AP)	D810		35mm (24-120mmAdj)		35.9 mm × 24.0 mm	4.88 µm × 4.89 µm	7,360 × 4,512 (36 MP)

Image Residuals

Image	RMS Error (pixels)			Number of Active Points			
	X	Y	Total	X	Y	Total	
DSC_4317.TIF	0.000	0.000	0.000	124	0.317	0.379	2,220
DSC_4315.TIF	0.011	0.004	0.012	325	0.219	0.357	1,122
DSC_4314.TIF	0.282	0.231	0.364	981	0.215	0.264	1,599
DSC_4315.TIF	0.207	0.280	0.348	925	0.189	0.289	1,606
DSC_4312.TIF	0.159	0.326	0.363	1,497	0.256	0.346	828
DSC_4313.TIF	0.292	0.289	0.411	1,310	0.261	0.375	698

Camera Calibration: Parameter Correlation Matrix

Camera: "Nikon D610 Adj 35mm (ISO 100 - AP)"

Parameter	C	X _p	Y _p	K ₁	K ₂	K ₃	K ₄	P ₁	P ₂	B ₁	B ₂	Max
C	1.00	0.02	0.01	0.42	-0.45	0.43	0.20	-0.09	-0.07	-0.02	-0.45	K ₁
X _p		1.00	-0.02	0.05	-0.05	0.03	-0.76	-0.01	-0.06	0.10	-0.76	P ₁
Y _p			1.00	0.00	-0.00	0.00	0.00	-0.77	0.11	0.12	-0.77	P ₂
K ₁				1.00	-0.51	0.78	0.33	-0.23	0.07	0.00	-0.51	K ₂
K ₂					1.00	-0.56	-0.23	0.16	-0.08	-0.02	-0.56	K ₃
K ₃						1.00	0.17	-0.11	0.08	0.02	-0.56	K ₄
P ₁							1.00	-0.08	0.03	0.03	-0.76	X _p
P ₂								1.00	-0.05	0.00	-0.77	Y _p
B ₁									1.00	-0.05	0.11	Y _p
B ₂										1.00	0.12	Y _p

Camera Calibration: Interior Orientation Results

Camera Name	Parameter	Final Value		Stdev
		(pixels)	(pixels)	
Nikon D610 Adj 35mm (ISO 100 - AP)	C	34.95		3.11
	X _p	2.02e-004	0.04	4.65e-003
	Y _p	7.53e-002	15.43	4.57e-003
	K ₁	-2.21e-004	-455.72	3.97e-006
	K ₂	5.94e-007	562.18	1.78e-008
	K ₃	-9.60e-010	-430.66	2.95e-011
	P ₁	-1.30e-005	-4.12	1.64e-006
	P ₂	5.39e-005	13.06	1.56e-006
	B ₁	1.20e-003	4.43	1.68e-005
	B ₂	-4.05e-004	-1.00	1.67e-005

Exterior Orientations

Image	Location (metre)			Rotation (°)			Tilt
	X	Y	Z	φ	κ	ω	
D6C_4317.TIF	538915.36 ± 0.02	101551.13 ± 0.02	2.03 ± 0.02	122.66 ± 0.11	-27.35 ± 0.17	16.40 ± 0.09	31.56
D6C_4319.TIF	538915.36 ± 0.02	101551.13 ± 0.02	2.03 ± 0.02	123.48 ± 0.12	-26.94 ± 0.19	107.01 ± 0.09	31.36
D6C_4314.TIF	538906.75 ± 0.01	101545.88 ± 0.01	1.62 ± 0.02	119.21 ± 0.07	-33.90 ± 0.12	16.22 ± 0.08	37.59
D6C_4315.TIF	538906.75 ± 0.01	101545.88 ± 0.01	1.62 ± 0.02	120.04 ± 0.07	-33.42 ± 0.12	106.99 ± 0.08	37.32
D6C_4312.TIF	538896.56 ± 0.01	101540.89 ± 0.02	1.49 ± 0.02	116.33 ± 0.07	-38.25 ± 0.12	17.19 ± 0.08	41.34
D6C_4313.TIF	538896.56 ± 0.01	101540.89 ± 0.02	1.49 ± 0.02	117.05 ± 0.07	-37.69 ± 0.12	108.00 ± 0.08	40.94
D6C_4309.TIF	538907.04 ± 0.01	101535.75 ± 0.01	1.22 ± 0.01	113.79 ± 0.07	-28.44 ± 0.12	11.22 ± 0.08	30.61
D6C_4310.TIF	538907.04 ± 0.01	101535.75 ± 0.01	1.22 ± 0.01	114.67 ± 0.07	-28.81 ± 0.12	102.01 ± 0.08	31.19
D6C_4307.TIF	538915.88 ± 0.02	101531.27 ± 0.01	1.25 ± 0.02	111.69 ± 0.07	-16.36 ± 0.12	6.46 ± 0.08	19.65
D6C_4308.TIF	538915.88 ± 0.02	101531.27 ± 0.01	1.25 ± 0.02	112.45 ± 0.07	-17.89 ± 0.12	97.02 ± 0.08	19.22
D6C_4304.TIF	538916.06 ± 0.01	101541.49 ± 0.01	1.59 ± 0.02	116.06 ± 0.07	-21.70 ± 0.12	10.70 ± 0.08	23.89
D6C_4305.TIF	538916.06 ± 0.01	101541.49 ± 0.01	1.59 ± 0.02	116.94 ± 0.07	-21.09 ± 0.12	101.41 ± 0.08	23.40
							25.01

Appendix B (iii) – Nikon D810 35mm Fixed/Prime Lens Interior Orientation

3DM CalibCam Adjustment Results
Interior Orientation – Control Network

Project Details

Project Name:	Nikon D810 35mm Fixed Calibration
Last Saved:	02/08/2016 at 17:19
Control Point File:	Nikon D810 35mm Fixed Calibration.MF
Number of Control Points:	12
Active Images:	DSC_5011.TIF; DSC_5014.TIF; DSC_5015.TIF; DSC_5016.TIF; DSC_5017.TIF; DSC_5018.TIF; DSC_5019.TIF; DSC_5020.TIF; DSC_5021.TIF; DSC_5022.TIF
Number of Active Images:	12
User Specified Image Accuracy:	X = 0.36 pixels, Y = 0.31 pixels
Units:	Metre

Results

Bundle Adjustment Performed:	02/08/2016 at 17:30 by H43
Status:	Successful
Position Variance Factor:	1.00
Computed Image Accuracy:	0.34 pixels (X = 0.36 pixels, Y = 0.31 pixels)
Number of Degrees of Freedom:	27.658

Camera Details

Camera Name	Camera	Lens	Image Size (pixels)
Type	Serial Number	Type	Serial Number
Nikon D810 35mm (Fixed Lens)	D810	35mm Fixed	
			35.9 mm x 24.0 mm
			4.88 µm x 4.89 µm
			7.560 x 4.912 (8.6 MP)

Image Residuals

Image	RMS Error (pixels)			Number of Active Points		
	X	Y	Total	X	Y	Total
DSC_5011.TIF	0.246	0.283	0.454	1,209		997
DSC_5012.TIF	0.166	0.238	0.308	553		2,229
DSC_5013.TIF	0.186	0.190	0.260	778		2,585
DSC_5014.TIF	0.250	0.257	0.359	1,498		1,700
DSC_5015.TIF	0.138	0.224	0.268	1,464		1,570
DSC_5016.TIF	0.186	0.139	0.232	1,600		886

Control Point Residuals

Control Point ID	Image Co-ordinate Residuals (pixels)			Ground Co-ordinate Residuals (metre)			Adjusted Ground Co-ordinates (metre)		
	X	Y	Z	X	Y	Z	X	Y	Z
101	6	0.204	0.172	0.01	-0.01	-0.00	538958.71	101572.91	43.99
102	10	0.362	0.151	-0.00	0.01	0.01	538945.74	101580.76	44.40
103	3	0.358	0.085	-0.01	0.01	0.00	538918.99	101588.90	45.14
104	1	0.002	0.009	-0.00	-0.01	0.01	538904.43	101597.31	45.57
210	3	0.201	0.235	0.03	-0.01	-0.02	538955.40	101568.90	5.29
211	3	0.030	0.227	-0.00	0.00	-0.02	538916.50	101585.65	4.51
Component SE		0.283		0.02	0.01	0.02			
				3D SE					0.02

Camera Calibration: Parameter Correlation Matrix

Camera: "Nikon D810 35mm (Fixed Lens)"

Parameter	C	X _c	Y _c	K ₁	K ₂	K ₃	P ₁	P ₂	B ₁	B ₂	Max	
C	1.00	-0.04	0.04	0.45	0.40	0.03	-0.06	0.11	-0.03	0.45	K ₁	
X _c		1.00	0.05	0.03	-0.03	0.02	-0.94	-0.07	-0.08	0.08	-0.94	P ₁
Y _c			1.00	-0.00	0.00	-0.00	-0.06	-0.91	-0.01	0.06	-0.91	P ₂
K ₁				1.00	-0.95	0.88	0.00	-0.11	-0.00	0.02	-0.95	K ₂
K ₂					1.00	-0.98	0.00	0.10	-0.01	-0.04	-0.98	K ₃
K ₃						1.00	-0.00	-0.08	0.02	0.04	-0.98	K ₁
P ₁							1.00	0.08	0.07	-0.06	-0.94	X _c
P ₂								1.00	0.03	-0.01	-0.91	Y _c
B ₁									1.00	-0.01	0.11	C
B ₂										1.00	0.08	X _c

Camera Calibration: Interior Orientation Results

Camera Name	Parameter	Fixed Value		Stdev Value
		(pixels)	(pixels)	
Nikon D810 35mm (Fixed Lens)	C	35.94		4.64e-003
	X _c	5.46e-008	1.94	1.56e-003
	Y _c	5.67e-002	19.83	1.44e-003
	K ₁	6.19e-005	127.78	8.41e-007
	K ₂	-4.36e-008	-41.91	3.42e-009
	K ₃	-2.00e-011	-8.96	5.17e-012
	P ₁	1.59e-006	0.50	4.53e-007
	P ₂	9.85e-006	2.39	4.21e-007
	B ₁	1.64e-003	6.10	3.66e-005
	B ₂	2.94e-005	0.07	3.46e-006

Exterior Orientations

Image	Location (meter)			Rotation (°)		
	X	Y	Z	φ	κ	τ
D6C_5011.TIF	538915.36 ± 0.01	101551.12 ± 0.01	2.04 ± 0.01	123.31 ± 0.02	-26.74 ± 0.01	13.51 ± 0.02
D6C_5012.TIF	538915.36 ± 0.01	101551.12 ± 0.01	2.04 ± 0.01	123.55 ± 0.02	-26.72 ± 0.01	104.00 ± 0.02
D6C_5013.TIF	538906.73 ± 0.01	101545.53 ± 0.01	1.66 ± 0.01	120.03 ± 0.02	-33.28 ± 0.01	17.09 ± 0.02
D6C_5014.TIF	538906.73 ± 0.01	101545.53 ± 0.01	1.66 ± 0.01	120.47 ± 0.02	-33.26 ± 0.01	107.68 ± 0.02
D6C_5015.TIF	538906.46 ± 0.01	101540.82 ± 0.01	1.33 ± 0.01	117.09 ± 0.02	-37.69 ± 0.01	16.44 ± 0.02
D6C_5016.TIF	538906.46 ± 0.01	101540.82 ± 0.01	1.33 ± 0.01	117.19 ± 0.02	-37.57 ± 0.01	106.75 ± 0.02
D6C_5017.TIF	538907.21 ± 0.01	101535.59 ± 0.01	1.27 ± 0.01	114.69 ± 0.02	-27.90 ± 0.01	11.27 ± 0.02
D6C_5018.TIF	538907.21 ± 0.01	101535.59 ± 0.01	1.27 ± 0.01	114.91 ± 0.02	-27.76 ± 0.01	101.66 ± 0.02
D6C_5019.TIF	538915.97 ± 0.01	101531.26 ± 0.01	1.90 ± 0.01	112.84 ± 0.02	-18.11 ± 0.01	97.04 ± 0.02
D6C_5019.TIF	538915.97 ± 0.01	101531.26 ± 0.01	1.90 ± 0.01	112.38 ± 0.02	-17.98 ± 0.01	6.60 ± 0.02
D6C_5021.TIF	538915.91 ± 0.01	101541.30 ± 0.01	1.74 ± 0.01	116.70 ± 0.02	-21.04 ± 0.01	10.50 ± 0.02
D6C_5021.TIF	538915.91 ± 0.01	101541.30 ± 0.01	1.74 ± 0.01	117.02 ± 0.02	-21.12 ± 0.01	100.94 ± 0.02
						23.29
						23.45
						24.80
						25.07

Appendix C – Brighton Marina Exterior Orientation

3DM CalibCam Adjustment Results
Exterior Orientation – Control Network

3DM Analyst Mine Mapping Suite

Project Details

Project Name:	2001.17
Last Saved:	24/07/2017 at 14:14
Control Point File:	2001.17.azf
Number of Control Points:	15
Active Images:	DSC_6882.TIF DSC_6893.TIF DSC_6894.TIF DSC_6895.TIF DSC_6896.TIF DSC_6897.TIF DSC_6898.TIF DSC_6899.TIF DSC_6900.TIF DSC_6901.TIF DSC_6902.TIF DSC_6903.TIF DSC_6904.TIF DSC_6905.TIF
Number of Active Images:	14
User-Specified Image Accuracy:	X = 0.16 pixels, Y = 0.17 pixels
Units:	Metre

Results

Bundle Adjustment Performance:	24/07/2017 at 14:24 by JBBS
Status:	Successful
Posterior Variance Factor:	1.01
Computed Image Accuracy:	0.17 pixels (X = 0.16 pixels, Y = 0.17 pixels)
Number of Degrees of Freedom:	25,627

Camera Details

Camera Name	Type	Serial Number	Type	Lens	Serial Number	Sensor Size	Pixel Size	Image Site (pixels)
Nikon 6810 35mm (Fixed Lens)	D810		35m Fixed			35.9 mm x 24.0 mm	4.88 µm x 4.89 µm	7,360 x 4,912 (8 MP)

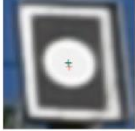
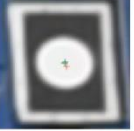
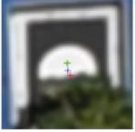
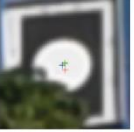
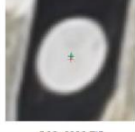
Image Residuals

Image	RMS Error (pixels)			Number of Active Points
	X	Y	Total	
DSC_6882.TIF	0.143	0.170	0.222	969
DSC_6893.TIF	0.118	0.149	0.189	971
DSC_6894.TIF	0.122	0.132	0.180	1,017
DSC_6895.TIF	0.118	0.111	0.162	1,119
DSC_6896.TIF	0.139	0.132	0.200	1,191
DSC_6897.TIF	0.141	0.124	0.194	1,222
DSC_6898.TIF	0.157	0.140	0.210	1,233

Image	RMS Error (pixels)			Number of Active Points
	X	Y	Total	
DSC_6899.TIF	0.133	0.166	0.226	1,304
DSC_6900.TIF	0.151	0.146	0.210	1,292
DSC_6901.TIF	0.158	0.160	0.225	1,244
DSC_6902.TIF	0.148	0.154	0.213	1,144
DSC_6903.TIF	0.130	0.163	0.222	1,092
DSC_6904.TIF	0.136	0.180	0.226	1,098
DSC_6905.TIF	0.143	0.158	0.214	1,007

Control Point Residuals

Control Point ID	Image Coordinate Residuals (pixels)			Ground Coordinate Residuals (metre)			Adjusted Ground Coordinates (metre)		
	X	Y	Z	X	Y	Z	X	Y	Z
102	6	0.058	0.163	0.02	-0.01	0.02	594190.25	102126.55	32.39
103	2	0.011	0.168	0.00	0.02	-0.02	594185.39	102127.77	31.84
104	14	0.238	0.682	-0.01	-0.01	0.01	594185.94	102122.85	31.61
108	14	0.108	0.147	0.00	-0.01	0.00	594180.05	102115.64	7.53
112	9	0.082	0.175	-0.01	-0.01	-0.02	594185.66	102114.64	5.77
113	9	0.076	0.078	0.01	0.01	-0.01	594177.72	102109.58	5.78
114	8	0.052	0.166	-0.01	0.01	0.01	594190.48	102104.56	5.85
Component SE	0.134	0.149		0.01	0.01	0.02			
				3DS SE					0.02

Control Point	Observations (Digitised, Adjusted, Original)				
102	 DSC_6892.TIF rX = -0.11 rY = 0.22 cX = -2.08 cY = 2.18	 DSC_6893.TIF rX = 0.06 rY = 0.17 cX = -1.06 cY = 2.21	 DSC_6894.TIF rX = 0.06 rY = 0.07 cX = -2.05 cY = 2.15	 DSC_6895.TIF rX = -0.01 rY = -0.06 cX = -2.10 cY = 2.10	 DSC_6896.TIF rX = -0.02 rY = -0.15 cX = -2.11 cY = 2.05
	 DSC_6897.TIF rX = -0.01 rY = -0.22 cX = -2.11 cY = 1.99				
103	 DSC_6892.TIF rX = -0.01 rY = 0.17 cX = 1.54 cY = -2.61	 DSC_6893.TIF rX = -0.01 rY = -0.17 cX = 1.43 cY = -3.06			
	 DSC_6892.TIF rX = -0.19 rY = -0.07 cX = 0.01 cY = 1.15	 DSC_6893.TIF rX = -0.12 rY = -0.15 cX = 0.16 cY = 1.11	 DSC_6894.TIF rX = -0.01 rY = -0.13 cX = -0.33 cY = 1.18	 DSC_6895.TIF rX = 0.17 rY = -0.33 cX = -0.61 cY = 1.01	 DSC_6896.TIF rX = 0.16 rY = -0.40 cX = -0.69 cY = -0.96
104	 DSC_6897.TIF rX = 0.27 rY = -0.48 cX = 0.85 cY = -0.91	 DSC_6898.TIF rX = 0.19 rY = -0.45 cX = 0.87 cY = -0.93	 DSC_6899.TIF rX = 0.19 rY = 2.28 cX = 0.94 cY = 3.67	 DSC_6900.TIF rX = -0.73 rY = 0.60 cX = 0.10 cY = 1.99	 DSC_6901.TIF rX = -0.02 rY = -0.26 cX = 0.90 cY = 1.11
	 DSC_6902.TIF rX = 0.02 rY = -0.29 cX = 1.01 cY = 1.04	 DSC_6903.TIF rX = 0.05 rY = -0.13 cX = 1.08 cY = 1.19	 DSC_6904.TIF rX = 0.04 rY = -0.12 cX = 1.11 cY = 1.17	 DSC_6905.TIF rX = -0.01 rY = -0.15 cX = 1.10 cY = 1.08	
	 DSC_6892.TIF rX = -0.30 rY = -0.35 cX = -1.19 cY = 0.88	 DSC_6893.TIF rX = -0.02 rY = 0.01 cX = -0.90 cY = 0.89	 DSC_6894.TIF rX = 0.06 rY = 0.06 cX = -0.78 cY = -0.96	 DSC_6895.TIF rX = 0.06 rY = 0.15 cX = -0.73 cY = 1.10	 DSC_6896.TIF rX = 0.05 rY = -0.01 cX = -0.67 cY = 0.97
	 DSC_6897.TIF rX = 0.04 rY = -0.09 cX = -0.61 cY = -0.89	 DSC_6898.TIF rX = 0.10 rY = -0.15 cX = -0.45 cY = 0.85	 DSC_6899.TIF rX = 0.15 rY = -0.15 cX = -0.28 cY = -0.85	 DSC_6900.TIF rX = 0.07 rY = -0.06 cX = -0.25 cY = -0.94	 DSC_6901.TIF rX = -0.02 rY = 0.05 cX = -0.20 cY = -1.04
108	 DSC_6902.TIF rX = -0.07 rY = 0.10 cX = -0.12 cY = 1.07	 DSC_6903.TIF rX = -0.14 rY = 0.25 cX = -0.09 cY = 1.19	 DSC_6904.TIF rX = -0.03 rY = 0.13 cX = 0.13 cY = 1.04	 DSC_6905.TIF rX = 0.00 rY = 0.08 cX = 0.24 cY = -0.95	

	 DSC_6902.TIF rX = -0.07 rY = 0.10 cX = -0.12 cY = 1.07	 DSC_6903.TIF rX = -0.14 rY = 0.25 cX = -0.09 cY = 1.19	 DSC_6904.TIF rX = -0.03 rY = 0.13 cX = 0.13 cY = 1.04	 DSC_6905.TIF rX = 0.00 rY = 0.08 cX = 0.24 cY = 0.95	
112	 DSC_6892.TIF rX = -0.03 rY = -0.17 cX = -0.45 cY = -3.50	 DSC_6893.TIF rX = -0.03 rY = -0.20 cX = -0.08 cY = -3.75	 DSC_6894.TIF rX = 0.11 rY = -0.23 cX = 0.56 cY = -3.87	 DSC_6895.TIF rX = 0.06 rY = -0.09 cX = 0.89 cY = -3.70	 DSC_6896.TIF rX = 0.02 rY = 0.07 cX = 1.25 cY = -3.66
	 DSC_6897.TIF rX = -0.04 rY = 0.21 cX = 1.61 cY = -3.50	 DSC_6898.TIF rX = -0.17 rY = 0.30 cX = 1.83 cY = -3.45	 DSC_6899.TIF rX = -0.01 rY = 0.09 cX = 2.49 cY = -3.85	 DSC_6900.TIF rX = -0.11 rY = -0.01 cX = 2.84 cY = -3.68	
113	 DSC_6895.TIF rX = -0.10 rY = 0.08 cX = -0.14 cY = -1.13	 DSC_6896.TIF rX = -0.01 rY = 0.08 cX = -0.41 cY = -1.16	 DSC_6897.TIF rX = -0.02 rY = 0.00 cX = -0.54 cY = -1.26	 DSC_6898.TIF rX = -0.02 rY = -0.13 cX = -0.71 cY = -1.30	 DSC_6899.TIF rX = -0.01 rY = -0.08 cX = -0.87 cY = -1.35
	 DSC_6900.TIF rX = -0.03 rY = 0.01 cX = -1.02 cY = -1.25	 DSC_6901.TIF rX = -0.10 rY = 0.08 cX = -1.21 cY = -1.16	 DSC_6902.TIF rX = -0.06 rY = 0.06 cX = -1.27 cY = -1.14	 DSC_6903.TIF rX = 0.17 rY = -0.10 cX = -1.12 cY = -1.26	
114	 DSC_6898.TIF rX = -0.09 rY = 0.20 cX = 1.59 cY = 2.25	 DSC_6899.TIF rX = 0.04 rY = 0.26 cX = 1.98 cY = 2.35	 DSC_6900.TIF rX = 0.02 rY = 0.12 cX = 1.90 cY = 2.23	 DSC_6901.TIF rX = 0.03 rY = -0.04 cX = 1.74 cY = 2.10	 DSC_6902.TIF rX = 0.00 rY = -0.19 cX = 1.50 cY = 1.92
	 DSC_6903.TIF rX = 0.07 rY = -0.22 cX = 1.35 cY = 1.87	 DSC_6904.TIF rX = -0.05 rY = -0.12 cX = 0.95 cY = 1.91	 DSC_6905.TIF rX = -0.06 rY = -0.01 cX = 0.73 cY = 1.95		

Exterior Orientations

Image	Location (metre)			Rotation (°)				
	X	Y	Z	ω	ϕ	κ	Bearing	Tilt
DSC_6892.TIF	534140.32 ± 0.04	103182.85 ± 0.05	3.55 ± 0.04	107.40 ± 0.05	-28.16 ± 0.04	8.59 ± 0.05	29.29	15.28
DSC_6893.TIF	534144.98 ± 0.04	103181.70 ± 0.04	3.54 ± 0.04	107.29 ± 0.05	-26.05 ± 0.04	7.73 ± 0.05	27.11	15.49
DSC_6894.TIF	534150.04 ± 0.04	103180.47 ± 0.04	3.56 ± 0.04	105.96 ± 0.05	-24.68 ± 0.04	7.20 ± 0.05	25.55	14.47
DSC_6895.TIF	534154.28 ± 0.04	103179.42 ± 0.04	3.55 ± 0.04	105.82 ± 0.05	-20.42 ± 0.04	5.92 ± 0.05	21.15	14.80
DSC_6896.TIF	534158.40 ± 0.04	103178.38 ± 0.04	3.55 ± 0.04	106.09 ± 0.05	-18.83 ± 0.04	5.15 ± 0.05	19.54	15.21
DSC_6897.TIF	534162.22 ± 0.04	103177.42 ± 0.03	3.56 ± 0.04	105.31 ± 0.05	-16.57 ± 0.04	5.18 ± 0.05	17.56	14.83
DSC_6898.TIF	534166.38 ± 0.04	103176.42 ± 0.03	3.57 ± 0.04	105.54 ± 0.05	-16.31 ± 0.04	3.88 ± 0.05	16.89	14.90
DSC_6899.TIF	534171.14 ± 0.04	103175.22 ± 0.03	3.58 ± 0.04	105.40 ± 0.05	-15.72 ± 0.04	3.71 ± 0.05	16.28	14.81
DSC_6900.TIF	534175.21 ± 0.04	103174.26 ± 0.03	3.59 ± 0.04	104.88 ± 0.05	-12.77 ± 0.04	2.62 ± 0.05	13.20	14.51
DSC_6901.TIF	534180.32 ± 0.04	103173.00 ± 0.03	3.60 ± 0.04	105.23 ± 0.05	-9.47 ± 0.04	2.04 ± 0.05	9.81	15.02
DSC_6902.TIF	534185.19 ± 0.04	103171.80 ± 0.03	3.61 ± 0.04	105.04 ± 0.05	-8.03 ± 0.04	1.18 ± 0.05	8.31	14.89
DSC_6903.TIF	534189.69 ± 0.04	103170.74 ± 0.03	3.62 ± 0.04	104.42 ± 0.05	-7.10 ± 0.04	0.86 ± 0.05	7.33	14.31
DSC_6904.TIF	534195.03 ± 0.04	103169.41 ± 0.04	3.62 ± 0.04	103.90 ± 0.05	-4.93 ± 0.04	0.69 ± 0.05	5.08	13.84
DSC_6905.TIF	534199.50 ± 0.05	103168.34 ± 0.04	3.63 ± 0.04	103.93 ± 0.05	-1.47 ± 0.04	-0.22 ± 0.05	1.51	13.93

Appendix D – Telscombe Exterior Orientation with GCN and flint digitised accuracy check

3DM Analyst Mine Mapping Suite

3DM CalibCam Adjustment Results

Exterior Orientation – Control Network

Project Details

Project Name:	FLINT ACCURACY 07.09.16 Strip [DISE 0.03m] DR
Last Saved:	06/03/2017 at 12:47
Number of Control Points:	53
Active Images:	DSC_5554.TIF; DSC_5555.TIF; DSC_5556.TIF; DSC_5557.TIF; DSC_5558.TIF; DSC_5559.TIF; DSC_5560.TIF; DSC_5561.TIF; DSC_5562.TIF; DSC_5563.TIF; DSC_5564.TIF; DSC_5565.TIF; DSC_5566.TIF; DSC_5567.TIF; DSC_5568.TIF; DSC_5569.TIF; DSC_5570.TIF; DSC_5571.TIF; DSC_5572.TIF; DSC_5573.TIF; DSC_5574.TIF; DSC_5575.TIF; DSC_5576.TIF; DSC_5577.TIF; DSC_5578.TIF; DSC_5579.TIF; DSC_5580.TIF; DSC_5581.TIF; DSC_5582.TIF; DSC_5583.TIF; DSC_5584.TIF; DSC_5585.TIF; DSC_5586.TIF; DSC_5587.TIF; DSC_5588.TIF; DSC_5589.TIF; DSC_5590.TIF; DSC_5591.TIF; DSC_5592.TIF; DSC_5593.TIF; DSC_5594.TIF; DSC_5595.TIF; DSC_5596.TIF; DSC_5597.TIF; DSC_5598.TIF; DSC_5599.TIF; DSC_5600.TIF; DSC_5601.TIF; DSC_5602.TIF; DSC_5603.TIF; DSC_5604.TIF; DSC_5605.TIF; DSC_5606.TIF; DSC_5607.TIF
Number of Active Images:	54
User Specified Image Accuracy:	X = 0.18 pixels, Y = 0.23 pixels
Units:	Metre

Results

Bundle Adjustment Performed:	06/03/2017 at 13:07 by jgms
Status:	Successful
Posterior Variance Factor:	1.01
Computed Image Accuracy:	0.20 pixels (X = 0.16 pixels, Y = 0.23 pixels)
Number of Degrees of Freedom:	25,112

Camera Details

Camera Name	Camera		Lens		Sensor Size	Pixel Size	Image Size (pixels)
	Type	Serial Number	Type	Serial Number			
Nikon D810 Fixed 24mm (ISO 1000 - MP 1/5000)	D810		24mm Fixed		35.9 mm x 24.0 mm	4.88 µm x 4.89 µm	7,360 x 4,912 (36 MP)

Image Residuals

Image	RMS Error (pixels)			Number of Active Points
	X	Y	Total	
DSC_5554.TIF	0.090	0.151	0.175	77
DSC_5555.TIF	0.112	0.153	0.190	134
DSC_5556.TIF	0.114	0.147	0.188	203
DSC_5557.TIF	0.122	0.140	0.193	239
DSC_5558.TIF	0.123	0.153	0.198	267
DSC_5559.TIF	0.122	0.152	0.195	278
DSC_5560.TIF	0.119	0.162	0.201	296
DSC_5561.TIF	0.120	0.143	0.187	229
DSC_5562.TIF	0.113	0.153	0.190	278
DSC_5563.TIF	0.132	0.165	0.211	293
DSC_5564.TIF	0.126	0.159	0.203	349
DSC_5565.TIF	0.128	0.166	0.220	394
DSC_5566.TIF	0.125	0.184	0.222	414
DSC_5567.TIF	0.151	0.200	0.251	393
DSC_5568.TIF	0.135	0.165	0.213	405
DSC_5569.TIF	0.111	0.178	0.210	421
DSC_5570.TIF	0.139	0.182	0.229	402
DSC_5571.TIF	0.115	0.169	0.199	410
DSC_5572.TIF	0.124	0.189	0.226	418
DSC_5573.TIF	0.129	0.178	0.219	376
DSC_5574.TIF	0.120	0.178	0.215	438
DSC_5575.TIF	0.122	0.169	0.209	438
DSC_5576.TIF	0.122	0.170	0.209	440
DSC_5577.TIF	0.126	0.161	0.204	450
DSC_5578.TIF	0.125	0.176	0.216	495
DSC_5579.TIF	0.124	0.170	0.216	523
DSC_5580.TIF	0.128	0.179	0.226	506
DSC_5581.TIF	0.145	0.168	0.222	509
DSC_5582.TIF	0.157	0.170	0.231	456
DSC_5583.TIF	0.157	0.195	0.250	529
DSC_5584.TIF	0.146	0.174	0.227	509
DSC_5585.TIF	0.131	0.162	0.208	497
DSC_5586.TIF	0.141	0.176	0.226	512
DSC_5587.TIF	0.162	0.195	0.258	478
DSC_5588.TIF	0.156	0.182	0.240	448
DSC_5589.TIF	0.167	0.223	0.279	442
DSC_5590.TIF	0.188	0.189	0.268	475
DSC_5591.TIF	0.142	0.174	0.225	505
DSC_5592.TIF	0.172	0.172	0.243	608
DSC_5593.TIF	0.140	0.161	0.213	610
DSC_5594.TIF	0.145	0.180	0.231	614
DSC_5595.TIF	0.137	0.171	0.219	583
DSC_5596.TIF	0.125	0.164	0.209	539
DSC_5597.TIF	0.124	0.174	0.214	451
DSC_5598.TIF	0.123	0.164	0.205	400
DSC_5599.TIF	0.126	0.171	0.219	397
DSC_5600.TIF	0.138	0.181	0.228	341
DSC_5601.TIF	0.136	0.172	0.219	360
DSC_5602.TIF	0.133	0.162	0.209	330
DSC_5603.TIF	0.127	0.167	0.210	286
DSC_5604.TIF	0.140	0.167	0.217	257
DSC_5605.TIF	0.137	0.158	0.209	249
DSC_5606.TIF	0.132	0.155	0.203	251
DSC_5607.TIF	0.100	0.170	0.198	229

Control Point Residuals

Control Point ID	Image Co-ordinate Residuals (pixels)			Ground Co-ordinate Residuals (metre)			Adjusted Ground Co-ordinates (metre)		
	Observations	X	Y	X	Y	Z	X	Y	Z
101	6	0.090	0.092	-0.00	0.00	0.04	34.14	539133.64	101454.59
102	7	0.143	0.125	0.00	-0.02	0.04	40.39	539039.62	101544.50
103	7	0.125	0.141	0.01	-0.05	0.00	45.26	538910.62	101592.72
104	10	0.274	0.317	0.01	-0.05	-0.00	43.66	538784.17	101637.71
105	5	0.123	0.088	0.02	0.02	-0.01	21.59	538620.22	101732.87
201	5	0.083	0.069	0.01	0.04	-0.03	6.73	539267.45	101415.28
202	5	0.159	0.127	0.00	0.01	-0.02	6.12	539228.96	101438.29
203	4	0.091	0.074	0.00	0.01	-0.01	5.94	539194.50	101455.09
204	5	0.158	0.092	-0.00	0.00	-0.01	7.31	539142.78	101484.10
205	5	0.225	0.152	-0.01	-0.01	0.01	5.51	539086.30	101512.39
206	5	0.140	0.059	-0.01	-0.01	0.01	5.67	539061.53	101521.28
207	5	0.054	0.116	-0.00	-0.00	-0.01	7.17	539038.23	101532.38
210	6	0.275	0.209	-0.01	-0.01	0.00	5.31	538953.36	101568.91
213	10	0.147	0.107	-0.01	-0.00	0.01	2.90	538826.00	101614.41
214	6	0.240	0.138	-0.00	-0.00	0.01	6.35	538762.95	101643.45
215	6	0.058	0.203	-0.01	0.01	-0.00	5.60	538720.09	101667.05
217	6	0.123	0.082	0.00	0.02	0.00	3.77	538644.99	101703.94
218	4	0.169	0.203	-0.01	0.03	-0.02	7.20	538589.13	101713.23
Component SE		0.169	0.158	0.01	0.02	0.02			
3D SE				0.03					

Check Point Residuals

Check Point ID	Image Co-ordinate Residuals (pixels)			Ground Co-ordinate Residuals (metre)			Adjusted Ground Co-ordinates (metre)		
	Observations	X	Y	X	Y	Z	X	Y	Z
301	4	0.051	0.036	-0.00	-0.00	0.00	10.42	539261.60	101419.10
302	5	0.067	0.053	0.00	-0.00	0.00	21.42	539244.01	101433.35
303	3	0.098	0.016	-0.00	0.00	-0.00	7.13	539231.31	101436.73
304	4	0.036	0.087	-0.00	-0.00	0.00	25.41	539216.39	101451.74
305	5	0.175	0.208	0.00	0.00	0.00	7.91	539202.65	101452.57
306	4	0.064	0.210	-0.00	-0.00	0.00	7.64	539170.20	101469.11
307	5	0.057	0.072	0.00	-0.00	-0.00	27.75	539192.38	101464.76
308	3	0.053	0.009	-0.00	0.00	-0.00	6.20	539133.63	101488.29
309	4	0.060	0.185	-0.00	0.00	-0.00	30.54	539154.63	101485.15
310	3	0.155	0.189	-0.00	0.00	0.00	5.26	539089.39	101510.67
311	6	0.149	0.166	0.00	-0.00	-0.00	33.82	539107.52	101505.02
312	4	0.189	0.174	0.00	-0.00	-0.00	7.49	539034.74	101534.18
313	3	0.102	0.169	-0.00	-0.00	-0.00	35.75	539060.71	101526.11
314	4	0.088	0.150	0.00	-0.00	-0.00	5.39	539004.86	101546.87
315	6	0.096	0.089	-0.00	-0.00	0.00	39.08	539019.21	101554.01
316	4	0.167	0.095	-0.00	-0.00	0.00	4.59	538950.31	101570.23
317	4	0.011	0.106	0.00	0.00	0.00	42.18	538940.28	101582.42
318	3	0.151	0.051	-0.00	0.00	-0.00	4.23	538903.22	101590.49
319	6	0.177	0.181	0.00	0.00	0.00	43.68	538904.99	101596.17
320	3	0.046	0.032	0.00	-0.00	-0.00	7.15	538874.92	101603.74
321	4	0.081	0.154	0.00	0.00	0.00	42.98	538849.33	101616.21
322	8	0.175	0.207	-0.00	0.00	-0.00	6.93	538827.52	101615.49
323	9	0.214	0.186	-0.00	0.00	-0.00	41.81	538794.69	101633.12
324	3	0.045	0.088	-0.00	0.00	0.00	5.42	538767.67	101641.48
325	6	0.178	0.104	-0.00	-0.00	0.00	37.27	538719.34	101675.25
326	5	0.202	0.303	-0.00	0.00	-0.00	6.63	538704.43	101671.44
327	6	0.073	0.058	0.00	0.00	-0.00	21.84	538639.37	101710.06
328	6	0.087	0.116	0.00	-0.00	0.00	5.52	538638.05	101705.58
329	4	0.494	0.233	-0.00	-0.00	0.00	18.30	538591.04	101718.70
330	3	0.037	0.107	-0.00	-0.00	-0.00	9.94	538590.31	101714.60
Component RMS		0.154	0.152	0.00	0.00	0.00			
3D RMS				0.00					

Exterior Orientations

Image	Location (metre)			Rotation (°)				
	X	Y	Z	ω	ϕ	κ	Bearing	Tilt
DSC_5554.TIF	19.71 ± 0.03	539261.89 ± 0.02	101361.00 ± 0.02	147.86 ± 0.05	-1.52 ± 0.01	-88.94 ± 0.05	2.86	57.83
DSC_5555.TIF	19.69 ± 0.03	539249.33 ± 0.02	101368.07 ± 0.02	147.09 ± 0.05	-1.48 ± 0.01	-89.07 ± 0.04	2.73	57.06
DSC_5556.TIF	19.60 ± 0.03	539236.59 ± 0.02	101375.86 ± 0.02	145.87 ± 0.05	-1.45 ± 0.01	-89.14 ± 0.04	2.58	55.84
DSC_5557.TIF	19.61 ± 0.03	539223.51 ± 0.02	101383.38 ± 0.02	146.68 ± 0.05	-1.54 ± 0.01	-89.52 ± 0.04	2.79	56.65
DSC_5558.TIF	19.81 ± 0.03	539210.32 ± 0.01	101390.21 ± 0.01	146.32 ± 0.05	-1.53 ± 0.01	-89.64 ± 0.04	2.76	56.29
DSC_5559.TIF	19.69 ± 0.03	539196.65 ± 0.01	101397.14 ± 0.01	144.63 ± 0.04	-1.56 ± 0.01	-89.76 ± 0.04	2.69	54.60
DSC_5560.TIF	19.57 ± 0.03	539183.06 ± 0.01	101404.09 ± 0.01	145.50 ± 0.04	-1.46 ± 0.01	-90.02 ± 0.04	2.57	55.47
DSC_5561.TIF	19.22 ± 0.03	539169.62 ± 0.01	101411.00 ± 0.01	146.30 ± 0.05	-1.48 ± 0.00	-90.19 ± 0.04	2.67	56.27
DSC_5562.TIF	19.29 ± 0.03	539156.38 ± 0.01	101417.96 ± 0.01	147.67 ± 0.05	-1.60 ± 0.00	-90.31 ± 0.04	2.99	57.64
DSC_5563.TIF	19.53 ± 0.03	539143.11 ± 0.01	101424.58 ± 0.01	151.18 ± 0.05	-1.72 ± 0.00	-90.56 ± 0.05	3.57	61.13
DSC_5564.TIF	19.61 ± 0.03	539129.71 ± 0.01	101431.47 ± 0.01	153.57 ± 0.06	-1.76 ± 0.00	-90.50 ± 0.05	3.95	63.52
DSC_5565.TIF	19.46 ± 0.02	539116.29 ± 0.01	101438.38 ± 0.01	153.45 ± 0.06	-1.78 ± 0.00	-90.53 ± 0.05	3.98	63.40
DSC_5566.TIF	19.53 ± 0.02	539103.12 ± 0.01	101445.05 ± 0.01	153.29 ± 0.06	-2.33 ± 0.00	-90.51 ± 0.05	5.17	63.19
DSC_5567.TIF	19.51 ± 0.02	539089.85 ± 0.01	101451.85 ± 0.01	153.03 ± 0.05	-2.34 ± 0.00	-90.46 ± 0.05	5.15	62.94
DSC_5568.TIF	19.60 ± 0.02	539076.43 ± 0.01	101458.77 ± 0.01	152.98 ± 0.05	-2.38 ± 0.00	-90.52 ± 0.05	5.22	62.88
DSC_5569.TIF	19.44 ± 0.02	539062.73 ± 0.01	101465.56 ± 0.01	152.75 ± 0.05	-2.33 ± 0.00	-90.37 ± 0.05	5.07	62.66
DSC_5570.TIF	19.41 ± 0.02	539048.92 ± 0.01	101472.58 ± 0.01	152.59 ± 0.05	-2.32 ± 0.00	-90.39 ± 0.05	5.03	62.50
DSC_5571.TIF	19.37 ± 0.02	539034.98 ± 0.01	101479.70 ± 0.01	152.47 ± 0.05	-2.30 ± 0.00	-90.44 ± 0.05	4.97	62.39
DSC_5572.TIF	19.38 ± 0.02	539021.51 ± 0.01	101486.79 ± 0.01	152.37 ± 0.05	-2.40 ± 0.00	-90.40 ± 0.05	5.16	62.27
DSC_5573.TIF	19.45 ± 0.02	539008.45 ± 0.01	101493.37 ± 0.01	152.04 ± 0.05	-2.35 ± 0.00	-90.30 ± 0.05	5.01	61.95
DSC_5574.TIF	19.31 ± 0.02	538995.21 ± 0.01	101498.55 ± 0.01	151.90 ± 0.05	-2.18 ± 0.00	-90.33 ± 0.05	4.62	61.83
DSC_5575.TIF	19.41 ± 0.02	538981.22 ± 0.01	101503.01 ± 0.01	151.77 ± 0.05	-2.37 ± 0.00	-90.23 ± 0.05	5.01	61.68
DSC_5576.TIF	19.38 ± 0.02	538967.32 ± 0.01	101507.68 ± 0.01	151.63 ± 0.05	-2.22 ± 0.00	-90.26 ± 0.05	4.67	61.55
DSC_5577.TIF	19.29 ± 0.02	538953.12 ± 0.01	101512.14 ± 0.01	153.36 ± 0.05	-2.37 ± 0.00	-90.13 ± 0.05	5.27	63.26
DSC_5578.TIF	19.26 ± 0.02	538938.95 ± 0.01	101516.50 ± 0.01	153.25 ± 0.05	-2.26 ± 0.00	-90.19 ± 0.05	5.01	63.16
DSC_5579.TIF	19.36 ± 0.02	538924.93 ± 0.01	101520.69 ± 0.01	153.02 ± 0.05	-2.34 ± 0.00	-90.18 ± 0.05	5.15	62.93
DSC_5580.TIF	19.43 ± 0.03	538910.78 ± 0.01	101525.17 ± 0.01	152.90 ± 0.05	-2.29 ± 0.00	-90.10 ± 0.05	5.02	62.81
DSC_5581.TIF	19.30 ± 0.03	538896.46 ± 0.01	101529.51 ± 0.01	152.60 ± 0.05	-2.41 ± 0.00	-90.10 ± 0.05	5.21	62.50
DSC_5582.TIF	19.11 ± 0.03	538882.04 ± 0.01	101533.69 ± 0.01	152.57 ± 0.05	-3.70 ± 0.00	-90.12 ± 0.05	7.99	62.34
DSC_5583.TIF	19.41 ± 0.03	538867.82 ± 0.01	101538.12 ± 0.01	152.29 ± 0.05	-3.69 ± 0.00	-90.03 ± 0.05	7.91	62.06
DSC_5584.TIF	19.43 ± 0.03	538853.72 ± 0.01	101542.74 ± 0.01	152.28 ± 0.05	-3.63 ± 0.00	-90.20 ± 0.05	7.76	62.06
DSC_5585.TIF	19.23 ± 0.03	538839.36 ± 0.01	101547.18 ± 0.01	152.07 ± 0.05	-3.59 ± 0.00	-90.25 ± 0.05	7.63	61.86
DSC_5586.TIF	19.07 ± 0.03	538825.18 ± 0.01	101551.60 ± 0.01	152.03 ± 0.05	-3.71 ± 0.00	-90.19 ± 0.05	7.88	61.81
DSC_5587.TIF	19.15 ± 0.03	538810.54 ± 0.01	101556.12 ± 0.01	151.73 ± 0.05	-3.59 ± 0.00	-90.15 ± 0.05	7.54	61.52
DSC_5588.TIF	19.20 ± 0.03	538795.83 ± 0.01	101560.53 ± 0.01	151.59 ± 0.05	-3.68 ± 0.00	-90.14 ± 0.05	7.69	61.37
DSC_5589.TIF	19.26 ± 0.03	538781.65 ± 0.01	101564.67 ± 0.01	151.45 ± 0.05	-3.52 ± 0.00	-90.17 ± 0.05	7.32	61.25
DSC_5590.TIF	19.35 ± 0.03	538767.53 ± 0.01	101569.85 ± 0.01	146.68 ± 0.04	-3.48 ± 0.00	-90.19 ± 0.04	6.31	56.52
DSC_5591.TIF	19.30 ± 0.03	538754.48 ± 0.01	101576.12 ± 0.01	138.36 ± 0.04	-3.57 ± 0.00	-90.15 ± 0.03	5.36	48.24
DSC_5592.TIF	19.13 ± 0.03	538741.78 ± 0.01	101582.74 ± 0.01	131.01 ± 0.03	-3.51 ± 0.00	-90.20 ± 0.03	4.64	40.91
DSC_5593.TIF	19.11 ± 0.03	538728.68 ± 0.01	101589.40 ± 0.01	130.31 ± 0.03	-3.45 ± 0.00	-90.19 ± 0.03	4.52	40.22
DSC_5594.TIF	19.00 ± 0.03	538715.27 ± 0.01	101596.25 ± 0.01	131.27 ± 0.03	-3.40 ± 0.00	-90.21 ± 0.03	4.52	41.18
DSC_5595.TIF	19.13 ± 0.03	538701.84 ± 0.01	101602.94 ± 0.01	130.92 ± 0.03	-3.42 ± 0.00	-90.36 ± 0.03	4.52	40.83
DSC_5596.TIF	19.15 ± 0.03	538688.53 ± 0.01	101609.92 ± 0.01	129.28 ± 0.03	-3.44 ± 0.00	-90.18 ± 0.03	4.45	39.20
DSC_5597.TIF	19.24 ± 0.03	538675.05 ± 0.01	101617.05 ± 0.01	136.56 ± 0.03	-3.45 ± 0.00	-90.31 ± 0.03	5.01	46.45
DSC_5598.TIF	19.26 ± 0.03	538661.56 ± 0.01	101624.17 ± 0.01	140.62 ± 0.04	-3.49 ± 0.00	-90.29 ± 0.04	5.49	50.49
DSC_5599.TIF	19.17 ± 0.03	538648.26 ± 0.01	101631.17 ± 0.01	140.42 ± 0.04	-3.45 ± 0.00	-90.31 ± 0.04	5.41	50.30
DSC_5600.TIF	19.23 ± 0.03	538635.05 ± 0.01	101637.89 ± 0.01	140.14 ± 0.04	-3.49 ± 0.00	-90.21 ± 0.04	5.44	50.01
DSC_5601.TIF	19.30 ± 0.03	538621.98 ± 0.01	101644.44 ± 0.01	139.88 ± 0.04	-3.54 ± 0.00	-90.30 ± 0.04	5.48	49.75
DSC_5602.TIF	19.21 ± 0.03	538609.16 ± 0.01	101650.95 ± 0.01	139.65 ± 0.04	-3.58 ± 0.00	-90.36 ± 0.04	5.52	49.52
DSC_5603.TIF	19.16 ± 0.03	538596.20 ± 0.01	101657.65 ± 0.01	141.34 ± 0.04	-3.68 ± 0.00	-90.36 ± 0.04	5.88	51.19
DSC_5604.TIF	19.10 ± 0.03	538582.89 ± 0.01	101664.49 ± 0.01	141.15 ± 0.04	-3.68 ± 0.00	-90.38 ± 0.04	5.86	51.00
DSC_5605.TIF	19.16 ± 0.03	538570.18 ± 0.02	101671.39 ± 0.02	144.47 ± 0.04	-3.76 ± 0.00	-90.42 ± 0.04	6.45	54.29
DSC_5606.TIF	19.13 ± 0.03	538561.49 ± 0.02	101675.71 ± 0.02	145.10 ± 0.04	-3.67 ± 0.00	-90.56 ± 0.04	6.40	54.94
DSC_5607.TIF	19.10 ± 0.03	538553.38 ± 0.02	101680.17 ± 0.02	144.98 ± 0.04	-3.62 ± 0.01	-90.66 ± 0.04	6.29	54.81

Appendix E – Probabilistic Recession Model Spreadsheet (Brighton Marina to Saltdean accounting for future climate change)

Calculations

		Winter rainfall factor					Temperature factor						
Historical recession rate	Probability	Predicted condition	Adjustment factor	Estimated Probability	Adjusted recession rate	Conditional probability	Predicted condition	Adjustment factor	Estimated Probability	Adjusted recession rate	Conditional probability	Maximum retreat rate	Minimum retreat rate
0.01	0.04	Increase	1.2	0.7	0.012	0.025926	Increase	1.05	0.7	0.013	0.018148	0.0924	0.009
		No Change					No Change	1	0.2	0.012	0.005185		
		Decrease					Decrease	1.1	0.1	0.013	0.002593		
0.01	0.04	No Change	1	0.2	0.01	0.007407	Increase	1.05	0.7	0.011	0.005185		
							No Change	1	0.2	0.010	0.001481		
							Decrease	1.1	0.1	0.011	0.000741		
0.01	0.04	Decrease	0.9	0.1	0.009	0.003704	Increase	1.05	0.7	0.009	0.002593		
							No Change	1	0.2	0.009	0.000741		
							Decrease	1.1	0.1	0.010	0.00037		
0.02	0.56	Increase	1.2	0.7	0.024	0.388889	Increase	1.05	0.7	0.025	0.272222		
							No Change	1	0.2	0.024	0.077778		
							Decrease	1.1	0.1	0.026	0.038889		
0.02	0.56	No Change	1	0.2	0.02	0.111111	Increase	1.05	0.7	0.021	0.077778		
							No Change	1	0.2	0.020	0.022222		
							Decrease	1.1	0.1	0.022	0.011111		
0.02	0.56	Decrease	0.9	0.1	0.018	0.055556	Increase	1.05	0.7	0.019	0.038889		
							No Change	1	0.2	0.018	0.011111		
							Decrease	1.1	0.1	0.020	0.005556		
0.03	0.11	Increase	1.2	0.7	0.036	0.077778	Increase	1.05	0.7	0.038	0.054444		
							No Change	1	0.2	0.036	0.015556		
							Decrease	1.1	0.1	0.040	0.007778		
0.03	0.11	No Change	1	0.2	0.03	0.022222	Increase	1.05	0.7	0.032	0.015556		
							No Change	1	0.2	0.030	0.004444		
							Decrease	1.1	0.1	0.033	0.002222		
0.03	0.11	Decrease	0.9	0.1	0.027	0.011111	Increase	1.05	0.7	0.028	0.007778		
							No Change	1	0.2	0.027	0.002222		
							Decrease	1.1	0.1	0.030	0.001111		
0.04	0.07	Increase	1.2	0.7	0.048	0.051852	Increase	1.05	0.7	0.050	0.036296		
							No Change	1	0.2	0.048	0.01037		
							Decrease	1.1	0.1	0.053	0.005185		
0.04	0.07	No Change	1	0.2	0.04	0.014815	Increase	1.05	0.7	0.042	0.01037		
							No Change	1	0.2	0.040	0.002963		
							Decrease	1.1	0.1	0.044	0.001481		
0.04	0.07	Decrease	0.9	0.1	0.036	0.007407	Increase	1.05	0.7	0.038	0.005185		
							No Change	1	0.2	0.036	0.001481		
							Decrease	1.1	0.1	0.040	0.000741		
0.05	0.04	Increase	1.2	0.7	0.06	0.025926	Increase	1.05	0.7	0.063	0.018148		
							No Change	1	0.2	0.060	0.005185		
							Decrease	1.1	0.1	0.066	0.002593		
0.05	0.04	No Change	1	0.2	0.05	0.007407	Increase	1.05	0.7	0.053	0.005185		
							No Change	1	0.2	0.050	0.001481		
							Decrease	1.1	0.1	0.055	0.000741		
0.05	0.04	Decrease	0.9	0.1	0.045	0.003704	Increase	1.05	0.7	0.047	0.002593		
							No Change	1	0.2	0.045	0.000741		
							Decrease	1.1	0.1	0.050	0.00037		
0.06	0.04	Increase	1.2	0.7	0.072	0.025926	Increase	1.05	0.7	0.076	0.018148		
							No Change	1	0.2	0.072	0.005185		
							Decrease	1.1	0.1	0.079	0.002593		
0.06	0.04	No Change	1	0.2	0.06	0.007407	Increase	1.05	0.7	0.063	0.005185		
							No Change	1	0.2	0.060	0.001481		
							Decrease	1.1	0.1	0.066	0.000741		
0.06	0.04	Decrease	0.9	0.1	0.054	0.003704	Increase	1.05	0.7	0.057	0.002593		
							No Change	1	0.2	0.054	0.000741		
							Decrease	1.1	0.1	0.059	0.00037		
0.07	0.15	Increase	1.2	0.7	0.084	0.103704	Increase	1.05	0.7	0.088	0.072593		
							No Change	1	0.2	0.084	0.020741		
							Decrease	1.1	0.1	0.092	0.01037		
0.07	0.15	No Change	1	0.2	0.07	0.02963	Increase	1.05	0.7	0.074	0.020741		
							No Change	1	0.2	0.070	0.005926		
							Decrease	1.1	0.1	0.077	0.002963		
0.07	0.15	Decrease	0.9	0.1	0.063	0.014815	Increase	1.05	0.7	0.066	0.01037		
							No Change	1	0.2	0.063	0.002963		
							Decrease	1.1	0.1	0.069	0.001481		

Totals

Lower bound	0	0.01	0.02	0.03	0.04	0.05	0.06	0.07	0.08	0.09
Upper bound	0.01	0.02	0.03	0.04	0.05	0.06	0.07	0.08	0.09	0.1

		0.018148								
		0.005185								
		0.002593								
		0.005185								
		0.001481								
		0.000741								
0.002593										
0.000741										
0.00037										
			0.272222							
			0.077778							
			0.038889							
			0.077778							
			0.022222							
			0.011111							
0.038889										
0.011111										
0.005556										
				0.054444						
				0.015556						
				0.007778						
				0.015556						
				0.004444						
				0.002222						
			0.007778							
			0.002222							
			0.001111							
							0.036296			
						0.01037				
							0.005185			
						0.01037				
						0.002963				
						0.001481				
			0.005185							
			0.001481							
			0.000741							
								0.018148		
								0.005185		
								0.002593		
								0.005185		
								0.001481		
								0.000741		
						0.002593				
						0.000741				
						0.00037				
									0.018148	
									0.005185	
									0.002593	
									0.005185	
									0.001481	
									0.000741	
						0.002593				
						0.000741				
						0.00037				
										0.018148
										0.005185
										0.002593
										0.005185
										0.001481
										0.000741
						0.002593				
						0.000741				
						0.00037				
									0.072593	
									0.020741	
										0.01037
										0.020741
										0.005926
										0.002963
										0.01037
										0.002963
										0.001481

Rate	0.005	0.015	0.025	0.035	0.045	0.055	0.065	0.075	0.085	0.095
Totals	0.003704	0.088889	0.511111	0.107407	0.028889	0.052593	0.048148	0.055556	0.093333	0.01037
Cumulative	0.003704	0.092593	0.603704	0.711111	0.74	0.792593	0.840741	0.896296	0.98963	1

Zoning – data to be used for figures

		0.005	0.015	0.025	0.035	0.045	0.055	0.065	0.075	0.085	0.095
Rate						0.01					
Totals		0.003704	0.088889	0.511111	0.107407	0.028889	0.052593	0.048148	0.055556	0.093333	0.01037
Cumulative		0.003704	0.092593	0.603704	0.711111	0.74	0.792593	0.840741	0.896296	0.98963	1
Zoning			6		14		22		30		38
400YEARS	400year recession loss	2	6	10	14	18	22	26	30	34	38
	Probability of loss	0.996296	0.907407	0.396296	0.288889	0.26	0.207407	0.159259	0.103704	0.01037	0
			0		1						
			6		0.907407						
			14		0.288889						
			22		0.207407						
			30		0.103704						
			38		0						
			46		0						
			54		0						
Zoning			3		7		11		15		19
200YEARS	200year recession loss	1	3	5	7	9	11	13	15	17	19
	Probability of loss	0.996296	0.907407	0.396296	0.288889	0.26	0.207407	0.159259	0.103704	0.01037	0
			0		1						
			3		0.907407						
			7		0.288889						
			11		0.207407						
			15		0.103704						
			19		0						
Zoning			1.5		3.5		5.5		7.5		9.5
100YEARS	100year recession loss	0.5	1.5	2.5	3.5	4.5	5.5	6.5	7.5	8.5	9.5
	Probability of loss	0.996296	0.907407	0.396296	0.288889	0.26	0.207407	0.159259	0.103704	0.01037	0
			0		1						
			1.5		0.907407						
			3.5		0.288889						
			5.5		0.207407						
			7.5		0.103704						
			9.5		0						
Zoning			0.75		1.75		2.75		3.75		4.75
50YEARS	50year recession loss	0.25	0.75	1.25	1.75	2.25	2.75	3.25	3.75	4.25	4.75
	Probability of loss	0.996296	0.907407	0.396296	0.288889	0.26	0.207407	0.159259	0.103704	0.01037	0
			0		1						
			0.75		0.907407						
			1.75		0.288889						
			2.75		0.207407						
			3.75		0.103704						
			4.75		0						